frontiers | Research Topics

Hydro-climate extremes and natural disasters during global warming: Observation, projection, and mitigation

Edited by
Peng Sun, Shuliang Zhang, Ming Luo, Shao Sun and Zhen Liu

Published in
Frontiers in Environmental Science
Frontiers in Ecology and Evolution

ISSN 1664-8714
ISBN 978-2-8325-2971-3
DOI 10.3389/978-2-8325-2971-3

About Frontiers

Frontiers is more than just an open access publisher of scholarly articles: it is a pioneering approach to the world of academia, radically improving the way scholarly research is managed. The grand vision of Frontiers is a world where all people have an equal opportunity to seek, share and generate knowledge. Frontiers provides immediate and permanent online open access to all its publications, but this alone is not enough to realize our grand goals.

Frontiers journal series

The Frontiers journal series is a multi-tier and interdisciplinary set of open-access, online journals, promising a paradigm shift from the current review, selection and dissemination processes in academic publishing. All Frontiers journals are driven by researchers for researchers; therefore, they constitute a service to the scholarly community. At the same time, the *Frontiers journal series* operates on a revolutionary invention, the tiered publishing system, initially addressing specific communities of scholars, and gradually climbing up to broader public understanding, thus serving the interests of the lay society, too.

Dedication to quality

Each Frontiers article is a landmark of the highest quality, thanks to genuinely collaborative interactions between authors and review editors, who include some of the world's best academicians. Research must be certified by peers before entering a stream of knowledge that may eventually reach the public - and shape society; therefore, Frontiers only applies the most rigorous and unbiased reviews. Frontiers revolutionizes research publishing by freely delivering the most outstanding research, evaluated with no bias from both the academic and social point of view. By applying the most advanced information technologies, Frontiers is catapulting scholarly publishing into a new generation.

What are Frontiers Research Topics?

Frontiers Research Topics are very popular trademarks of the *Frontiers journals series*: they are collections of at least ten articles, all centered on a particular subject. With their unique mix of varied contributions from Original Research to Review Articles, Frontiers Research Topics unify the most influential researchers, the latest key findings and historical advances in a hot research area.

Find out more on how to host your own Frontiers Research Topic or contribute to one as an author by contacting the Frontiers editorial office: frontiersin.org/about/contact

Hydro-climate extremes and natural disasters during global warming: Observation, projection, and mitigation

Topic editors

Peng Sun — Anhui Normal University, China
Shuliang Zhang — Nanjing Normal University, China
Ming Luo — Sun Yat-sen University, China
Shao Sun — Chinese Academy of Meteorological Sciences, China
Zhen Liu — Center for Climate Physics, Institute for Basic Science, Republic of Korea

Citation

Sun, P., Zhang, S., Luo, M., Sun, S., Liu, Z., eds. (2023). *Hydro-climate extremes and natural disasters during global warming: Observation, projection, and mitigation*. Lausanne: Frontiers Media SA. doi: 10.3389/978-2-8325-2971-3

Table of contents

frontiers | Frontiers in Environmental Science

TYPE Editorial
PUBLISHED 13 July 2023
DOI 10.3389/fenvs.2023.1246007

OPEN ACCESS

EDITED AND REVIEWED BY
Abu Reza Md. Towfiqul Islam,
Begum Rokeya University, Bangladesh

*CORRESPONDENCE
Shao Sun,
sunshao@cma.gov.cn

RECEIVED 24 June 2023
ACCEPTED 05 July 2023
PUBLISHED 13 July 2023

CITATION
Sun S, Sun P, Zhang S, Luo M and Liu Z (2023), Editorial: Hydro-climate extremes and natural disasters during global warming: observation, projection, and mitigation.
Front. Environ. Sci. 11:1246007.
doi: 10.3389/fenvs.2023.1246007

Editorial: Hydro-climate extremes and natural disasters during global warming: observation, projection, and mitigation

Shao Sun[1]*, Peng Sun[2], Shuliang Zhang[3], Ming Luo[4] and Zhen Liu[5]

[1]State Key Laboratory of Severe Weather, Chinese Academy of Meteorological Sciences, Beijing, China, [2]School of Geography and Tourism, Anhui Normal University, Wuhu, China, [3]School of Geography, Nanjing Normal University, Nanjing, China, [4]School of Geography and Planning, Sun Yat-Sen University, Guangzhou, China, [5]Center for Climate Physics, Institute for Basic Science, Busan, Republic of Korea

KEYWORDS

climate change, natural hazard, climate mitigation, climate adaptation, climate modelling, weather forecast, risk analysis

Editorial on the Research Topic
Hydro-climate extremes and natural disasters during global warming: observation, projection, and mitigation

In the face of global warming and its far-reaching consequences, understanding and mitigating hydro-climate extremes and natural disasters have become critical priorities. This Research Topic brings together a collection of research papers that shed light on the observation, projection, and mitigation of these phenomena in the context of a changing climate. In this editorial, we will delve into three key areas: hydrometeorological forecasting, climate projection, and climate impacts, drawing insights from the titles and abstracts of the selected articles.

The first segment of this Research Topic focuses on advancements in hydrometeorological forecasting. We are thrilled to showcase four research papers that explore innovative methodologies and techniques in this field. In terms of rainfall nowcasting methods, Zhu et al. proposes a nowcasting method that utilizes long short-term memory (LSTM) networks to achieve accurate rainfall predictions up to 6 h ahead. The method incorporates atmospheric conditions to reduce radar estimate errors, resulting in improved forecast performance compared to conventional extrapolation approaches. On a monthly scale, Yan et al. presents a runoff prediction model that combines machine learning and feature importance analysis, which improved the simulation capability of the monthly runoff prediction model. The model utilizes mutual information and feature importance ranking methods to select suitable predictors from global climate factors and local hydrometeorological information. The results demonstrate improved prediction accuracy compared to other commonly used models.

In order to enhance the prediction accuracy of local precipitation area and intensity, Duan et al. explores the impact of the upper gravity-wave damping layer on precipitation predictions in complex terrain. The study uses the Weather Research and Forecasting model and conducts sensitivity tests for a strong precipitation event in southern Gansu, China. The results clarified the influence of the upper gravity-wave damping layer on precipitation over complex terrain. In addition, Deng et al. conducted a case study in the Poyang Lake Basin of

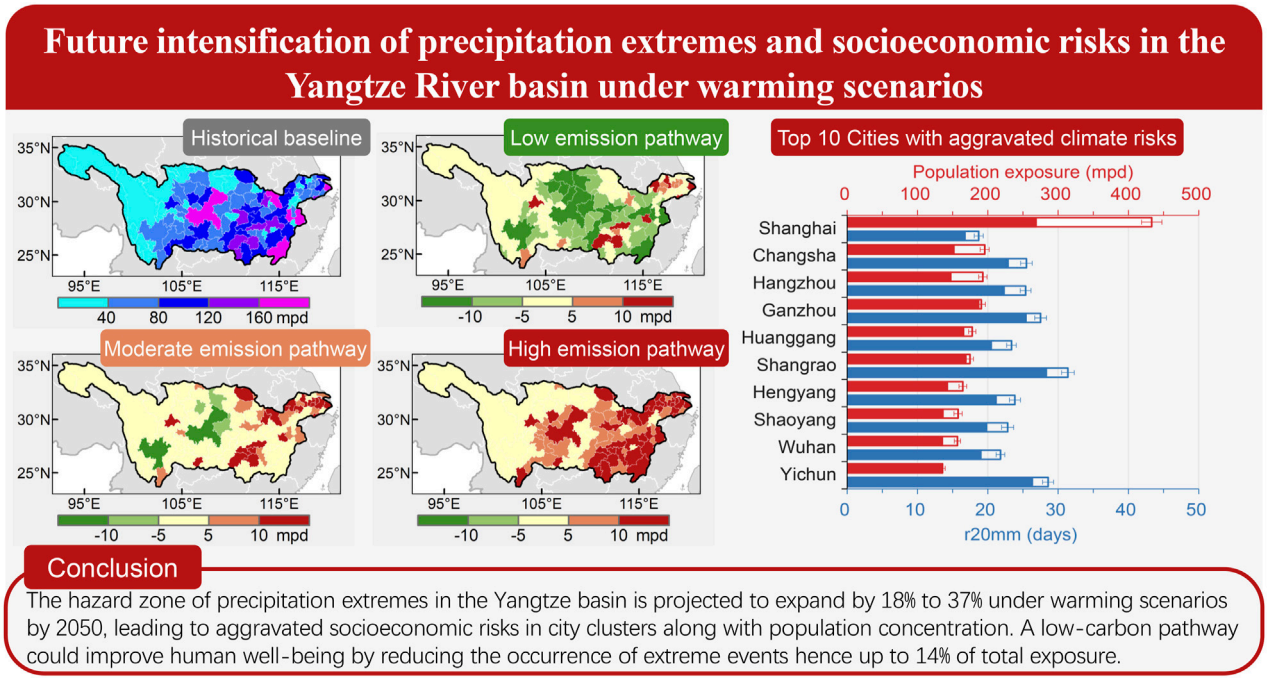

FIGURE 1
Population exposure to precipitation extremes in the historical baseline, and its projected evolutions under low, moderate, and high emission scenarios in the Yangtze River basin around 2050.

China to explore the sensitivity of different parameterization schemes in the Weather Research and Forecast model (WRF) for simulating heavy precipitation events. Various combinations of cumulus schemes, microphysical schemes, and land surface schemes are evaluated. The findings provide insights into the optimal parameterization schemes for simulating extreme precipitation events.

Moving forward, the subsequent editorials will delve into the areas of climate projection, shedding light on their significance in addressing hydro-climate extremes. New advances in climate modelling capabilities have brought higher-resolution and accurate climate simulations, which was used by Rettie et al. to provide an overview of projected changes in climate extremes indices for Ethiopia based on downscaled daily climate datasets. The analysis examines the magnitude and spatial patterns of trends in climate extremes under different emission scenarios, which contributes to a better understanding of the projected changes in climate extremes in Ethiopia. Focusing on southeast China coast, Li et al. highlighted the importance of data reliability in estimating changes in humid-heat extremes. The study compares observational and reanalysis datasets across China and identifies inhomogeneity in relative humidity series. The findings reveal underestimation of increasing rates for frequency and intensity of humid-heat extremes in southeast China due to data inhomogeneity.

The third segment of this Research Topic focuses on climate impacts and socioeconomic risks. As accelerated climate change continues to impact regions worldwide, it is crucial to understand and address the specific risks posed by extreme events in vulnerable areas. The Yangtze River basin, with its well-developed economy and susceptibility to climate extremes, represents a critical region that requires urgent attention. In a recent study, Sun et al. quantified the historical and projected population exposure to precipitation extremes in the basin, projected the expansion process of hazard zone for precipitation extremes, and revealed the contributing factors behind climate risk. The study highlighted the tendency for population growth and migration toward the lower Yangtze basin, leading to exacerbated socioeconomic risks in megacities (Figure 1). However, the research also emphasized that a low-carbon pathway could improve human wellbeing by reducing the occurrence of extreme events hence up to 14% of total exposure.

The southeastern China coast is a typical region around the globe that affected by heavy rainstorms. In this Research Topic, Ye et al. investigated and assessed the comprehensive risk of non-typhoon rainstorms in Fujian Province of China. By establishing an index system and employing risk assessment methods, the study identified the spatial pattern of non-typhoon rainstorm risks, emphasizing the dominant role of disaster-causing factors and the influence of topography on hazard distribution. The findings provide valuable insights for understanding and managing non-typhoon rainstorm risks in the region.

In southwestern China, wildfires have caused significant losses of life and property. A paper titled *Synthesized assessments of wildfire risks over southwestern China* conducted by Xu et al. contributes to localized wildfire risk assessments by considering essential elements such as hazard, vulnerability, and disaster prevention/mitigation capacity. The study revealed high wildfire risk areas in the western region of 103°E and the northern region of 28°N, particularly in low-altitude suburban regions with high climate hazards. These risk maps facilitate a comprehensive understanding of current and future

patterns of wildfire risks, aiding in the formulation of effective prevention and suppression policies.

Urbanization has a significant effect on human perceived temperatures (HPT). A case study in South China conducted by Lin and Guo quantitatively assessed the impacts of urbanization on mean and extreme HPT, highlighting the substantial increases in mean HPT and the frequency of extreme HPT events, particularly in highly urbanized areas such as the Pearl River Delta. These findings emphasize the need to consider human comfort in urban planning and adaptation strategies for subtropical humid climate zones.

Collectively, these research papers provide valuable insights into climate risks and extreme events in various regions of China. They underscore the urgency of addressing these challenges and highlight the importance of considering factors such as population dynamics, topography, and urbanization in risk assessments and mitigation strategies. Policymakers, researchers, and stakeholders must collaborate to develop sustainable approaches that enhance climate resilience, protect vulnerable populations, and ensure the sustainable development of these regions. By combining scientific knowledge with effective policies and practices, we can strive towards a more resilient and climate-ready world.

We hope that the findings presented in this Research Topic will foster further interdisciplinary collaborations, stimulate innovative research approaches, and contribute to evidence-based strategies for mitigating the impacts of hydro-climate extremes and natural disasters amidst global warming. We extend our gratitude to the authors for their valuable contributions and to the reviewers for their diligent efforts in ensuring the scientific rigor and quality of the published research. Most importantly, we would like to express our appreciation to the editorial team and the reviewers for their continuous support and guidance throughout the publication process. Their dedication and expertise have been instrumental in bringing this Research Topic to fruition.

Author contributions

All authors listed have made a substantial, direct, and intellectual contribution to the work and approved it for publication.

Conflict of interest

The authors declare that the research was conducted in the absence of any commercial or financial relationships that could be construed as a potential conflict of interest.

Publisher's note

frontiers | Frontiers in Environmental Science

TYPE Original Research
PUBLISHED 10 November 2022
DOI 10.3389/fenvs.2022.1044969

OPEN ACCESS

EDITED BY
Shao Sun,
Chinese Academy of Meteorological Sciences, China

REVIEWED BY
Chenghai Wang,
Lanzhou University, China
Wen Huo,
Institute of Desert Meteorology, China

*CORRESPONDENCE
H. X. Duan,
duanhx@iamcma.cn

SPECIALTY SECTION
This article was submitted to Atmosphere and Climate, a section of the journal Frontiers in Environmental Science

RECEIVED 15 September 2022
ACCEPTED 27 October 2022
PUBLISHED 10 November 2022

CITATION
Duan HX, Zhang TJ, Gong CS, Zhou GL and Zhu W (2022), Influence of the upper gravity-wave damping layer on precipitation over complex terrain. *Front. Environ. Sci.* 10:1044969. doi: 10.3389/fenvs.2022.1044969

Influence of the upper gravity-wave damping layer on precipitation over complex terrain

H. X. Duan[1,2,3]*, T. J. Zhang[1,2,3], C. S. Gong[1,2,3], G. L. Zhou[1,2,3] and WeiWei Zhu[4]

[1]Institute of Arid Meteorology, China Meteorological Administration, Lanzhou, China, [2]Key Laboratory of Arid Climatic Change and Reducing Disaster of Gansu Province, Lanzhou, China, [3]Northwestern Regional Center of Numerical Weather Prediction, China, [4]Changdu Meteorological Bureau of Tibet, Changdu, China

The upper boundary condition of a numerical model can significantly influence the model prediction results. This study used the Weather Research and Forecasting model to introduce the Rayleigh damping layer in the complex terrain of southern Gansu, China. Sensitivity tests are conducted for a strong precipitation process that occurred in 2016. Meanwhile, the effects of the upper gravity-wave damping layer and vertical velocity damping term of different schemes are explored. The results show that the upper gravity-wave damping layer can effectively reduce the error caused by false gravity waves in the complex terrain of southern Gansu Province. Moreover, the applicability of this model in the complex terrain of northwestern China is discussed. Overal, prediction of the precipitation area and intensity is improved. Specifically, the introduction of an implicit gravity-wave damping layer has a more significant damping effect on the upwardly propagating gravity-wave.

KEYWORDS

upper gravity-wave absorption, complex terrain, precipitation, WRF model, energy flux

Highlights

- The use of upper gravity-wave damping layer can improve the forecast of precipitation area in complex terrain area.
- The use of upper gravity-wave damping layer can reduce the number of false precipitation reports for Tibet plateau slopes.
- Implicit gravity-wave damping layer has a more significant damping effect on the upwardly propagating gravity-wave.

Introduction

Development of gravity-waves can trigger heavy rain on the mesoscale (Uccellini, 1975; Li 1978; Stobie et al., 1983; Uccellini and Koch, 1987; Xu et al., 2013). Many studies

have shown that the excitation sources of gravity waves are mostly located in the troposphere, but the fluctuations can propagate vertically to the middle and upper levels, affecting the middle atmosphere circulation and energy balance, and the material exchange and distribution of the entire atmosphere (Bretherton 1969; Holton 1982; Huang 1985). It is quite difficult to accurately reflect the influence of gravity waves on the upper model boundary in a numerical model, which, traditionally including rigid covers and constant pressure surfaces, can completely reflect the energy of upwardly propagating gravity-waves. A feasible improvement is to add a damping layer to optimize the influence of gravity wave energy on the top of the boundary layer. This layer can use the horizontal diffusion or Rayleigh damping, and its damping coefficient increases with height (Klemp and Lilly, 1978; Durran and Klemp, 1983).

Klemp and Durran (1983) proposed a radiation upper boundary condition for a mesoscale numerical model that allows vertically propagating internal gravity-waves to be transmitted out of the computational region with minimal reflection. Klemp et al. (2008) followed by proposing a new technique, in which an implicit Rayleigh damping term is applied only to the vertical velocity, as a final adjustment at the end of each small (acoustic) time step. This technique has immense potential in idealistic experiments and practical numerical forecasting applications.

The damping plays a significant role in the development of atmospheric circulation at the top of the atmosphere. However, they are exclusively based on theoretical research and fail to apply the model in weather forecasting, especially in complex terrains. Accordingly, this study first introduces the data and the mode test design. Subsequently, the influence of Rayleigh damping absorption on a heavy precipitation process in the complex terrain of the central and southern Gansu Province, China is analyzed from the perspectives of precipitation pattern and gravity-wave-related diagnostic quantity. Finally, the influence of Rayleigh damping absorption on heavy precipitation in the complex terrain is summarized and discussed.

Model, experimental design, and data

This study applied the Weather Research and Forecasting model (WRF) 3.9.1, with horizontal resolutions of 27 km, 9 km, and 3 km, and 40 vertical layers. D03 has a total of 562 × 376 grid points. Initial and boundary conditions refer to the 6-h data from the Global Forecast System (GFS) developed by the National Center of Environmental Prediction (NCEP) (http://www2.mmm.ucar.edu/wrf/users/download/get_sources_wps_geog.html). Details about models and areas for simulation can be found in the study by Duan et al. (2018). The specified physical models are as follows: Noah Land Surface Model (Ek et al., 2003), Rapid Radiative Transfer Model (RRTM), Long Wave Radiation Model (Mlawer et al., 1997), Dudhia Short Wave Radiation Model (Dudhia, 1989), Asymmetric Convective (ACM 2) Planetary Boundary Layer Model (Pleim, 2007a; Pleim, 2007b), and Kain-Fritsch Cumulus Convection Scheme (Kain, 2004) and Thompson Microphysics Scheme (Thompson et al., 2008). We did not employ a convective scheme in our smallest domain because the grid spacing of 2 km should be fine enough to handle explicit convection. Table 1 shows the sensitivity test schemes of the upper gravity-wave damping layer or an implicit gravity-wave damping layer (3) vertical velocity damping flagvertical velocity damping.

TABLE 1 Test design Damp_opt:0: no diffusion layer; 1: increased diffusion layer; 3: implicit gravity-wave damping layer.

	W_damping	Zdamp(m)	Damp_opt
CTRL	0	50	0
TEST 1	0	50	1
TEST 2	1	50	1
TEST 3	0	100	1
TEST 4	1	100	1
TEST 5	0	50	3
TEST 6	1	50	3
TEST 7	0	100	3
TEST 8	1	100	3

Zdamp is the damping depth (m) from model top. Damp_opt is Upper Damping in WRF model: Either a layer of increased diffusion (damp_opt = 1) or a Rayleigh relaxation layer (2) or an implicit gravity-wave damping layer (3), can be added near the model top to control reflection from the upper boundary.W_damping is vertical velocity damping flag. Vertical motion can be damped to prevent the model from becoming unstable with locally large vertical velocities. (0, is no vertical velocity damping, 1is vertical velocity damping).

Additionally, the data used for verification of gravity-wave diagnostic quantity was drawn from the ERA5 hourly data (https://cds.climate.copernicus.eu/cdsapp#!/dataset/reanalysis-era5-pressure-levels?tab=form).

Results

Impact on precipitation forecasting

An event of large-scale precipitation occurred in the eastern part of northwestern China from 0800 to 2300 BT 22 June 2016. There were showers/thunderstorms in the area to the east of Wuwei City, Gansu Province, China. There were heavy rainfall in the cities of Dingxi, Longnan, Tianshui, and Pingliang. Additionally, downpours were reported in three villages and towns of the Min County, Dingxi City and Dangchang

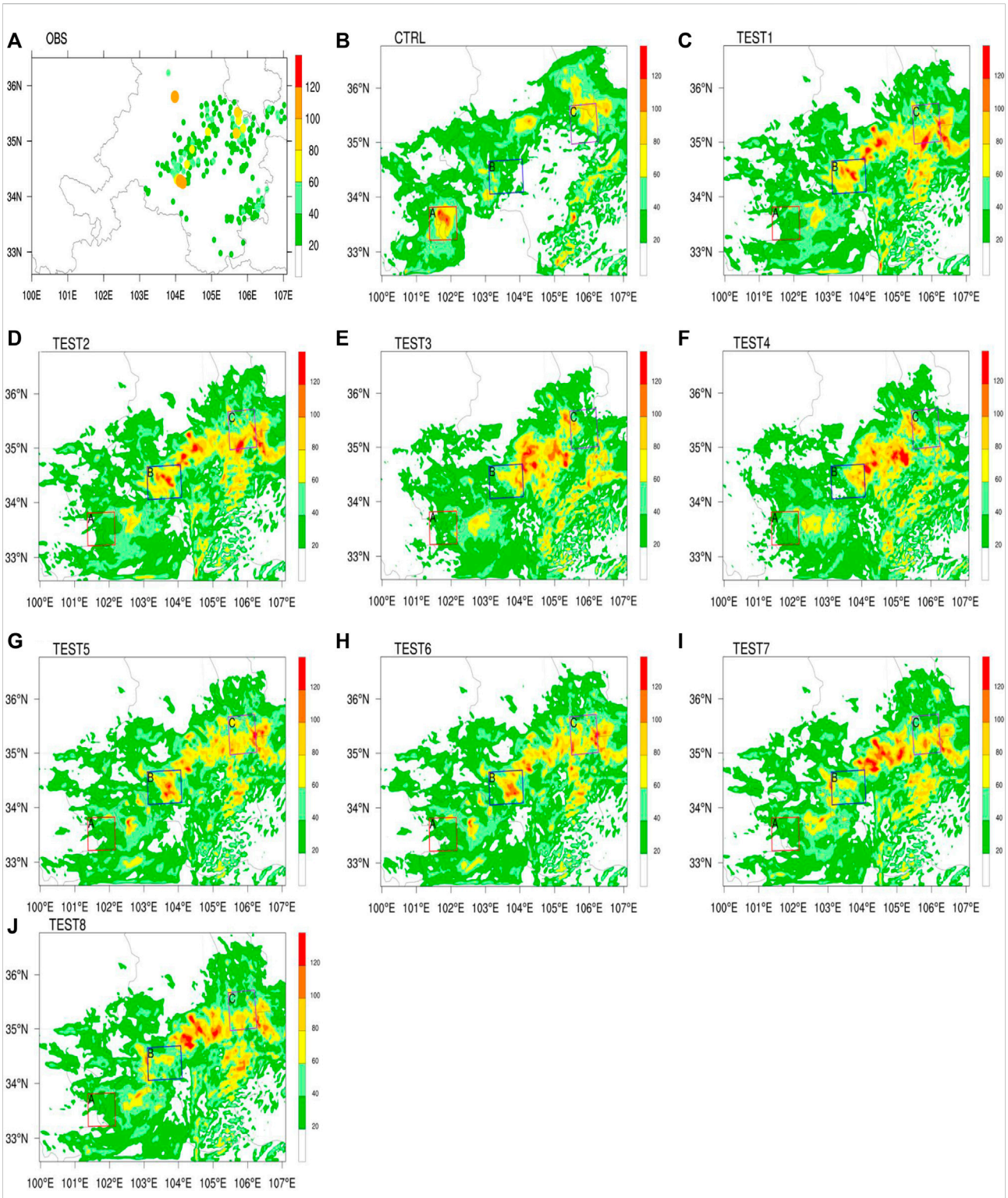

FIGURE 1
24-h precipitation distribution map (0800 BT June 22 to 0800 BT 23 June 2016, units: mm) **(A)** Observation by the Gansu Provincial Regional Station **(B)** CTRL **(C–J)** TESTs 1–8.

County, Longnan City (Figure 1A). A total of 24 stations received short-term heavy precipitation in cities such as Weinan, Dingxi, Gannan, Pingliang, and Qingyang. The maximum hourly precipitation intensity reached 38.8 mm in Mazichuan Town, Min County (at 2200 BT June 22). Among the 1047 towns and villages that received precipitation in Gansu Province, 342 received moderate rain, 175 heavy rain, 35 rainstorm, and three downpour. Substantial precipitation occurred in Mazichuan Town, Min County (120.4 mm); Awu Town, Dangchang County (111.7 mm); Hadapu Town, Dangchang County (107.9 mm); Jingning County (89.2 mm); Jiahe Town, Jingning County (81.7 mm); and Sigou Town, Min County (78.4 mm). The amount of precipitation in Lanzhou City was 7.7 mm.

The 24-h precipitation predicted by the CTRL mainly occurred in the eastern part of northwestern China, with moderate rain mainly received in the eastern part of Qinghai Province, the central and eastern parts of Gansu Province, and the central part of Shaanxi Province (Figure 1B). Rainstorms primarily impacted the Gannan, Dingxi, and Pingliang Areas of Gansu Province as well as the southern part of Ningxia Province. Rainstorm-impacted areas in the Longnan and Tianshui Areas of Gansu Provinces were relatively scattered. The maximum 24-h precipitation reached 156 mm—the precipitation center being the Gannan and Ganzi Areas. The CTRL achieved a good forecast effect in terms of the downpour at a single station in the Longnan Area as well as the areas where rain fell in the Tianshui Area. Moreover, two SW-NE extended rainfall belts were successfully predicted by the CTRL, although their actual locations were more northwestern. However, the forecast of strong precipitation in Area A proved to be empty forecasting, and strong precipitation in southern Dingxi was not predicted. After the upper gravity-wave damping/diffusion was introduced, significant changes in the overall precipitation pattern were observed compared to those in the CTRL, although the precipitation conditions of the eight TESTs were not much different (Figures 1C–J). Specifically, precipitation in Area A was significantly reduced from the level of downpour in the CTRL to the level of moderate rain. When the upper gravity-wave layer was a diffusion layer (Figures 1C,D) (that is, TESTs 1 and 2), precipitation in amounts exceeding 25 cm mainly fell in the central and eastern parts of Gansu Province, and rainstorms primarily occurred in the central and southern parts of Dingxi, Tianshui, and west Pingliang. In contrast, when the upper gravity-wave layer was an implicit gravity-wave damping layer with a model layer height of 50 mb (that is, TESTs 5 and 6), the rainfall areas resembled those in TESTs 1 and 2, with certain deviations in the heavy precipitation centers; these deviations in TESTs 5 and 6 mainly occurred in the southern part of the Dingxi Area and the western part of the Pingliang Area. Moreover, scattered precipitation was predicted in the central part of Gansu Province, which was closer to the actual observation. The results show that the precipitation areas predicted by TEST 3/4 are more concentrated, and the heavy precipitation centers are mainly concentrated in the central part of Gansu Province; meanwhile, the prediction intensity of B and C is relatively small. Strong precipitation areas predicted by TESTs 7 and 8 were more concentrated mainly in the northern and central parts of Dingxi, Gansu Province, while scattered and strong precipitation was observed in the Tianshui and Pingliang Areas. Overall, the precipitation predicted in the southern part of Dingxi was actually of weak density.

In general, all the sensitivity tests significantly improved the false forecasting of rainstorm in the southwestern part of Area A in the CTRL, and they had strong predictions regarding the precipitation in the central parts of Dingxi, Tianshui, and Pingliang. From the perspectives of precipitation area and intensity, the results of TESTs 5 and 6 regarding precipitation area and intensity were closer to the observational data in this precipitation process.

Influence on gravity-waves and vertical velocity

Qin et al. (2007) argued that atmospheric gravity-waves at night are more stable than those during daytime, which is more conducive to the excitation of gravity-waves. Shear instability in the lower atmosphere may trigger gravity-waves. Figure 2 shows the vertical profile of the pseudoequivalent potential temperature at 1900 BT 22 June 2016, in Area A with the strongest empty forceasting intensity. This period witnessed the strongest precipitation in Area A. Specifically, the vertical profile of the pseudoequivalent potential temperature of ERA5 data at 2200 BT 22 June 2016 reflects the influence of the upper gravity-wave damping layer on the stability in the complex terrain (Figure 2A). The middle and lower parts of the atmosphere (450–700 mb) above Area A are featured by convective unstable stratification, whereas that at 450–300 mb is characterized by natural stratification. When the height is 300–150 mb, the contour map of the pseudoequivalent potential temperature becomes sparse and relatively flat, with minor fluctuations. In contrast, the contour map above 150 mb is denser and straighter. According to the vertical profile of the pseudoequivalent potential temperature by the CTRL (Figure 2B), the interval below 500 mb is the main host to the unstable convective stratification, whereas the interval of 400–150 mb is mainly dominated by natural stratification, where the contour map of the pseudoequivalent potential temperature is sparse and significantly fluctuates in the whole longitude zone. Meanwhile, the contour map of the pseudoequivalent potential temperature is denser and accompanied by stronger disturbances in the interval above 150 mb, with the disturbance able to reach upwardly until 50 mb. In contrast, the pseudoequivalent potential temperatures of TESTs 1–4 are similar in the interval below 150 mb, but they become dense

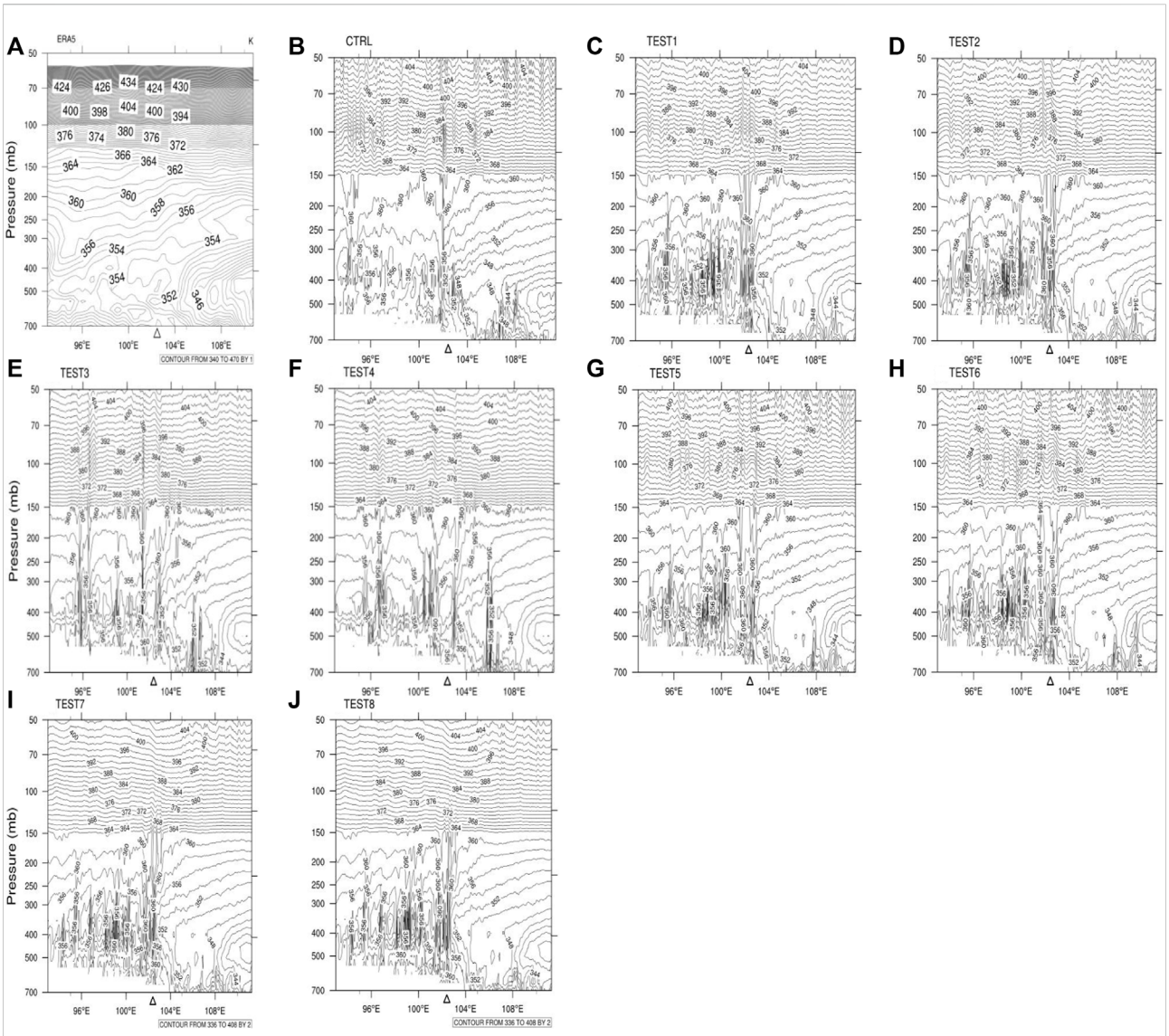

FIGURE 2
Vertical profiles of the pseudoequivalent potential temperature at 1900 on 22 June 2016 over Area A (units: K) **(A)** ERA5, **(B)** CTRL, **(C–J)** TESTs 1–8.

and straight in the interval above 150 mb, which, together with the strong fluctuation above Area A, demonstrate the upward transmission of the gravity-wave disturbance until 50 mb. Compared to other sensitivity TESTs and ERA5, TEST 3/4 is slightly different from other experiments in that it is more stable in predicting the pseudoequivalent potential temperature over Area A, and the disturbance above 150MB is straighter than in other experiments. TESTs 7 and 8 have similar vertical profiles of pseudoequivalent potential temperatures in the interval below 150 mb. However, the pseudoequivalent potential temperatures of TESTs 7 and 8 are similar to those of ERA5, the contour map of which is dense and straight. Regardless of weak fluctuation in the 150–300 mb interval, there is little fluctuation in the upper atmosphere, which indicates an implicit gravity-wave damping layer for the upper gravity-wave damping layer parameter. Moreover, the model significantly reduces the upward propagation height of the gravity-wave generated by the undulating terrain, when the upper adsorption boundary layer is 100 mb. Correspondingly, the upward propagation of unstable energy is suppressed, accompanied by the eventually reduced occurrence of false precipitation. Additionally, the prediction of the precipitation situation by each TEST suggests the unobvious influence of the vertical velocity damping term on the TEST results.

Figure 3 shows the distribution of vertical velocity and potential temperature at 150 hPa. ERA5 shows that Area A

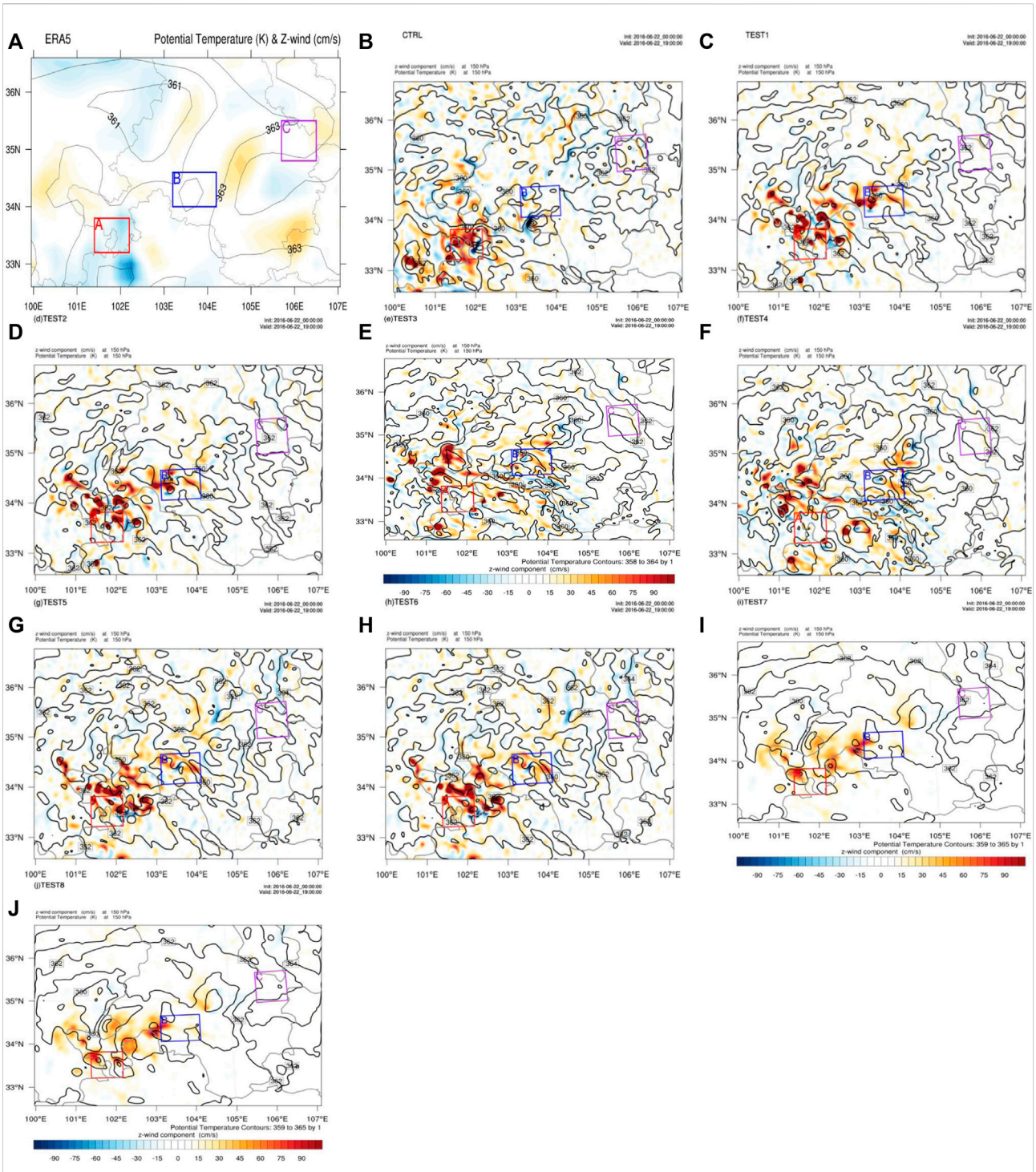

FIGURE 3
150 hPa pseudoequivalent potential temperature level distribution map (unit: K).

has obvious subsidence movement, whereas Areas B and C have no obvious vertical movement (Figure 3A). Additionally, the three areas are not in the high potential temperature area or the dense potential temperature isoline zone. Area A predicted by the CTRL still has a strong upward movement at 150 hPa (Figure 1B). Meanwhile, the area is still in the high potential temperature zone, and the potential temperature isolines are relatively dense. There is weak upward movement in Area B, and the potential

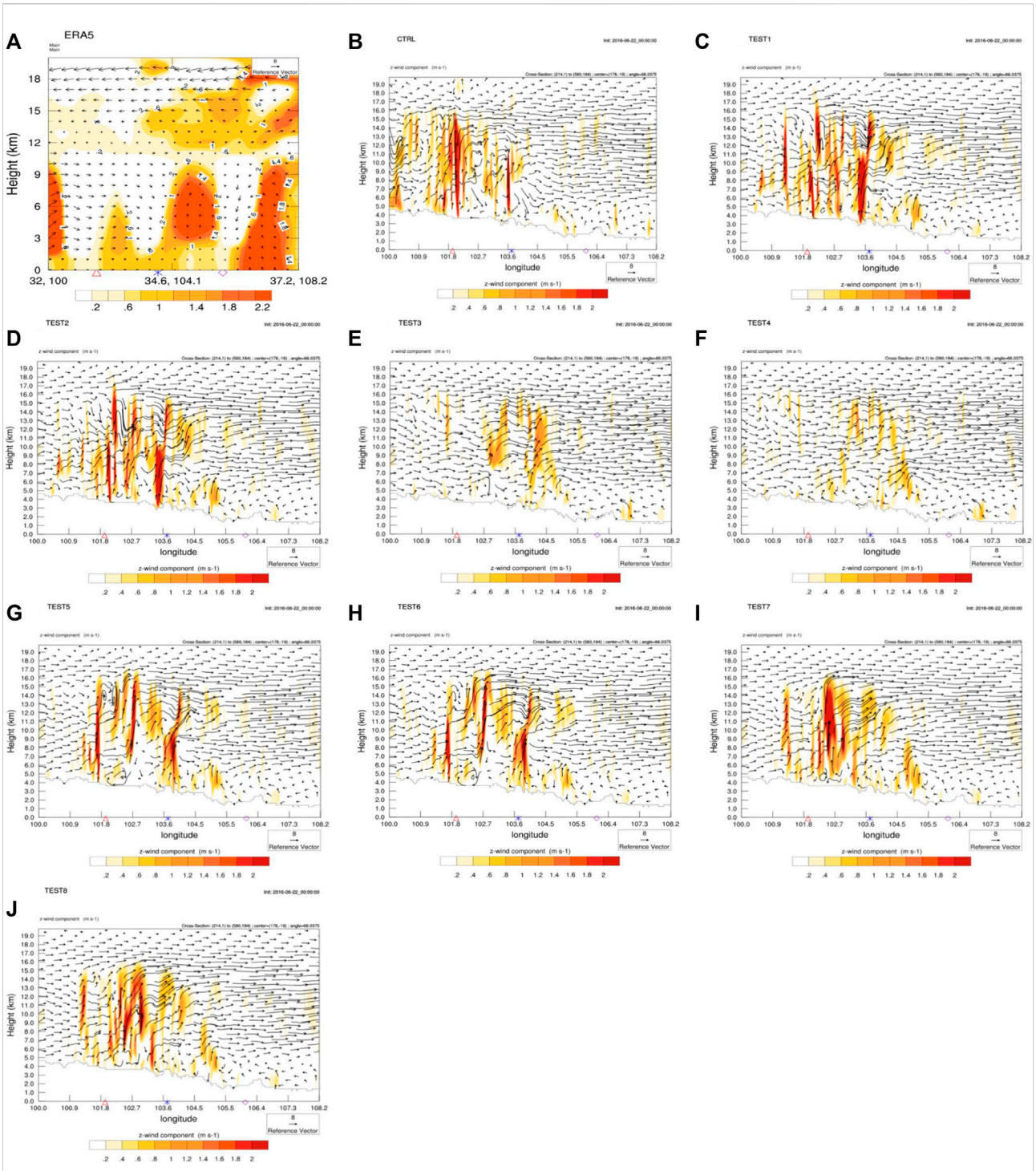

FIGURE 4
Vertical section of vertical velocity (shaded, unit: m/s) and vertical wind field (arrow, unit: m/s) over Area A, China at 19:00 on 22 June 2016 (unit: K) **(A)** ERA5; **(B)** CTRL **(C–J)** TESTs 1–8

temperature isolines are relatively dense, whereas there is little upward movement and no intensive potential temperature isolines in Area C. TEST 1/2/5/6 is similar, both of them have ascending movement in Area. The accending movement area is scattered, and the ascending movement is obviously weaker than that of the CTRL (Figures 3C, D, G, H). The ascending

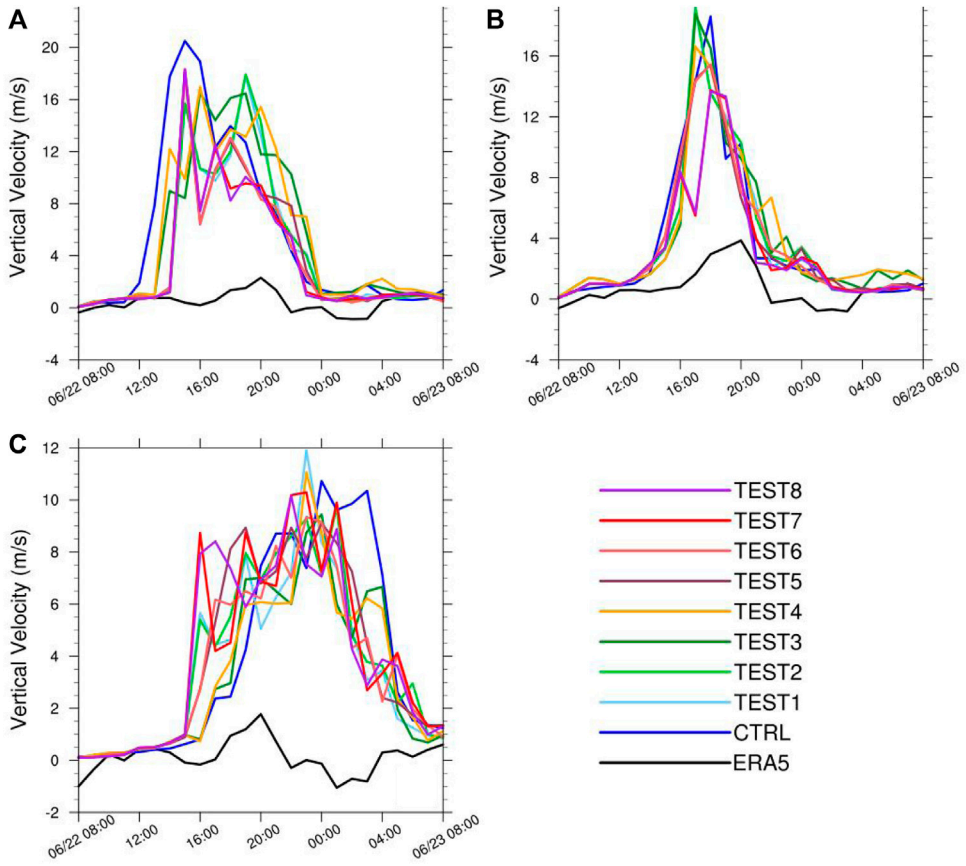

FIGURE 5
Variations in maximum vertical velocity with time in Areas **(A)** a; **(B)** b; **(C)** c (units: m/s).

movement in Area B was significantly stronger than that of the CTRL, and there was no ascending movement in Area C. The ascending motion of TEST 3/4 in Areas A and B is weaker than that in other experiments, and there is no obvious vertical motion in Area C (Figures 3E,F). The obvious difference between TEST 7/8 and other experiments is that their predicted potential temperature isolines are more sparse (Figures 3I,J). Additionally, the ascending motion of Areas A and B predicted by the two methods is obviously weaker at 150 hPa, which is similar to other experiments. The common feature of all the experiments is that they can obviously inhibit the strong upward movement of the CTRL in Area A, and adjust the intensity of the upward movement in Area B to make it closer to the actual situation.

Figure 4 shows the vertical profiles of vertical velocity and wind field over Areas A, B, and C. The result of ERA5 shows a horizontal movement of southwest wind over Area A; the vertical velocity is less than 0.2 m/s and there is little upward movement (Figure 4A). There is an obvious upward movement in Area B and its northeast. There is a weak subsidence over Area C. There is a strong upward movement in Area A predicted by the CTRL without the absorption of upper gravity wave, and the southwest air flow is uplifted here; so, strong precipitation is predicted by the CTRL in Area A (Figure 4B). In contrast, the CTRL has predicted weak ascending motion in Area B, but the ascending motion range is small. There is no ascending movement in Area C, so the CTRL has no good forecast effect on precipitation in Areas B and C. Compared to the CTRL, TEST 1/2 significantly decreased the vertical velocity in Area A, and increased the intensity of vertical velocity in Area B (Figures 4C,D). TEST 3/4 has the smallest prediction of vertical velocity in Areas A, B, and C (Figures 3E,F). There is little ascending movement in Areas A and C, and the prediction of vertical velocity in Area B is obviously weak, which is also a reason for the significant deviation of precipitation in the three areas. The vertical velocity profiles predicted by TESTs 5–8 are similar (Figures 4G–J), which obviously weaken the strong upward movement in Area A of the CTRL, and also enhance the upward movement in Area B. This is also a reason why the four experiments weaken the false precipitation in Area A and enhance the precipitation intensity forecast in Area B. However, none of

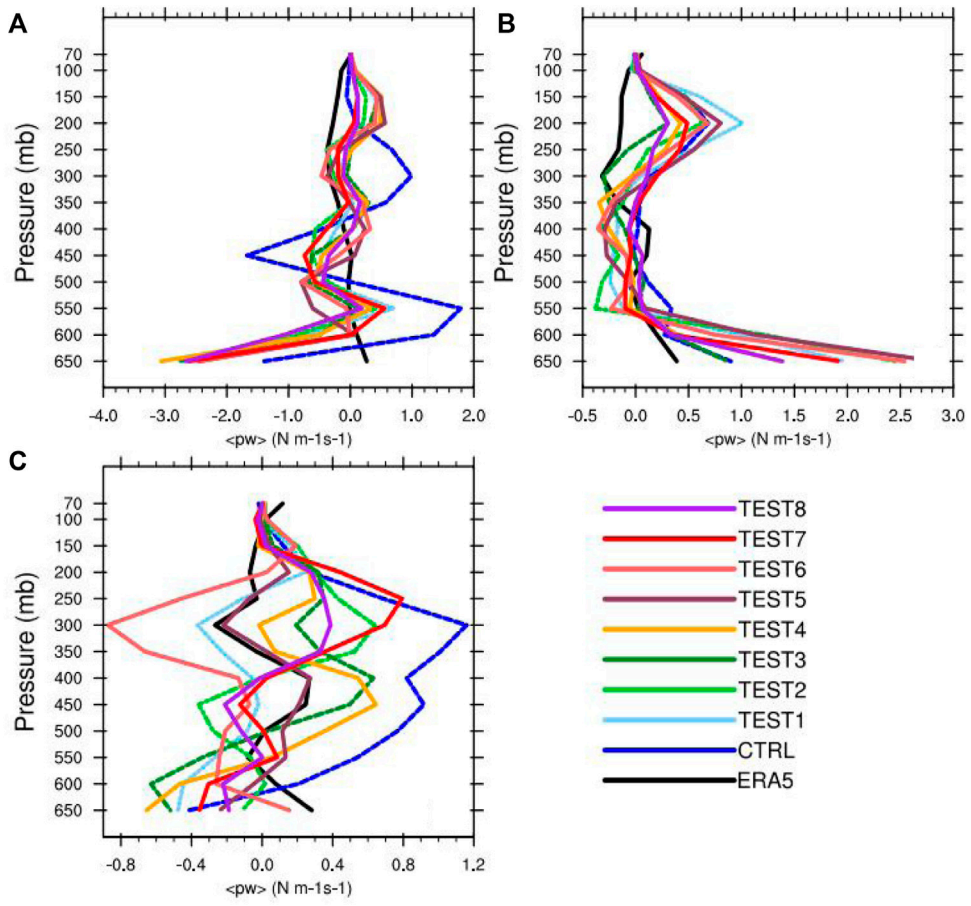

FIGURE 6
Vertical profile of time-averaged energy flux over Areas **(A)** a; **(B)** b; **(C)** c.

the eight experiments in TESTs 1–8 predicted a strong upward movement over Area C; thus, the prediction of precipitation in Area C was weaker than the actual situation.

Figure 5 shows the variation of the maximum vertical velocity over time for Area A. There was no obvious upward movement over Area A during the entire precipitation period from 0000 BT June 22 to 0000 BT June 23, as shown in the ERA5 data. Therefore, there was also no obvious precipitation in Area A. In contrast, the maximum vertical velocity predicted by the CTRL without the upper gravity-wave damping layer reached a maximum of 20.7 m/s at 1500 BT June 22, which was the largest among all experiments, followed by TESTs 8 and 7 (both 18.3 m/s) and TEST 2/1 (15.8 m/s). The maximum vertical velocity for TEST 3/4, 17 m/s, occurred at 16:00. After 16:00, the maximum vertical speed of all tests is gradually decreasing. The maximum vertical velocity for ERA5, 2.3 m/s, occurred at 2000. At this time, the closest test to ERA5 is TEST8/7. Throughout the process, the maximum vertical speed of all tests was larger than that of ERA5. Therefore, it is safe to conclude that the introduction of upper gravity-wave adsorption can significantly weaken the vertical velocity over a complex terrain. Especially for TESTs 7 and 8, their upper gravity-wave adsorbing layers are implicit gravity-wave damping layers, and they can more obviously absorb the upwardly propagating false gravity-wave generated by the complex terrain, and thus, reduce the false vertical velocity caused by the terrain.

ERA5 data showed a strong upward movement over Area B from 1800 to 2000 BT. The upwelling motion in Area B predicted by the nine WRF numerical experiments is 2 hours earlier than that predicted by ERA5, and the intensity is also greater than that predicted by ERA5. Among them, TEST 2/3 is the strongest and TEST 7/8 is the weakest. The ascending movement of Area C reflected by ERA5 was weaker than that reflected by A/B, and there was a sinking movement from 0100 to 0400 BT on June 23. In the numerical experiment, the ascending movement of Area C was continuous from 1600 BT on June 22 to 0400 BT on June 23; however, the ascending movement was weaker than that of Areas A and B.

For a more quantitative assessment, we calculated the vertical energy fluxes from the upper troposphere to the stratosphere in the Area A predicted by these experiments (Figure 4). The flux of the upwardly propagating wave energy is always positive, whereas that of the momentum is positive for the rightward propagating gravity-wave but negative for the leftward propagating one. Therefore, the wave energy flux is more informative than the vertical momentum flux. The energy flux significantly varies because of the response to the pulsating convective updraft. Therefore, a small difference in the evolution of the vertical profile can lead to a significant change in the energy flux distribution in the stratosphere (Klemp et al., 2008). According to the vertical distribution of energy flux in the ERA5 data, all the layers have positive energy flux, which implies upwardly propagating energy flux—except for the troposphere in the 300–250 mb interval. Moreover, the energy flux in the stratosphere above 200 mb is significantly larger than that in the troposphere. For the CTRL, the energy flux is negative at the upper troposphere in the 450–375 mb interval, which suggests downwardly propagating gravity-wave energy; it is positive in the upper troposphere to the middle layer of the stratosphere above 375 mb, reaching a maximum of 23.7 $Nm^{-1}s^{-1}$ at 300 mb. This indicates obvious upwardly propagating energy wave energy at these heights as predicted by the model. TESTs 1–4 share similar energy flux predictions with the CTRL, namely, the positive energy flux in the interval above 400 mb until the middle stratosphere, with a maximum that is much smaller than that in the CTRL occurring in the 400–350 mb interval. Therefore, it can be inferred that the diffusion layer, when used as the wave damping layer, has a certain diffusion ability for the false gravity-wave energy in the middle and upper layers, which reduces the propagation height of the false gravity-wave in the stratosphere generated by the terrain. In contrast, when an implicit gravity-wave damping layer is used as the upper gravity-wave damping layer (that is, TESTs 7 and 8), the energy flux is only positive in the intervals of 400–300 mb and in the vicinity of 150 mb; this implies that upwardly propagating gravity-wave has weak energy and it is negative in the intervals, suggesting downwardly propagating wave energy. Therefore, it can be said that the implicit gravity-wave damping layer can absorb the false gravity-wave in the middle and upper layers of the model, which further constrains the upward propagation of false gravity-wave, thus effectively reducing

Conclusion

It remains highly challenging to prevent the artificial reflection of gravity-wave energy from the upper boundary of the mesoscale analog domain for numerical weather prediction applications. In the past, research in this area paid more attention to the study of its theory, and less research on its effect in practical application.This study employs a new scheme for the upper gravity-wave adsorption layer to analyze an actual precipitation event. The WRF model is applied to study the effect of the upper gravity-wave damping layer on the strong precipitation in complex terrain through sensitivity tests of a strong precipitation process above the complex terrain of Gansu Province, China, on June 22–23, 2016. A false gravity-wave can propagate until the middle layer of the stratosphere over the complex terrain in the CTRL without introduction of the upper gravity-wave adsorption layer, which implies a strong prediction of vertical velocity, and thus, generation of more false precipitation reports. In contrast, the introduction of an upper gravity-wave adsorption layer can well suppress the upward propagation of the false gravity-wave generated by the complex terrain. Specifically, when the implicit gravity-wave damping layer is used as the upper gravity-wave damping layer, the damping effect on the vertically propagating energy of internal gravity-waves is more significant. Moreover, the vertical velocity damping term has little effect on the test results because of the suppression of vertical movement that improves operational robustness and prevents the model from becoming unstable when a local large vertical velocity is present. This only affects the core of a strong updraft, and therefore, has a minor impact on the results (Klemp et al., 2008).

It is worth noting that as the conclusions of this study are obtained only through a case of precipitation, more cases are required for further verification and more comprehensive evaluation in the future. In addition, the similarities and differences in the role of this upper gravitational wave absorber layer in complex terrain and flat terrain will also be aspects that we need to pay attention to in the future. And, the global warming has exacerbated the instability of the climate system, making certain extreme weather events increasingly likely. Then, what is the effect of this upper gravitational wave absorption on the process of extreme precipitation, which will also be a problem that we need to further study.

Plain language summary

To adapt to the characteristics of terrain height fluctuation and its significant drop in northwest China and to address the problem of false precipitation reports for the steep terrain area of plateau slopes, the absorption parameter of upper gravity wave is added to the model. This parameter can reduce the propagation of false gravity wave caused by terrain to the upper layer of the model. When the upper damping layer of gravity wave is an implicit damping layer, the damping effect on the vertical propagation of gravity wave energy can be more significant. The proposed scheme can improve the forecast of heavy rainfall for the steep terrain of plateau slopes, especially in Area A, while reducing the number of false precipitation reports.

Data availability statement

The raw data supporting the conclusion of this article will be made available by the authors, without undue reservation.

Author contributions

HD initiated the study. HD, TZ, CG, and GZ interpreted the data. HD wrote the article.

Acknowledgments

The first author gratefully acknowledges the funding provided by Northwest Regional Numerical Forecasting Innovation Team Fund (GSQXCXTD-2017-02) and Scientific Research Talents Fund of the Gansu Meteorological Bureau. Natural Science Foundation of Tibet Autonomous Region (XZ202001ZR0028G).

Conflict of interest

The authors declare that the research was conducted in the absence of any commercial or financial relationships that could be construed as a potential conflict of interest.

Publisher's note

All claims expressed in this article are solely those of the authors and do not necessarily represent those of their affiliated organizations, or those of the publisher, the editors and the reviewers. Any product that may be evaluated in this article, or claim that may be made by its manufacturer, is not guaranteed or endorsed by the publisher.

References

Bretherton, F. P. (1969). Momentum transport by gravity waves. *Q. J. R. Meteorol. Soc.* 95, 213–243. doi:10.1002/qj.49709540402

Duan, H. X., Li, Y. H., Zhang, T. J., Pu, Z., Zhao, C., and Liu, Y. (2018). Evaluation of the forecast accuracy of near-surface temperature and wind in northwest China based on the WRF model. *J. Meteorol. Res.* 32 (3), 469–490. doi:10.1007/s13351-018-7115-9

Dudhia, J. (1989). Numerical study of convection observed during the Winter Monsoon Experiment using a mesoscale twodimensional model. *J. Atmos. Sci.* 46, 3077–3107.

Durran, D. R., and Klemp, J. B. (1983). A compressible model for the simulation of moist mountain waves. *Mon. Wea. Rev.* 111, 2341–2361. doi:10.1175/1520-0493(1983)111<2341:acmfts>2.0.co;2

Ek, M. B., Mitchell, K. E., Lin, Y., Rogers, E., Grunmann, P., Koren, V., et al. (2003). Implementation of Noah land surface model advances in the National Centers for Environmental Prediction operational mesoscale Eta model. *J. Geophys. Res.* 108, 2002JD003296. doi:10.1029/2002jd003296

Holton, J. R. (1982). The role of gravity wave induced drag and diffusion in the momentum budget of the mesosphere. *J. Atmos. Sci.* 39, 791–799. doi:10.1175/1520-0469(1982)039<0791:trogwi>2.0.co;2

Huang, R. H. (1985). The studies on the stratospheric and mesospheric dynamics. *Chin. J. Atmos. Sci. (in Chinese)* 9 (4), 413–422. doi:10.3878/j.issn.1006-9895.1985.04.11

Kain, J. S. (2004). The Kain–Fritsch convective parameterization: An update. *J. Appl. Meteor.* 43, 170–181. doi:10.1175/1520-0450(2004)043<0170:tkcpau>2.0.co;2

Klemp, J. B., Dudhia, J., and Hassiotis, A. D. (2008). An upper gravity-wave absorbing layer for NWP applications. *Mon. Wea. Rev.* 136, 3987–4004. doi:10.1175/2008mwr2596.1

Klemp, J. B., and Durran, D. R. (1983). An upper boundary condition permitting internal gravity-wave radiation in numerical mesoscale models. *Mon. Wea. Rev.* 111, 430–444. doi:10.1175/1520-0493(1983)111<0430:aubcpi>2.0.co;2

Klemp, J. B., and Lilly, D. K. (1978). Numerical simulation of hydrostatic mountain waves. *J. Atmos. Sci.* 35, 78–107. doi:10.1175/1520-0469(1978)035<0078:nsohmw>2.0.co;2

Li, M. C. (1978). Studies on the gravity-wave initiation of the excessively heavy rainfall. *Chinese J. Atmos. Sci.* 2 (3), 201–209.

Mlawer, E. J., Taubman, S. J., Brown, P. D., Iacono, M. J., and Clough, S. A. (1997). Radiative transfer for inhomogeneous atmospheres: RRTM, a validated correlated-k model for the longwave. *J. Geophys. Res.* 102, 16663–16682. doi:10.1029/97jd00237

Pleim, J. E. (2007a). A combined local and nonlocal closure model for the atmospheric boundary layer. Part I: Model description and TESTing. *J. Appl. Meteorol. Climatol.* 46, 1383–1395. doi:10.1175/jam2539.1

Pleim, J. E. (2007b). A combined local and nonlocal closure model for the atmospheric boundary layer. Part II: Application and evaluation in a mesoscale meteorological model. *J. Appl. Meteorol. Climatol.* 46, 1396–1409. doi:10.1175/jam2534.1

Qin, W. J., Shou, S. W., Li, Q. T., Wang, Y. Q., and Peng, J. L. (2001). Research on the dynamics factors influencing development of inertial gravity waves. *Plateau Meteorology* 26 (3), 519–524.

Stobie, J. G., Einaudi, F., and Uccellini, L. W. (1983). A case study of gravity-waves-convective storms interaction: 9 may 1979. *J. Atmos. Sci.* 40 (12), 2804–2830. doi:10.1175/1520-0469(1983)040<2804:acsogw>2.0.co;2

Thompson, G., Field, P. R., Rasmussen, R. M., and Hall, W. D. (2008). Explicit forecasts of winter precipitation using an improved bulk microphysics scheme. Part II: Implementation of a new snow parameterization. *Mon. Wea. Rev.* 136, 5095–5115. doi:10.1175/2008MWR2387.1

Uccellini, L. W. (1975). A case study of apparent gravity wave initiation of severe convective storms. *Mon. Wea. Rev.* 103 (6), 497–513. doi:10.1175/1520-0493(1975)103<0497:acsoag>2.0.co;2

Uccellini, L. W., and Koch, S. E. (1987). The synoptic setting and possible energy sources for mesoscale wave disturbances. *Mon. Wea. Rev.* 115 (3), 721–729. doi:10.1175/1520-0493(1987)115<0721:tssape>2.0.co;2

Xu, Y., Yan, J. H., Wang, Q. Q., and Dong, J. B. (2013). A low-level gravity-wave triggering mechanism for rainstorm of warm zone in South China. *Plateau Meteor* 32 (4), 1050–1061. (in Chinese). doi:10.7522/j.issn.1000-0534.2012.00100

frontiers | Frontiers in Environmental Science

TYPE Original Research
PUBLISHED 10 November 2022
DOI 10.3389/fenvs.2022.1058054

OPEN ACCESS

EDITED BY
Shao Sun,
Chinese Academy of Meteorological Sciences, China

REVIEWED BY
Tangao Hu,
Hangzhou Normal University, China
Jiefeng Wu,
Nanjing University of Information Science and Technology, China
Aixia Feng,
China Meteorological Administration, China

*CORRESPONDENCE
Jinyu Ye,
jinyuyezi@126.com

SPECIALTY SECTION
This article was submitted to Atmosphere and Climate, a section of the journal Frontiers in Environmental Science

RECEIVED 30 September 2022
ACCEPTED 27 October 2022
PUBLISHED 10 November 2022

CITATION
Ye J, Zhang R, Lin G, Zhang M and Gao L (2022), Comprehensive risk assessment of non-typhoon rainstorms over the southeastern coastal region of China. *Front. Environ. Sci.* 10:1058054. doi: 10.3389/fenvs.2022.1058054

Comprehensive risk assessment of non-typhoon rainstorms over the southeastern coastal region of China

Jinyu Ye[1,2,3]*, Rongyan Zhang[4], Guangfa Lin[1,2,3], Mingfeng Zhang[1,2,3] and Lu Gao[1,2,3]

[1]Institute of Geography, Fujian Normal University, Fuzhou, China, [2]Fujian Provincial Engineering Research Center for Monitoring and Assessing Terrestrial Disasters, Fuzhou, China, [3]School of Geographical Science, Fujian Normal University, Fuzhou, China, [4]Fujian Climate Center, Fuzhou, China

The daily precipitation data (20-20 o'clock) of 66 meteorological stations from 1981 to 2020 were collected. According to the definition of rainstorm day and rainstorm process, 614 non-typhoon rainstorm processes data were obtained after removing the typhoon rainstorm processes data. Combined with the topographic data, the geological disaster points data and the social economic data, this study established an indices system from four aspects: disaster-causing factors, disaster-formative environment, disaster-affected bodies, and disaster prevention and mitigation abilities. Based on the analytic hierarchy process, the entropy method and the correlation coefficient analysis method, the combination weighting was assigned to carry out the non-typhoon rainstorm disaster risk assessment. The results show that the spatial pattern of the comprehensive risk of non-typhoon rainstorm in Fujian Province is completely different from that of typhoon rainstorm in this study area. It shows a gradually increasing trend from the eastern coastal area to the mountainous area in the northwest. The risk areas above middle were observed in the northwestern Fujian and the narrow coastal area of southeastern Fujian. Risk of most of the areas between the two mountain ranges in the middle and northwest of Fujian was relatively lower. The disaster-causing factors were the dominant risk factors of non-typhoon rainstorm. The spatial pattern of non-typhoon rainstorm hazard is obviously affected by the topography of Fujian Province. The comprehensive risk pattern of a specific historical non-typhoon rainstorm case is significantly different from that of the general comprehensive risk of non-typhoon rainstorm disasters. In terms of historical cases, most of the higher-risk and high-risk areas of non-typhoon rainstorm cases were generally small, and were concentrated in northwestern Fujian, but the comprehensive risk pattern of different cases was significantly different.

KEYWORDS

non-typhoon rainstorm, risk assessment, combination weighting method, spatial characteristics, disaster system

1 Introduction

The intensity and frequency of various natural disaster events have increased due to the recent climate change (Chen et al., 2022; Li et al., 2021; Chan et al., 2021; Li et al., 2020; Shang et al., 2019). The rainstorm flood disasters account for about 40% (Zhou et al., 2019). Consequently, developing effectively methods of rainstorm disasters risk assessment and zoning has increasingly attracted the attention of relevant scholars and government departments, and has become a hot research issue (Zhou et al., 2019; Xie and LiuXu, 2022a; Huang et al., 2022; Qiu et al., 2022; Xu et al., 2022). Located on the southeastern coast of China (Figure 1), Fujian Province is among the provinces worst affected by rainstorm disasters. There are two main types of rainstorms affecting Fujian Province, the typhoon rainstorm and the non-typhoon rainstorm. This study carries out risk assessment research for non-typhoon rainstorm disasters.

There have been many research results on the risk of rainstorm disaster. Ma et al. (2021) established risk assessment model based on a set of index system including regional vulnerability, adaptability and restorability of cities and weighted clustering assessment to realize the risk assessment of urban rainstorm and flood disaster. Wu et al. (2021) established an indicator system for urban rainstorm flooding based on an urban element analysis and determined the relative importance of the indicators based on the RF algorithm to identify the urban rainstorm flood disaster-sensitive indicator. Li et al. (2020) used the Bohai Rim, China, as a case study, and studied the risk of rainstorms under different return periods. Zhou et al. (2019) systematically reviewed the research history and the achievements of research progress on risk assessment of heavy rainfall and flood disasters in China. Chen et al., 2019b established the cloud matter-element model by coupling the cloud model with the matter-element analysis method, and assessed the risk of urban rainstorm disasters in Nanjing from 2011 to 2016. Wang et al. (2019) established a rainstorm disaster risk assessment model and conducted a graded assessment, and analyzed its impact on agriculture. Li et al. (2019) assessed the risk of rainstorm and flood disasters based on the hazard grades/indices

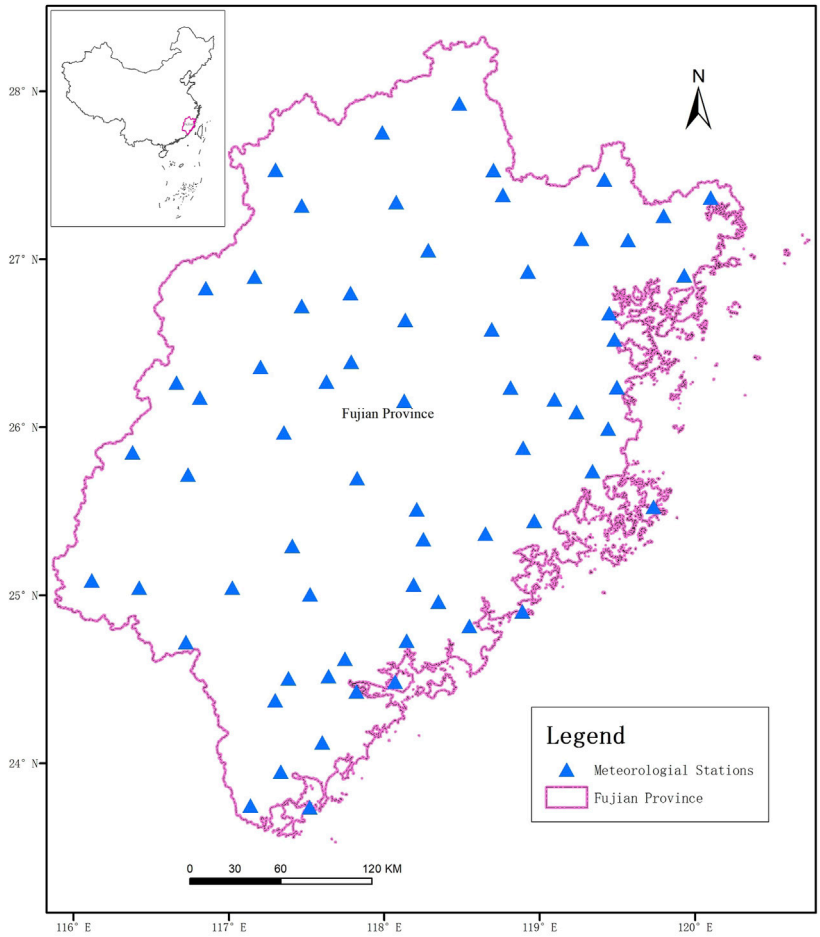

FIGURE 1
Location of study area and meteorological stations.

in Qinghai Province. Xu et al. (2018) studied the climate change characteristics of rainstorm and risk assessment of rainstorm rainfall in Jinshan of Shanghai in recent 60 years. In recent years, there are also many studies on the types and characteristics of rainstorm disasters. Jou (2020) reviewed the non-typhoon heavy rain research in Taiwan for the past 30 years. Chen et al. (2019) and Lin et al. (2017) divided the rainstorms in the southeastern coastal areas of China into the rainstorms that occurred in the pre-flood season from April to June and the typhoon rainstorms that occurred from July to September according to the time nodes, and carried out rainstorm flood researches based on the classification. These studies provide rich experience, theories and methods for rainstorm disaster risk assessment. However, most of the rainstorm disaster risk assessments did not distinguish different rainstorm types. In fact, the climatic characteristics of different types of rainstorms are obviously different, and the risk patterns are significantly different. On the other hand, researches have shown that the southeastern coastal areas of China are affected by typhoons from April to October (Ye, 2015). Typhoon rainstorms may occur in the pre-flood season, and the frontal rainstorms may also occur in typhoon season (Ying et al., 2011; Zhao et al., 2020). Therefore, the classification of typhoon rainstorm and non-typhoon rainstorm based on time node is not reasonable.

Consequently, distinguishing typhoon rainstorms from non-typhoon rainstorms scientifically and reasonably, and carrying out risk assessments based on different types of rainstorm disasters can improve the pertinence of risk prevention, which is of great significance for disaster prevention and mitigation departments. This study collected rainstorm data from 66 major meteorological stations in Fujian Province from 1981 to 2020. According to the influence time of each typhoon every year, the non-typhoon rainstorm data was obtained by excluding the typhoon rainstorm data. Combined with the ground basic data, the non-typhoon rainstorm disaster risk assessment was carried out. The objectives were to: 1) focus on the impact of non-typhoon rainstorms and discuss the risk assessment methods of non-typhoon rainstorms, 2) analyze the characteristics of non-typhoon rainstorms hazard, the sensitivity of disaster-formative environment, the vulnerability of disaster-affected bodies and the ability of disaster prevention and mitigation, 3) obtain the spatial pattern of non-typhoon rainstorm risks. The outcome of this study can provide effective scientific support for decision-making of disaster prevention and mitigation departments.

2 Data and methods

2.1 Data source

As shown in Table 1, it lists the main data and their source. The non-typhoon rainstorm data come from the Fujian Climate Center. According to the definitions of rainstorm day and rainstorm process in the Provisional Regulations on Disaster Weather Forecasting Services in Fujian Province issued by the Science, Technology and Forecast Division of Fujian Meteorological Bureau, that is, a rainstorm day refers to at least three stations with daily rainfall exceeding 50 mm and a rainstorm process refers to a weather process with more than one consecutive rainstorm day. The daily precipitation data (20-20 o'clock) of 66 meteorological stations (Figure 1) from 1981 to 2020 were collected. The rainstorm processes data were extracted based on the definitions of rainstorm day and rainstorm process. According to the influence time of each typhoon every year, 614 non-typhoon rainstorm processes data were obtained after removing the typhoon rainstorm processes data. The basic information and disaster data of non-typhoon rainstorm cases that have affected Fujian Province during 1981–2020 come from Climatological Bulletin of Fujian Province (2001–2020) and the Climate of FUJIAN (Second Edition) (Lu and Wang, 2012). The topographic data of Disaster-formative environment is a 30 m resolution DEM generated from the 1:100000 topographic map of Fujian Province. The geological disaster points data come from the website of Fujian Provincial Department of Natural Resources, and the geological disaster points density is obtained by statistical analysis and calculation with town level administrative region as the basic unit. Most of the data related to the vulnerability of disaster-affected bodies and ability of disaster prevention and mitigation come from the 2021 Fujian Statistical Yearbook and the 7th National Census Bulletin of nine prefecture-level cities in Fujian Province, China.

2.2 Methods

2.2.1 Indices system

According to the disaster system theory (Shi, 2002; Shi et al., 2014), disaster risk is the result of the comprehensive effect of disaster-causing factors, disaster-formative environment and disaster-affected bodies. Based on the study on disaster mechanism of non-typhoon rainstorm and the characteristics of disaster-formative environment and disaster-affected bodies in Fujian Province, the characterization indicators of non-typhoon rainstorm disaster risk were selected from four aspects: hazard of the disaster-causing factors, sensitivity of the disaster-formative environment, vulnerability of the disaster-affected body and disaster prevention and mitigation ability.

Disaster-causing factor is the direct cause of disaster. It is a universal natural phenomenon that is generally unavoidable and difficult to change. Hazard analysis of disaster-causing factor is the basis of risk assessment. Its core is studying the characteristics of the spatiotemporal conditions, probability, and intensity of disaster-causing factors, and then obtaining the hazard results. The spatiotemporal conditions refer to determining the time span and spatial scope of the impact of the disaster-causing

TABLE 1 Data source.

Dataset	Source
The non-typhoon rainstorm data of 66 major meteorological stations in Fujian Province from 1981 to 2020	Fujian Climate Center
The basic information and disaster data of non-typhoon rainstorm cases that have affected Fujian Province during 1981–2020	Climatological Bulletin of Fujian Province (2001–2020) and the Climate of FUJIAN (Second Edition)
The geological disaster points data	Website of Fujian Provincial Department of Natural Resources
The data related to the vulnerability of disaster-affected bodies and the ability of disaster prevention and mitigation	2021 Fujian Statistical Yearbook and the 7th National Census Bulletin of nine prefecture-level cities in Fujian Province

factors. Therefore, this study analyzed the hazard of the disaster-causing factors based on the intensity and spatiotemporal scope analysis of non-typhoon rainstorms.

The disaster-formative environment refers to the natural environment in the area affected by rainstorm, which has regional differences. The overlay of different disaster-formative environments, different disaster-causing factors and different disaster-affected body will produce different types of disasters. The more sensitive the disaster-formative environment is, the greater the risk of disasters. Among the influencing factors of disaster-formative environment, the most important are terrain factors. The changes of terrain factors will cause a series of changes in other elements such as hydrology, climate, soil and vegetation. Therefore, the sensitivity analysis of terrain factors can be used to reflect the sensitivity of non-typhoon rainstorm disaster-formative environment. Consequently, this study selected the elevation, slope, terrain relief and the density of potential geological disaster points to analyze the sensitivity of the non-typhoon rainstorm disaster-formative environment in Fujian.

The disaster-affected body refers to the human socio-economic system in the rainstorm disaster affected area. Its characterization indicators include population density, wealth accumulation, crop sown area, urban morphological characteristics and infrastructure conditions. The combination and spatial distribution of their quantity and quality are the main causes of rainstorm disasters. The vulnerability of non-typhoon rainstorm disaster-affected bodies refers to the characteristics of disaster-affected bodies that are easily damaged and injured by rainstorm. The greater the vulnerability value, the weaker the ability of the disaster-affected body to resist the impact of rainstorm disasters, and the greater the risk. On the contrary, it shows that the stronger the ability of the disaster-affected body to resist the impact of rainstorm disasters, the smaller the risk. This study analyzed the vulnerability of non-typhoon rainstorm disaster-affected bodies in Fujian Province based on the analysis of population and social economy.

The main purpose of disaster prevention and mitigation is to reduce the loss of life and property caused by disasters. The ability of disaster prevention and mitigation is also reflected in the prediction before disaster, the response and rescue when disaster occurs, and the recovery and reconstruction after disaster. According to the National Comprehensive Disaster Prevention and Mitigation Plan (2016–2020) and the Emergency Response Law of the People's Republic of China, combined with the actual situation of Fujian Province, this study selected relevant indicators from three aspects: the monitoring and early warning capabilities, emergency response and rescue capabilities and post disaster recovery ability to characterize the disaster prevention and mitigation ability of non-typhoon rainstorm disasters.

In summary, twenty-four indices from four aspects were selected to characterize the risk of non-typhoon rainstorm disaster (Table 2).

2.2.2 Index weight-determination method

Commonly used index weight-determination methods include subjective weighting and objective weighting. Subjective weighting method determines the weight of each index by scoring according to the importance of index. It includes cycle scoring method, binomial coefficient method, analytic hierarchy process, etc. Since this method determines the weight by individual judgment of experts, it has greater randomness when there are many indicators. Objective weighting method uses the objective information reflected by each index to weight, such as correlation coefficient weighting method, entropy method, etc. Although this method can reflect the amount of information of each index, it cannot benefit from the knowledge and experience of decision-makers (Sahoo et al., 2016). Considering that the combination weighting method gives each index a different weight based on the data characteristics and empirical judgment, provides additional insights into overcoming the one-sidedness of a single subjective or objective weighting method (Xie et al., 2022b), and has been commonly employed (Tian et al., 2020; Xie and LiuXu, 2022a; Xie et al., 2022b; Wu et al., 2022). Therefore, this study used the combination weighting method to determine the index weight. Using the idea of analytic hierarchy process (AHP) for reference, the importance degree was judged in the first-level indicators layer with less classification, and the weights were determined by AHP, while the weights of the second and third-level indicators layer were determined by the

TABLE 2 Indices system of the non-typhoon rainstorm disaster risk assessment of Fujian Province, China.

First-level indices	Second-level indices	Third-level indices
Hazard of disaster-causing factors (0.5246)	Hazard of rainstorm intensity (0.5082)	Maximum daily rainfall during rainstorm (0.1209)
		Maximum accumulated rainfall during rainstorm (0.1211)
		Maximum rainfall in 1 h during rainstorm (0.1369)
		Maximum rainfall in 3 h during rainstorm (0.1293)
	Hazard of rainstorm spatiotemporal scope (0.4918)	Days of rainstorm (0.1474)
		Days of heavy rainstorm (0.1416)
		Days of extreme rainstorm (0.2029)
Sensitivity of disaster-formative environment (0.2082)	Sensitivity of terrain factor (0.8580)	Elevation (0.1693)
		Slope (0.1807)
		Terrain relief (0.2268)
		Density of potential geological disaster points (0.2813)
	Sensitivity of river factor (0.1420)	Distance to river (0.1420)
Vulnerability of disaster-affected bodies (0.1582)	Vulnerability of population (0.3989)	Density of population (0.1748)
		Proportion of female population (0.2241)
	Vulnerability of social economy (0.6011)	Density of GDP (0.1473)
		Density of building (0.2469)
		Sown density of crops (0.2069)
Ability of disaster prevention and mitigation (0.1091)	Ability of monitoring and early warning (0.3719)	Density of meteorological stations (0.2134)
		The number of weathermen per 10,000 people (0.1584)
	Ability of emergency response and rescue (0.3518)	Density of Highway (0.1488)
		The number of beds in health institutions per 10,000 people (0.1068)
		The number of employees in health institutions per 10,000 people (0.0962)
	Ability of post disaster recovery (0.2763)	Per capita budgetary revenue of local government (0.1558)
		Annual per capita disposable income of urban households (0.1205)

Note: The values in brackets represent the weight of each indicator.

correlation coefficient weighting method and entropy method (see Table 2). Among them, the hazard indices of disaster-causing factors were weighted by correlation coefficient method, while the sensitivity indices of disaster-formative environment, vulnerability indices of disaster-affected body and the ability indices of disaster prevention and mitigation were comprehensively weighted by correlation coefficient method and entropy method. The average weight calculated by the two methods was taken as the weight of the corresponding indicator.

2.2.2.1 Data standardization

There are many influential factors involved in the comprehensive risk assessment. Different factors are represented by different indicators, and the dimensions and magnitudes of each indicator are also different, so it needs to be standardized. The range standardization method was used in this study. The calculation formula is shown in Eqs 1, 2.

$$r_{ij} = \frac{x_{ij} - min(x_{ij})}{max(x_{ij}) - min(x_{ij})} \quad (1)$$

$$r_{ij} = \frac{max(x_{ij}) - x_{ij}}{max(x_{ij}) - min(x_{ij})} \quad (2)$$

where r_{ij} is the standardized value of the *ith* evaluating object on the *j*th index, and max(x_{ij}) and $min(x_{ij})$ are the maximum and minimum of the *i*th evaluating object on the *j*th index, respectively. Among the indices, Eq. 1 should be used for those that strengthen the evaluating result, while Eq. 2 should be used for those that weaken the result.

2.2.2.2 The analytic hierarchy process method

The AHP method is one of the most widely employed subjective weighting methods. The AHP can integrate the effects of various variables and comprehensively consider the subjective experience of the data (Xie et al., 2022b). The weights

TABLE 3 Scales of Judgment matrix and their meanings.

Scale	Meaning
1	Indicates that two factors are of equal importance when compared
3	Indicates that the former is slightly more important than the latter when the two factors are compared
5	Indicates that the former is obviously more important than the latter when the two factors are compared
7	Indicates that the former is strongly more important than the latter when the two factors are compared
9	Indicates that the former is extremely more important than the latter when the two factors are compared
2, 4, 6, 8	Represents the median value of the above adjacent judgments
Reciprocal	If the ratio of the importance of factor i to factor j is a_{ij}, then the ratio of the importance of factor j to factor i is $a_{ji} = 1/a_{ij}$

of the four first-level indices were calculated by AHP method. The calculation steps were as follows:

① Construction of judgment matrix

The numbers 1–9 and their reciprocal were used as scales (see Table 3) to compare the four factors in pairs and construct the judgment matrix A.in which, A is the judgment matrix, a_{ij} represents the judgment value of the relative importance of factor a_i to factor a_j, and n is the number of factors.

② The weight of each index was calculated by sum-product method.
③ In order to prove the scientific nature and rationality of weights, a consistency test was required.

$$\boldsymbol{A} = [\boldsymbol{a}_{\mathrm{ij}}]_{n\times n}\,(\boldsymbol{i},\boldsymbol{j} = \boldsymbol{1},\boldsymbol{2},....,\boldsymbol{n}) \tag{3}$$

Firstly, the maximum characteristic root and consistency index CI of the judgment matrix were calculated. Then the average random consistency index RI was found to be 0.89. And then the consistency ratio CR was calculated to be 0.0436, less than 0.1, indicating that the comparison between the factors in the judgment matrix was reasonable, which further indicated that the index weight calculated in step (2) was reasonable.

2.2.2.3 The correlation coefficient weighting method

Correlation coefficient weighting method determines the weight according to the internal relationship between indicators (Li, 2007). It has no clear constraint on factors and can solve the correlation problem between factors. The calculation steps were as follows:

① The correlation coefficient matrix U of the m evaluation indices was obtained.

$$\boldsymbol{U} = \begin{bmatrix} \boldsymbol{u_{11}} & \boldsymbol{u_{12}} & \cdots & \boldsymbol{u_{1m}} \\ \boldsymbol{u_{21}} & \boldsymbol{u_{22}} & \cdots & \boldsymbol{u_{2m}} \\ \cdots & \cdots & \cdots & \cdots \\ \boldsymbol{u_{m1}} & \boldsymbol{u_{m2}} & \cdots & \boldsymbol{u_{mm}} \end{bmatrix} \tag{4}$$

in which, U is the correlation coefficient matrix, u_{ij} ($i, j = 1,2, \ldots, m$) is the correlation coefficient between the ith evaluation index and the jth evaluation index.

② The multivariate correlation coefficients between the ith evaluation index and other m-1 evaluation indices were calculated by Eq. 5.

$$\boldsymbol{\rho_i} = \boldsymbol{u_i^T U_{m-1}^{-1} u_i}\,(\boldsymbol{i} = \boldsymbol{1},\boldsymbol{2},\cdots,\boldsymbol{m}) \tag{5}$$

in which, U_{m-1}^{-1} is the inverse matrix of the correlation coefficient matrix of m-1 indices excluding the ith index, and u_i is the m-1 dimensional column vector of the ith column vector in U after removing the element i.

③ The weight w_i of each evaluation index can be obtained by normalizing the reciprocal of ρ_i as Eq. 6.

$$\boldsymbol{w_i} = \prod\nolimits_{j\neq i}\boldsymbol{\rho_j}\Big/\sum\nolimits_{l=1}^{m}\prod\nolimits_{j\neq i}\boldsymbol{\rho_j} \tag{6}$$

2.2.2.4 The entropy method

The entropy method determines the index weight by using the spatial fluctuations of the data, which can eliminate human interference and make the evaluation result more objective (Ye et al., 2020). The calculation steps were as follows:

① Suppose there are l evaluating objects, and each object has m evaluating indices, then an original indices value matrix X is formed.

$$\boldsymbol{X} = [\boldsymbol{x}_{\mathrm{ij}}]_{l\times m}\ (\boldsymbol{i} = \boldsymbol{1},\boldsymbol{2},\ ...,\boldsymbol{l};\ \boldsymbol{j} = \boldsymbol{1},\ \boldsymbol{2},\ ...,\ \boldsymbol{m}) \tag{7}$$

② Eqs 1, 2 is used to standardize the original indices value matrix X to generate standardized matrix R, and r_{ij} is the element of R.
③ According to the traditional entropy concept, the entropy of each evaluating index can be defined as

$$\boldsymbol{H_j} = -\frac{\sum_{i=1}^{l}\boldsymbol{f_{ij}}\,\boldsymbol{ln f_{ij}}}{\boldsymbol{ln\, l}}\ (\boldsymbol{j} = \boldsymbol{1},\ \boldsymbol{2},\ \ldots,\ \boldsymbol{m}) \tag{8}$$

Where $f_{ij} = r_{ij}/\sum_{i=1}^{l} r_{ij}$, to make lnf_{ij} be meaningful, f_{ij} is set as

$$f_{ij} = \frac{1 + r_{ij}}{\sum_{i=1}^{l}(1 + r_{ij})} \tag{9}$$

④ The weight of the entropy of each evaluating index can be expressed as

$$W = [w_j]1 \times m, w_j = \frac{1 - H_j}{m - \sum_{j=1}^{m} H_j} (j = 1, 2, \ldots, m) \tag{10}$$

in which, $0 \le w_j \le 1$, $\sum_{j=1}^{m} w_j = 1$.

2.2.3 Comprehensive risk assessment method

Weighted comprehensive evaluation method considers the overall impact of various factors on the assessment object. It groups various specific indices together, and uses a quantitative index to express the advantages and weaknesses of the whole evaluation object. This method is commonly used. It is especially suitable for comprehensive analysis, evaluation and optimization of technology, decision-making, or a case study (Zhang and Li, 2007; Ye et al., 2020). The risk of non-typhoon rainstorm disaster relates to many factors with different influences. Therefore, the weighted comprehensive evaluation method was used to group the specific indices together, which can be expressed as

$$C = \sum_{k=1}^{m} w_k c_k \tag{11}$$

where C is the value of the composite risk index; c_k is the standard value of the kth indicator; and w_k is the weight of the kth indicator.

3 Results

According to the characteristics of the non-typhoon rainstorm disasters in Fujian Province, the risk analysis of non-typhoon rainstorm disasters was carried out from four aspects: Hazard of the disaster-causing factors, sensitivity of the disaster-formative environment, vulnerability of the disaster-affected bodies and ability of the disaster prevention and mitigation. The risk assessment indices system and the assessment model based on GIS were combined to complete the non-typhoon rainstorm disaster risk assessment in Fujian Province, China.

3.1 Hazard analysis of the disaster-causing factors

On the basis of obtaining the relevant data of non-typhoon rainstorm hazard indicators, the standardization process was carried out according to Eq. 1, and then the non-typhoon rainstorm hazard index of each site was calculated according to the calculated indicator weights (Table 2) and Eq. 11. The spatial distribution pattern of non-typhoon rainstorm hazard in Fujian Province was obtained by using GIS spatial interpolation method and natural breakpoint classification method, as shown in Figure 2 and Table 4.

As can be seen from Figure 2 and Table 4, the spatial pattern of non-typhoon rainstorm hazard in Fujian Province is very different from that of typhoon rainstorm hazard in this study area (Ye, 2015; Ye et al., 2020). It generally presents a gradually increasing distribution pattern from the eastern coastal areas to the western mountainous areas. In addition to the northwest of Fujian, the middle or above hazard areas were also observed in the narrow and long area of the southeast coast of Fujian. The higher hazard areas and the high hazard areas accounted for 9.45% and 14.43% of the province's area respectively, and were mainly observed in the northwest of Fujian with Wuyishan, Guangze, Jianning, and Ninghua as the center, and Zhangpu, Yunxiao and Zhao'an in the southeast corner of Fujian. The middle hazard areas accounted for 22.16% of the province, including some counties (cities) outside the high hazard areas in the northwest and west of Fujian, and some counties (cities) in the northeast and southeast coast of Fujian. The central Fujian province and most of the areas between the northwestern and central mountain ranges of Fujian exhibited low and lower hazard, which accounted for 53.96% of the province. The spatial pattern of non-typhoon rainstorm hazard is obviously affected by the topography of Fujian Province. Most of the non-typhoon rainstorms in Fujian province were systematic frontal precipitation caused by interaction of cold and warm air. The cold air moving south was blocked by the Wuyi Mountain Range in the northwest of Fujian and moved slowly. When the warm and humid air flow from the southeastern sea intruded Fujian along the two mountain ranges in the middle and northwest of Fujian, heavy precipitation occurred and fell on the southeast side of the two mountain ranges under the combined action of cold air and topography uplifting. During the rainy season, the rainstorm started from the southeastern coast, intruded the inland areas of Fujian along the southeast-northwest direction, and would be intensified by the uplifting effect of the topography. Therefore, the distribution of the two middle or above hazard areas in Figure 2 was consistent with the distribution pattern of the climate characteristics of the non-typhoon rainstorm in Fujian. The main rainstorm region was in the northwest of Fujian, and the secondary rainstorm region was in the southeast coast of Fujian. Most of the areas between the two mountain ranges received relatively little rainfall, and exhibited relatively lower hazard.

3.2 Sensitivity analysis of the disaster-formative environment

For the sensitivity of the disaster-formative environment, the lower the altitude, the smaller the terrain relief, and the closer the area to the river, the more likely it is to be affected by rainstorm-flood disasters. The greater the slope and the more potential geological disaster points, the greater the sensitivity, and the more likely the rainstorm will cause geological disasters such as

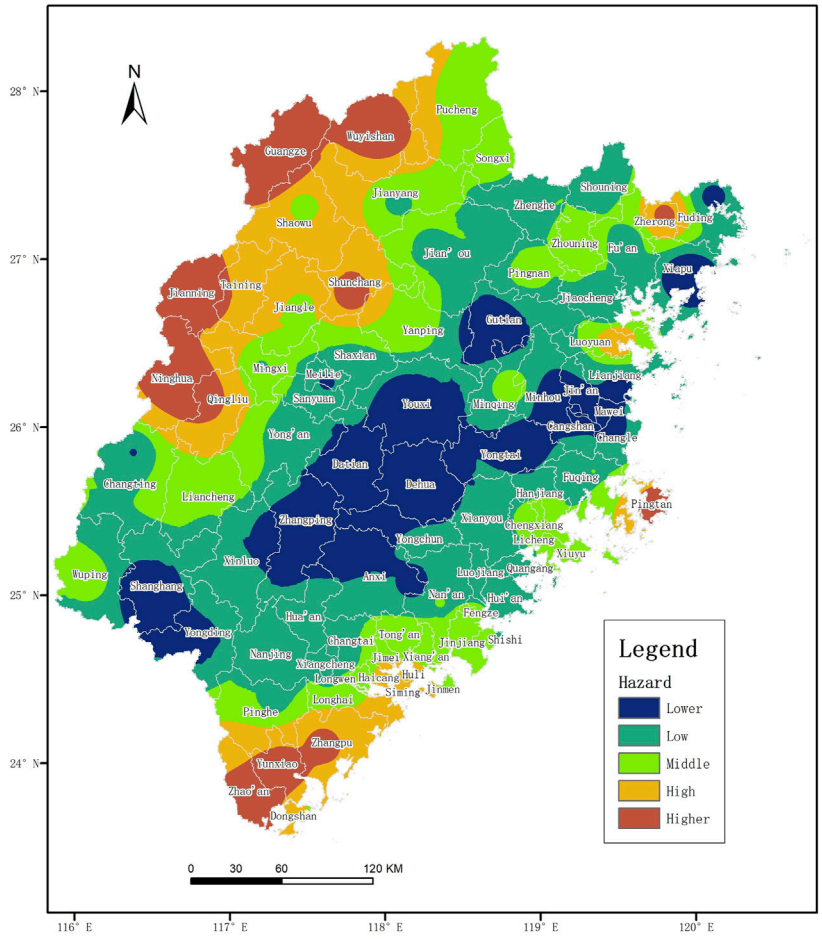

FIGURE 2
Hazard of non-typhoon rainstorm.

TABLE 4 Proportion of different hazard levels over the whole province.

Hazard level	The area proportion (%)	Typical counties (cities)
Higher	9.45	Wuyishan, Guangze, Jianning, Ninhua
High	14.43	Taining, Qingliu, Shaowu, Shunchang
Middle	22.16	Pucheng, Yanping, Mingxi, Liancheng
Low	35.81	Nanjing, Nan'an, Xianyou, Jiaocheng
Lower	18.15	Zhangping, Dehua, Yontai, Xiapu

landslides and debris flows. Therefore, when standardizing the data related to the sensitivity factors of the disaster-formative environment, slope and density of potential geological disaster points were regarded as positive indicators, which were standardized by Eq. 1. And elevation, terrain relief and distance to the river were regarded as negative indicators, which were standardized by Eq. 2. On this basis, the sensitivity index of disaster-formative environment was calculated according to the calculated weights (Table 2) and Eq. 11. The spatial distribution pattern of the disaster-formative environment sensitivity in Fujian Province was obtained by natural breakpoint classification method, as shown in Figure 3.

As can be seen from Figure 3, The higher sensitivity areas and the high sensitivity areas were observed in the eastern coastal

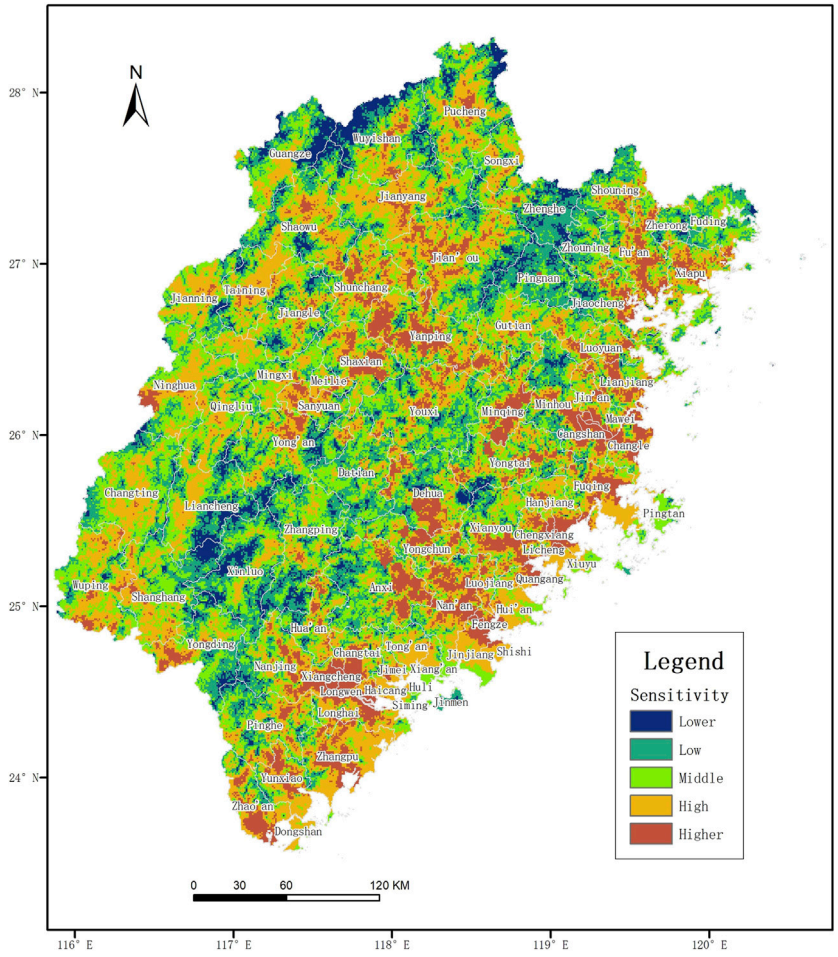

FIGURE 3
Sensitivity of the disaster-formative environment.

areas and river valley, accounted for 12.96% and 29.43% of the province's area respectively. Among them, the southeastern coastal areas were the most prominent. The middle sensitivity areas accounted for 29.90% of the province. The low sensitivity areas and the lower sensitivity areas were mainly located in the high-altitude areas of the two mountains of central and western Fujian, and accounted for 28.04% of the province. This distribution pattern also indicated that the environment-formative sensitivity of non-typhoon rainstorm disaster was generally high in Fujian Province due to the fragmented terrain and numerous rivers.

3.3 Vulnerability analysis of the disaster-affected bodies

The standardization of the relevant data of disaster-affected bodies was carried out according to Eq. 1, and then the disaster-affected bodies vulnerability index of each county (city) was calculated according to the calculated indicator weights (Table 2) and Eq. 11. According to the classification of natural breakpoints, the spatial pattern of vulnerability of non-typhoon rainstorm disaster-affected bodies in Fujian Province was obtained as shown in Figure 4 and Table 5.

As can be seen from Figure 4 and Table 5, the spatial difference of the disaster-affected bodies vulnerability in Fujian Province is clear, and presents a pattern of higher or high in the east and lower or low in the west. The areas with higher and high vulnerability were mostly concentrated in the southeastern coastal areas, accounting for 14.78% of the province. The middle vulnerability regions accounted for 26.96% of the province, and were observed in some counties (cities) in the eastern coast, Nanping city and Longyan city. The vulnerability of most counties (cities) in central, western and northeastern Fujian was low or lower, accounting for 58.26% of the province.

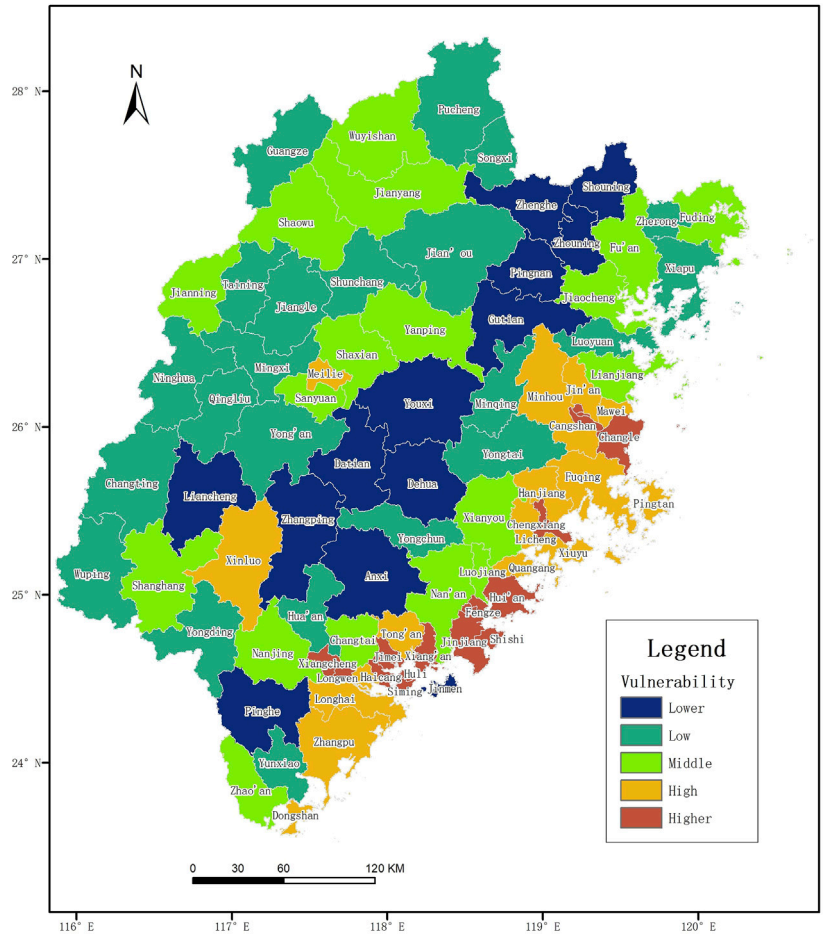

FIGURE 4
Vulnerability of the disaster-affected bodies.

TABLE 5 Proportion of different vulnerability levels over the whole province.

Vulnerability level	The area proportion (%)	Main counties (cities)
Higher	3.32	Cangshan, Chengxiang, Fengze, Siming
High	11.46	Fuqing, Hanjiang, Quangang, Tong'an
Middle	26.96	Shaxian, Nan'an, Xianyou, Fuding
Low	36.21	Changting, Ninghua, Pucheng, Xiapu
Lower	22.05	Pinghe, Datian, Pingnan, Zhenhe

3.4 Ability analysis of the disaster prevention and mitigation

The impact of disaster prevention and mitigation ability on rainstorm disaster is negative, that is, a region with strong disaster prevention and mitigation ability can greatly reduce the impact of rainstorm disaster. After obtained the relevant index data of the disaster prevention and mitigation ability, the standardization process was carried out according to Eq. 2. Comprehensive calculation was made according to the calculated index weight (Table 2) and Eq. 11 to obtain the comprehensive index of disaster prevention and mitigation ability. The spatial pattern of disaster prevention and mitigation ability for non-typhoon rainstorm disasters in

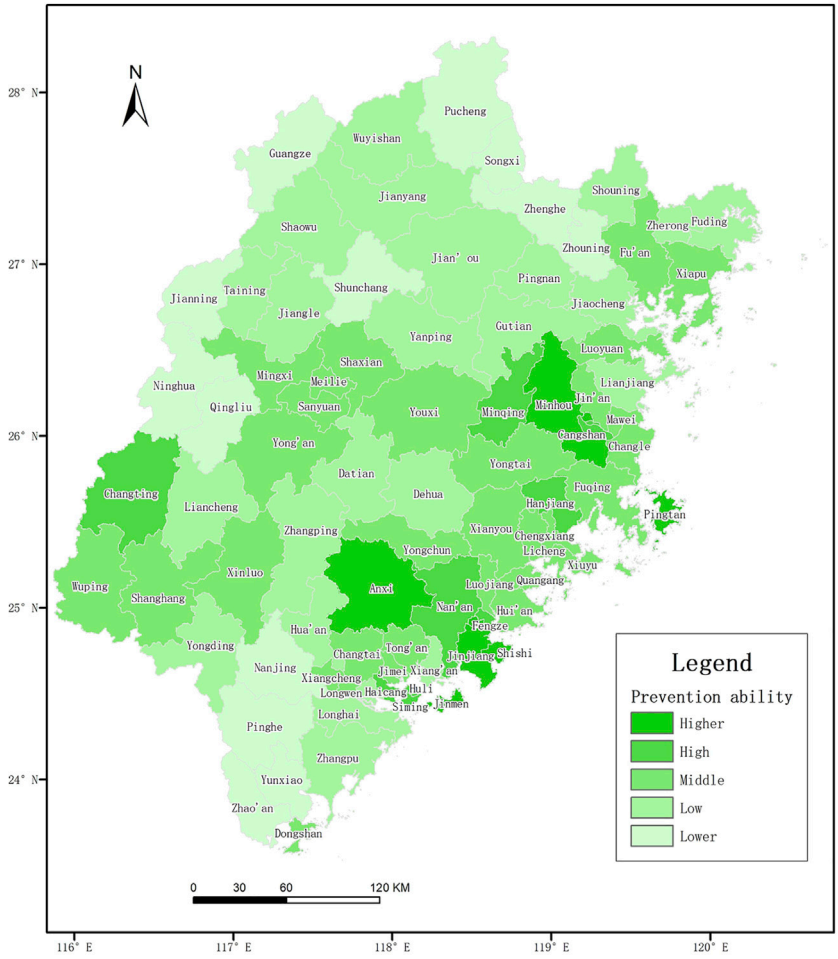

FIGURE 5
Spatial distribution pattern of the disaster prevention and mitigation ability.

TABLE 6 Proportion of different prevention and mitigation ability levels over the whole province.

Prevention and mitigation ability level	The area proportion (%)	Main counties (cities)
Higher	5.28	Siming, Jinjiang, Fenze, Gulou
High	6.47	Nan'an, Hangjiang, Cangshan, Minqing
Middle	30.44	Tong'an, Xianyou, Fuqing, Xiapu
Low	38.17	Yongding, Jiangle, Shaowu, Shouning
Lower	19.64	Pinghe, Ninghua, Pucheng, Zhouning

Fujian Province was obtained according to the classification of natural breakpoints, as shown in Figure 5 and Table 6.

It can be seen from Figure 5 and Table 6 that the spatial difference of the ability of disaster prevention and mitigation in Fujian Province is obvious. Counties (cities) with higher and high ability of disaster prevention and mitigation were mostly concentrated in the eastern coastal area north of Zhangzhou City and Longyan city, accounting for 11.75% of the province's area. Counties (cities) with middle ability of disaster prevention and mitigation accounted for 30.44% of

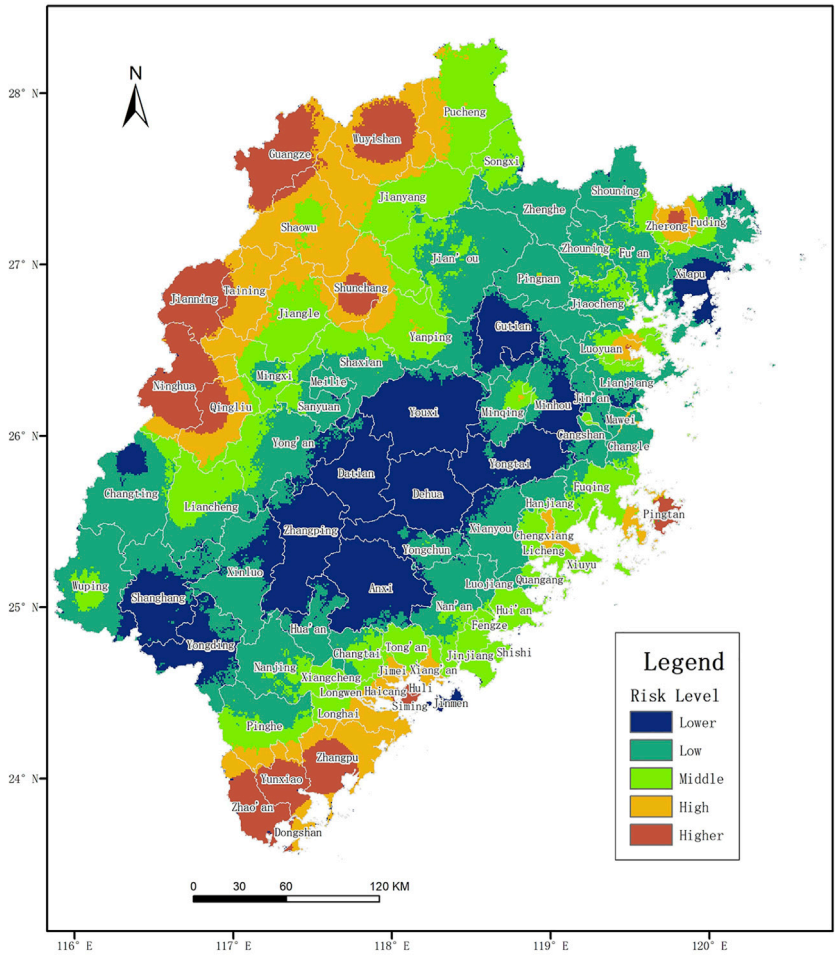

FIGURE 6
The spatial distribution pattern of the comprehensive risk of non-typhoon rainstorm disaster.

the province. And the disaster prevention and mitigation ability of the mountainous counties (cities) in Ningde City and most of the counties (cities) in Zhangzhou city, Sanming city and Nanping city was low or lower, accounting for 58.08% of the province.

3.5 Comprehensive risk analysis

Based on the above analysis of non-typhoon rainstorm disaster-causing factors hazard, disaster-formative environment sensitivity, disaster-affected bodies vulnerability, and disaster prevention and mitigation ability, comprehensive calculation was made according to the related index weight (Table 2) and Eq. 11. Spatial pattern of the comprehensive risk of non-typhoon rainstorm in Fujian Province was obtained according to the natural breakpoint classification, as shown in Figure 6 and Table 7.

As can be seen from Figure 6 and Table 7, Spatial pattern of the comprehensive risk of non-typhoon rainstorm in Fujian Province is completely different from that of typhoon rainstorm in this study area (Ye, 2015). Its variation trend of non-typhoon rainstorm is similar to that of non-typhoon rainstorm hazard mentioned above, and increases gradually from the southeast coastal area to the mountainous area in the northwest. The risk areas above middle were observed in the northwestern Fujian and the narrow coastal area of southeastern Fujian. Risk of most of the areas between the two mountain ranges in the middle and northwest of Fujian was relatively low. It indicated that the disaster-causing factors of rainstorm were the dominant risk factors of non-typhoon rainstorm. The areas with higher and high risk were basically consistent with the corresponding level of non-typhoon rainstorm hazard, accounting for 9.49% and 13.23% of the province respectively. In addition to some counties (cities) in northwestern Fujian and central Fujian, the middle risk was also

TABLE 7 Proportion of different comprehensive risk levels over the whole province.

Risk level	The area proportion (%)	Main counties (cities)
Higher	9.49	Wuyishan, Guangze, Jianning, Ninhua
High	13.23	Taining, Qingliu, Shaowu, Shunchang
Middle	21.59	Pucheng, Jiangle, Yanping, Mingxi,
Low	34.34	Nanjing, Nan'an, Xianyou, Pingnan
Lower	21.36	Zhangping, Dehua, Yontai, Xiapu

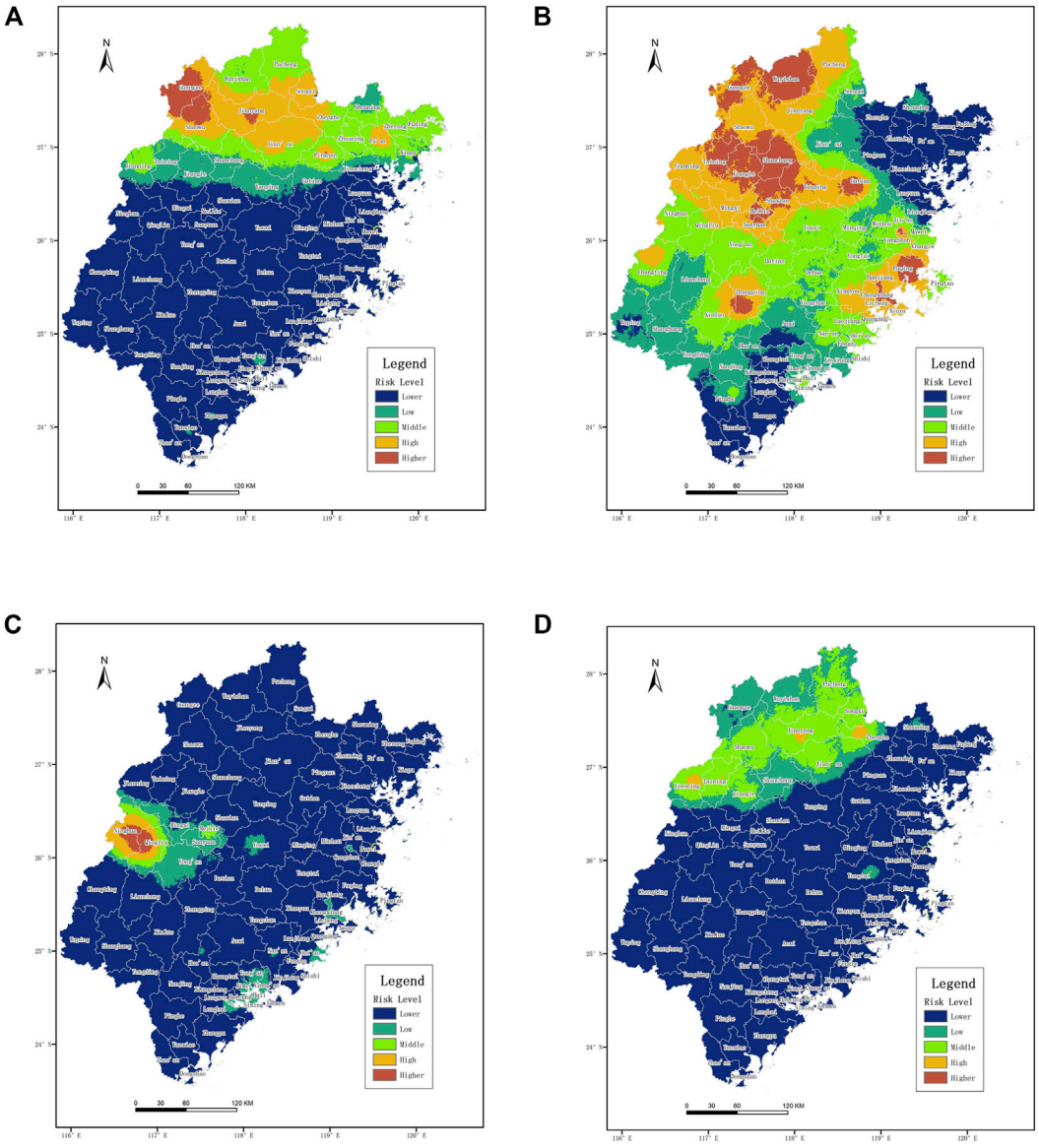

FIGURE 7
Spatial distribution pattern of the comprehensive risk of four non-typhoon rainstorm cases. **(A)** 19980619-0624. **(B)** 20100614-0626. **(C)** 20150519-0520. **(D)** 20160505-0510.

observed in some counties (cities) in southeast coastal areas and Fuding, Zherong in northeastern Fujian, which accounted for 21.59% of the province. Inland mountainous areas along the eastern coast, most counties (cities) in southwestern Fujian, and most counties (cities) in central Fujian exhibited low or lower risk, which accounted for 34.34% and 21.36% of the province respectively.

The risk assessment results obtained by above methods reflect the general pattern of the comprehensive risk of non-typhoon rainstorm disasters in the study area, which can also be called the climatic characteristics. In fact, for a single rainstorm case, the spatial pattern of its risk is also different due to inconsistency of the rainstorm cause and the spatial and temporal range of impact. Therefore, in order to illustrate the reliability of the analysis results, four historical cases of non-typhoon rainstorm were selected for verification, and the results are shown in Figure 7.

It can be seen from Figure 7 that the spatial pattern of comprehensive risk of non-typhoon rainstorm disasters in the four historical cases is significantly different from that of the general comprehensive risk of non-typhoon rainstorm disasters in Figure 6. In terms of historical cases, most of the higher-risk and high-risk areas of non-typhoon rainstorm cases were concentrated in northwestern Fujian, but the comprehensive risk pattern of different cases was significantly different.

As can be seen from Figure 7A, the higher-risk and high-risk areas of rainstorm from June 19 to 24, 1998 were mainly observed in Nanping City in northern Fujian, and the risk was relatively low in the southeastern coast of Fujian and most of the areas in central and western Fujian. According to the relevant records, due to the continuous precipitation, the reservoirs in northern Fujian were full, the water level of rivers rose sharply, and Jianxi and Futunxi had suffered multiple floods that exceeded the dangerous water level. And Guangzhuang, Shaowu, Jian'ou and many other counties (cities) were flooded. These flooded counties (cities) were mostly concentrated in the higher-risk and high-risk areas in Figure 7A.

As can be seen from Figure 7B, the rainstorm from June 14 to 26, 2010 lasted for nearly half a month and affected a wide range of areas. Its higher-risk and high-risk areas were widely distributed, mainly included Sanming and Nanping in the northwest of Fujian Province and some counties (cities) in Fuzhou and Putian in the central coastal area. Ningde in the northeast of Fujian, Zhangzhou and Xiamen in the southeast of Fujian, and some counties (cities) in the southwest of Fujian exhibited low or lower risk. According to the Climatological Bulletin of Fujian Province (2010), the rainstorm process was characterized by long duration, large amount of rainfall, wide range of heavy rain, strong rainfall intensity and concentrated area of heavy rain. Heavy rainstorms and extremely heavy rainstorms were mostly concentrated in Nanping city and Sanming city. There were seven counties (cities) of Nanping, Shaxian, Shunchang, Jiangle, Changting, Jianning and Taining with process rainfall 300% above normal. And four counties (cities) of Nanping, Shunchang, Taining and Fuqing ranked the highest precipitation in the same period since 1961. The continuous heavy rainstorm brought severe disasters and losses to Fujian Province. It caused 59,500 houses to collapse, 78 deaths and 79 persons missing, and a direct economic loss of 14.46 billion yuan. These worst-hit areas are the higher-risk and high-risk areas in Figure 7B.

As can be seen from Figure 7C, the impact area of the rainstorm from May 19 to 20, 2015 was relatively small. Its higher-risk and high-risk areas were only observed in Ninghua and Qingliu of Sanming City, and areas outside Sanming City were all exhibited low or lower risk. According to the Climatological Bulletin of Fujian Province (2015), the western and southern parts of Fujian Province experienced heavy rains or extremely heavy rains. The daily rainfall of Qingliu broke the historical maximum precipitation record, and the daily rainfall of Ninghua ranked the second in the history of this station during the same period. Some urban areas and towns in Qingliu, Ninghua and Changting counties were flooded for more than 10 h, with the maximum water depth exceeding 2 m. The flooded areas recorded here were consistent with the middle-to-higher risk areas shown in Figure 7C.

It can be seen from Figure 7D that the rainstorm from May 5 to 10, 2016 mainly impacted the Sanming and Nanping cities, and the middle-risk and high-risk areas were mainly observed in these areas. According to the Climatological Bulletin of Fujian Province (2016), From May 5th to 10th, a large-scale heavy rain process occurred in Fujian Province, which was characterized by long duration, concentrated heavy rainfall area, and large amount of rainfall. Sanming and Nanping cities, where the heavy rainfall was concentrated, were severely affected. The severely affected areas recorded here were consistent with the middle-high risk areas shown in Figure 7D.

The risk pattern of the above four historical cases of non-typhoon rainstorm shows that the higher-risk and high-risk areas of a single non-typhoon rainstorm case are generally small. Except for the rainstorm in June 2010, the higher-risk and high-risk areas of the other three cases were limited to a small local area. The intensity, duration, scope and concentration of rainstorm directly affect its hazard, and then affect the spatial pattern of comprehensive risk.

4 Discussion

As for the natural disaster risk in the study area, previous studies mainly focused on typhoon disaster (Ye et al., 2020; Zhu et al., 2017; Ye, 2015; Chen, 2007b), and paid less attention to the risk of rainstorm disaster. A few risk assessments for rainstorm disasters did not distinguish different types of rainstorms. Ye (2015) carried out the risk assessment of typhoon rainstorm based on different landing paths. The results showed that the risk

of typhoon rainstorm in Fujian Province gradually decreased from the eastern coastal area to the western inland area, and the high-risk areas were mainly concentrated in the coastal areas, but the risk pattern of typhoon rainstorm notably differ between different landing paths. The result showed that the spatial pattern of the comprehensive risk of non-typhoon rainstorm in Fujian Province is completely different from that of typhoon rainstorm. It shows a gradually increasing trend from the eastern coastal area to the mountainous area in the northwest. But the risk areas above middle were observed in the northwestern Fujian and the narrow coastal area of southeastern Fujian. Chen (2007a) constructed the index system and assessment model from two aspects of disaster-causing factors and disaster-affected bodies, and carried out the risk assessment of rainstorm flood disasters in Fujian Province. The study showed that the high-risk areas of rainstorm flood disasters were mainly distributed in the eastern coastal areas from north to south and the windward slope areas of the Wuyi Mountain Range in the northwest, but it did not distinguish rainstorm types. This paper not only focused on the study of non-typhoon rainstorm, but also made great improvements in data acquisition, index selection, evaluation model construction, etc. It was verified by examples. The results showed that the high-risk and higher-risk areas in northwestern Fujian were consistent with the results of Chen (2007a), but the overall pattern of risk and the high and higher-risk areas in the east coast were different. The high and higher-risk areas in the east were only observed in the narrow coastal area of the southeast. Therefore, it is necessary to distinguish different types of rainstorm and carry out different types of rainstorm disaster risk assessment, and the research results are more scientific and reasonable.

Existing studies have shown that non-typhoon rainstorms in Fujian Province can be further divided into spring rainstorm, rainy season rainstorm, summer rainstorm, autumn rainstorm and winter rainstorm according to different seasons, and the temporal and spatial distribution and intensity characteristics of rainstorms in different seasons were significantly different. Among them, the rainy season rainstorm was the most intense and the most serious non-typhoon rainstorm. The cases given in this paper all belonged to the rainy season rainstorm, which were significantly representative. Further research may consider classifying non-typhoon rainstorms by season and carry out more targeted risk assessment based on non-typhoon rainstorms in different seasons.

5 Conclusion

Based on the non-typhoon rainstorm data of major meteorological stations in Fujian Province in the recent 40 years, combined with ground basic data and social economic data, this study established an indices system from four aspects: Disaster-causing factors, disaster-formative environment, disaster-affected bodies, and disaster prevention and mitigation abilities. Based on the analytic hierarchy process, the entropy method and the correlation coefficient analysis method, the combination weighting was assigned to carry out the non-typhoon rainstorm disaster risk assessment. The main conclusion are as follows:

1) The spatial pattern of the comprehensive risk of non-typhoon rainstorm in Fujian Province is completely different from that of typhoon rainstorm in this study area. It shows a gradually increasing trend from the eastern coastal area to the mountainous area in the northwest. But the risk areas above middle were observed in the northwestern Fujian and the narrow coastal area of southeastern Fujian.
2) The variation trend of the non-typhoon rainstorm comprehensive risk is similar to that of non-typhoon rainstorm hazard. It indicated that the disaster-causing factors were the dominant risk factors of non-typhoon rainstorm. The spatial pattern of non-typhoon rainstorm hazard is obviously affected by the topography of Fujian Province. Moreover, intensity, duration, impact scope and concentration of non-typhoon rainstorm also directly affect its hazard, and then affect the spatial pattern of comprehensive risk.
3) The comprehensive risk pattern of a specific historical non-typhoon rainstorm case is significantly different from that of the general comprehensive risk of non-typhoon rainstorm disasters. In terms of historical cases, most of the higher-risk and high-risk areas of non-typhoon rainstorm cases were generally small, and were concentrated in northwestern Fujian, but the comprehensive risk pattern of different cases was significantly different.
4) The rainy season rainstorm is the most representative non-typhoon rainstorm. And the temporal and spatial distribution and intensity characteristics of non-typhoon rainstorms in different seasons are significantly different. Further research may consider classifying non-typhoon rainstorms by season and carry out more targeted risk assessment based on non-typhoon rainstorms in different seasons.

Data availability statement

The original contributions presented in the study are included in the article/supplementary material, further inquiries can be directed to the corresponding author.

Author contributions

JY designed the research, JY and RZ collected the data, JY, RZ and MZ contributed to the data processing and analysis, JY prepared the original draft, RZ, GL and LG edited and reviewed the manuscript. All authors have read and agreed to the published version of the manuscript.

Funding

This research was supported by the Public Welfare Projects of Science and Technology Department of Fujian Province, China (2021R002006, 2018R10344).

Acknowledgments

The meteorological data were provided by Fujian Climate Center. The geological disaster points data came from the website of Fujian Provincial Department of Natural Resources (https://zrzyt.fujian.gov.cn/). The population and social economy data come from the website of Fujian Provincial Bureau of Statistics (https://tjj.fujian.gov.cn/).

Conflict of interest

The authors declare that the research was conducted in the absence of any commercial or financial relationships that could be construed as a potential conflict of interest.

Publisher's note

All claims expressed in this article are solely those of the authors and do not necessarily represent those of their affiliated organizations, or those of the publisher, the editors and the reviewers. Any product that may be evaluated in this article, or claim that may be made by its manufacturer, is not guaranteed or endorsed by the publisher.

References

Chan, F. K. S., Yang, L. E., Scheffran, J., Mitchell, G., Adekola, O., Griffiths, J., et al. (2021). Urban flood risks and emerging challenges in a Chinese delta: The case of the Pearl River Delta. *Environ. Sci. Policy* 122, 101–115. doi:10.1016/j.envsci.2021.04.009

Chen, J. F., Chen, M. C., Gao, S. P., Xu, J. P., and Zhou, P. (2019). Risk assessment of rainstorm disasters in Nanjing based on cloud matter-element model [J]. *J. Econ. Water Resour.* 37 (2), 67–72+88. doi:10.3880/j.issn.1003-9511.2019.02.012

Chen, X., and Brown, F. K. (2007a). Asymmetry of chemical similarity. *ChemMedChem* 14 (4), 180–182. (in Chinese). doi:10.1002/cmdc.200600161

Chen, X. (2007b). Risk assessment and zonation of typhoon disasters in Fujian Province [J]. *Chin. J. Ecol.* 26 (6), 961–966. doi:10.13292/j.1000-4890.2007.0173

Chen, X. W., Gao, L., Chen, Y., Deng, H. J., Liu, M. B., and Lin, B. Q., (2019b). Study on the classification of typhoon and non-typhoon related rainstorm flood [J]. *China Flood Drought Manag.* 29 (4), 18–21. doi:10.16867/j.issn.1673-9264.2018251

Chen, Y., Wang, L., Zhao, J. H., Zhang, Y. X., Zhao, S. S., Li, W. , et al. (2022). Climatic characteristics and major meteorological events over China in 2021 [J]. *Meteorol. Mon.* 48, 470–478. doi:10.7519/j.issn.1000-0526.2022.022501

Huang, J., Zhang, F. M., and Hu, Z. H. (2022). Spatio-temporal evolution of rainstorm disaster in Anhui Province based on the comprehensive precipitation indices with multi-indicators [J]. *J. Catastrophology* 37 (2), 111–116. doi:10.3969/j.issn.1000-811X.2022.02.018

Jou, B. J. (2020). Non-typhoon heavy rain research in taiwan for the past 30 years: A review [J]. *Torrential Rain Disasters* 39 (2), 109–116. doi:10.3969/j.issn.1004-9045.2020.02.001

Li, B. N. (2007). *Fuzzy mathematics and application [M]*. Hefei: Hefei University of Technology Publishing House. (in Chinese).

Li, W., Zhao, S. S., Chen, Y., Wang, Q., and Ai, W. (2021). State of China's climate in 2020. *Atmos. Ocean. Sci. Lett.* 14, 100048. doi:10.1016/j.aosl.2021.100048

Li, W. Z., Yu, D., Feng, X. L., and Zhang, T. F. (2019). Risk assessment of rainstorm and flood disasters based on the hazard grades/indices in Qinghai Province [J]. *J. Glaciol. Geocryol.* 41 (3), 680–688.

Li, Y., Zhang, Z. R., Gong, S. Y., Liu, M., and Zhao, Y. (2020). Risk assessment of rainstorm disasters under different return periods: A case study of Bohai Rim, China. *Ocean. Coast. Manag.* 187, 105107. doi:10.1016/j.ocecoaman.2020.105107

Lin, Z. D., Chen, X. W., Lin, M. S., and Chen, Y. (2017). Spatial and temporal variations of storm-floods in Xixi watershed of southeast coastal region [J]. *Mt. Res.* 35 (4), 488–495. doi:10.16089/j.cnki.1008-2786.000246

Lu, S. J., and Wang, Y. (2012). *The climate of FUJIAN*. Second Edition. Beijing: China Meteorological Press. (in Chinese).

Ma, S. Q., Lyu, S. R., and Zhang, Y. D. (2021). Weighted clustering-based risk assessment on urban rainstorm and flood disaster. *Urban Clim.* 39, 100974. doi:10.1016/j.uclim.2021.100974

Qiu, C., Liu, H. B., Wan, C. C., Zhao, L. N., and Wen, J. H. (2022). Tempo-spatial variation and cause analysis of rainstorms and related flood disasters in shandong from 1984 to 2019[J]. *J. Catastrophology* 37 (4). https://kns.cnki.net/kcms/detail/61.1097.P.20220708.1703.009.html.

Sahoo, M., Sahoo, S., Dhar, A., and Pradhan, B. (2016). Effectiveness evaluation of objective and subjective weighting methods for aquifer vulnerability assessment in urban context. *J. Hydrology* 541, 1303–1315. doi:10.1016/j.jhydrol.2016.08.035

Shang, Z. H., Cao, H. L., Lin, M. P., and Zhan, H. Y. (2019). Review of typhoon disaster risk assessment for agriculture in China [J]. *J. Catastrophology* 34 (2), 168–172. doi:10.3969/j.issn.1000-811X.2019.02.030

Shi, P. J., Lv, L. L., Wang, M., Wang, J. A., and Chen, W. F. (2014). Disaster system: Disaster cluster, disaster chain and disaster compound [J]. *J. Nat. Disasters* 23 (6), 1–12. doi:10.13577/j.jnd.2014.0601

Shi, P. J. (2002). Theory on disaster science and disaster dynamics [J]. *J. Nat. Disasters* 11 (3), 1–9. doi:10.13577/j.jnd.2002.0301

Tian, M., Shen, Y. H., and Zhang, Y. R. (2020). Risk assessment of wind-hailstorm in typical mountainous area of yunnan based on combination weighting method [J]. *J. Catastrophology* 35 (2), 110–115. doi:10.3969/j.issn.1000-811X.2020.02.021

Wang, Y., Zhang, X. Y., Zhang, Q., Li, L. L., and Huang, Y. (2019). Assessment on storm disaster risk and its impact on agriculture [J]. *J. Meteorological Sci.* 39 (1), 137–142. doi:10.3969/2018jms.0001

Wu, J. R., Chen, X. L., and Lu, J. Z. (2022). Assessment of long and short-term flood risk using the multi-criteria analysis model with the AHP-Entropy method in Poyang Lake basin. *Int. J. Disaster Risk Reduct.* 75, 102968. doi:10.1016/j.ijdrr.2022.102968

Wu, M. M., Wu, Z. N., Ge, W., Wang, H., Shen, Y., and Jiang, M. (2021). Identification of sensitivity indicators of urban rainstorm flood disasters: A case study in China. *J. Hydrology* 599, 126393. doi:10.1016/j.jhydrol.2021.126393

Xie, J., Liu, W., Xu, Y. S., and Lei, C. M. (2022a). Rainstorm disaster risk assessment in Xining area in rainy season based on the AHP weight method and entropy weight method [J]. *J. Nat. Disasters* 31 (3), 60–74. doi:10.13577/j.jnd.2022.0306

Xie, X., Zhang, J. Y., Lian, Y. Q., Lin, K., Gao, X., Lan, T., et al. (2022b). Cloud model combined with multiple weighting methods to evaluate hydrological alteration and its contributing factors. *J. Hydrology* 610, 127794. doi:10.1016/j.jhydrol.2022.127794

Xu, W., Yang, X. Y., Xu, J., Lu, J. L., and Xia, Y. (2018). Study on climate change characteristics of rainstorm and risk assessment of rainstorm rainfall in Jinshan of Shanghai in recent 60 years [J]. *Torrential Rain Disasters* 37 (6), 177–182. doi:10.3969/j.issn.1004-9045.2019.02.010

Xu, Y. Q., Chen, L., Liu, Y. H., Li, S., Zhou, X. X., and Na, R. B. (2022).

Comparative analysis of natural disaster risk assessment based on different spatial resolution data--taking rainstorm and flood disaster as an example [J]. *J. Catastrophology* 37 (3), 61–68. doi:10.3969/j.issn.1000-811X.2022.03.011

Ye, J. Y., Lin, G. F., Zhang, M. F., and Gao, L. (2020). Hazard analysis of typhoon disaster-causing factors based on different landing paths: A case study of fujian province, China. *Nat. Hazards (Dordr).* 100, 811–828. doi:10.1007/s11069-019-03843-6

Ye, J. Y. (2015). *Typhoon disaster chains integrated risk assessment model and information tupu based on multi-dimensional matrix*. Fuzhou, China: Doctoral Dissertation of Fujian Normal University. (in Chinese).

Ying, M., Yang, Y. H., Chen, B. D., and Zhang, W. (2011). Climatic variation of tropical cyclones affecting China during the past 50 years. *Sci. China Earth Sci.* 54, 1226–1237. doi:10.1007/s11430-011-4213-2

Zhang, J. Q., and Li, N. (2007). *Quantitative methods and applications of risk assessment and management on main meteorological disasters[M]*. Beijing: Beijing Normal University Press. (in Chinese).

Zhao, J., Wang, J. A., and Zhu, H. S. (2020). *Geography of China*. Second Edition. Beijing: Higher Education Press. (in Chinese).

Zhou, Y. H., Peng, T., and Shi, R. Q. (2019). Research progress on risk assessment of heavy rainfall and flood disasters in China [J]. *Torrential Rain Disasters* 38 (5), 494–501. doi:10.3969/j.issn.1004-9045.2019.05.011

Zhu, J., Lu, Y., Li, G. P., and Ren, F. M. (2017). Risk assessment of typhoon disasters in fujian province of each county[J]. *J. Catastrophology* 32 (3), 204209. doi:10.3969/j.issn.1000-811X.2017.03.034

frontiers | Frontiers in Environmental Science

TYPE Original Research
PUBLISHED 17 November 2022
DOI 10.3389/fenvs.2022.1049840

OPEN ACCESS

EDITED BY
Peng Sun,
Anhui Normal University, China

REVIEWED BY
Yanlai Zhou,
Wuhan University, China
Abinash Sahoo,
National Institute of Technology, India

*CORRESPONDENCE
Lei Yan,
yanl@whu.edu.cn

SPECIALTY SECTION
This article was submitted to Atmosphere and Climate, a section of the journal Frontiers in Environmental Science

RECEIVED 21 September 2022
ACCEPTED 03 November 2022
PUBLISHED 17 November 2022

CITATION
Yan L, Lei Q, Jiang C, Yan P, Ren Z, Liu B and Liu Z (2022), Climate-informed monthly runoff prediction model using machine learning and feature importance analysis.
Front. Environ. Sci. 10:1049840.
doi: 10.3389/fenvs.2022.1049840

Climate-informed monthly runoff prediction model using machine learning and feature importance analysis

Lei Yan[1,2]*, Qingwen Lei[1,2], Cong Jiang[3], Pengtao Yan[4], Zheng Ren[1,2], Bin Liu[1,2] and Zhangjun Liu[5]

[1]College of Water Conservancy and Hydropower, Hebei University of Engineering, Handan, China, [2]Hebei Key Laboratory of Intelligent Water Conservancy, Hebei University of Engineering, Handan, China, [3]School of Environmental Studies, China University of Geosciences, Wuhan, China, [4]School of Physics and Electronic Engineering, Xingtai University, Xingtai, China, [5]Jiangxi Academy of Water Science and Engineering, Nanchang, China

Accurate runoff prediction can provide a reliable decision-making basis for flood and drought disaster prevention and scientific allocation of water resources. Selecting appropriate predictors is an effective way to improve the accuracy of runoff prediction. However, the runoff process is influenced by numerous local and global hydrometeorological factors, and there is still no universal approach about the selection of suitable predictors from these factors. To address this problem, we proposed a runoff prediction model by combining machine learning (ML) and feature importance analysis (FIA-ML). Specifically, take the monthly runoff prediction of Yingluoxia, China as an example, the FIA-ML model uses mutual information (MI) and feature importance ranking method based on random forest (RF) to screen suitable predictors, from 130 global climate factors and several local hydrometeorological information, as the input of ML models, namely the hybrid kernel support vector machine (HKSVM), extreme learning machine (ELM), generalized regression neural network (GRNN), and multiple linear regression (MLR). An improved particle swarm optimization (IPSO) is used to estimate model parameters of ML. The results indicated that the performance of the FIA-ML is better than widely-used long short-term memory neural network (LSTM) and seasonal autoregressive integrated moving average (SARIMA). Particularly, the Nash-Sutcliffe Efficiency coefficients of the FIA-ML models with HKSVM and ELM were both greater than 0.9. More importantly, the FIA-ML models can explicitly explain which physical factors have significant impacts on runoff, thus strengthening the physical meaning of the runoff prediction model.

KEYWORDS

runoff prediction, mutual information, random forest, feature importance analysis, teleconnection

1 Introduction

Water resources are important for social and economic development and the ecological environment, and accurate runoff forecasting can provide a reasonable decision-making basis for the optimal allocation and utilization of water resources (Huang et al., 2014; Xiong et al., 2019; Feng et al., 2020a; Yan et al., 2021a; Jian et al., 2022). However, under changing environments, the runoff process and associated hydrological system have been altered by human activities and climate change (Song et al., 2018; Sun et al., 2018, 2022; Jiang et al., 2019; Lu et al., 2020; Yan et al., 2020; Hu et al., 2022), and the runoff series becomes nonlinear and nonstationary, which makes it challenging to capture the variation characteristics of runoff (Sun et al., 2014; Lin et al., 2020; Yan et al., 2021b; Samantaray et al., 2022a; Samantaray et al., 2022b; Samantaray et al., 2022c; Zhou et al., 2022). Therefore, there is an urgent need to develop a runoff prediction model with robustness and high forecasting accuracy under a changing environment (Sit et al., 2020; Niu et al., 2021; Zhao et al., 2021). In recent years, there have been many studies trying to transform the complex runoff series into stationary sub-sequences using wavelets or mode decomposition methods, and then predict the sub-sequences to improve the accuracy of prediction (Meng et al., 2019; Feng et al., 2020b; Niu et al., 2020). However, these studies often ignore the relationship between hydrometeorological factors and the variation characteristics of runoff.

As revealed by recent studies, the changing characteristics of runoff process are controlled by numerous factors, such as astronomy, meteorology, ocean, and underlying surface conditions (Tang et al., 2018; Shi et al., 2021; Bian et al., 2022; Ma et al., 2022). When there are no significant changes for the underlying surface conditions, the runoff process mainly depends on precipitation and evaporation, which are influenced by atmospheric circulations (Talaee et al., 2014; Huang et al., 2017; Luo et al., 2017). On the other hand, the interaction between the ocean and the atmosphere drives the exchange of matter and energy between regions of the Earth, which can affect regional weather and climate change (Nugent and Matthews, 2012; Singh and Roxy, 2022). Therefore, the sea temperature indices, such as Pacific Decadal Oscillation Index (PDO) and El Niño–Southern Oscillation index (ENSO), are also important affecting factors of runoff (Yang et al., 2021; You et al., 2021). From the analysis of the physical mechanism of runoff, atmospheric circulation, sea temperature index, precipitation, and evaporation are all important influencing factors in the runoff prediction.

Variations of runoff are closely related to large-scale climate factors in hydrometeorological teleconnection analysis (Lima and Lall, 2010; Peters et al., 2013; Steinschneider and Lall, 2016; Wang et al., 2022). Therefore, many studies combining teleconnection analysis have been proposed to strengthen the physical meaning of runoff prediction. Wang et al. (2020) established a runoff prediction model by combining teleconnection analysis and ensemble empirical mode decomposition (EEMD) and achieved good application results, but they mentioned the cross-correlation method used in their paper is not suitable for analyzing nonlinearity and non-stationary time series. Maity and Kashid (2011) combined genetic programming (GP) with importance analysis, and used global climate factors and local meteorological variables as predictors to carry out the weekly-scale runoff forecasting for the Mahanadi River in India. It has been proved that the model derived by GP for a complex runoff system can effectively improve the accuracy of weekly runoff prediction. Yang et al. (2017) selected 17 known climate phenomenon indices, such as PDO and ENSO, and used several machine learning (ML) regression models to predict and simulate the runoff 1-month in advance of headwater reservoirs in USA and China. The results indicated that the climate phenomenon indices are beneficial for improving the accuracy of monthly or seasonal reservoir runoff prediction.

Based on the previous studies, we can find that enriching the input features of regression models is an effective method to improve the accuracy of runoff prediction. However, since numerous physical factors are expected to jointly affect the variation of runoff, there is expected to exist a mutual correlation among these factors. Thus, finding a suitable set of predictors from the high-dimensional data, consist of physical factors, as the input of the runoff prediction model is still a challenge for medium and long-term runoff prediction. In information theory, mutual information (MI) method is a powerful tool for analyzing linear and nonlinear relationships between variables (Elkiran et al., 2021), but simply selecting predictors through correlation analysis provided by MI will introduce many redundant features (Tiwari and Chaturvedi 2022). To solve this problem, in traditional high-dimensional data preprocessing, principal component analysis (PCA) is typically used to reduce dimensionality and it can effectively reduce redundant variables and feature dimensions (Ouyang et al., 2022). But PCA cannot accurately measure the importance of each feature on runoff prediction results. Thus, how to select the input predictors of regression model needs further investigation. In this study, we attempted to develop a runoff prediction model by combining ML with importance analysis for each feature (FIA-ML) to improve the accuracy of runoff prediction and explain the variation law of runoff from the view of physical causes.

In a summary, the aims of this study are: 1) to select appropriate predictors according to the importance measures computed by random forest (RF) for each feature; and 2) to construct the runoff prediction models by fitting the correlation between predictors and monthly runoff based on the ML models, whose hyper-parameters are optimized by an improved particle swarm optimization (IPSO). To fulfill these aims, the monthly

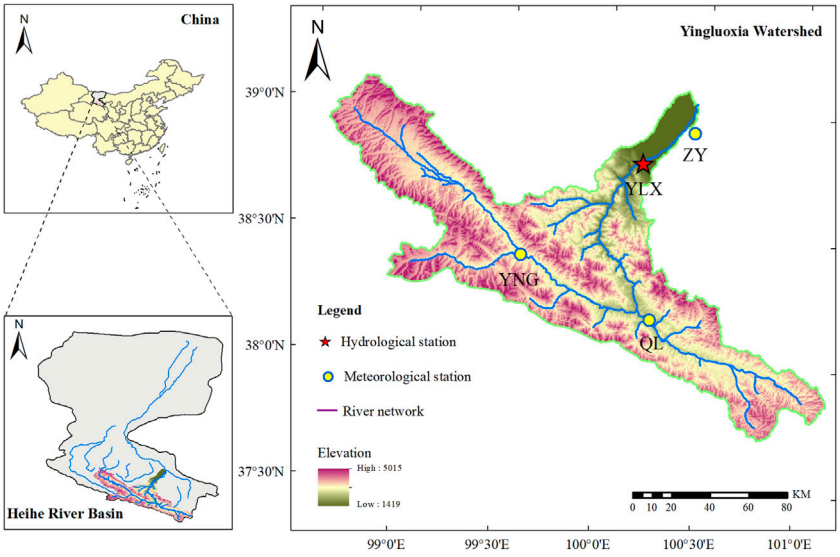

FIGURE 1
The location of the study area and meteorological observation stations. YNG denotes Yeniugou (Meteorological station 1), ZY denotes Zhangye (Meteorological station 2), QL denotes Qilian (Meteorological station 3) and YLX denotes Yingluoxia (Hydrological station).

runoff data collected from the Yingluoxia station in China was selected for illustration purposes, and the performance of the developed FIA-ML models was compared with two widely-used runoff time series analysis models, i.e., long short-term memory neural network (LSTM) and seasonal autoregressive integrated moving average (SARIMA).

2 Study area and data

2.1 Hydrological characteristics of the study area

The Heihe River Basin (HRB) is the second-largest inland watershed in Northwest China, whose geographic coordinates are roughly between 98° – 101°E and 38° – 42°N, with a drainage area of about 142, 900km^2. From the upper to the lower reaches of HRB, the annual average precipitation is: 284, 112, and 41 mm, respectively, and the annual average water surface evaporation is: 891, 1221, and 1,372–2081 mm, respectively. The climate of HRB is mainly influenced by the westerly circulation in the middle and high latitudes and the polar cold air mass, and the precipitation is sparse and concentrated.

The HRB originates from the Qilian Mountains in the south, with a total length of 821 km. It flows through Qinghai, Gansu, and Inner Mongolia provinces and finally into Juyanhai. In this study, the Yingluoxia basin (YLX) is selected as the study area, which is in the upper reaches of the HRB, with a controlled catchment area of about 10, 018km^2 (Figure 1). The main sources of surface water supply in YLX are the melting of snow and ice in the mountains and atmospheric precipitation, and the base flow is mainly supplied by groundwater, and most of the water resources of YLX concentrate in spring and summer. We collected 684 months of runoff data at YLX from 1960 to 2016 for the further analysis and research. The average annual runoff of YLX is 16.41 × 10^{8}m^3. Meanwhile, the Mann-Kendall method (Mann, 1945; Kendall, 1975) was used to analyze the trend of the annual runoff series. The results indicated that the annual runoff series showed an upward trend after 1980, and a significant upward trend was detected after 1988. The annual runoff rising rate is 0.1 × 10^{8}m^3/yr from 1960 to 2016. The increasing trend of the annual runoff of YLX is most likely due to global warming, since YLX is in the upper reaches of the HRB and is less affected by human activities (Wen et al., 2019; Zou et al., 2022).

2.2 Meteorological and large-scale climate factors

The 130 large-scale climate factors used in this study are provided by the National Climate Center of China Meteorological Administration (NCC-CMA) (https://cmdp.ncc-cma.net/cn/download.htm), including 88 atmospheric circulation indices, 26 sea temperature indices, and 16 other indices. In this study, these large-scale climate factors are sequentially numbered for 1–130, which is consistent with the

serial number of the datasets provided by the NCC-CMA. As for the local meteorological information, namely the evaporation (factor numbers: 131–133) and precipitation data (factor numbers: 134–136) of the Yeniugou (YNG), Zhangye (ZY), and Qilian (QL) meteorological stations, are collected from the National Tibetan Plateau/Third Pole Environment Data Center (https://data.tpdc.ac.cn/zh-hans/). In addition, we also considered the previous runoff of YLX (factor number: 137) as a factor. Therefore, a total of 137 physical factors were considered for further building the monthly runoff prediction model in this study.

3 Methodologies

3.1 Mutual information based on *k*-nearest neighbors

Mutual information (MI) is a nonparametric statistical method used to measure the degree of correlation between variables. MI does not have any special requirements for the distribution type of variables, and it can describe both linear and nonlinear correlation. Therefore, it has been widely used in variable selection in hydrology, meteorology, and other fields (He et al., 2015; Fang et al., 2018). Given variables X and Y, the MI between them is defined as follows:

$$I(X;Y) = \iint \mu(x,y)\log\frac{\mu(x,y)}{\mu_X(x)\mu_Y(y)}dxdy \tag{1}$$

where $\mu(x, y)$ represents the joint probability density of variables X and Y. $\mu_X(x)$ and $\mu_Y(y)$ are the marginal probability densities of X and Y, respectively. The greater the MI, the more information the variable X contains about Y, in other words, it would demonstrate a stronger dependence between these two variables.

MI has difficulties in estimating probability density. Thus, Kraskov et al. (2004) proposed a method based on k-nearest neighbors to avoid directly estimating the probability density of the variables. As for the significance test of MI, the method proposed by Sharma (2000) is applied, and the significance level is set to be 0.01 in this study.

3.2 Feature importance analysis based on random forest

Random forest (RF) is an extended variant of the bagging parallel ensemble learning method (Breiman, 2001). During the training period, it uses bootstrap sampling to generate a subset of training samples. Therefore, each base learner only uses about 63.2% of the samples in the initial training set, and the remaining 36.8% of the samples can be used as the validation set to evaluate the generalizability of RF. This way of assessing the generalization of the model is called out-of-bag (OOB) estimation.

As shown in many studies, reasonable predictors can significantly improve the accuracy and robustness of the regression model in runoff prediction (Taormina and Chau, 2015; Sharifi et al., 2017). RF can efficiently deal with the multivariate samples and measure the importance of each variable (Genuer et al., 2010; Hapfelmeier et al., 2014). The importance measure of each feature in runoff forecasting is computed as follows: 1) to obtain the mean square error vector $\{MSE_t|t = 1, 2, \ldots, T\}$ for the T base decision trees in OOB estimation; 2) shuffling each feature of the OOB samples in turn, and the variation of MSE_t for each feature perturbation is represented by the following matrix.

$$\begin{bmatrix} MSE_{11} & MSE_{12} & \cdots & MSE_{1T} \\ MSE_{21} & MSE_{22} & \cdots & MSE_{2T} \\ \vdots & \vdots & \ddots & \vdots \\ MSE_{m1} & MSE_{m2} & \cdots & MSE_{mT} \end{bmatrix} \tag{2}$$

where m and T are the number of features and the number of decision trees, respectively. MSE_{mt} is the OOB mean square error of the t base decision tree after shuffling the $m-$th feature. Therefore, Eq. 3 can be used to measure the perturbation degree of the $m-$th feature to the model.

$$H_m^{oob} = \frac{1}{T}\sum_{t=1}^{T}(MSE_{mt} - MSE_t) \tag{3}$$

If the feature is shuffled, the greater the accuracy of OOB estimation decreases, the greater the degree of disturbance to the model by the feature. By normalizing H_m^{oob} to the range of [0,1], the importance measure of each feature (FIM) can be obtained. In previous studies, the impurity weighted increments of the leaf nodes of the tree model were mostly used to measure the importance of features (Zuo et al., 2020). However, the impurity-based method usually causes the feature importance to drop rapidly, and the identification of feature importance is relatively insensitive. Therefore, we used the decreases of accuracy of OOB estimation to measure the influence of each feature on the runoff prediction result in this study.

3.3 Regression model

3.3.1 Hybrid kernel support vector machine

Support vector machines (SVM) can solve nonlinear problems, mainly using the kernel function to map the input factors to the high-dimensional space and then performing linear regression. Different kernel functions will significantly affect the fitting ability of SVM to different kinds of nonlinear problems. Among the commonly used kernel functions, the polynomial kernel function κ_{Poly} (see Eq. 4) has strong generalization ability

and weak learning ability. On the contrary, the localized Gaussian radial basis kernel function κ_{Rbf} (see Eq. 5) has robust learning ability, but its generalization ability is relatively weak. According to the Mercer kernel theory, it can effectively overcome the shortcomings of the existing kernel functions by combining these two types of kernel functions into a new hybrid kernel function (Zheng et al., 2005; Zhou et al., 2018). Therefore, the polynomial kernel function and the Gaussian radial basis kernel function are combined into a hybrid kernel function κ_{HK} (see Eq. 6), and the hybrid kernel support vector machine (HKSVM) is developed in this study.

$$\kappa_{Poly}(\boldsymbol{x}, \boldsymbol{x}_i) = (\gamma_p(\boldsymbol{x} \cdot \boldsymbol{x}_i) + 1)^3 \tag{4}$$

$$\kappa_{Rbf}(\boldsymbol{x}, \boldsymbol{x}_i) = \exp(\gamma_r \|\boldsymbol{x} - \boldsymbol{x}_i\|^2) \tag{5}$$

$$\kappa_{HK}(\boldsymbol{x}, \boldsymbol{x}_i) = \lambda\kappa_{Poly} + (1 - \lambda)\kappa_{Rbf} \tag{6}$$

where $\boldsymbol{x}$ is the input predictors, and $\boldsymbol{x}_i$ is the input predictors of the i – th training sample. γ_p and γ_r are the kernel parameters. $\lambda \in [0, 1]$ represents the proportion of κ_{Poly} and κ_{Rbf} in the hybrid kernel function κ_{HK}. It should be noted that HKSVM also has two important parameters, which are the penalty factor C and the insensitivity coefficient ε.

3.3.2 Extreme learning machine

Extreme learning machine (ELM) is a machine learning method based on feedforward neural network. ELM consists of a three-layer structure: input layer, hidden layer, and output layer. During the training period, the weights of the output layer can be obtained by the least square method (LSM). Given the input predictors $\boldsymbol{x}$, the runoff prediction value y is calculated by the following equation:

$$y(\boldsymbol{x}) = \sum_{l=1}^{L} \boldsymbol{\beta}_l G(\boldsymbol{\omega}_l, b_l, \boldsymbol{x}) \tag{7}$$

where L is the number of hidden layer neurons. $\boldsymbol{\omega}_l$ and b_l are the input weights and thresholds of the hidden layer neurons, respectively. $G(\cdot)$ is the activation function. $\boldsymbol{\beta}_l$ is the connection weight vector connecting the hidden layer neurons and the output layer neurons, which can be obtained by the Moore-Penrose generalized inverse method (Huang et al., 2006).

3.3.3 General regression neural network

Generalized Regression Neural Network (GRNN) is of high fault tolerance and strong robustness, which is suitable for solving nonlinear problems and can also handle unstable data. The network structure of GRNN consists of the input layer, mode layer, summation layer and output layer. After the input predictors $\boldsymbol{x}$ is input from the input layer, the following Eq. 8 can express the runoff prediction value.

$$y(\boldsymbol{x}) = \frac{\sum_{i=1}^{N} y_i \exp[-\|\boldsymbol{x} - \boldsymbol{x}_i\|^2 / 2\sigma^2]}{\sum_{i=1}^{N} \exp[-\|\boldsymbol{x} - \boldsymbol{x}_i\|^2 / 2\sigma^2]} \tag{8}$$

where N is the number of training samples, and y_i is the observed runoff corresponding to the i – th training sample. σ is the smoothing factor.

3.3.4 Multiple linear regression

Multiple Linear Regression (MLR) can be used to fit a linear relationship between multiple independent and dependent variables. After the specific MLR equation is obtained through training, the dependent variable can be predicted by the following equation:

$$y(x) = b_0 + b_1 x_1 + b_2 x_2 + \cdots + b_m x_m + \mu \tag{9}$$

where x_i and b_i are the i – th input predictor and regression coefficient, respectively. μ is a random error satisfying the Gaussian distribution. The solution of the regression coefficients in Eq. 9 usually adopts the LSM.

3.4 Hyper-parameters optimization for regression models

The performance of machine learning (ML) may be limited in practice since its forecasting results are largely influenced by the choice of hyper-parameters. Therefore, it is critical to obtain the hyper-parameters combination with the best generalization performance. In this study, we use the K-Fold cross-validation method (Soper, 2021) to evaluate the model performance. However, the cross-validation results of ML models are sensitive to the choice of hyper-parameters. When using conventional particle swarm optimization algorithms to estimate their hyper-parameters, there are problems of premature maturity and local convergence. To overcome these problems, we employed an improved particle swarm optimization algorithm (IPSO) in this study to determine a set of hyper-parameters that optimize the cross-validation results. Please refer to Lei et al. (2022) for more details about IPSO. The hyper-parameters that need to be tuned by IPSO are displayed in Table 1.

3.5 Model performance evaluation metrics

In this study, we selected several indicators to quantitatively analyze the performance of various models, which are Nash-Sutcliffe efficiency (NSE), root mean square error (RMSE), the coefficient of correlation (R), and Kling-Gupta efficiency (KGE) (Gupta et al., 2009).

TABLE 1 The range of hyper-parameters to be optimized for the model used in this paper.

Model	Hyper-parameter	Search range	Parameter type
RF	The number of trees in the forest	[10, 200]	Integer
	The maximum depth of the tree	[10, 100]	Integer
	Min samples split	(0, 1]	Real
	Min samples leaf	(0, 0.5]	Real
HKSVM	Polynomial kernel parameter	$[2^{-10}, 2^{10}]$	Real
	Gaussian radial basis kernel parameter	$[2^{-10}, 2^{10}]$	Real
	The proportion of κ_{Poly} and κ_{Rbf}	[0, 1]	Real
	Penalty factor C	$[2^{-10}, 2^{10}]$	Real
	Insensitivity coefficient ε	[0, 1]	Real
ELM	The number of hidden layer neurons L	[1, 100]	Integer
	Random state	$[2^0-1, 2^{32}-1]$	Integer
GRNN	Smoothing factor σ	$[10^{-10}, 10]$	Real

The value range of *NSE* is $(-\infty, 1]$. The closer it is to 1, the better the prediction effect and the higher the reliability of the model. It is calculated by the following equation:

$$NSE = 1 - \frac{\sum_{i=1}^{n}\left(y_{o,i} - y_{s,i}\right)^2}{\sum_{i=1}^{n}\left(y_{o,i} - \bar{y}_o\right)^2} \tag{10}$$

where n is the number of testing samples. $y_{o,i}$ and $y_{s,i}$ are the i – th observed value and predicted value. $\bar{y}_o$ is the mean of the observed series.

The smaller the RMSE, the higher the prediction accuracy. It is calculated by the following equation:

$$RMSE = \sqrt{\frac{1}{n}\sum_{i=1}^{n}\left(y_{o,i} - y_{s,i}\right)^2} \tag{11}$$

R is a statistical indicator that reflects the correlation between the predictions and the observations. The closer it is to 1, the higher the prediction accuracy. It is calculated by the following equation:

$$R = \frac{\sum_{i=1}^{n}\left(y_{o,i} - \bar{y}_o\right)\left(y_{s,i} - \bar{y}_s\right)}{\sqrt{\sum_{i=1}^{n}\left(y_{o,i} - \bar{y}_o\right)^2 \sum_{i=1}^{n}\left(y_{s,i} - \bar{y}_s\right)^2}} \tag{12}$$

where $\bar{y}_s$ is the mean of the predicted series.

KGE is a new metric proposed to address the deficiencies of *NSE* in model calibration and evaluation. It is calculated by the following equation:

$$KGE = 1 - \sqrt{(r-1)^2 + \left(\frac{\sigma_s}{\sigma_o} - 1\right)^2 + \left(\frac{\mu_s}{\mu_o} - 1\right)^2} \tag{13}$$

where r is the linear regression coefficient between the observed and predicted values. μ_o, σ_o, μ_s, σ_s correspond to the mean and standard deviation of the observed and predicted series, respectively.

3.6 Monthly runoff prediction using the proposed feature importance analysis and machine learning model

The main purpose of this study is to screen out suitable input predictors for the ML models and to explore which physical factors have a significant impact on the monthly runoff of YLX station. In this study, the monthly runoff of the first 564 months (1960–2006) of YLX station was used as training data to train the model, and the monthly runoff of the last 120 months (2007–2016) was used as testing data to test the predictive accuracy of the monthly runoff prediction model. The flowchart of the monthly runoff prediction model by combining ML with feature importance analysis (FIA-ML) is presented in Figure 2.

This study proposed a novel monthly runoff prediction model combining ML with teleconnection analysis, which is different from the commonly used time series analysis model (TSAM). Therefore, to show the superiority of the proposed FIA-ML model, it is necessary to make a comparison with some traditional TSAMs. In the following analysis, we compared the FIA-ML model with the widely used long short-term memory neural network (LSTM) and seasonal autoregressive integrated moving average (SARIMA) in previous studies. LSTM is a variant of recurrent neural network (RNN), which can effectively solve the gradient explosion or disappearance of simple RNN, and control the transfer of runoff time series information through a gating mechanism (Yuan et al., 2018; Ghose et al., 2022). Considering that the monthly runoff series is affected by the interaction of seasonal effects, long-term trend effects and random

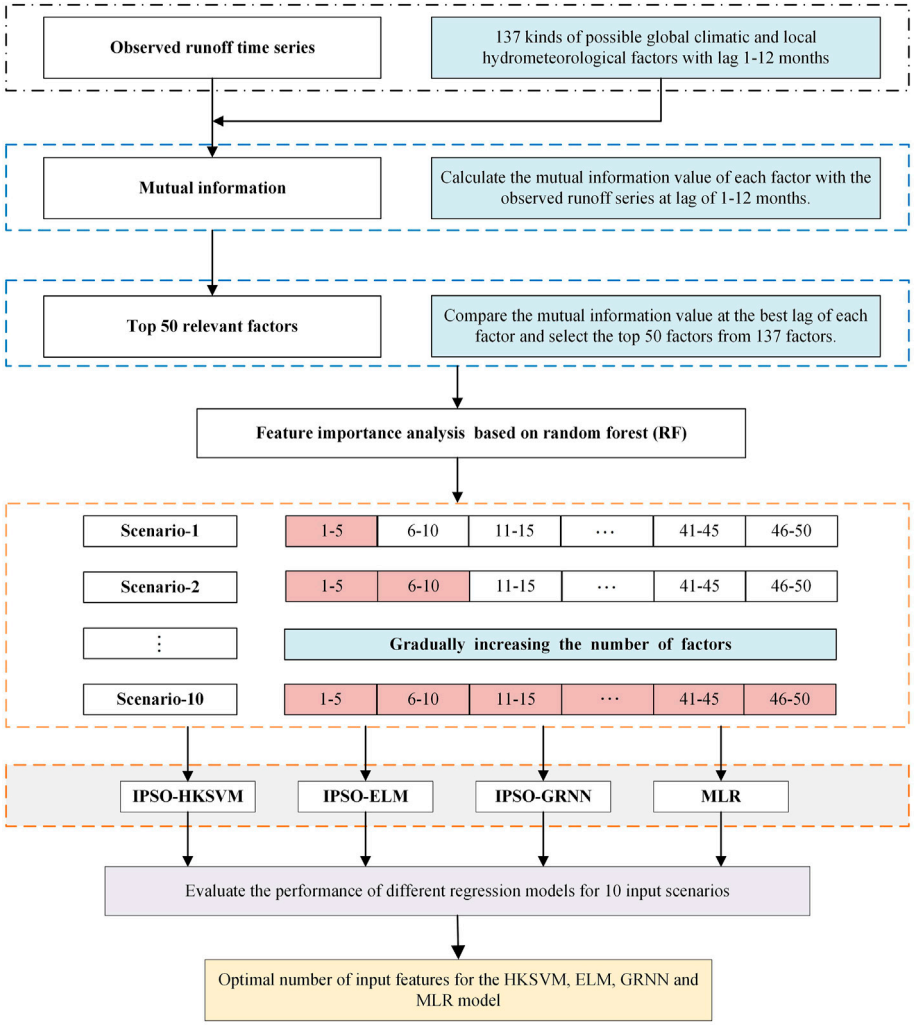

FIGURE 2
The flowchart of monthly runoff prediction using the FIA-ML model.

fluctuations, SARIMA transforms the nonstationary monthly runoff series into stationary series by performing trend difference and seasonal difference operation, and then establish a statistical analysis model (Valipour, 2015). The TSAM requires less basin information and is easy to use, so it has been widely used in practice. However, with the impact of changing environmental on the stationariness of the runoff series, the prediction accuracy of TSAM will also be affected to a certain extent. In contrast, although the FIA-ML model is more complex, it fully considers a variety of physical factors affecting runoff, and it has better application prospects in the context of climate change. It should be noted that when comparing the runoff prediction accuracy of TSAM and FIA-ML models below, the input predictors of the FIA-ML models adopted their corresponding best input scenario.

4 Results and discussion

4.1 selection of model input predictors

The choice of model input predictors will directly affect the final runoff prediction results. In this study, we aimed to construct a set of physical predictors for the runoff prediction model by identifying the key physical factors affecting runoff, from the 137 physical factors including large-scale climate index, precipitation, and evaporation, etc. To ensure the quality of the data and the reliability of this study, we directly discarded the physical factors with missing data to avoid unreasonable interpolation. It should be mentioned that the influence of the physical factors on runoff has a lag effect. Thus, in this study, the predictors with 1–12-month lags were employed to inform the

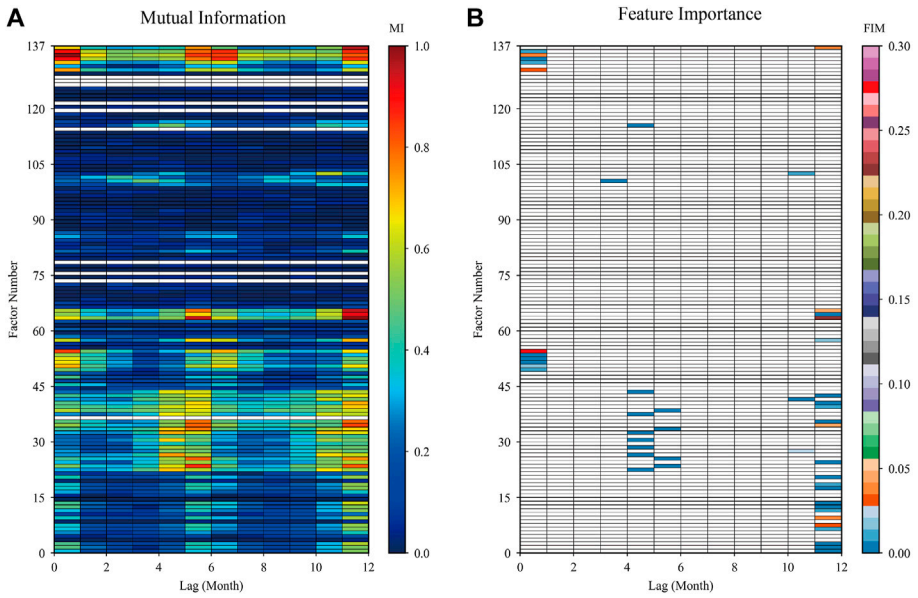

FIGURE 3
the mutual information value among the 137 factors and the observed runoff at a lag of 1–12 months, and the blanks are missing factors **(A)**, and the importance score of the physical factors whose mutual information values are ranked in the top 50, which are filled with color **(B)**.

runoff prediction model, considering the seasonal variation characteristics of monthly runoff.

As shown in Figure 3, there are several comments should be noted as follows: 1) among the 88 large-scale circulation factors, NPVI (factor number 55: Northern Hemisphere Polar Vortex Intensity Index) with a 1-month lag and EATI (factor number 64: East Asian Trough Intensity Index) with a 12-month lag are the most important factors for improving the accuracy of runoff prediction. 2) The effect of evaporation on runoff is more important than precipitation, which is consistent with the climate characteristics of more evaporation and less precipitation in Northwest China. 3) YLX basin was less affected by oceanic action, such as ENSO and PDO. Among the sea temperature indices, the influence of IOWPA (factor number 101: Indian Ocean Warm Pool Area Index) with a 4-month lag and WPWPA (factor number 103: Western Pacific Warm Pool Area Index) with an 11-month lag was relatively significant.

In this study, we synthesized 10 scenarios (Figure 2) for 4 prediction models, that is HKSVM (M1), ELM (M2), GRNN (M3), and MLR (M4). Thus, four metrics, namely NSE, KGE, RMSE and R, are used to find the optimal input scenario for each model. According to the level of MI (Figure 3A), we selected the top 50 physical factors, and then RF is used to order the importance of these factors (Figure 3B). Based on the order of importance, we sequentially added 5 physical factors each time as the model input. So, a total of 10 input scenarios was generated (Figure 2). Synthesizing the prediction accuracy of the four regression models under 10 input scenarios, the HKSVM and MLR perform best in scenario 4, and the ELM and GRNN perform best in scenario 3. It can be seen from Figure 4 that with the increase of input features, the prediction accuracy of each model firstly becomes better, but after the optimal input scenario appears, increasing the input features is not conducive to further improve the prediction accuracy. There are two main reasons for this result: 1) the input features are too few to reveal the complex variation mechanism of runoff, but the increase the number of input features will introduce some redundant features; 2) if the number of input features are too large, it will increase the observation error of samples and the complexity of the model, which is not good for training the model and could weaken its promotion potential. Therefore, this study adopted the method of gradually increasing the number of input features in order of the feature importance, and selected the best predictors set according to the performance of each model during the testing period.

4.2 Monthly runoff prediction simulation

The statistical results of the prediction accuracy evaluation indicators of each model during the training period and the testing period were summarized in Table 2. The training period is the learning phase of the model, and the quality of the learning will directly affect the actual runoff prediction effect. In practical engineering, the performance of the model during the testing

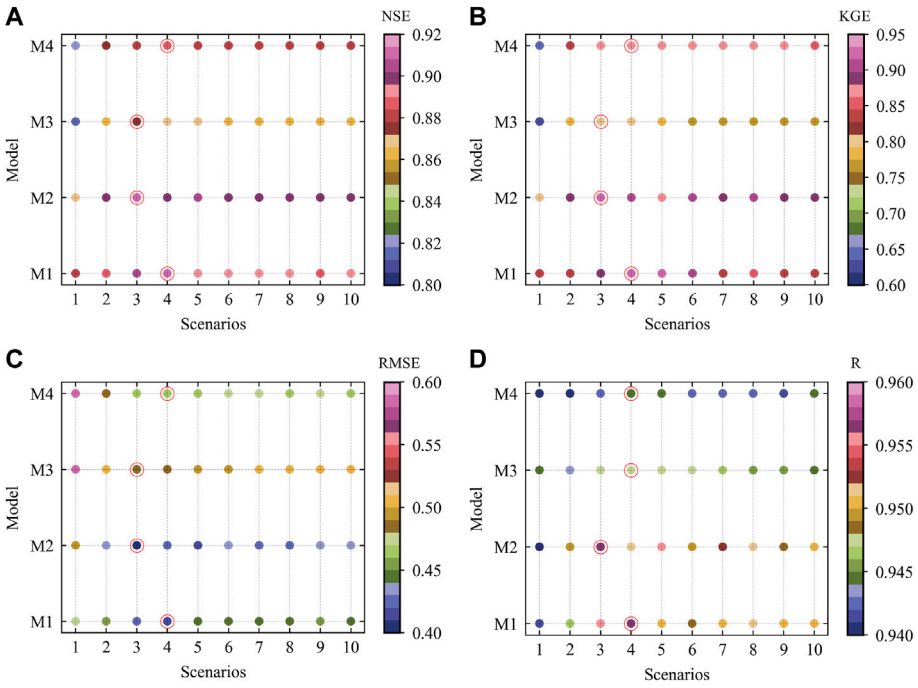

FIGURE 4
The results of NSE **(A)**, KGE **(B)**, RMSE **(C)**, and R **(D)** of each model for 10 input scenarios. The best input scenario is selected by the red circle. The models represented by M1-M4 are shown in Table 2.

TABLE 2 Prediction accuracy evaluation metrics of different models during training and testing period.

Model		Training period				Testing period			
		NSE	KGE	RMSE	R	NSE	KGE	RMSE	R
FIA-ML	HKSVM (M1)	0.863	0.924	0.429	0.934	0.908	0.930	0.411	0.956
	ELM (M2)	0.844	0.879	0.456	0.919	0.911	0.920	0.406	0.956
	GRNN (M3)	0.985	0.955	0.141	0.993	0.873	0.802	0.484	0.948
	MLR (M4)	0.817	0.855	0.493	0.904	0.885	0.873	0.460	0.945
TSAM	LSTM (M5)	0.839	0.905	0.464	0.918	0.870	0.795	0.490	0.946
	SARIMA (M6)	0.831	0.850	0.476	0.912	0.868	0.763	0.494	0.949

phase is usually more concerned, because it reflects the generalization ability and practical application effect of the model. As shown in Table 2, the overall performance of FIA-ML models showed better during the testing period, compared with the runoff time series analysis models. Furthermore, among the FIA-ML models, HKSVM and ELM have better runoff forecasting ability, which further demonstrates that choosing an appropriate machine learning algorithm is also a way to improve the accuracy of runoff prediction. Besides, we can see that GRNN is the best model during the training period, but its performance is not good enough during the testing period. Obviously, GRNN shows overfitting, which is because GRNN is too sensitive to the samples appearing in the learning stage, resulting in the lack of ability to explore the general variation of out-of-sample data. In contrast, HKSVM combines the advantages of polynomial kernel and Gaussian radial basis kernel function, and has relatively strong learning ability and generalization ability. To further compare the effect of each model in practical application, we show the fitting quality of each model during the testing period Figures 5,6,7,8.

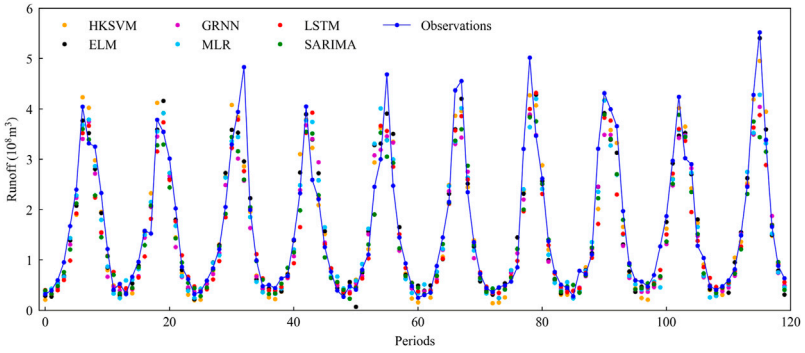

FIGURE 5
Comparison of observed and fitted runoff by different models for 2007–2016 (testing period).

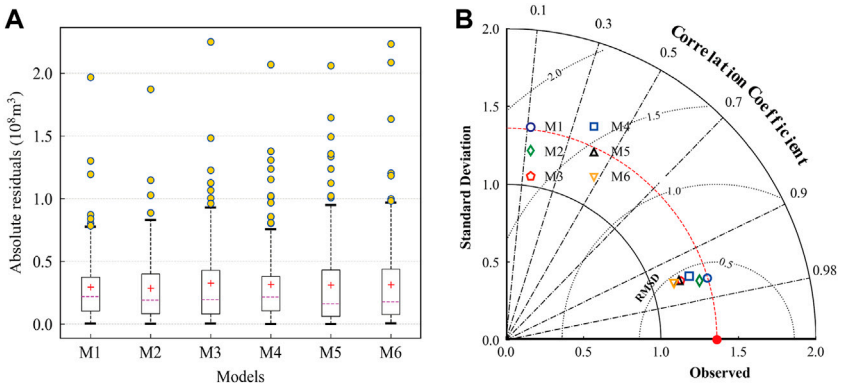

FIGURE 6
Boxplot of absolute residuals **(A)** and Taylor diagrams **(B)** of the results of monthly runoff prediction during the testing period. The models represented by M1–M6 are shown in Table 2.

Figure 5 shows the fitting performance of the 120-month runoff observations and the predictions of the monthly runoff prediction models during the testing simulation phase. The monthly runoff of YLX during the wet season fluctuates obviously across different years. The FIA-ML models can relatively better capture the variation of monthly runoff, especially with HKSVM and ELM regression models.

Figure 6A is a boxplot of absolute residuals, which can describe the distribution of the difference between the predicted and observed values. Figure 6B is a Taylor diagram (Taylor, 2001), which skillfully integrates the correlation coefficient, centered root mean square error, and standard deviation into a polar plot, avoiding the limitations of a single evaluation metric. Therefore, it can more intuitively show the difference between the predicted and observed values. One can see from Figure 6 that the simulation prediction results of M1 (HKSVM) and M2 (ELM) are closer to the actual runoff observations. This indicated that ELM and HKSVM have more robust capabilities to reveal the correlation between predictors and observed runoff.

Figure 7 shows the linear relationship between the observed runoff and the simulated value obtained by different prediction methods during the testing period. It is found that both the FIA-ML models and the runoff time series analysis models are feasible in tracking the dynamic changes of monthly runoff. In addition, ELM has the best effect from the perspective of R^2, and MLR is the worst. While if we analyze from the trend line of linear fitting, HKSVM is closer to the actual trend line, and the runoff time series analysis models perform worse.

In practical engineering, the prediction accuracy of peak monthly runoff is more significant than runoff in other months. For this reason, we compared the prediction effect of

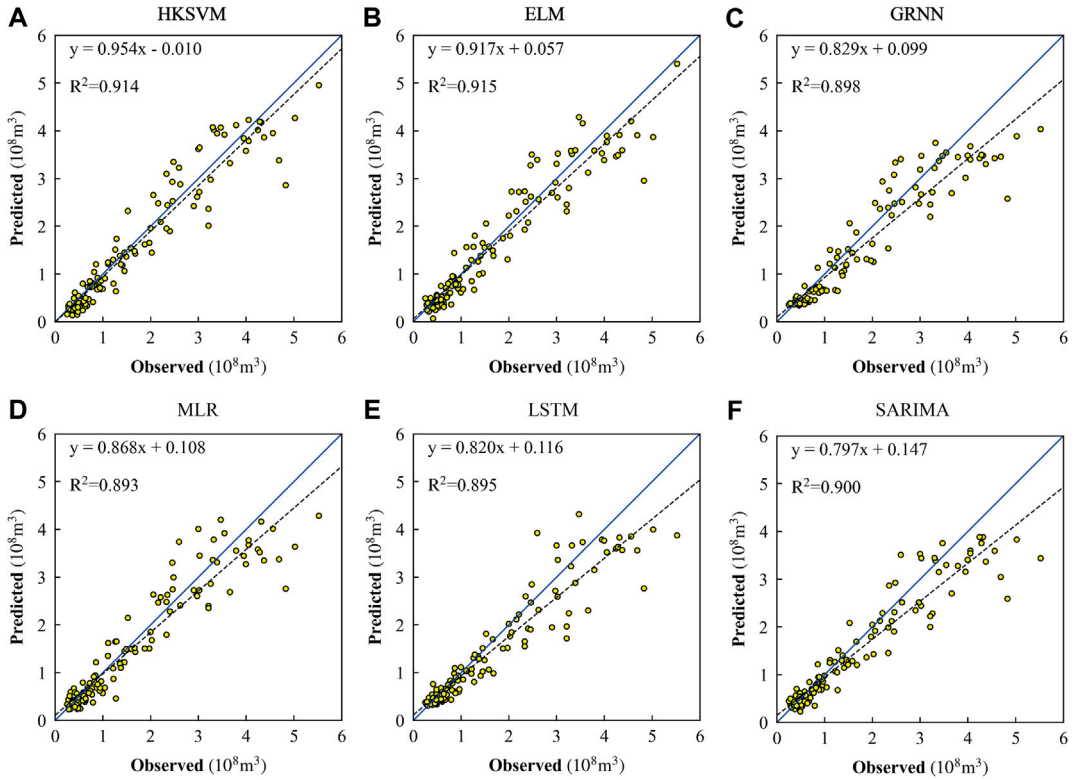

FIGURE 7
Scatter plot of observations and predictions by HKSVM **(A)**, ELM **(B)**, GRNN **(C)**, MLR **(D)**, LSTM **(E)**, and SARIMA **(F)** during the testing period.

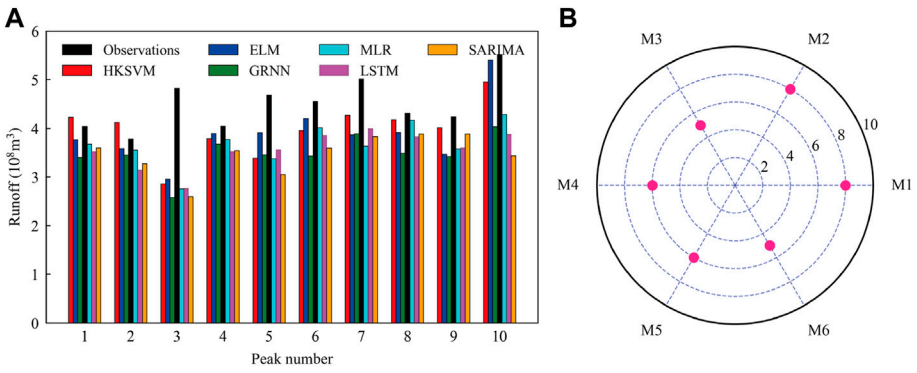

FIGURE 8
Observations and predictions of peak monthly runoff with different models during the testing period are displayed in **(A)**, and the number of years that the predictions of each model meet the design requirements is displayed in **(B)**. The models represented by M1-M6 are shown in Table 2.

each model on peak monthly runoff during the testing period. According to the standard for hydrological information and hydrological forecasting formulated by the Ministry of Water Resources of China, for medium and long-term runoff prediction, when the relative error of the prediction result is less than 20%, it is considered a valid prediction value (Zhang et al., 2011). As displayed in Figure 8, M1 (HKSVM) and M2 (ELM) have eight years to meet the design requirements, but the performance of M3 (GRNN) and M6 (SARIMA) are relatively poor, with only five years to meet the design requirements.

4.3 Discussion

When using ML for runoff prediction, the choice of predictors is critical. Because the quality of the effective information carried by the features will directly affect the accuracy of runoff prediction. Our simulations revealed that appropriately increasing the number of features can improve the accuracy of monthly runoff prediction. However, too many input features will increase the complexity of training the model and reduce the ability to capture the general changing characteristics of runoff process. In this study, the NSEs of FIA-ML models (M1-M4) were initially 0.878, 0.866, 0.815, and 0.818. When the optimal number of input features for each model was reached, their NSEs were improved by 3.4%, 5.2%, 7.1%, and 8.2%, respectively. However, if the number of input features continue to increase, the accuracy of runoff prediction will not continue to get better. This should be mainly because too many inputs will make the model training subject to some abnormal information interference, and reduce the training efficiency.

Although RF is an effective tool to measure the feature importance, it also has some shortcomings. One of the most important issues is that if there are too many input features in RF, the efficiency and accuracy of calculating the importance score of each feature will be affected. Thus, this study first uses MI to select the top 50 factors related to the observed runoff, which is equivalent to a rough screening from numerous possible factors. The method combined RF with MI can effectively overcome the shortcomings of the single use RF or MI to select predictors as the inputs of the ML models.

Compared with the TSAM, the FIA-ML model can improve the NSE by up to 5%, and more importantly, can explain the variation characteristics of runoff from the physical meaning. However, it should be noted that although the FIA-ML models can improve the prediction accuracy to a certain extent, some issues should be noted in the application. One is that the meteorological information we used is relatively less in this study, so, in future work, we can further consider more meteorological factors related to prediction of monthly runoff. Another is that although the IPSO can effectively improve the global search ability of particles, there is still the problem of falling into local convergence, so it is necessary to explore a more efficient methods for improving the global search ability in selecting model hyper-parameters. In addition, simply depending on the correlation between the runoff process and these physical factors is not enough to fully reveal the variation characteristics of runoff, since the runoff prediction system is open and complex. Therefore, the system dynamics characteristics of the runoff process can be considered in machine learning in further studies.

5 Conclusion

We proposed the model by combining ML with the feature importance analysis (FIA-ML), which can select key predictors from the numerous physical factors and effectively integrate hydrometeorological information and teleconnection climate factors into the ML models. This paper verified the applicability of the model in the YLX basin, and compared with the traditional time series analysis model (TSAM). Under changing environments, the TSAM cannot accurately capture the impact of climate change on the characteristics of runoff variability. By contrast, the FIA-ML models not only have better runoff prediction ability, but can, more importantly, explain which physical factors have a significant impact on the runoff in the YLX basin.

The FIA-ML models can effectively improve the learning efficiency of ML models and the accuracy of runoff prediction. Especially, HKSVM and ELM optimized by IPSO have a good fitting ability for the relationship between observed runoff and input predictors. Therefore, the FIA-ML model is a useful attempt to improve the accuracy of runoff prediction by establishing the teleconnection between climate change and runoff change.

Data availability statement

The original contributions presented in the study are included in the article/Supplementary Material, further inquiries can be directed to the corresponding author.

Author contributions

LY: conceptualization, formal analysis, writing-original draft, writing-review and editing, supervision. QL: methodology, writing-original draft, writing-review, and editing. CJ: writing-original draft. PY: writing-review and editing. BL: writing-review and editing. ZR: writing-review and editing. ZL: writing-review and editing.

Funding

This study is financially supported jointly by the National Natural Science Foundation of China (No. 51909053, U2240201, 51909112), the Youth Foundation of Education Department of Hebei Province (QN2019132), Xingtai City Science and Technology Bureau (2021ZZ032), all of which are greatly appreciated.

Acknowledgments

We are very grateful to the editors and reviewers for their critical comments and thoughtful suggestions.

Conflict of interest

The authors declare that the research was conducted in the absence of any commercial or financial relationships that could be construed as a potential conflict of interest.

Publisher's note

References

Bian, Y., Sun, P., Zhang, Q., Luo, M., and Liu, R. (2022). Amplification of non-stationary drought to heatwave duration and intensity in eastern China: Spatiotemporal pattern and causes. *J. Hydrol. X.* 612, 128154. doi:10.1016/j.jhydrol.2022.128154

Breiman, L. (2001). Random forests. *Mach. Learn.* 45 (1), 5–32. doi:10.1023/A:1010933404324

Elkiran, G., Nourani, V., Elvis, O., and Abdullahi, J. (2021). Impact of climate change on hydro-climatological parameters in North Cyprus: Application of artificial intelligence-based statistical downscaling models. *J. Hydroinform.* 23 (6), 1395–1415. doi:10.2166/hydro.2021.091

Fang, W., Huang, S., Huang, Q., Huang, G., Meng, E., and Luan, J. (2018). Reference evapotranspiration forecasting based on local meteorological and global climate information screened by partial mutual information. *J. Hydrol. X.* 561, 764–779. doi:10.1016/j.jhydrol.2018.04.038

Feng, Z., Liu, S., Niu, W., Li, S., Wu, H., and Wang, J. (2020a). Ecological operation of cascade hydropower reservoirs by elite-guide gravitational search algorithm with Lévy flight local search and mutation. *J. Hydrol. X.* 581, 124425. doi:10.1016/j.jhydrol.2019.124425

Feng, Z., Niu, W., Tang, Z., Jiang, Z., Yang, X., Liu, Y., et al. (2020b). Monthly runoff time series prediction by variational mode decomposition and support vector machine based on quantum-behaved particle swarm optimization. *J. Hydrol. X.* 583, 124627. doi:10.1016/j.jhydrol.2020.124627

Genuer, R., Poggi, J. M., and Tuleau-Malot, C. (2010). Variable selection using random forests. *Pattern Recognit. Lett.* 31 (14), 2225–2236. doi:10.1016/j.patrec.2010.03.014

Ghose, D. K., Mahakur, V., and Sahoo, A. (2022). "Monthly runoff prediction by hybrid CNN-LSTM model: A case study," in *Communications in computer and information science* (Cham: Springer), 1614. doi:10.1007/978-3-031-12641-3_31

Gupta, H. V., Kling, H., Yilmaz, K. K., and Martinez, G. F. (2009). Decomposition of the mean squared error and NSE performance criteria: Implications for improving hydrological modelling. *J. Hydrol. X.* 377 (1-2), 80–91. doi:10.1016/j.jhydrol.2009.08.003

Hapfelmeier, A., Hothorn, T., Ulm, K., and Strobal, C. (2014). A new variable importance measure for random forests with missing data. *Stat. Comput.* 24 (1), 21–34. doi:10.1007/s11222-012-9349-1

He, X., Guan, H., and Qin, J. (2015). A hybrid wavelet neural network model with mutual information and particle swarm optimization for forecasting monthly rainfall. *J. Hydrol. X.* 527, 88–100. doi:10.1016/j.jhydrol.2015.04.047

Hu, Y., Liang, Z., Huang, Y., Yao, Y., Wang, J., and Li, B. (2022). A nonstationary bivariate design flood estimation approach coupled with the most likely and expectation combination strategies. *J. Hydrol. X.* 605, 127325. doi:10.1016/j.jhydrol.2021.127325

Huang, G., Zhu, Q., and Siew, C. K. (2006). Extreme learning machine: Theory and applications. *Neurocomputing* 70 (1–3), 489–501. doi:10.1016/j.neucom.2005.12.126

Huang, S., Chang, J., Huang, Q., and Chen, Y. (2014). Monthly streamflow prediction using modified EMD-based support vector machine. *J. Hydrol. X.* 511, 764–775. doi:10.1016/j.jhydrol.2014.01.062

Huang, S., Li, P., Huang, Q., Leng, G., Hou, B., and Ma, L. (2017). The propagation from meteorological to hydrological drought and its potential influence factors. *J. Hydrol. X.* 547, 184–195. doi:10.1016/j.jhydrol.2017.01.041

Jian, S., Yin, C., Wang, Y., Yu, X., and Li, Y. (2022). The possible incoming runoff under extreme rainfall event in the Fenhe river basin. *Front. Environ. Sci.* 10, 812351. doi:10.3389/fenvs.2022.812351

Jiang, C., Xiong, L., Yan, L., Dong, J., and Xu, C.-Y. (2019). Multivariate hydrologic design methods under nonstationary conditions and application to engineering practice. *Hydrol. Earth Syst. Sci.* 23 (3), 1683–1704. doi:10.5194/hess-23-1683-2019

Kendall, M. G. (1975). *Rank correlation methods*. London: Grifin.

Kraskov, A., Stögbauer, H., and Grassberger, P. (2004). Estimating mutual information. *Phys. Rev. E* 69 (6), 066138. doi:10.1103/PhysRevE.69.066138

Lei, Q., Yan, L., Lu, D., Bu, J., and Luo, Y. (2022). Research on P-III distribution maximum likelihood estimation based on particle swarm optimization algorithm. *Chin. Rur. Water Hydropow.* 2022 (7), 128–131+139.

Lima, C. H. R., and Lall, U. (2010). Spatial scaling in a changing climate: A hierarchical bayesian model for non-stationary multi-site annual maximum and monthly streamflow. *J. Hydrol. X.* 383 (3-4), 307–318. doi:10.1016/j.jhydrol.2009.12.045

Lin, K., Sheng, S., Zhou, Y., Liu, F., Li, Z., Chen, H., et al. (2020). The exploration of a Temporal Convolutional Network combined with Encoder-Decoder framework for runoff forecasting. *Hydrol. Res.* 51 (5), 1136–1149. doi:10.2166/nh.2020.100

Lu, F., Song, X., Xiao, W., Zhu, K., and Xie, Z. (2020). Detecting the impact of climate and reservoirs on extreme floods using nonstationary frequency models. *Stoch. Environ. Res. Risk Assess.* 34 (1), 169–182. doi:10.1007/s00477-019-01747-2

Luo, K., Tao, F., Deng, X., and Moiwo, J. P. (2017). Changes in potential evapotranspiration and surface runoff in 1981–2010 and the driving factors in Upper Heihe River Basin in Northwest China. *Hydrol. Process.* 31 (1), 90–103. doi:10.1002/hyp.10974

Ma, Z., Sun, P., Zhang, Q., Zou, Y., Lv, Y., Li, H., et al. (2022). The characteristics and evaluation of future droughts across China through the CMIP6 multi-Model ensemble. *Remote Sens. (Basel).* 14 (5), 1097. doi:10.3390/rs14051097

Maity, R., and Kashid, S. S. (2011). Importance analysis of local and global climate inputs for basin-scale streamflow prediction. *Water Resour. Res.* 47 (11), W11504. doi:10.1029/2010WR009742

Mann, H. B. (1945). Nonparametric tests against trend. *Econometrica* 13 (3), 245–259. doi:10.2307/1907187

Meng, E., Huang, S., Huang, Q., Fang, W., Wu, L., and Wang, L. (2019). A robust method for non-stationary streamflow prediction based on improved EMD-SVM model. *J. Hydrol. X.* 568, 462–478. doi:10.1016/j.jhydrol.2018.11.015

Niu, W., Feng, Z., Chen, Y., Zhang, H., and Wang, L. (2020). Annual streamflow time series prediction using extreme learning machine based on gravitational search algorithm and variational mode decomposition. *J. Hydrol. Eng.* 25 (5), 04020008. doi:10.1061/(ASCE)HE.1943-5584.0001902

Niu, W., Feng, Z., Feng, B., Xu, Y., and Min, Y. (2021). Parallel computing and swarm intelligence based artificial intelligence model for multi-step-ahead hydrological time series prediction. *Sustain. Cities Soc.* 66, 102686. doi:10.1016/j.scs.2020.102686

Nugent, K. A., and Matthews, H. D. (2012). Drivers of future northern latitude runoff change. *Atmosphere-Ocean* 50 (2), 197–206. doi:10.1080/07055900.2012.658505

Ouyang, Y., Grace, J. M., Parajuli, P. B., and Caldwell, P. V. (2022). Impacts of multiple hurricanes and tropical storms on watershed hydrological processes in the Florida panhandle. *Climate* 10 (3), 42. doi:10.3390/cli10030042

Peters, D. L., Atkinson, D., Monk, W. A., Tenenbaum, D. E., and Baird, D. J. (2013). A multi-scale hydroclimatic analysis of runoff generation in the Athabasca River, Western Canada. *Hydrol. Process.* 27 (13), 1915–1934. doi:10.1002/hyp.9699

Samantaray, S., Das, S. S., Sahoo, A., and Satapathy, D. P. (2022a). Monthly runoff prediction at Baitarani river basin by support vector machine based on Salp swarm algorithm. *Ain Shams Eng. J.* 13 (5), 101732. doi:10.1016/j.asej.2022.101732

Samantaray, S., Sah, M. K., Chalan, M. M., Sahoo, A., and Mohanta, N. R. (2022b). "Runoff prediction using hybrid SVM-PSO approach," in *Lecture notes in networks and systems* (Singapore: Springer), 446. doi:10.1007/978-981-19-1559-8_29

Samantaray, S., Sahoo, A., Das, S. S., and Satapathy, D. P. (2022c). Development of rainfall-runoff model using anfis with an integration of gis: A case study. *Curr. Dir. Water Scarcity Res.* 7, 201–223. doi:10.1016/B978-0-323-91910-4.00013-3

Sharifi, A., Dinpashoh, Y., and Mirabbasi, R. (2017). Daily runoff prediction using the linear and non-linear models. *Water Sci. Technol.* 76 (4), 793–805. doi:10.2166/wst.2017.234

Sharma, A. (2000). Seasonal to interannual rainfall probabilistic forecasts for improved water supply management: Part 1-A strategy for system predictor identification. *J. Hydrol. X.* 239 (1- 4), 232–239. doi:10.1016/S0022-1694(00)00346-2

Shi, X., Huang, Q., and Li, K. (2021). Decomposition-based teleconnection between monthly streamflow and global climatic oscillation. *J. Hydrol. X.* 602, 126651. doi:10.1016/j.jhydrol.2021.126651

Singh, V. K., and Roxy, M. K. (2022). A review of ocean-atmosphere interactions during tropical cyclones in the north Indian Ocean. *Earth. Sci. Rev.* 226, 103967. doi:10.1016/j.earscirev.2022.103967

Sit, M., Demiray, B. Z., Xiang, Z., Ewing, Y. S., and Demir, I. (2020). A comprehensive review of deep learning applications in hydrology and water resources. *Water Sci. Technol.* 82 (12), 2635–2670. doi:10.2166/wst.2020.369

Song, X., Lu, F., Wang, H., Xiao, W., and Zhu, K. (2018). Penalized maximum likelihood estimators for the nonstationary Pearson type 3 distribution. *J. Hydrol. X.* 567, 579–589. doi:10.1016/j.jhydrol.2018.10.035

Soper, D. S. (2021). Greed Is Good: Rapid hyperparameter optimization and model selection using greedy *k*-fold cross validation. *Electronics* 10 (16), 1973. doi:10.3390/electronics10161973

Steinschneider, S., and Lall, U. (2016). Spatiotemporal structure of precipitation related to tropical moisture exports over the eastern United States and its relation to climate teleconnections. *J. Hydrometeorol.* 17 (3), 897–913. doi:10.1175/JHM-D-15-0120.1

Sun, A. Y., Wang, D., and Xu, X. (2014). Monthly streamflow forecasting using Gaussian process regression. *J. Hydrol. X.* 511, 72–81. doi:10.1016/j.jhydrol.2014.01.023

Sun, P., Ma, Z., Zhang, Q., Singh, V. P., and Xu, C-Y. (2022). Modified drought severity index: Model improvement and its application in drought monitoring in China. *J. Hydrol. X.* 612, 128097. doi:10.1016/j.jhydrol.2022.128097

Sun, P., Wen, Q., Zhang, Q., Singh, V. P., Sun, Y., and Li, J. (2018). Nonstationarity-based evaluation of flood frequency and flood risk in the Huai River basin, China. *J. Hydrol. X.* 567, 393–404. doi:10.1016/j.jhydrol.2018.10.031

Talaee, P. H., Tabari, H., and Ardakani, S. S. (2014). Hydrological drought in the west of Iran and possible association with large-scale atmospheric circulation patterns. *Hydrol. Process.* 28 (3), 764–773. doi:10.1002/hyp.9586

Tang, J., Li, Q., and Chen, J. (2018). Summertime runoff variations and their connections with Asian summer monsoons in the Yangtze River basin. *J. Water Clim. Chang.* 9 (1), 89–100. doi:10.2166/wcc.2017.142

Taormina, R., and Chau, K. W. (2015). Data-driven input variable selection for rainfall–runoff modeling using binary-coded particle swarm optimization and extreme learning machines. *J. Hydrol. X.* 529, 1617–1632. doi:10.1016/j.jhydrol.2015.08.022

Taylor, K. E. (2001). Summarizing multiple aspects of model performance in a single diagram. *J. Geophys. Res.* 106 (D7), 7183–7192. doi:10.1029/2000JD900719

Tiwari, A., and Chaturvedi, A. (2022). A hybrid feature selection approach based on information theory and dynamic butterfly optimization algorithm for data classification. *Expert Syst. Appl.* 196, 116621. doi:10.1016/j.eswa.2022.116621

Valipour, M. (2015). Long-term runoff study using SARIMA and ARIMA models in the United States. *Mater. Apps.* 22 (3), 592–598. doi:10.1002/met.1491

Wang, J., Wang, X., Lei, X., Wang, H., Zhang, X., You, J., et al. (2020). Teleconnection analysis of monthly streamflow using ensemble empirical mode decomposition. *J. Hydrol. X.* 582, 124411. doi:10.1016/j.jhydrol.2019.124411

Wang, W., Yang, P., Xia, J., Zhang, S., and Cai, W. (2022). Coupling analysis of surface runoff variation with atmospheric teleconnection indices in the middle reaches of the Yangtze River. *Theor. Appl. Climatol.* 148 (3-4), 1513–1527. doi:10.1007/s00704-022-04013-8

Wen, X., Feng, Q., Deo, R. C., Wu, M., Yin, Z., Yang, L., et al. (2019). Two-phase extreme learning machines integrated with the complete ensemble empirical mode decomposition with adaptive noise algorithm for multi-scale runoff prediction problems. *J. Hydrol. X.* 570, 167–184. doi:10.1016/j.jhydrol.2018.12.060

Xiong, L., Yan, L., Du, T., Yan, P., Li, L., and Xu, W. (2019). Impacts of climate change on urban extreme rainfall and drainage infrastructure performance: A case study in wuhan city, China. *Irrig. Drain.* 68 (2), 152–164. doi:10.1002/ird.2316

Yan, L., Xiong, L., Jiang, C., Zhang, M., Wang, D., and Xu, C-Y. (2021a). Updating intensity–duration–frequency curves for urban infrastructure design under a changing environment. *WIREs Water* 8 (3), e1519. doi:10.1002/wat2.1519

Yan, L., Xiong, L., Luan, Q., Jiang, C., Yu, K., and Xu, C-Y. (2020). On the applicability of the expected waiting time method in nonstationary flood design. *Water Resour. manage.* 34, 2585–2601. doi:10.1007/s11269-020-02581-w

Yan, L., Xiong, L., Ruan, G., Zhang, M., and Xu, C-Y. (2021b). Design flood estimation with varying record lengths in Norway under stationarity and nonstationarity scenarios. *Hydrol. Res.* 52 (6), 1596–1614. doi:10.2166/nh.2021.026

Yang, P., Xia, J., Luo, X., Meng, L., Zhang, S., Cai, W., et al. (2021). Impacts of climate change-related flood events in the Yangtze River Basin based on multi-source data. *Atmos. Res.* 263, 105819. doi:10.1016/j.atmosres.2021.105819

Yang, T., Asanjan, A. A., Welles, E., Gao, X., Sorooshian, S., and Liu, X. (2017). Developing reservoir monthly inflow forecasts using artificial intelligence and climate phenomenon information. *Water Resour. Res.* 53 (4), 2786–2812. doi:10.1002/2017WR020482

You, Y., Liu, J., Zhang, Y., Beck, H. E., Gu, H., and Kong, D. (2021). Impacts of El Niño–southern oscillation on global runoff: Characteristic signatures and potential mechanisms. *Hydrol. Process.* 35 (10), e14367. doi:10.1002/hyp.14367

Yuan, X., Chen, C., Lei, X., Yuan, Y., and Adnan, R. M. (2018). Monthly runoff forecasting based on LSTM–ALO model. *Stoch. Environ. Res. Risk Assess.* 32 (8), 2199–2212. doi:10.1007/s00477-018-1560-y

Zhang, Q., Wang, B., He, B., Peng, Y., and Ren, M. (2011). Singular spectrum analysis and ARIMA hybrid model for annual runoff forecasting. *Water Resour. manage.* 25 (11), 2683–2703. doi:10.1007/s11269-011-9833-y

Zhao, X., Lv, H., Lv, S., Sang, Y., Wei, Y., and Zhu, X. (2021). Enhancing robustness of monthly streamflow forecasting model using gated recurrent unit based on improved grey wolf optimizer. *J. Hydrol. X.* 601, 126607. doi:10.1016/j.jhydrol.2021.126607

Zheng, S., Liu, J., and Tian, J. (2005). An efficient star acquisition method based on SVM with mixtures of kernels. *Pattern Recognit. Lett.* 26 (2), 147–165. doi:10.1016/j.patrec.2004.09.003

Zhou, X., Chen, W., Liu, Q., Shen, H., Cai, S., and Lei, X. (2022). Future runoff forecast in Hanjiang River Basin based on Wetspa model and CMIP6 model. *Front. Environ. Sci.* 10, 980949. doi:10.3389/fenvs.2022.980949

Zhou, X., Jiang, P., and Wang, X. (2018). Recognition of control chart patterns using fuzzy SVM with a hybrid kernel function. *J. Intell. Manuf.* 29 (1), 51–67. doi:10.1007/s10845-015-1089-6

Zou, Y., Sun, P., Ma, Z., Lv, Y., and Zhang, Q. (2022). Snow cover in the three stable snow cover areas of China and spatio-temporal patterns of the future. *Remote Sens. (Basel).* 14 (13), 3098. doi:10.3390/rs14133098

Zuo, G., Luo, J., Wang, N., Lian, Y., and He, X. (2020). Decomposition ensemble model based on variational mode decomposition and long short-term memory for streamflow forecasting. *J. Hydrol. X.* 585, 124776. doi:10.1016/j.jhydrol.2020.124776

frontiers | Frontiers in Environmental Science

TYPE Original Research
PUBLISHED 04 January 2023
DOI 10.3389/fenvs.2022.1102864

OPEN ACCESS

EDITED BY
Shao Sun,
Chinese Academy of Meteorological Sciences, China

REVIEWED BY
Jiabo Yin,
Wuhan University, China
Yaojie Yue,
Beijing Normal University, China

*CORRESPONDENCE
Lu Gao,
l.gao@foxmail.com

SPECIALTY SECTION
This article was submitted to Atmosphere and Climate, a section of the journal Frontiers in Environmental Science

RECEIVED 19 November 2022
ACCEPTED 15 December 2022
PUBLISHED 04 January 2023

CITATION
Deng C, Chi Y, Huang Y, Jiang C, Su L, Lin H, Jiang L, Guan X and Gao L (2023), Sensitivity of WRF multiple parameterization schemes to extreme precipitation event over the Poyang Lake Basin of China.
Front. Environ. Sci. 10:1102864.
doi: 10.3389/fenvs.2022.1102864

Sensitivity of WRF multiple parameterization schemes to extreme precipitation event over the Poyang Lake Basin of China

Chao Deng[1,2], Yongxiang Chi[3], Yuansen Huang[4], Caiying Jiang[4], Lingjun Su[2], Hui Lin[5], Lizhi Jiang[5], Xiaojun Guan[5] and Lu Gao[1,2,6,7]*

[1]Institute of Geography, Fujian Normal University, Fuzhou, China, [2]College of Geographical Science, Fujian Normal University, Fuzhou, China, [3]Fujian Institute of Geological Survey, Fuzhou, China, [4]Nanping meteorological bureau of Fujian Province, Nanping, China, [5]Fujian Key Laboratory of Severe Weather, Fuzhou, China, [6]Fujian Provincial Engineering Research Center for Monitoring and Accessing Terrestrial Disasters, Fujian Normal University, Fuzhou, China, [7]Key Laboratory for Humid Subtropical Eco-geographical Processes of the Ministry of Education, Fujian Normal University, Fuzhou, China

Global warming leads to more frequent and more violent extreme weather events, which cause severe natural disasters. The sensitivity of physical schemes in numerical weather prediction models for extreme precipitation is a significant challenge. To simulate a heavy precipitation process from 1 July 2020 to 10 July 2020 over the Poyang Lake Basin, where floods occur frequently, the Weather Research and Forecast model (WRF) was employed. The observation (OBS) from 92 meteorological stations was applied to evaluate WRF performance. To assess the optimal parameter, 27 combinations of multiphysics schemes based on three cumulus schemes (CUs), three microphysical schemes (MPs) and three land surface schemes (LSMs) were employed in WRF simulation. The Euclid distance (ED) was derived to evaluate the performance of the modelled total cumulative precipitation (TCP). The results showed that the simulation generally reproduced the spatial distribution of precipitation and captured the storm centre. In general, WRF underestimated the observation for most areas but overestimated the observation in the northeastern part of the basin. For total cumulative precipitation (TCP), the spatial correlation coefficients ranged from 0.6 to 0.8. M11 had the highest value of 0.796. The scores (TS, POD, FAR) of M15 were 0.66, 0.79, and 0.21, respectively. With the maximum similarity of 0.518, M7 (BMJ-WDM6-Noah) showed the best performance in ED based on six evaluation metrics. The mean values of OBS and M19 were 259.34 and 218.33 mm, respectively. M19 (NT-Thompson-Noah) was closest to the OBS for the range of the TCP. In terms of daily precipitation, the CC of M3 was maximum (0.96), and the RMSE of M24 was minimum (11.9 mm. day^{-1}). The minimum error between the simulation and OBS was found for M3 (NT-Thompson-Noah). Therefore, with a comprehensive evaluation, five optimal combinations of physical schemes (M22, M19, M9, M3, M21) were found for the PLB, which is of great significance for extreme precipitation simulation and flood forecasting.

KEYWORDS
WRF, parameterization schemes, extreme precipitation, sensitivity, Poyang Lake Basin

Introduction

Global climate change affects the water cycle, which can easily cause the changes in precipitation and patterns for different regions, ultimately resulting in extreme precipitation (Yang Q et al., 2021; O'Gorman 2015). Precipitation is an important parameter of atmospheric motion as well as the water cycle. The natural disasters triggered by rainstorms have brought significant socioeconomic losses and human casualties (Jonkman 2005; Jia et al., 2022; Qiao et al., 2022). Due to climate warming, the frequency and intensity of extreme precipitation events have increased globally for most areas (Sun and Ao 2013; Stegall and Kunkel 2019; Yin et al., 2021; Yin et al., 2022). Gradually, several studies have found that extreme precipitation events increase frequently in China, concentrating in the southeastern region and the Yangtze River basin area, especially during the rainy season from April to September (Bao et al., 2015; Gao et al., 2017; Yao et al., 2022). With a humid subtropical climate, Poyang Lake Basin (PLB) is located in the middle and lower reaches of the Yangtze River, China. However, the PLB often suffers serious floods, drought and other disasters due to the climatic characteristics and topography in summer (Wu et al., 2021; Yang X Xet al. 2021). According to the statistics, the No. 1 flood that occurred in the basin in July 2020 alone affected more than 5.21 million people and 455 thousand hectares of crops. Therefore, it is important to enhance the forecasting of extreme precipitation events for the purpose of reducing the damage caused.

The formation of extreme precipitation is a complex multiscale process. Although many different definitions have been adopted to the extreme precipitation, there is no uniform criteria of extreme precipitation events. Some studies select percentile and absolute critical value method to identify extreme precipitation (Liu et al., 2017). For example, the long-term 90th or 95th percentile of daily precipitation series is selected as extreme value (Camuffo et al., 2020). According to the precipitation grading system in China, the rainstorm is identified when the daily precipitation exceeds 50 mm. In addition, the series of extreme climate indices are commonly used (Lei et al., 2021). The precipitation event selected in this study reached the rainstorm level (average daily precipitation exceeds 50 mm) according to the criteria from China Meteorology Administration. Compared with traditional precipitation observation methods, quantitative precipitation forecasting (QPF) can obtain more precipitation information and effectively prevent intense precipitation and floods (Gao et al., 2022). Therefore, numerical weather prediction (NWP), which is based on precise physical control equations, can solve the problem of precipitation dynamics (Sun et al., 2014). Generally, NWP models are usually divided into global climate models (GCMs) and regional climate models (RCMs) at different simulated area ranges (Yi et al., 2018). However, the global climate models (GCMs) are not ideal for representing the intensity of extreme precipitation events on a small spatial scale. Some studies contend that GCMs are generally not capable of capturing intense precipitation signals due to their coarse resolutions (Mahajan et al., 2015). Additionally, the physical processes of the models are not fully expressed. However, the regional climate models (RCMs), such as the PSU/NCAR mesoscale model (MM5) and Weather Research and Forecast (WRF) meet the requirement of high spatial and temporal resolution for the simulation of complex areas with specific terrain, and at the same time, they simulate complex local processes that are easily overlooked and resolve detailed regional atmospheric and ground processes (Bao et al., 2015). The RCMs capture fine-scale features such as topographic precipitation, rain shadows and storms and describe regional-scale physical and parametric structures (Jin et al., 2010). Additionally, previous studies found that RCMs were capable of simulating precipitation in complicated terrain areas (Ji et al., 2018). However, the simulation is still limited by factors such as subgrid parameters, which has become a challenge for numerical weather prediction (NWP) systems (Yang et al., 2019).

As a new generation of mesoscale high-resolution prediction models, WRF employed for atmospheric research and operational forecasting describes the land–atmosphere continuum processes in detail with higher spatial and temporal resolutions (Di et al., 2017). Compared to MM5, WRF has a more source-oriented physical parameterization scheme and a more complete dynamics framework (Chinta et al., 2021). With a stable model and an assimilated data function, it effectively reduces the error of precipitation forecasting, which works better for extreme precipitation simulations. In the WRF simulation process, uncertainties dominated by the initial boundary conditions, spatial resolution, and physical schemes affect the accuracy of precipitation prediction. Many previous studies have indicated that physical schemes play a significant role in climate models, atmospheric circulation models and mesoscale numerical prediction models. As the parameters primarily responsible for calculating atmospheric water vapour, cloud liquid water, cloud ice, and various types of precipitation, microphysical schemes (MPs) are highly sensitive in predicting convective storms and precipitation especially for intense precipitation simulations (Rajeevan et al., 2010; Cossu and Hocke 2014). Cumulus schemes (CUs) describe the changes in heat and water vapour caused by updrafts, downdrafts, and compensatory movements outside the clouds (Wu et al., 2019). Therefore, the accuracy of precipitation forecasting can

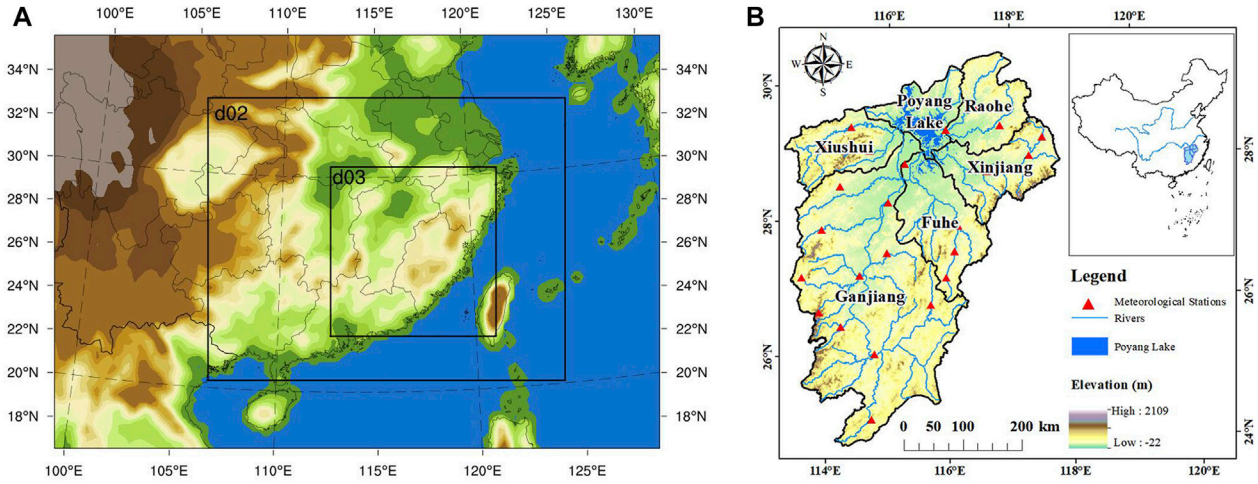

FIGURE 1
Location of study area. **(A)** WRF model domains with three grids (d01-27, d02-9, d03-3 km). **(B)** Topographic features of the Poyang Lake Basin, China.

be improved by suitable parameter schemes. In addition, the occurrence of intense precipitation is also influenced by the subsurface (Jin et al., 2010). Atmospheric circulation has been influenced by land surface schemes (LSMs), which reveal land–air interactions (Di et al., 2015; Lv et al., 2020). The land surface scheme controls the transport of water and heat fluxes in the soil, as well as the water vapour and heat exchange between the land surface and atmosphere. The performance of physical parameterization combinations varies by study area (Yang et al., 2019). Therefore, it is necessary to study the region-specific sensitivity of physical parameterization combinations to forecast future events.

Many simulations of heavy rainfall or storms in Yangtze River basin which has a huge water system and complex terrain have been carried out based on WRF (Wang et al., 2012; Ma et al., 2015; Yao et al., 2022). Previous studies frequently adopted the fixed physical parameterization schemes and hardly considered the combination of physical parameters schemes. It is difficult for one single set of physical schemes to maintain its best performance consistently for different areas and accurately capture the physical processes of extreme precipitation. In particular, the physical parameterization schemes of simulation are sensitive to terrain changes. Therefore, it is necessary to evaluate a set of appropriate physical parameterization schemes on local scales. This study focused on the parameterization sensitivity of cloud microphysical schemes, cumulus schemes, and land surface schemes by using WRF to improve the understanding of how to accurately simulate extreme rainfall. Additionally, the suitable combination members were selected to evaluate the reliability of WRF in extreme precipitation prediction. The observation interpolated from 92 meteorological stations were applied to validate the total cumulative precipitation (TCP). To compare the performance of WRF combination members, an extreme precipitation over the PLB was simulated from 1 July 2020 to 10 July 2020.

The objectives of this study include 1) whether WRF simulations can capture the spatial and temporal characteristics of extreme precipitation over Poyang Lake Basin, 2) how sensitive the extreme precipitation is to different combinations of physical schemes, and 3) which model is a reliable combination scheme for PLB? It is of great significance to study extreme precipitation in the PLB.

Data and methods

Observation

The Poyang Lake Basin (PLB) is located in the centre of Southeast China (Figure 1), between 113.74°-118.47°E and 24.57°–30.01°N, with a total area of 16.22 km^2 × 104 km^2. The PLB that is comparatively flat encompasses five subbasins: Xiushui (subbasin size: 3548 km^2), Ganjiang (8048 km^2), Fuhe (15,811 km^2), Xinjiang (15,535 km^2), and Raohe (6374 km^2). The basin has a humid subtropical climate, which is controlled by the East Asian monsoon (Lei et al., 2022). Therefore, it has obvious seasonal characteristics and an uneven spatial distribution for precipitation, with mainly falling from April to June, leading to frequent floods in summer. The basin is an important flood storage and detention area for the Yangzte River, as it connects to the main stream of the Yangtze River. Additionally, the Poyang Lake is the largest freshwater lake in China (Wagner et al., 2016; Zhang et al., 2016).

TABLE 1 Meteorological stations information.

Id	Name	Latitude (°N)	Longitude (°E)	Elevation (m)	Id	Name	Latitude (°N)	Longitude (°E)	Elevation (m)
1	Tianmen	30.39	113.19	31.9	47	Wuyi	27.43	118	222.1
2	Wuhan	30.38	114.17	23.6	48	Pucheng	27.55	118.32	276.9
3	Honghu	29.49	113.24	27.4	49	Jianyang	27.2	118.07	169.6
4	Jiayu	29.58	113.50	61.7	50	Jian'ou	27.03	118.19	154.9
5	Yueyang	29.23	113.05	51.6	51	Yunhe	27.58	119.37	150.6
6	Xiushui	29.02	114.34	117.4	52	Shouning	27.32	119.25	815.9
7	Pingjiang	28.43	113.35	106.3	53	Rui'an	27.48	120.37	5.7
8	Yifeng	28.25	114.47	91.7	54	Fuding	27.2	120.12	36.2
9	Youxian	27.00	113.20	102.5	55	Ningdu	26.22	115.50	209.1
10	Zhuzhou	27.50	113.09	74.6	56	Guangchang	26.48	116.11	143.9
11	Lianhua	27.08	113.56	194.5	57	Ninghua	26.14	116.38	342.9
12	Yichun	27.48	114.23	131.3	58	Taining	26.53	117.09	252.2
13	Ji'an	27.05	114.55	71.2	59	Youxi	26.1	118.09	204.8
14	Guidong	26.00	113.56	835.9	60	Xiapu	26.53	120.00	56.8
15	Jinggang shan	26.38	114.06	843.0	61	Ningde	26.4	119.31	32.4
16	Suichuan	26.15	114.20	126.1	62	Fuzhou	26.05	119.17	84.0
17	Ganzhou	25.50	114.50	137.5	63	Changting	25.51	116.22	310
18	Nanxiong	25.08	114.19	149.7	64	Shanghang	25.03	116.25	198.0
19	Yingshan	30.44	115.37	123.8	65	Zhangping	25.18	117.24	205.3
20	Ningguo	30.37	118.58	89.4	66	Longyan	25.06	117.01	376.0
21	Huangshan	30.08	118.09	1840.4	67	Jiuxian	25.43	118.06	1653.5
22	Hangzhou	30.19	120.12	41.7	68	Pingtan	25.31	119.47	32.4
23	Yangxin	29.50	115.10	45.8	69	Shaoguan	24.48	113.35	121.3
24	Lushan	29.35	115.59	1215.0	70	Fogang	23.52	113.32	97.2
25	Wuning	29.16	115.05	116.0	71	Yingde	24.1	113.24	74.5
26	Poyang	29.01	116.40	40.1	72	Longnan	24.53	114.46	206.3
27	Qimen	29.55	117.50	142.0	73	Lianping	24.22	114.29	214.8
28	Jingde	29.10	117.15	61.5	74	Xinfeng	24.03	114.12	198.6
29	Tunxi	29.43	118.17	142.7	75	Xunwu	24.57	115.29	297.8
30	Chun'an	29.37	119.01	171.4	76	Longchuan	24.06	115.15	179.6
31	Jinhua	29.07	119.39	62.6	77	Yongding	24.51	116.49	226.9
32	Shengzhou	29.36	120.49	104.3	78	Dabu	24.21	116.42	81.0
33	Yiwu	29.19	120.04	90.0	79	Meixian	24.18	116.07	116
34	Jing'an	28.51	115.22	78.9	80	Chongwu	24.54	118.55	21.8
35	Nanchang	28.40	115.58	46.9	81	Xiamen	24.31	118.09	139.4
36	Zhangshu	28.01	115.22	30.4	82	Qingyuan	23.43	113.01	79.2

(Continued on following page)

TABLE 1 (*Continued*) Meteorological stations information.

Id	Name	Latitude (°N)	Longitude (°E)	Elevation (m)	Id	Name	Latitude (°N)	Longitude (°E)	Elevation (m)
37	Dexing	28.51	117.34	88.5	83	Gaungzhou	23.08	113.19	70.7
38	Guixi	28.17	117.06	60.8	84	Dongguan	23.02	113.45	56.0
39	Yushan	28.40	118.15	116.3	85	Heyuan	23.44	114.41	70.8
40	Shangrao	28.22	118.02	118.2	86	Zengcheng	23.18	113.49	30.8
41	Lishhui	28.27	119.54	63.0	87	Huiyang	23.05	114.28	108.5
42	Xianju	28.52	120.44	83.0	88	Wuhua	23.56	115.46	135.9
43	Yongfeng	27.21	115.25	85.7	89	Zijin	23.38	115.11	176.8
44	Nancheng	27.33	116.36	80.8	90	Shantou	23.21	116.40	2.9
45	Nanfeng	27.12	116.23	111.5	91	Huilai	23.02	116.18	14.4
46	Shaowu	27.20	117.28	218.0	92	Nan'ao	23.26	117.02	7.2

The meteorological stations (located in the simulated nested area) were provided by the China Meteorological Center (Table 1). The stations were distributed with large elevation differences, ranging from 5.7 to 1840.4 m. Normally, the station data represent the weather conditions on different subsurfaces. Generally, a bilinear interpolation method was employed to compare the accuracy of WRF simulation. The observations from meteorological stations were interpolated into the innermost 3 km grid of the WRF by using the Cressman algorithm (Yin et al., 2014) to validate the simulation results. The initial and lateral boundary field information of WRF was driven by Final Operational Global Analysis (FNL) reanalysis from the National Centers for Environmental Prediction with a horizontal resolution of $1^{\circ} \times 1^{\circ}$ and 34 vertical pressure levels at 6-h intervals (00, 06, 12, and 18 UTC).

WRF model configuration

The WRF model is a fully compressible, non-hydrostatic model, with the grid of Arakawa C and terrain following eta-coordinates. The model system integrates numerical weather prediction, atmospheric simulation and data assimilation (Jackson et al., 2008). WRF version 4.3 was used in this study. Three domains with a grid spacings of 27 (d01), 9 (d02), and 3 km (d03), respectively, were employed for the simulation (Figure 1). The domain sizes were 115 × 79, 202 × 160, and 280 × 286, respectively. The Lambert conformal conic projection was used as the model horizontal coordinates. The time steps were 90 s. Additionally, one-way nesting was applied in this study. The simulation of the three domains was initialized at 00 UTC 1 on July 2020 to 00 UTC on 11 July 2020. To ensure the accuracy of the simulated results, the first 36 h of the simulations were considered the model spin-up time, which was excluded from the data analysis. The model outputs at every 6 hours were employed for evaluation. The USGS data were used for topographic data with resolutions of 5, 2 m and 30 s, respectively. The regions of domains were set up with full consideration of the surrounding terrain and the influence of key weather and climate systems, avoiding cross regions with vastly different climate characteristics or geographic features in the simulation. The physical parameter schemes involved in this precipitation simulation experiment included the cumulus scheme (CU), microphysical scheme (MP) and land surface scheme (LSM). The specific combination members of the WRF model were listed in Table 2. The cumulus schemes (CUs) selected were Betts-Miller-Janjic (BMJ), Kain-Fritsch (KF) and New Tiedtke (NT). The microphysical schemes (MPs) evaluated were WRF Single-Moment 6-class (WSM6), Thompson and WRF Double-Moment 6 (WDM6), respectively. The suitable land surface models (LSMs) included Noah, Noah-MP and CLM4, respectively. In addition, the other WRF physical parameter schemes were found for the Rapid Radiative Transfer Model (RRTM) long wave radiation, Dudhia short wave radiation and Yonsei University (YSU) planetary boundary layer scheme. The cumulus scheme was not applied to the d03 domain (3 km) due to the high spatial resolution.

Evaluation criteria

To quantitatively validate the accuracy of the WRF results, the surface-scale and point-scale evaluation systems for the simulated results were established. Six statistical metrics were selected to verify the simulation performance of the precipitation. The statistical indicators of continuity included the correlation coefficient (CC), root mean square error (RMSE) and bias (Moazami et al., 2014; Kumar et al., 2017). The CC was used

TABLE 2 Combinations of physical parameterization schemes in WRF simulations.

Model number	Cumulus scheme (CU)	Microphysics scheme (MP)	Land surface Scheme (LSM)
M1	BMJ	WSM6	Noah
M2	BMJ	WSM6	Noah-MP
M3	BMJ	WSM6	CLM4
M4	BMJ	Thompson	Noah
M5	BMJ	Thompson	Noah-MP
M6	BMJ	Thompson	CLM4
M7	BMJ	WDM6	Noah
M8	BMJ	WDM6	Noah-MP
M9	BMJ	WDM6	CLM4
M10	KF	WSM6	Noah
M11	KF	WSM6	Noah-MP
M12	KF	WSM6	CLM4
M13	KF	Thompson	Noah
M14	KF	Thompson	Noah-MP
M15	KF	Thompson	CLM4
M16	KF	WDM6	Noah
M17	KF	WDM6	Noah-MP
M18	KF	WDM6	CLM4
M19	NT	WSM6	Noah
M20	NT	WSM6	Noah-MP
M21	NT	WSM6	CLM4
M22	NT	Thompson	Noah
M23	NT	Thompson	Noah-MP
M24	NT	Thompson	CLM4
M25	NT	WDM6	Noah
M26	NT	WDM6	Noah-MP
M27	NT	WDM6	CLM4

to measure the linear correlations between simulation and spatially interpolated observations. RMSE was used to measure the average error. Bias was employed to measure the precision of the results. The results with high CC and low RMSE indicate good simulation performance. Categorical statistical metrics (Sen et al., 2014; Jiang et al., 2021) were employed to evaluate the detection capacity for simulations, including the probability of detection (POD), false alarm ratio (FAR) and threat score (TS). The POD reflects the detection ability of a certain precipitation magnitude, FAR represents the empty report of the model on the precipitation magnitude, and TS is a comprehensive score for checking the performance of the model for eliminating the impact of random hits. The definition, formula and optimal value for the indices are shown in Table 2. The 95th percentile of the corresponding precipitation fields was selected as the threshold, which providing the comparison for the spatial distributions of the intense precipitation (Table 3).

It is difficult to accurately select the parameterized scheme combination with the best comprehensive performance based on only one single evaluation and analysis. The emphasis of each metric was different. Therefore, Euclid distance (ED)

TABLE 3 Definition of evaluation criteria.

Metric	Formula	Optimal value	Range
CC	$CC = \frac{\sum_{i=1}^{n}(O_i-\overline{O_i})(M_i-\overline{M_i})}{\sqrt{\sum_{i=1}^{n}(O_i-\overline{O_i})^2}\sqrt{\sum_{i=1}^{n}(M_i-\overline{M_i})^2}}$	1	(0,1)
RMSE	$MRSE = \sqrt{\frac{1}{n}\sum_{i=1}^{n}(M_i - O_i)}$	0	(0, +∞)
Bias	$Bias = \frac{M_i-O_i}{O_i} \times 100$	0	(-∞, +∞)
TS	TS = hits/(hits + misses + falsealarms)	1	(0,1)
POD	POD = hits/(hits + misses)	1	(0,1)
FAR	FAR = falsealarms/(hits + falsealarms)	0	(0,1)

Notes: Where O_i presents the observed value for precipitation on a grid point, M_i presents the simulated value on a grid point. n is the numbers of grids for simulations and observation. The hits indicts the precipitation events are simultaneously detected by the data of models and interpolated observation data. Misses represents the precipitation events detected by interpolated observation data but not by the model. Falsealarms represents the daily precipitation events detected by the model but not interpolated gauge data.

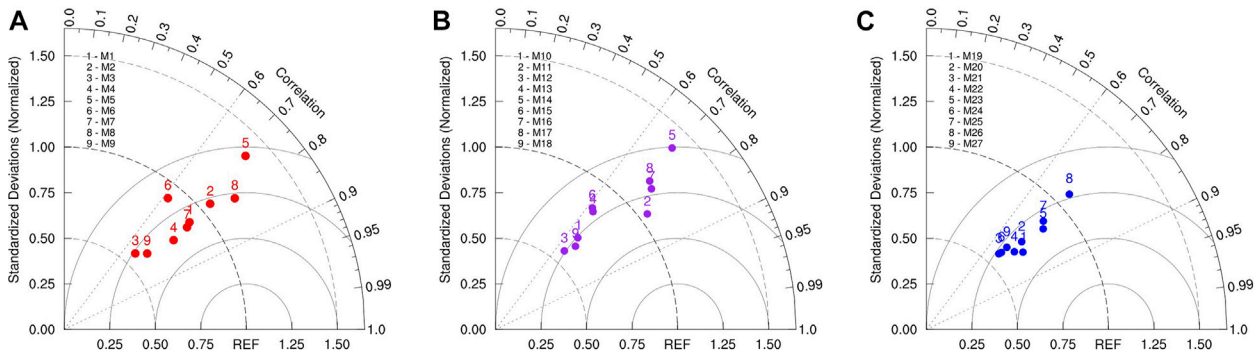

FIGURE 2
Taylor diagram of TCP for WRF combination members. **(A)** WRF combinations for BMJ cumulus schemes; **(B)** KF cumulus schemes; **(C)** NT cumulus schemes.

(Van Cooten et al., 2009), which is defined as measuring the absolute distance between two points in multidimensional spaces, was employed to quantitatively and comprehensively evaluate each combination of WRF physical parameterization schemes. To represent different evaluation metrics, ED was of great significance in the optimal combination of numerical weather model parameterization schemes. Specifically, the six metrics of CC, MSRE, Bias, TS, POD and FAR were synthesized by a vector Se, defined as follows:

$$S_e = \{\mu(CC), \mu(RMSE), \mu(Bias), \mu(TS), \mu(POD), \mu(FAR)\} \quad (1)$$

The values of the six metrics were further scaled to between 0 and 1. Then, the optimal theoretical values for the metrics were formed into vector [So (1,01,1,0)]. ED was calculated as the magnitude of difference of the vector Se and the vector So. With a lower value of ED, one combination member has better performance. For a more visual comparison, the similarity S defined by ED was employed, which can be formulated as follows:

$$S = \frac{1}{d+1} \quad (2)$$

where d represents the value of ED, and S represents similarity. The range is from 0 to 1. The higher S is, the smaller ED is, which means better simulation.

Results

Evaluation of TCP in WRF simulations

Figure 2 shows the comparison results of the simulations and observation (OBS) under different physical parameterization schemes. The value of reference points (REF) in the taylor

TABLE 4 Scores of evaluation metrics for total cumulative precipitation.

Model number	TS	POD	FAR	Model number	TS	POD	FAR
M1	0.46	0.63	0.37	M15	0.66	0.79	0.21
M2	0.24	0.39	0.61	M16	0.30	0.46	0.54
M3	0.47	0.64	0.36	M17	0.05	0.09	0.91
M4	0.22	0.36	0.64	M18	0.27	0.43	0.57
M5	0.55	0.71	0.29	M19	0.38	0.55	0.45
M6	0.28	0.44	0.56	M20	0.20	0.34	0.66
M7	0.63	0.77	0.23	M21	0.39	0.57	0.43
M8	0.26	0.42	0.58	M22	0.55	0.71	0.29
M9	0.44	0.61	0.39	M23	0.28	0.44	0.56
M10	0.26	0.41	0.59	M24	0.28	0.44	0.56
M11	0.15	0.26	0.74	M25	0.45	0.62	0.38
M12	0.36	0.53	0.47	M26	0.08	0.16	0.84
M13	0.01	0.02	0.98	M27	0.19	0.32	0.68
M14	0.02	0.05	0.95	-	-	-	-

diagram reached 1, and the central normalized RMSE was 0. In terms of cumulus schemes (CU), the simulation results were divided into three groups for comparison. Figure 2A shows the simulation results from M1 to M9. The cumulus schemes were all BMJs. The correlation coefficient for M8 was highest with a value of 0.793. In terms of the performance of the results from M10 to M18 with the cumulus schemes of KF, M11 had the highest value of 0.796, which is shown in Figure 2B. Similarly, Figure 2C shows the results from M19 to M27, which had the same cumulus schemes as KF. M19 had a good performance for correlation coefficient, with a value of 0.781. In terms of standard deviation, the values of M11, M2, M26, and M1 in the simulations were closest to 1, which indicated good performance. The distribution of the standard deviation was more dispersed for the simulated results of scheme combinations using the cumulus scheme of BML and KF, which means there was a large difference in simulation capability. The simulated results using the cumulus scheme of NT were relatively concentrated, mainly between 0.5 and 1. The spatial correlation coefficients between the simulated and observed values for 27 combinations were concentrated from 0.6 to 0.8. The highest correlation coefficient values were found for M8, M11, M19, and M4. The combinations with the lowest correlation coefficients (below 0.65) were M6, M13, and M15. Overall, M11 performed well in terms of the correlation coefficient and standard deviation. Among the three CU schemes investigated in this study, the WRF combination members using KF displayed larger central root mean square error, lower correlation coefficient, and poorer standard deviation. Therefore, the BML and NT schemes performed better for extreme precipitation over the PLB.

Table 4 shows the performance of categorical statistical metrics (TS, POD, FAR) for 27 WRF combination members. This revealed the accuracy of precipitation forecasting. For the TS metric, the highest score was found for M15, followed by M7, M5, and M22, which were more than 0.5. However, M13, M14, M17, and M26 had the lowest scores (below 0.1). For POD, the highest score was found for M15, followed by M7, M5, and M22, which all exceeded 0.7. M13, M14, and M17 had the lowest scores (below 0.1). M5, M7, M15, and M22 showed better FAR scores (below 0.3), especially M15, which has the lowest value of 0.21, indicating a low false alarm rate. However, M13, M14, M17, and M26 showed worse performance with high FAR scores (over 0.8). Overall, M15 performed best, followed by M7, M5, and M22, while M13, M14, and M17 performed worst among the three evaluation metrics. The combination members using the BMJ and KF schemes were better than those using KF in precipitation forecasting for WRF simulations. Additionally, with the same CU and MP schemes, the precision of M15 was better than those of M13 (with the Noah LSM) and M14 (with the Noah-MP LSM), which were mainly controlled by the land surface scheme.

Table 5 shows the similarity based on ED ranking from highest to lowest for 27 combinations in terms of TCP. The value of similarity ranged from 0.333 to 0.518. The values of WRF combination members were relatively close and concentrated from 0.4 to 0.5. The highest value was found for M7, which indicated that M7 displayed the best performance for the simulation of TCP. The lowest value was found for M14.

TABLE 5 Similarity by Euclidean distance for WRF combination members.

Model number	Similarity	Ranking	Model number	Similarity	Ranking	Model number	Similarity	Ranking
M7	0.518	1	M5	0.433	10	M4	0.404	19
M22	0.496	2	M23	0.428	11	M27	0.395	20
M25	0.476	3	M12	0.420	12	M11	0.393	21
M1	0.474	4	M8	0.419	13	M6	0.390	22
M19	0.468	5	M18	0.416	14	M26	0.373	23
M9	0.464	6	M24	0.414	15	M10	0.360	24
M3	0.448	7	M16	0.409	16	M17	0.348	25
M15	0.437	8	M20	0.407	17	M13	0.335	26
M21	0.437	9	M2	0.405	18	M14	0.333	27

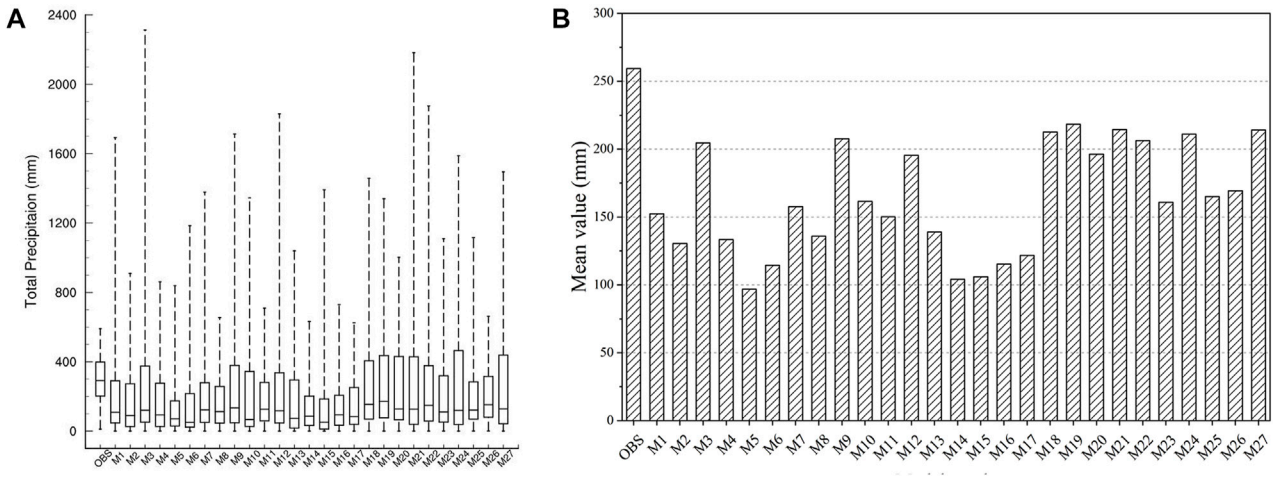

FIGURE 3
TCP of observation and WRF simulations. **(A)** Range of TCP for simulation and observation. Thick horizontal lines in boxes indicate the median values, and boxes show the inner-quartile (25%–75%). **(B)** Mean values of the TCP.

M22, M25, and M1 demonstrated high values of similarity, followed by M7. Among the five combination members with the highest values, the simulations using WDM6 and WSM6 for the MP scheme, which configured the same CU scheme options of BMJ, were more suitable for extreme precipitation forecasting. In terms of the NT cumulus scheme, Thompson and WDM6 were more suitable for the simulation configuration. Noah was found to be the best land surface scheme. Therefore, the combination member of BMJ-WDM6-Noah performed best.

Figure 3 shows the range and mean value of the TCP for the observation (OBS) and WRF simulation. The TCP is shown in Figure 3A. The value of observation was relatively concentrated, with the quartile (25%–75%) ranging from 200 to 400 mm. The differences among the simulated results were significant. For example, M5, M14, M15, and M16 demonstrated relatively smaller ranges, while M21, M24, and M27 displayed larger ranges. All simulation members underestimated the median values compared to the OBS. The median value of M19 was closest to OBS. For maximum values, all simulation members were higher than OBS, especially M9 and M21, which had the largest difference. In terms of mean values (Figure 3B), the deviation between M19 and OBS was smallest, followed by M3, M9, M18, M21, M22, M24, and M27 (over 200 mm), with relatively small differences from OBS. Additionally, M18, M19, M20, M21, M24, and M27 overestimated the 75th percentile values compared to OBS. However, the difference among them was small. In general, the deviation between M19 and OBS was the smallest. Therefore, M19 was regarded as the optimal member among the 27 simulation scheme combinations.

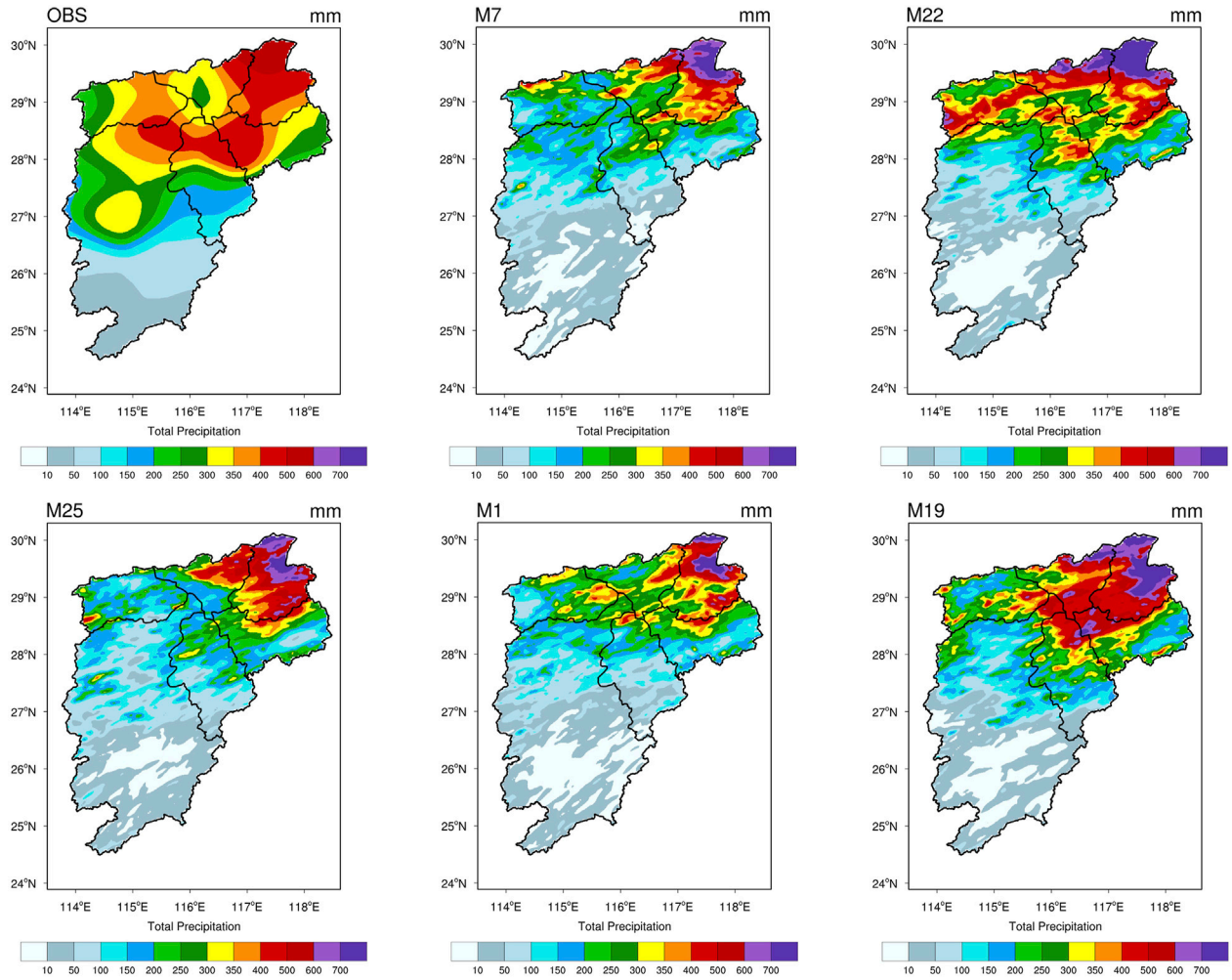

FIGURE 4
Spatial distribution of TCP for OBS and WRF combination members.

Spatial evaluation of TCP in WRF simulations

Figure 4 illustrates the spatial distributions of TCP for WRF combination members and OBS by interpolation. Spatially, the OBS indicated that the TCP generally increased from south to north of PLB, exhibiting a clear gradient, with the maximum precipitation in the northeast and the minimum in the south of the basin. The low value appeared near Poyang Lake. The storm centre with high values (over 400 mm) was mainly located in the northeastern PLB, specifically the Raohe Basin, the western Xinjiang Basin, and a small part of the northern Ganjiang and Fuhe Basins. According to the simulated combination members, the results can basically reproduce the spatial distribution characteristics of the TCP showing an increasing trend from south to north as a whole. The storm centre with high values appeared in the northeastern PLB. The maximum precipitation (over 600 mm)of the WRF simulation was higher than the observed value. The high value appeared in Poyang Lake, which was contrary to the result of OBS. This may be due to the lack of meteorological stations near Poyang Lake, resulting in some differences between the observations by spatial interpolation and simulations. The distribution of the storm centre (high value) was different from the OBS. The simulation combination members underestimated the coverage of the high value area, which was further north relative to the OBS. The performance of the simulation combination members was different. In terms of the storm centre, the distributions of M7 and M1 were relatively small and concentrated in the Raohe Basin, with the maximum precipitation in the northeastern PLB. The distribution of M22 was relatively large and mainly concentrated in the Raohe Basin, Xiushui Basin, and Poyang Lake, and the maximum precipitation was in the northern Raohe Basin. M25 was mainly distributed in the Raohe Basin, the

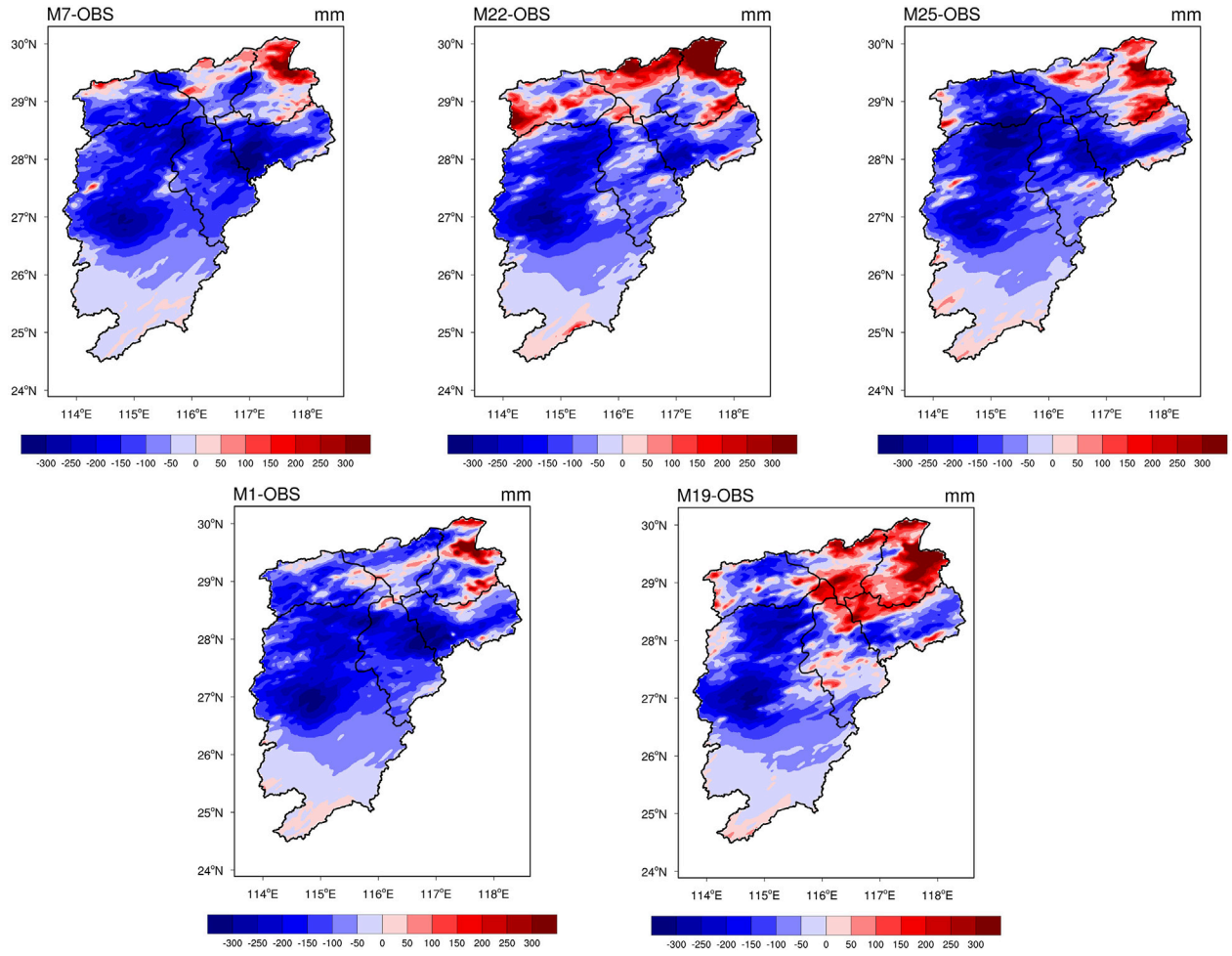

FIGURE 5
Bias distribution of WRF combination members compared to observed precipitation by interpolation (simulation minus observation).

northeastern area of Poyang Lake (more than 400 mm) and the northern Ganjiang and Fuhe Basins. However, less precipitation was found in the southwestern PLB. In contrast, the precipitation centre of M19 covered the largest area with a distribution of five subbasins, which can more effectively capture the precipitation of the PLB.

To more intuitively analyse the spatial difference, Figure 5 describes the bias distribution of WRF simulations compared to the interpolated observation (simulated value minus the observed value). Overall, a negative value indicated that the WRF simulation underestimated the OBS, while a positive value indicated an overestimation. The largest underestimation was found in the central and western regions of the PLB, concentrated in the central and northern parts of the Ganjiang Basin. In addition, the junction areas of Xinjiang and Fuhe Basin underestimated precipitation. The overestimated areas were

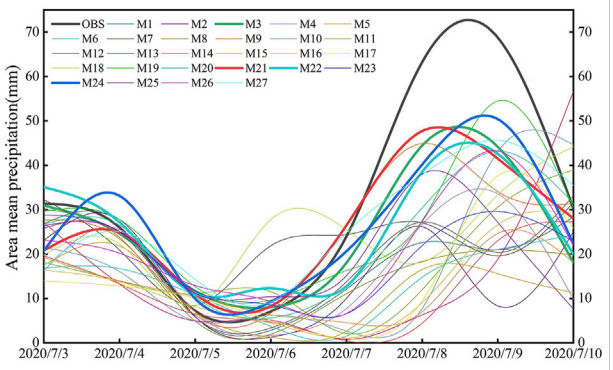

FIGURE 6
Time series of average daily precipitation for observation and WRF simulations.

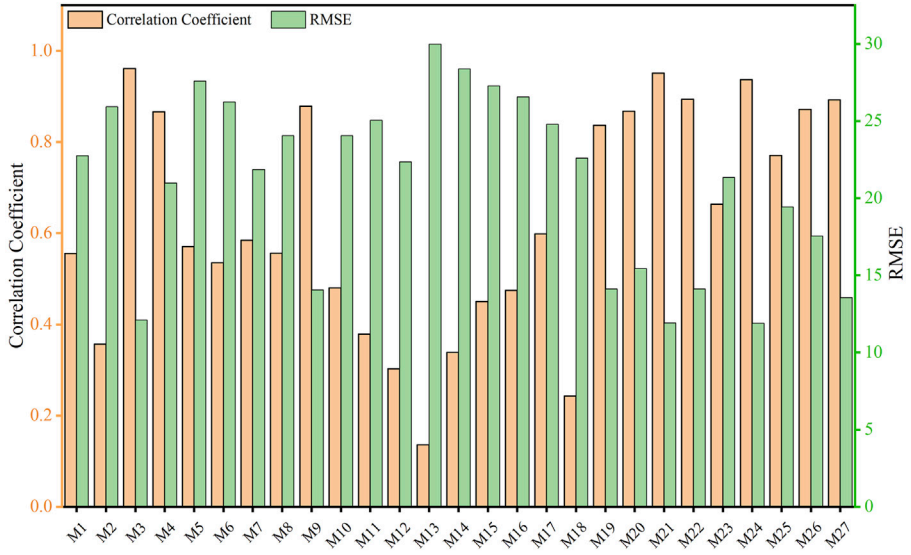

FIGURE 7
The correlation coefficient and RMSE for 27 WRF combination members.

found in the northeastern part of the BLP, mainly in the Raohe Basin and Poyang Lake. Specifically, the overestimation areas for M22 and M19 were larger than those of M7, M25, and M1. The overestimated area for M22 was distributed in the northern Raohe Basin, Poyang Lake, and Xiushui Basin. For M19, overestimation is found at the junction with Xinjiang and the Fuhe Basin, especially in the Raohe Basin and Poyang Lake. Additionally, the overestimated areas were scattered in the middle of the Fuhe Basin but did not appear in other simulations.

Temporal validation of daily precipitation

Figure 6 shows the time series of average daily precipitation of the observations and 27 combination members over the PLB. For the OBS (black line), the minimum value appeared on 6 July 2020 with a value of 7.09 mm. The maximum value was found on 9 July 2020 with a value of 68.78 mm. For WRF simulations, most of the combination members fit the OBS well from 3 July and 7 July, while the simulated values were underestimated compared to the OBS from 7 July to 10 July. In particular, the maximum overestimation occurred at the peak of rainfall. Among the combination members, M3 demonstrated the best performance, followed by M21, M22, and M24 (thick lines). However, M13, M18, and M12 displayed great differences compared to the OBS, resulting in poor fittings. Figure 7 shows the correlation coefficient (CC) and root mean square error (RMSE) for 27 WRF simulations. For CC, the maximum value (0.96) was found for M3, followed by M21, M24, M22, and M27. In terms of RMSE, the minimum value of M24 was 11.9 mm. day^{-1}, followed by M21, M3, M27, and M22. Overall, for the change in average daily precipitation, the best performers were M21, M3, M24, and M22, while the worst performer was M13.

For those combination members with good performance in daily precipitation, M22, M3, and M21 performed better in TCP evaluation, while M24 performed worse. Among the five combinations (M7, M22, M25, M1, and M19) with the best performance of TCP, M19, and M25 performed well with small bias for daily precipitation, while M7 and M1 displayed large bias.

Discussion

Identification of suitable WRF combinations for physical schemes

This study selected a typical extreme precipitation event in the PBL. The study area is located in the lower reaches of the Yangtze River basin, where the precipitation variation is large, and the terrain with many mountains is complex, resulting in difficulty for simulation. In this study, the high-resolution WRF model was used to simulate precipitation, which was especially beneficial to the areas with complex terrain. We found that WRF basically simulated the spatial distribution of precipitation that the storm centre was located in the north of the PLB, which was similar to a previous study. Yu et al. (2011) captured the rainstorm centre and the main rain belt by using WRF, which

was distributed from northeast to southwest in the Yangtze River Basin. Bao et al. (2015) found that WRF showed a high spatial pattern correlation with observations in extreme precipitation simulations. Therefore, the WRF model has been proven to be effective in simulating extreme precipitation. However, the simulation is influenced by other factors that can lead to certain deviations. For example, the deviation near Poyang Lake may be affected by the lack of meteorological stations. For comparison with simulations, the meteorological stations were interpolated in the grid of WRF by bilinear interpolation method. Although the errors of results were limited by the distances and numbers of the ground stations, the required spatial resolution of observation was obtained by interpolation method (Yang Q et al., 2021). Global or regional precipitation products such as the Tropical Rainfall Measuring Mission (TRMM) and China Precipitation Analysis (CPA) data have been increasingly applied to the validation of model results, which effectively overcome the impact of sparse ground stations (Nooni et al., 2022). Therefore, the precipitation datasets from satellite and reanalysis product can be also considered in WRF evaluation in future work. The maximum deviation in the central and northern parts of the Ganjiang Basin may be affected by the mountainous terrain (Argüeso et al., 2012; Bian et al., 2022). In addition, it may also be affected by the uneven spatiotemporal distribution of precipitation.

Compared with fixed physical parameterization schemes, the combination of microphysical schemes, cumulus schemes and land surface schemes performs differently in extreme precipitation. For extreme precipitation simulations, it is still a challenge to identify the optimal configuration from a large number of combined physical schemes (Zhou et al., 2018). Our findings showed that the performance of WRF combinations in simulating extreme precipitation is restricted by evaluation metrics. It is difficult for one combination to maintain its best performance consistently in all metrics. In terms of the evaluation of TCP, the combination of M7 (BMJ-WDM6-Noah) was the most suitable simulation, followed by M22 (NT-Thompson-Noah). Combined with the daily precipitation evaluation, M3 (NT-Thompson-Noah) was the optimal combination due to the minimum bias of daily precipitation. Although M7, M25, and M1 performed well in the total rainfall evaluation, their daily precipitation error was large. M24 and M27 showed small daily precipitation errors, but displayed worse performance in the total cumulative precipitation assessment. This may be related to the serious underestimation of the simulation value from 7 July to 10 July. The results reveal that the identification of physical schemes is based on the study area and precipitation characteristics. The temporal evaluation and spatial distribution of precipitation have brought uncertainty to the simulation. Therefore, the appropriate combination should be determined by the research emphasis. Based on the comprehensive factor, five optimal WRF combinations are identified for the extreme precipitation in the PLB (Table 6). Therefore, the construction of a quantitative and integrated parametric scheme combination evaluation method is an important issue for future research on precipitation simulation.

Applicability of physical schemes

Research on physical schemes has received extensive attention, such as the comparison of microphysical schemes, radiation schemes, cumulus schemes and the performance of WRF ensembles. Many studies have confirmed that the magnitude and distribution of precipitation are sensitive to the CU and MP schemes (Zhou et al., 2018; Ma et al., 2019). Our findings demonstrated that the performance of the KF evaluated in this study was the worst, which is different from the results of previous studies. One possible reason is the regional dependencies for different cumulus schemes (Yu et al., 2011). By comparing the three microphysical schemes of WSM6, WDM6 and Thompson, we found that Thompson was the best for the simulation in the PLB, which indicated that the scheme containing more complete and complex cloud physical processes in the high-resolution simulation was more advantageous. The investigation was also similar to previous evaluation studies. Merino et al. (2022) found that the Thompson scheme had the best performance in the verification of extreme precipitation in the Mediterranean by using the station data. For the microphysical parameter evaluation of extreme precipitation in the central Himalayas, the model results driven by the Thompson scheme were found to have the best consistency with the observation results (Karki et al., 2018).

Few relevant studies have focused on parameter schemes over PLB, especially for the sensitivity of microphysical schemes (Wagner et al., 2013). Previous studies have found that the WSM6 scheme has a good simulation effect in most areas of China. Our results demonstrated that WDM6 of MP outperforms WSM6 in the case of the same cumulus scheme. WDM6 and Thompson have advantages in simulating convective clouds of precipitation due to the double moment method scheme (Xue et al., 2021).

The WRF members behaved differently for each of the evaluation metrics, resulting in a challenge in identifying the suitable combination of physical schemes. Therefore, the confirmation of the physical scheme was based on actual needs, which gradually became an indicative factor. As physical processes in atmospheric simulations are susceptible to topographic and climatic conditions, the physical scheme plays a decisive role in the simulation process. The accuracy of WRF simulation is influenced by driving conditions, domain

TABLE 6 Optimal combinations of WRF physical schemes.

Ranking	Model number	Cumulus scheme	Microphysics scheme	Land surface scheme	Lw radiation	SW radiation	Planetary boundary layer scheme
1	M22	NT	Thompson	Noah	RRTMG	Dudhia	YSU
2	M19	NT	WSM6	Noah	RRTMG	Dudhia	YSU
3	M9	BMJ	WDM6	CLM4	RRTMG	Dudhia	YSU
4	M3	BMJ	WSM6	CLM4	RRTMG	Dudhia	YSU
5	M21	NT	WSM6	CLM4	RRTMG	Dudhia	YSU

scales and terrains. Therefore, the NWP precipitation evaluation index system needs to be constructed to improve the simulation accuracy. By optimizing the combination of parameterization schemes, the simulation results are more reliable than the default parameters of the model. These investigations demonstrate a reference for regional extreme precipitation forecasting. The limitation of this study was the number of extreme precipitation events. The extreme precipitation events selected in this study was a typical event, which has more serious negative impact on Poyang Lake Basin. Previous studies have shown that the rainstorm in the first 10 days of July is an important reason for the flood in the PLB, accounting for a large proportion of historical disasters. Therefore, this rainstorm is a typical event, it can represent the basic law of rainstorm (similar atmospheric physical mechanisms) and flood in this basin. We set up comparative ensemble tests as many as possible to reduce the errors caused by this typical event. In general, our research is universal and representative. In addition, the different initial and lateral boundary conditions for WRF should also be explored for more accurate forecasting of extreme weather events at the local scale.

Conclusion

This study simulated extreme precipitation events over the PLB by numerical weather forecasting from 1 July to 10 July 2020. To reproduce the extreme precipitation process, 27 combination members of WRF physical schemes were designed, with three CU schemes (KF, BMJ, GF), three MP schemes (WDM6, WSM6, Thompson) and three land surface schemes (Noah, Noah-MP, CLM4). Additionally, compared to the observations interpolated by data from 92 meteorological stations data, the appropriate WRF configurations were identified by spatial and temporal evaluation. Then, the major findings were summarized as follows.

1) The spatial comparison showed that the WRF model basically simulated the spatial and temporal distribution of extreme precipitation over the PLB and captured the precipitation centre in the northeast of the PLB. However, compared with the observed value, the WRF combinations showed the overestimation mainly in the Raohe Basin and Poyang Lake. The largest underestimation was found in the central and western regions of the PLB, concentrated in the central and northern parts of the Ganjiang Basin.
2) For TCP, the metrics of CC, RMSE, Bias, TS, POD, and FAR were employed to validate the performance of WRF combination members. The spatial correlation coefficients ranged from 0.6 to 0.8 for WRF combination members. And M11 has the highest value of 0.796. For standard deviation, the values of M11, M2, M26, and M1 in the simulations were closest to 1. In terms of categorical statistical metrics, the highest scores (TS, POD, FAR) were found for M15, followed by M7. The TS, POD and FAR of M15 were 0.66, 0.79, and 0.21, respectively. Based on the comprehensive ED metric, the value of similarity ranged from 0.333 to 0.518. M7 with maximum similarity (0.518) demonstrated the best performance in extreme precipitation simulation. The quartile (25%–75%) of observation ranged from 200 to 400 mm. The mean value of OBS and M19 were 259.34 and 218.33 mm, respectively. The deviation between M19 and OBS was smallest. In addition, M19 performed well in the range of the TCP.
3) For the error analysis of daily precipitation, the maximum value of CC was 0.96, which was found for M3. The minimum value of RMSE was 11.9 mm. day^{-1}, which was found for M24. The simulated values were underestimated compared to the OBS from 7 July to 10 July. M3 (BMJ-WSM6-CLM4) and M21 (NT-WSM6-CLM4) were optimal among the members. In general, five optimal combinations of WRF physical schemes (M22, M19, M9, M3, M21) were selected for extreme precipitation simulation over the PLB in this study.

Data availability statement

The original contributions presented in the study are included in the article/supplementary material, further inquiries can be directed to the corresponding author.

Author contributions

LG and CD designed the research scheme and completed model simulation, CD prepared the original draft, LG edited and reviewed the manuscript, CD, YH, and CJ contributed to the data collection and processing, YC, LS, HL, LJ, and XG contributed to the discussion. All authors have read and agreed to the published version of the manuscript.

Funding

This work was supported by the National Natural Science Foundation of China (Grant No. 42271030), Fujian Provincial Funds for Distinguished Young Scientists (Grant No. 2022J06018).

Conflict of interest

The authors declare that the research was conducted in the absence of any commercial or financial relationships that could be construed as a potential conflict of interest.

Publisher's note

All claims expressed in this article are solely those of the authors and do not necessarily represent those of their affiliated organizations, or those of the publisher, the editors and the reviewers. Any product that may be evaluated in this article, or claim that may be made by its manufacturer, is not guaranteed or endorsed by the publisher.

References

Argüeso, D., Hidalgo-Muñoz, J. M., Gámiz-Fortis, S. R., Esteban-Parra, M. J., and Castro-Díez, Y. (2012). Evaluation of WRF mean and extreme precipitation over Spain: Present climate (1970–99). *J. Clim.* 25 (14), 4883–4897. doi:10.1175/jcli-d-11-00276.1

Bao, J., Feng, J., and Wang, Y. (2015). Dynamical downscaling simulation and future projection of precipitation over China. *J. Geophys. Res. Atmos.* 120 (16), 8227–8243. doi:10.1002/2015jd023275

Bian, Y., Sun, P., Zhang, Q., Luo, M., and Liu, R. J. J. o. H. (2022). Amplification of non-stationary drought to heatwave duration and intensity in eastern China: Spatiotemporal pattern and causes. *J. Hydrology* 612, 128154. doi:10.1016/j.jhydrol.2022.128154

Camuffo, D., Becherini, F., and della Valle, A. (2020). Relationship between selected percentiles and return periods of extreme events. *Acta Geophys.* 68 (4), 1201–1211. doi:10.1007/s11600-020-00452-x

Chinta, S., Yaswanth Sai, J., and Balaji, C. (2021). Assessment of WRF model parameter sensitivity for high-intensity precipitation events during the Indian summer monsoon. *Earth Space Sci.* 8 (6). doi:10.1029/2020ea001471

Cossu, F., and Hocke, K. (2014). Influence of microphysical schemes on atmospheric water in the Weather Research and Forecasting model. *Geosci. Model Dev.* 7 (1), 147–160. doi:10.5194/gmd-7-147-2014

Di, Z., Duan, Q., Gong, W., Wang, C., Gan, Y., Quan, J., et al. (2015). Assessing WRF model parameter sensitivity: A case study with 5 day summer precipitation forecasting in the greater beijing area. *Geophys. Res. Lett.* 42 (2), 579–587. doi:10.1002/2014gl061623

Di, Z., Duan, Q., Wang, C., Ye, A., Miao, C., and Gong, W. (2017). Assessing the applicability of WRF optimal parameters under the different precipitation simulations in the Greater Beijing Area. *Clim. Dyn.* 50 (5-6), 1927–1948. doi:10.1007/s00382-017-3729-3

Gao, L., Huang, J., Chen, X. W., Chen, Y., and Liu, M. B. (2017). Risk of extreme precipitation under nonstationarity conditions during the second flood season in the southeastern coastal region of China. *J. Hydrometeorol.* 18 (3), 669–681. doi:10.1175/jhm-d-16-0119.1

Gao, L., Wei, J., Lei, X., Ma, M., Wang, L., Guan, X., et al. (2022). Simulation of an extreme precipitation event using ensemble-based WRF model in the southeastern coastal region of China. *Atmosphere* 13 (2), 194. doi:10.3390/atmos13020194

Gao, W., Chang, N.-B., Wang, J., Kan, Y., Liu, C., Liu, Y., et al. (2015). "Evaluation of WRF microphysics and cumulus parameterization schemes in simulating a heavy rainfall event over Yangtze River delta," in Proceeding of the Remote Sensing and Modeling of Ecosystems for Sustainability XII. Paper presented at the.

Jackson, C. S., Sen, M. K., Huerta, G., Deng, Y., and Bowman, K. P. (2008). Error reduction and convergence in climate prediction. *J. Clim.* 21 (24), 6698–6709. doi:10.1175/2008jcli2112.1

Ji, D., Dong, W., Hong, T., Dai, T., Zheng, Z., Yang, S., et al. (2018). Assessing parameter importance of the weather research and forecasting model based on global sensitivity analysis methods. *J. Geophys. Res. Atmos.* 123 (9), 4443–4460. doi:10.1002/2017jd027348

Jia, H., Chen, F., Pan, D., Du, E., Wang, L., Wang, N., et al. (2022). Flood risk management in the Yangtze River basin—comparison of 1998 and 2020 events. *Int. J. Disaster Risk Reduct.* 68, 102724. doi:10.1016/j.ijdrr.2021.102724

Jiang, Q., Li, W. Y., Fan, Z. D., He, X. G., Sun, W. W., Chen, S., et al. (2021). Evaluation of the ERA5 reanalysis precipitation dataset over Chinese Mainland. *J. Hydrology* 595, 125660. doi:10.1016/j.jhydrol.2020.125660

Jin, J., Miller, N. L., and Schlegel, N. (2010). Sensitivity study of four land surface schemes in the WRF model. *Adv. Meteorology* 2010, 1–11. doi:10.1155/2010/167436

Jonkman, S. N. (2005). Global perspectives on loss of human life caused by floods. *Nat. Hazards* 34 (2), 151–175. doi:10.1007/s11069-004-8891-3

Karki, R., Hasson, S. u., Gerlitz, L., Talchabhadel, R., Schenk, E., Schickhoff, U., et al. (2018). WRF-based simulation of an extreme precipitation event over the Central Himalayas: Atmospheric mechanisms and their representation by microphysics parameterization schemes. *Atmos. Res.* 214, 21–35. doi:10.1016/j.atmosres.2018.07.016

Kumar, D., Pandey, A., Sharma, N., and Flugel, W. A. (2017). Evaluation of TRMM-precipitation with rain-gauge observation using hydrological model J2000. *J. Hydrologic Eng.* 22 (5). doi:10.1061/(asce)he.1943-5584.0001317

Lei, X., Xu, W., Chen, S., Yu, T., Hu, Z., Zhang, M., et al. (2022). How well does the ERA5 reanalysis capture the extreme climate events over China? Part I: Extreme precipitation. *Front. Environ. Sci.* 10, 921658. doi:10.3389/fenvs.2022.921658

Lei, X. Y., Gao, L., Ma, M. M., Wei, J. H., Xu, L. G., Wang, L., et al. (2021). Does non-stationarity of extreme precipitation exist in the Poyang Lake Basin of China? *J. Hydrology-Regional Stud.* 37, 100920. doi:10.1016/j.ejrh.2021.100920

Liu, B. J., Chen, X. H., Chen, J. F., and Chen, X. H. (2017). Impacts of different threshold definition methods on analyzing temporal-spatial features of extreme precipitation in the Pearl River Basin. *Stoch. Environ. Res. Risk Assess.* 31 (5), 1241–1252. doi:10.1007/s00477-016-1284-9

Lv, M., Xu, Z., and Yang, Z. L. (2020). Cloud resolving WRF simulations of precipitation and soil moisture over the central Tibetan plateau: An assessment of various physics options. *Earth Space Sci.* 7 (2). doi:10.1029/2019ea000865

Ma, J. H., Wang, H. J., and Fan, K. (2015). Dynamic downscaling of summer precipitation prediction over China in 1998 using WRF and CCSM4. *Adv. Atmos. Sci.* 32 (5), 577–584. doi:10.1007/s00376-014-4143-y

Ma, Y., Yang, Y., Qiu, C., and Wang, C. (2019). Evaluation of the WRF-lake model over two major freshwater lakes in China. *J. Meteorological Res.* 33 (2), 219–235. doi:10.1007/s13351-019-8070-9

Mahajan, S., Evans, K. J., Branstetter, M., Anantharaj, V., and Leifeld, J. K. (2015). "Fidelity of precipitation extremes in high resolution global climate simulations," in Proceeding of the Annual International Conference on Computational Science (ICCS), Reykjavik, ICELAND (Amsterdam, Netherlands: Reykjavik Univ). Paper presented at the 15th.

Merino, A., García-Ortega, E., Navarro, A., Sánchez, J. L., and Tapiador, F. J. (2022). WRF hourly evaluation for extreme precipitation events. *Atmos. Res.* 274, 106215. doi:10.1016/j.atmosres.2022.106215

Moazami, S., Golian, S., Kavianpour, M. R., and Hong, Y. (2014). Uncertainty analysis of bias from satellite rainfall estimates using copula method. *Atmos. Res.* 137, 145–166. doi:10.1016/j.atmosres.2013.08.016

Nooni, I. K., Tan, G. R., Yan, H. M., Chaibou, A. A. S., Habtemicheal, B. A., Gnitou, G. T., et al. (2022). Assessing the performance of WRF model in simulating heavy precipitation events over East africa using satellite-based precipitation product. *Remote Sens.* 14 (9), 1964. doi:10.3390/rs14091964

O'Gorman, P. A. (2015). Precipitation extremes under climate change. *Curr. Clim. Change Rep.* 1 (2), 49–59. doi:10.1007/s40641-015-0009-3

Qiao, Y., Xu, W., Meng, C., Liao, X., and Qin, L. (2022). Increasingly dry/wet abrupt alternation events in a warmer world: Observed evidence from China during 1980–2019. *Int. J. Climatol.* 42 (12), 6429–6440. doi:10.1002/joc.7598

Rajeevan, M., Kesarkar, A., Thampi, S. B., Rao, T. N., Radhakrishna, B., and Rajasekhar, M. (2010). Sensitivity of WRF cloud microphysics to simulations of a severe thunderstorm event over Southeast India. *Ann. Geophys.* 28 (2), 603–619. doi:10.5194/angeo-28-603-2010

Sen, B., Kilinc, R., Sen, B., and Sonuc, E. (2014). Validation of daily precipitation estimates of the regional climate model regcm4 over the domains in Turkey with NWP verification techniques. *Fresenius Environ. Bull.* 23 (8A), 1892–1903.

Stegall, S. T., and Kunkel, K. E. (2019). Simulation of daily extreme precipitation over the United States in the CMIP5 30-yr decadal prediction experiment. *J. Appl. Meteorology Climatol.* 58 (4), 875–886. doi:10.1175/jamc-d-18-0057.1

Sun, J. Q., and Ao, J. (2013). Changes in precipitation and extreme precipitation in a warming environment in China. *Chin. Sci. Bull.* 58 (12), 1395–1401. doi:10.1007/s11434-012-5542-z

Sun, J., Xue, M., Wilson, J. W., Zawadzki, I., Ballard, S. P., Onvlee-Hooimeyer, J., et al. (2014). Use of NWP for nowcasting convective precipitation: Recent progress and challenges. *Bull. Am. Meteorological Soc.* 95 (3), 409–426. doi:10.1175/bams-d-11-00263.1

Van Cooten, S., Elmore, K. L., Barbe, D. E., McCorquodale, J. A., and Reed, D. J. (2009). A statistical methodology to discover precipitation microclimates in Southeast Louisiana: Implications for coastal watersheds. *J. Hydrometeorol.* 10 (5), 1184–1202. doi:10.1175/2009jhm1076.1

Wagner, S., Fersch, B., Kunstmann, H., Yuan, F., Yang, C., and Yu, Z. (2013). "Hydrometeorological modelling for Poyang Lake region, China," in Proceeding of the International Association of Hydrological Sciences Symposium on Climate and Land Surface Changes in Hydrology, Gothenburg, SWEDEN (Wallingford, England: IAHS-IAPSO-IASPEI Joint Assemply). Paper presented at the.

Wagner, S., Fersch, B., Yuan, F., Yu, Z. B., and Kunstmann, H. (2016). Fully coupled atmospheric-hydrological modeling at regional and long-term scales: Development, application, and analysis of WRF-HMS. *Water Resour. Res.* 52 (4), 3187–3211. doi:10.1002/2015wr018185

Wang, S. Z., Yu, E. T., and Wang, H. J. (2012). A simulation study of a heavy rainfall process over the Yangtze River valley using the two-way nesting approach. *Adv. Atmos. Sci.* 29 (4), 731–743. doi:10.1007/s00376-012-1176-y

Wu, Q., Xu, B., Wang, Y. H., and Zhan, M. J. (2021). Intraseasonal evolution and climatic characteristics of hourly precipitation during the rainy season in the Poyang Lake Basin, China. *Geomatics Nat. Hazards Risk* 12 (1), 1931–1947. doi:10.1080/19475705.2021.1953619

Wu, T. J., Min, J. Z., and Wu, S. (2019). A comparison of the rainfall forecasting skills of the WRF ensemble forecasting system using SPCPT and other cumulus parameterization error representation schemes. *Atmos. Res.* 218, 160–175. doi:10.1016/j.atmosres.2018.11.016

Xue, H. L., Zhou, X., Luo, Y. L., and Yin, J. F. (2021). Impact of parameterizing the turbulent orographic form drag on convection-permitting simulations of winds and precipitation over South China during the 2019 pre-summer rainy season. *Atmos. Res.* 263, 105814. doi:10.1016/j.atmosres.2021.105814

Yang, L., Wang, S., Tang, J., Niu, X., and Fu, C. (2019). Evaluation of the effects of a multiphysics ensemble on the simulation of an extremely hot summer in 2003 over the CORDEX-EA-II region. *Int. J. Climatol.* 39 (8), 3413–3430. doi:10.1002/joc.6028

Yang, Q., Yu, Z., Wei, J., Yang, C., Gu, H., Xiao, M., et al. (2021). Performance of the WRF model in simulating intense precipitation events over the Hanjiang River Basin, China – a multi-physics ensemble approach. *Atmos. Res.* 248, 105206. doi:10.1016/j.atmosres.2020.105206

Yang, X. X., Wu, J., Liu, J., and Ye, X. C. (2021). Changes of extreme precipitation and possible influence of ENSO events in a humid basin in China. *Atmosphere* 12 (11), 1522. doi:10.3390/atmos12111522

Yao, R., Zhang, S. L., Sun, P., Dai, Q., and Yang, Q. T. (2022). Estimating the impact of urbanization on non-stationary models of extreme precipitation events in the Yangtze River Delta metropolitan region. *Weather Clim. Extrem.* 36, 100445. doi:10.1016/j.wace.2022.100445

Yi, L., Zhang, W., and Wang, K. (2018). Evaluation of heavy precipitation simulated by the WRF model using 4D-var data assimilation with TRMM 3B42 and GPM IMERG over the huaihe River basin, China. *Remote Sens.* 10 (4), 646. doi:10.3390/rs10040646

Yin, J. B., Guo, S. L., Wang, J., Chen, J., Zhang, Q., Gu, L., et al. (2022). Thermodynamic driving mechanisms for the formation of global precipitation extremes and ecohydrological effects. *Sci. China-Earth Sci.* doi:10.1007/s11430-022-9987-0

Yin, J., Guo, S., Gentine, P., Sullivan, S. C., Gu, L., He, S., et al. (2021). Does the hook structure constrain future flood intensification under anthropogenic climate warming? *Environ. Sci.* 57 (2). doi:10.1029/2020WR028491

Yin, Z. H., Zhang, P. Y., and Cheng, M. H. (2014). Research on attaining methods of rainfall "truth" by assessment of radar measurement of rainfall. *Acta Phys. Sin.* 63 (23), 239201. doi:10.7498/aps.63.239201

Yu, E., Wang, H., Gao, Y., and Sun, J. (2011). Impacts of cumulus convective parameterization schemes on summer monsoon precipitation simulation over China. *Acta Meteorol. Sin.* 25 (5), 581–592. doi:10.1007/s13351-011-0504-y

Zhang, Q., Xiao, M. Z., Singh, V. P., and Wang, Y. Q. (2016). Spatiotemporal variations of temperature and precipitation extremes in the Poyang Lake basin, China. *Theor. Appl. Climatol.* 124 (3-4), 855–864. doi:10.1007/s00704-015-1470-6

Zhou, J. Z., Zhang, H. R., Zhang, J. Y., Zeng, X. F., Ye, L., Liu, Y., et al. (2018). WRF model for precipitation simulation and its application in real-time flood forecasting in the Jinshajiang River Basin, China. *Meteorology Atmos. Phys.* 130 (6), 635–647. doi:10.1007/s00703-017-0542-9

frontiers | Frontiers in Environmental Science

TYPE Original Research
PUBLISHED 10 January 2023
DOI 10.3389/fenvs.2022.1104039

OPEN ACCESS

EDITED BY
Ming Luo,
Sun Yat-sen University, China

REVIEWED BY
Chao Li,
East China Normal University, China
Guojie Wang,
Nanjing University of Information Science and Technology, China

*CORRESPONDENCE
Yang Chen,
ychen@cma.gov.cn

SPECIALTY SECTION
This article was submitted to Atmosphere and Climate, a section of the journal Frontiers in Environmental Science

RECEIVED 21 November 2022
ACCEPTED 23 December 2022
PUBLISHED 10 January 2023

CITATION
Li X, Chen Y, Zhu Y, Shi Y, An N and Liao Z (2023), Underestimated increase and intensification of humid-heat extremes across southeast China due to humidity data inhomogeneity.
Front. Environ. Sci. 10:1104039.
doi: 10.3389/fenvs.2022.1104039

Underestimated increase and intensification of humid-heat extremes across southeast China due to humidity data inhomogeneity

Xuezhu Li[1], Yang Chen[1]*, Yani Zhu[2], Yan Shi[2], Ning An[1] and Zhen Liao[1]

[1]State Key Laboratory of Severe Weather, Chinese Academy of Meteorological Sciences, Beijing, China, [2]National Meteorological Information Center, Beijing, China

When co-occurring with elevated levels of ambient relative humidity (RH), hot extremes are more perceivable and consequently more health-damaging. Quantifying changes in humid-heat extremes has therefore gained considerable scientific and societal attention, but a fundamental yet critical aspect to the estimation—data reliability—has been largely downplayed in previous analysis. By comparing ~10 observational and reanalysis datasets to fully-homogenized observations across China, we report ubiquitous inhomogeneity in RH series in these popularly-used datasets [including HadISD(H) and ERA5], which accordingly produce unrealistically strong drying trends 2–3 times the homogenized dataset-based estimate during 1979–2013 in warm-moist southeast China. Locally, an inhomogeneity-caused exaggeration of drying by a magnitude of 1% decade^{-1} translates into a significant underestimation of increasing rates for frequency and intensity of humid-heat extremes by more than 1.2 days decade^{-1} and .07% decade^{-1} respectively. From a regional perspective, these inhomogeneous records have underestimated the frequency increase of extremes by up to 2 days decade^{-1} and their intensification by up to .4°C decade^{-1} in southeast China. Extremes identified *via* homogenized and non-homogenized datasets also differ in the bivariate joint distribution structure, with former cases featuring similarly hot temperatures yet discernably lower humidity.

KEYWORDS

humid-heat extremes, data inhomogeneity, relative humidity, drying bias, multivariate compound events

1 Introduction

It is unequivocal that human influence has warmed the atmosphere, leading to more frequent, more intense, longer-lasting, and more widespread hot temperature extremes worldwide (IPCC, 2021). These hot extremes are a major cause of suffering and death as punctuated by some of the deadly cases such as the 2003 European event (~70,000 mortality) and the 2010 Russian event (~50,000 mortality, Hoag, 2014). The combination of extremely high temperatures with high humidity, i.e., the so-called humid-heat stress, represents a greater threat to human health, as it lowers the cooling efficiency of sweat, therefore making it difficult or even impossible for the body to prevent overheating (Mora et al., 2017; Buzan and Huber, 2020; IPCC, 2021; Vecellio et al., 2022). Hence, considerable efforts have been devoted to

defining, monitoring and understanding extreme humid-heat events, based on diverse metrics configuring temperature and humidity as well as other relevant variables (e.g., winds and radiation) in different ways (Delworth et al., 1999; Diffenbaugh et al., 2007; Stull, 2011; Willett and Sherwood, 2012; Fischer and Knutti, 2013).

Regardless of metrics used, humid heat extremes have exhibited significantly increasing trends for frequency and intensity in most continents (Rogers et al., 2021; Tuholske et al., 2021). When incorporating humidity into the indices in a highly non-linear manner, these increases are markedly larger than their temperature-only counterparts (Delworth et al., 1999; Wang and Zhu, 2020; Rogers et al., 2021). Even at the current level of global warming, several populous regions, including North and South China, Eastern India, and the Middle East (Freychet et al., 2020; Saeed et al., 2021; Raymond et al., 2020; Mora et al., 2017), have experienced humid-heat extremes very close to or even above upper physiological limit. Though the survivability limits are still exceeded only on the rarest of occasions for now, the likelihood of exceedance is expected to grow rapidly in future warmer climates in these hotspots (Dunne et al., 2013; Mora et al., 2017; Kang and Eltahir, 2018; Saeed et al., 2021).

For the bivariate extremes, data quality of both air temperature and relative humidity (RH) matters to the accuracy of estimate for their long-term changes, and hence to assessments of related human health impacts and risks as well as adaptation planning (Sherwood, 2018; Brouillet and Joussaume, 2019). In contrast to high-quality air temperature datasets provided by multiple agencies, observational records of relative humidity are subject to large uncertainties resulting primarily from data inhomogeneity, and thus should be used with caution (IPCC, 2021; Schröder et al., 2019). It has been observed that global mean and boreal midlatitude summer-mean surface RH slightly increased during 1973–2000, followed by a steep decline based on the HadISDH (Willett et al., 2014; Douville and Plazzotta, 2017; Dunn et al., 2017); however, none of the CMIP5 models could capture such evolution. It is not yet clear if this discrepancy is related to the misrepresentation of internal variability in simulations or observational data inhomogeneity. Byrne and O'Gorman (2018) provided a candidate theory suggesting that the observed negative trends for relative humidity over midlatitude continents were linked to warming over the neighbouring oceans. The observational and theoretical uncertainties along with the observation-simulation discrepancy, preclude any robust detection and attribution conclusion with respect to relative humidity changes (IPCC, 2021).

The inhomogeneity issue in relative humidity records stands out starkly over China, the southeastern parts in particular, which may be related to the technical defects of humidity sensors under high temperature and humidity environments there (Yu and Mu, 2008; Zhu et al., 2015). The dielectric parameter of the humicap varies volatilely at high humidity and even more drastically combined with high temperatures, making observed humidity deviating far from real values. Using quality-controlled yet non-homogenized observations, the annual China Climate Bulletin released before 2014 used to report a significant decreasing trend in nationwide surface RH (China Climate Bulletin, 2014); whilst turning to a homogenized RH dataset instead, RH is believed to remain essentially unchanged since 1961 as concluded in the post-2014 Bulletins. Zhu et al. (2015) detected break points in the RH series observed in more than 68% of stations across China, mainly occurring during 2000–2005, coincident with the massive automation of the observing system. Without diving into the history of instrument replacement, conventional homogenization procedures by automatic software are reluctant to accurately detect and properly address potential region-wide inhomogeneities from the source (e.g., homogenized HadISDH, Willett et al., 2014).

Despite improved awareness of RH inhomogeneity (Li et al., 2020c; Wang and Sun, 2021; Zhang et al., 2021), the extent to which such inhomogeneity distorts the estimate for past and future changes in humid-heat extremes has been seldomly quantified (Freychet et al., 2020). The ERA5 (Hersbach et al., 2018) and HadISD (Dunn et al., 2016), are the most widely-used datasets to analyze humid-heat extremes at impact-relevant scales (sub-daily to daily) worldwide (Li et al., 2020b; Raymond et al., 2020; Speizer et al., 2022), with *in-situ* observations adding values to understanding on the regional heterogeneity (Luo and Lau, 2018; Wang et al., 2019; Li et al., 2020a). If RH is inhomogeneous in these datasets, the derived quantification of long-term changes in extremes would be biased. The recent availability of two homogenized RH datasets covering the domain of mainland China (Zhu et al., 2015; Li et al., 2020a) offers us a unique chance to revisit the existing understanding of humid-heat extremes in the populous region as a showcase, calling for more emphasis on the importance of RH data quality in characterizing the multivariate extreme event worldwide.

We do this by comprehensively comparing homogenized observations with popularly-used ~10 datasets including raw station-based observations, gridded observations and reanalysis (detailed information see Supplementary Table S1). In addition to the differences in local-to-regional changes in RH and humid-heat extremes, we will also compare the T-RH joint distribution during humid-heat extremes, i.e., the impact-relevant nature of events, in homogenized and non-homogenized datasets.

2 Materials and methods

2.1 Data

There are currently two homogenized datasets including daily mean T and RH, available in China. One is based on raw daily records observed at 2,479 meteorological stations and was homogenized by using the PMTred and PMFT methods (Wang, 2008a; Wang, 2008b), with identified "break points" in the time series further manually double-checked with metadata to pin down its origin from any of site relocation, replacement/upgrading of observing instruments, or changes in observing timing and reporting protocol (Zhu et al., 2015, referred to as **OBS-1** and used as the reference hereafter). The other is homogenized with respect to a dataset containing 756 stations, alternatively using the MASH method but not compared to the metadata (Li et al., 2020a; termed as **OBS-2** hereafter). Raw daily observations from 2,479 stations across China are used for comparison, named OBS-3. Notably, the **OBS-3** is most commonly used to study humid-heat as well as other types (e.g., precipitation) of weather extremes across China. It was often claimed as "a homogenized dataset" (Luo and Lau, 2018; Kong et al., 2020) by referring to Xu et al. (2013). As a matter of fact, the homogenization in Xu et al. (2013) was conducted with respect to daily temperatures only, and other variables in the datasets including RH were only quality-controlled by the data developer—National Meteorological Information Center—by means of detecting, flagging and

correcting suspect/wrong values if possible (Zhu et al., 2015; Xu et al., 2021).

Three gridded datasets produced by site observations are also considered, including the CN05.1 (Wu and Gao, 2013) covering mainland China at a resolution of .25°, the HadISD v3.3.0—global sub-daily station dataset based on the ISD dataset from NOAA's NCEI, where temperature, dewpoint temperature, sea-level pressure are quality controlled (Dunn et al., 2016), and the HadISDH—homogenized global gridded (5° × 5°) monthly mean land surface air temperature and humidity datasets based on the HadISD dataset (Smith et al., 2011; Willett et al., 2014).

As a supplement or sometimes proxy to observations, reanalysis data with greater spatial coverage and fewer missing values is also broadly taken for the analysis of humid-heat extremes both globally and regionally. The potential inhomogeneity of reanalyzed relative humidity, however, has been seldomly noted and examined. To this end, we also collected reanalysis data for RH as many as possible, including ERA5 (.25° × .25°, Hersbach et al., 2018), ERA-Interim (.75° × .75°, Dee et al., 2011), JRA-55 (.8° × .8°, Kobayashi et al., 2015), NCEP-DOE 2 (2.5° × 2.5°, Kanamitsu et al., 2002), and CRA-40 (.125° × .8°, Liao et al., 2021). Detailed information on datasets used could be found in Supplementary Table S1.

Given that period common to observations and reanalysis datasets started in 1979 and the formal homogenization for OBS-1 was conducted with respect to raw records before 2014, a 35-year period over 1979–2013 is selected for comparison amongst datasets. Though the homogenized dataset—OBS-1 is claimed to be extended to the very recent, the extension was actually made by simply concatenating post-2013 automatic observations, which are found potentially inhomogeneous again due to the re-parameterization of the automatic observing instrument. So further homogenization efforts are needed to reconcile period-specific inhomogeneities stemming from different sources.

2.2 Data pre-processing, metrics, extremes and methods

Before conducting the analysis, all reanalysis data are adjusted by their scaling and offsetting factors specified in the netcdf files. Also, the time zone of each dataset is converted to local standard time of homogenized station observations to guarantee the consistency of follow-up comparisons.

Given closer relevance of summertime humid heat stress to human health impacts, we put our focus on the summer season spanning from June to August. In the OBS-1 and OBS-3 datasets, we only use 2,270 stations that operate continuously throughout the study period without missing values. Since HadISDH only provides monthly-mean data and unknown errors of CRA-40 temperature data occur in 2013 (details see below), these two sets of data are not involved in the calculation of extreme events.

Heat stress indicators that characterize human thermal discomfort due to high air temperature and humidity are diverse, with varying levels of equation complexity, input parameters and their weightings, and physiological assumptions (e.g., a person of average height, weight, health, and in moderate clothing). All indices consider T and RH. We here adopt three representative indices, including wet-bulb temperature (Tw), wet-bulb globe temperature (WBGT), and NOAA-developed heat index (HI), to account for linear and non-linear combinations between heat and humidity (Supplementary Figure S1) as well as their distinct impacts on human health (Buzan and Huber, 2020). The multi-indices comparison also acknowledges their different sensitivities to RH (Sherwood, 2018), especially in extreme states (Buzan and Huber, 2020), thus acting to strengthen the robustness of our quantification of influences from RH inhomogeneity on trend estimates for humid-heat extremes.

The thermodynamic wet bulb temperature (Tw) refers to the temperature of wet air when it changes adiabatically to the saturated state, and is usually measured by a wet bulb thermometer. Given Tw above 31°C physical labor becomes difficult (Sherwood and Huber, 2010); while, when its value approaches or even exceeds 35°C, evaporative cooling from sweating is no longer effective as a means of dissipating body heat. Some recent pieces of evidence also point to the danger of much lower Tw values to even young, healthy people (Asseng et al., 2021; Vecellio et al., 2022). Considering the availability of observational meteorological variables, we follow the empirical expression of Tw proposed by Stull (2011) that:

$$\begin{aligned}\mathbf{Tw} = \mathbf{T} \times \boldsymbol{atan}\left[\mathbf{0.151997}\,(\mathbf{RH\%} + \mathbf{8.313659})^{\frac{1}{2}}\right] + \mathbf{atan}\,(\mathbf{T} + \mathbf{RH\%}) \\ - \boldsymbol{atan}\,(\mathbf{RH\%} - \mathbf{1.676331}) + \mathbf{0.00391838} \times (\mathbf{RH\%})^{\frac{3}{2}} \\ \times \boldsymbol{atan}\,(\mathbf{0.023101RH\%}) - \mathbf{4.686035}\end{aligned}$$

WBGT is another typical measure of heat stress expressed as a linear combination of wet-bulb temperature, black globe temperature, and air temperature (Yaglou and Minard, 1957). The WBGT is employed as the ISO standard for thermal comfort (ISO, 1989) and is in use by a number of bodies including the military, civil engineers, and sports associations, with established thresholds relating directly to levels of physical activity (Willett and Sherwood, 2012). Considering the availability of variables used for calculation, we here adopt a "simplified WBGT" (sWBGT) version, developed by the Australian Bureau of Meteorology (ACSM, 1984), which depends only on T and humidity and represents heat stress for average daytime shady conditions outdoors (Willett Sherwood, 2012; Fischer and Knutti, 2013):

$$\mathbf{sWBGT} = \mathbf{0.56T} + \mathbf{0.393}\boldsymbol{e} + \mathbf{3.94}$$

where water vapor pressure e (hPa) is expressed as a function of air T and RH:

$$\boldsymbol{e} = \left(\frac{\boldsymbol{RH}}{\mathbf{100}}\right)^{*}\mathbf{6.105}\boldsymbol{e}^{\left(17.27T/237.7+T\right)}$$

The third index used here is the HI developed by Rothfusz (1990) and further refined and recommended by the National Oceanic and Atmospheric Administration (NOAA) with explicit thresholds warning of different levels of danger (Diffenbaugh et al., 2007). The HI is directly comparable to air temperature, with their difference informing the feels-like amplification effect of moisture on T (Delworth et al., 1999). The index is expressed as a polynomial equation composed of T and RH:

$$\begin{aligned}\mathbf{HI} = -\mathbf{42.379} + \mathbf{2.04901523}^{*}\mathbf{T} + \mathbf{10.14333127}^{*}\mathbf{RH} \\ - \mathbf{0.22475541}^{*}\mathbf{T}^{*}\mathbf{RH} - \mathbf{0.00683783}^{*}\mathbf{T}^{*}\mathbf{T} \\ - \mathbf{0.05481717}^{*}\mathbf{RH}^{*}\mathbf{RH} + \mathbf{0.00122874}^{*}\mathbf{T}^{*}\mathbf{T}^{*}\mathbf{RH} \\ + \mathbf{0.00085282}^{*}\mathbf{T}^{*}\mathbf{RH}^{*}\mathbf{RH} - \mathbf{0.00000199}^{*}\mathbf{T}^{*}\mathbf{T}^{*}\mathbf{RH}^{*}\mathbf{RH}\end{aligned}$$

where T is air temperature in degrees F and RH is RH in percent.

If the RH is less than 13% and the temperature falls between 80° and 112°F, then the following adjustment needs to be subtracted from HI:

$$\textbf{Adjustment} = [(13 - \textbf{RH})/4]^{*}\textit{SQRT}\{[17 - \textit{ABS}(\textbf{T} - 95)]/17\}$$

On the other hand, if the RH is greater than 85% and the temperature is between 80° and 87°F, then the following adjustment is added to HI:

$$\textbf{Adjustment} = [(\textbf{RH} - 85)/10]^{*}[(87 - \textbf{T})/5]$$

In case that conditions of temperature and humidity warrant a HI value below 80°F, HI is re-calculated as:

$$\textbf{HI} = 0.5^{*}\{\textbf{T} + 61.0 + [(\textbf{T} - 68.0)^{*}1.2] + (\textbf{RH}^{*}0.094)\}$$

All heat stress indices are finally converted to values in °C.

For each station or grid, summertime daily heat stress values are firstly calculated based on the aforementioned three indices respectively, and then all samples during 1979–2008 (a 30-year reference period) are pooled and empirically ranked to obtain local 95th percentiles of each heat stress index used as thresholds to identify their extremes.

With respect to the index considered, we count the number of threshold-exceeding days in each summer as the frequency of extreme humid-heat events, and the average amongst these extreme heat stress values represents the mean intensity of extremes of the year.

Given the same network density of OBS-1 and OBS-3, biases in the trend estimate for T, RH and extreme heat stress due to data inhomogeneity could be measured by a direct site-to-site comparison; whilst as with the comparison between station observations and gridded observations/reanalysis of different resolutions, we prepare a box-average series using all stations or grids at a scale of 5° × 5°, and calculate the areal-weighted mean of box values across a region to produce the regional-mean series. We did not interpolate station- and gridded- data onto the same mesh grid, to avoid untraceable uncertainties from interpolation algorithms.

We use ordinary least squares scheme to quantify linear trends for T, RH and extreme events, along with students' *t*-test to evaluate the significance (at the .05 level). As a cross-validation, we additionally employ Kendall's tau slope estimator (results now shown), and report highly consistent results in terms of both trend magnitude and significance. To isolate and quantify the influence of RH inhomogeneity on the estimate for changes in extreme humid-heat events at a local scale (Figure 3), we configure homogenized T from the OBS-1 to both homogenized RH (OBS-1) and raw RH (OBS-3). More specifically, we regress station-based differences in trends for extremes evaluated *via* homogenized and non-homogenized data onto the underlying differences in RH trends.

3 Results

During 1979–2013, daily mean air temperature exhibits significant warming trends across China in both homogenized and raw site observations (Figures 1A, B), characteristic of highly similar spatial patterns and local-to-regional magnitudes for trends between the two (Figure 1C). This suggests a minor influence of potential temporal inhomogeneity in T on the estimate for long-term changes of the variable. By contrast, the pattern, magnitude, significance and even the sign of trends for RH differ pronouncedly between homogenized and non-homogenized station-based observational datasets. The inhomogeneity issue in relative humidity is particularly stark in southeast China (south of 30N, east of 105E, black rectangle in Figures 1D, E), leading to widespread biases in trend estimates for RH with incorrect signs there (Figure 1F). The region (black rectangle) is typical of humid-hot subtropical climates in favor of the occurrence of oppressive heat (Supplementary Figure S1; Vargas Zeppetello et al., 2022) with the two variables playing equivalently important roles to cause extremes there (Buzan and Huber, 2020).

With respect to the identified RH inhomogeneity hotspot, we further expand the comparison to gridded observations and widely-used reanalysis data at a regional scale. Large interannual to inter-decadal variability could be found in the domain-average RH series in homogenized observations (black curve, OBS-1, Figure 2A), experiencing a relatively wet regime before 2000 followed by a shift to a dry episode. This might be explained *via* a moist static energy balance perspective in the context of equal fractional changes in specific humidity over land and neighboring oceans (Byrne and O'Gorman, 2018) through remote moisture transport and local evapotranspiration processes (Byrne and O'Gorman, 2016; Douville et al., 2020).

Though the regional variability is generally captured by other datasets, the RH drop around 2000, when coincidentally the observational network across China shifted from manual to automatic practices (2000–2005), is exaggerated in non-homogenized datasets (except for CRA-40). This is mainly because of the systematic difference in manual and automatic observing instruments, with the lower values recorded in the latter period (e.g., Supplementary Figure S2, RH) deemed more accurate and used since then (Zhu et al., 2015). The inhomogeneity gives rise to long-term drying trends of unrealistically high magnitude and significance (Figure 2B). Specifically, the regional drying rate estimated by OBS-1 is around −.47%/decade; while the estimate based on OBS-3 is −1.43%/decade, almost three times sharper than the correct one. In particular, the HadISDH was commonly used as homogenized observations to calculate heat stress indices globally (Raymond et al., 2020; Rogers et al., 2021). Our analysis brings into question the homogeneity of HadISDH over southeastern China, suggesting that detecting region-wide inhomogeneities by automated methods (Dunn et al., 2014) without knowing detailed histories of station information (e.g., relocation and instrument replacement) might be less effective than expected. Another extensively-used dataset—ERA5 also suffers from severe inhomogeneities in RH for the region, and is therefore not suitable to characterize humid-heat extremes at sub-daily to daily scales in the region (Freychet et al., 2020). Encouragingly, incorporating into homogenized station observations (OBS-1), the CRA-40 reanalysis newly released by the China Meteorological Administration performs well in reproducing both variability and trends of RH in southeastern China. Though expanding the study region northward to 35N does not alter the comparison of trend magnitude and significance amongst datasets in any significant manner (figure omitted), it might introduce confounding factors related to differential representation of irrigation in the 30–35N latitudinal band, an intensely irrigated region (Kang and Eltahir, 2018). So, to distinguish influences of data inhomogeneity from other similar confounding factors, southeastern China to the south of 30N is a better candidate study area.

Though air temperature records were also subject to changes in observing sites, instruments and timing, the inhomogeneities from these sources seemed to pose a trivial influence on the temporal variability and long-term trends as well as their significance of domain-averaged series of air temperature (Supplementary Figure S3, OBS-1 and OBS-2 vs. OBS-3).

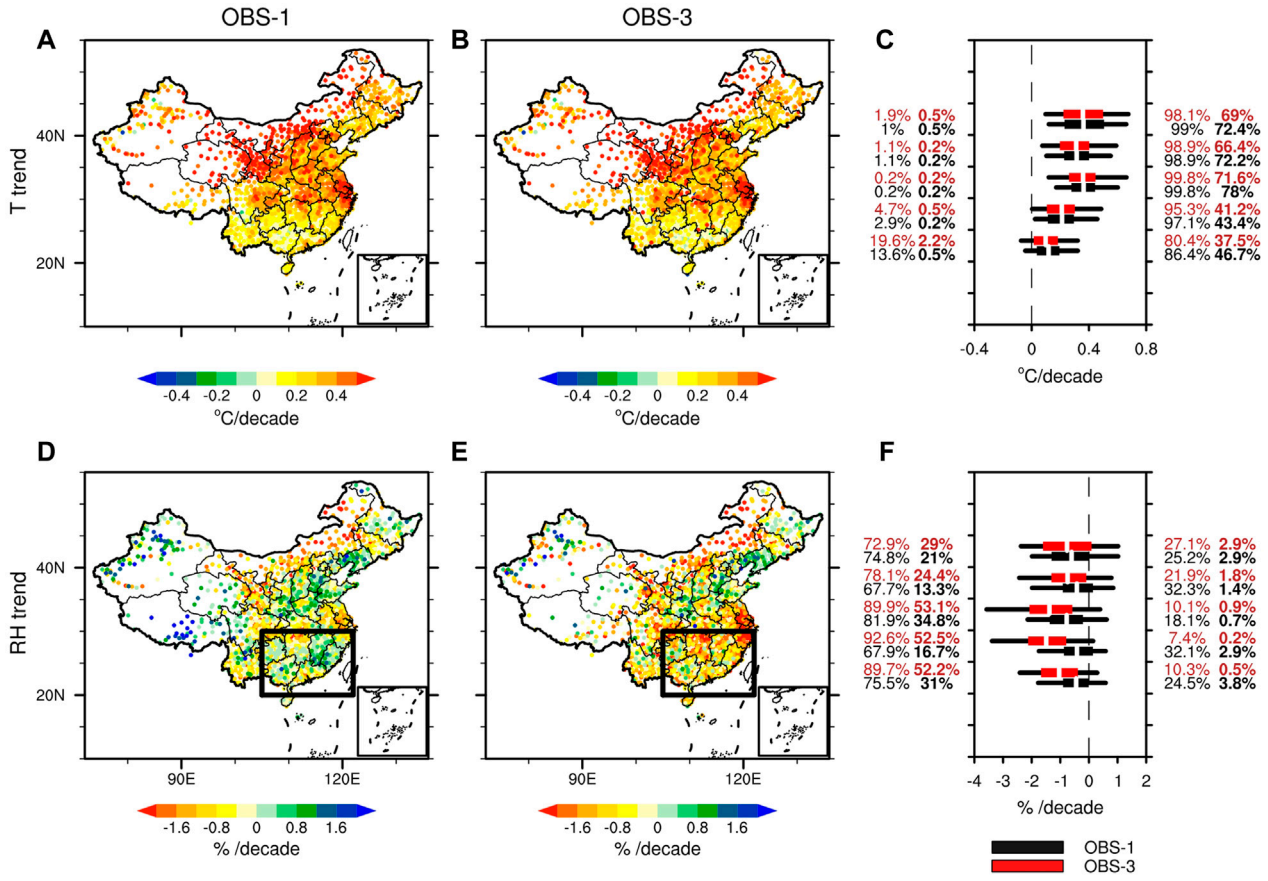

FIGURE 1
Trends for summertime T and RH in China during 1979–2013. **(A,B)** show T trends (°C per decade) estimated by OBS-1 (homogenized) and OBS-3 (non-homogenized), respectively. The box-and-whisker plots shown in **(C)** presents the distribution of T trends amongst stations within each 5°latitudinal band, including the 5th, 25th, median, 75th, and 95th percentiles in OBS-1 (black) and OBS-3 (red). The numbers labeled to the negative/positive side of the *x*-axis indicate the fraction of stations observing negative/positive trends within the latitudinal band, in which the fraction of station registering significant trends are bold-highlighted in the second column. **(D–F)** are the same as **(A–C)** but for RH.

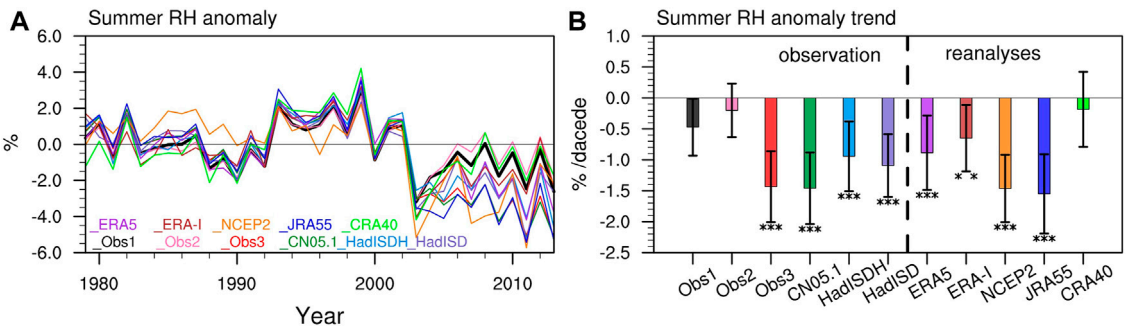

FIGURE 2
Domain-averaged series of RH over southeastern China during 1979–2013 based on eleven datasets **(A)** and their linear trends **(B)**. The RH series is pre-processing into anomalies with respect to the 1979–2008 climatology. The error bars in **(B)** enclose the 95% confidence interval of trend estimates, with symbols "**" and "***" indicating their significance at the .05 and .01 levels respectively.

The differences in magnitudes and significances of trends for air temperature amongst datasets are much less conspicuous than those for relative humidity. Notably, despite better performance in representing RH during 1979–2013 in CRA-40, for unknown reasons, its temperature records in 2013 are inconsistent with counterparts from any of other datasets. This year's error in temperature records has reported back to the data developer for improvement, and the flaw also excludes CRA-40 for participation in follow-up analysis on extremes.

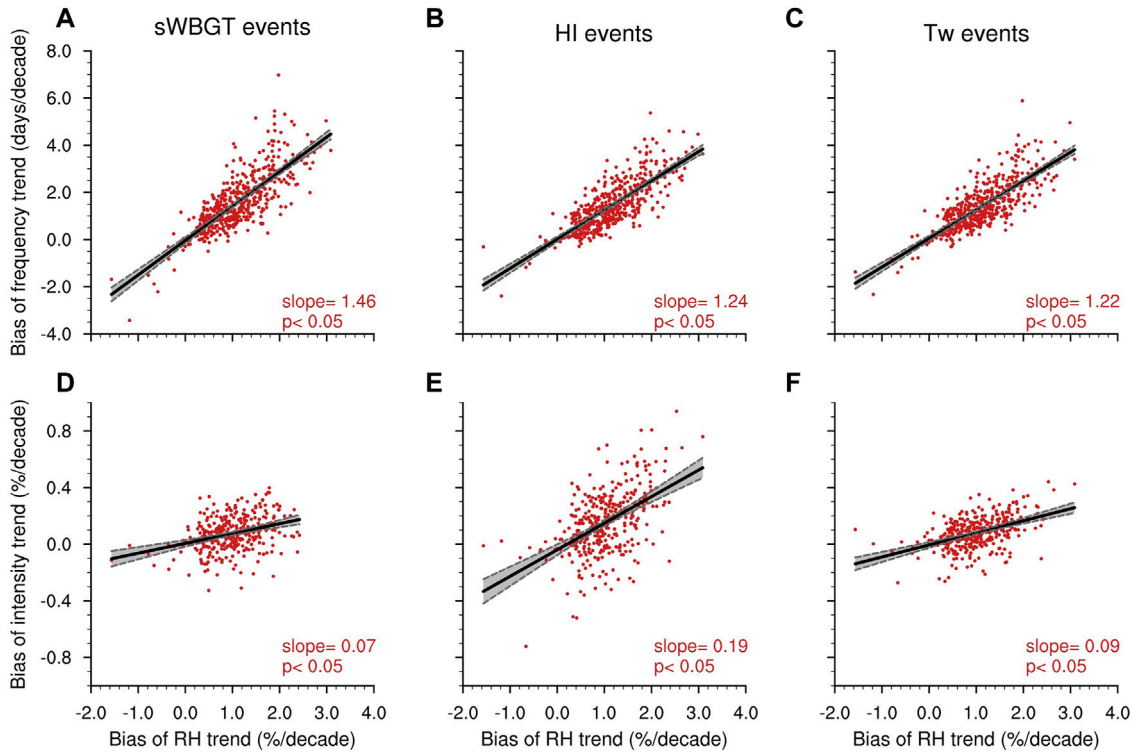

FIGURE 3
Influences of local RH trend bias (homogenized OBS1 minus non-homogenized OBS3) on the estimate for trends for frequency **(A–C)** and intensity **(D–F)** of humid-heat extremes across southeast China, identified using three indicators. To improve comparability in intensity amongst indicators **(D–F)**, the trend for intensity at each station is normalized by local indicator climatology. Linear regressions are shown by black curves and the 95% regression confidence intervals are shaded in grey, with regression coefficients (Slope) and significance (P) indicated at the lower-right of each panel.

We next quantify extent to which the RH inhomogeneity in observation and reanalysis datasets distorts the trend estimate for humid-heat metrics, similarly starting with a site-by-site comparison (OBS-1 vs. OBS-3). We do this by regressing the differential trends for extremes in homogenized and non-homogenized observations onto the differences of RH trends in them (homogeneous trend minus non-homogeneous one). As indicated by Figures 3A–C, given the same atmospheric warming (local trends for T from OBS-1), an exaggeration of drying trend by 1% decade^{-1} due to RH inhomogeneity translates into an underestimation of increasing trends for humid-heat extremes' frequency by more than 1.2 days decade^{-1}, with extreme sWBGT events influenced most. The RH inhomogeneity also significantly abates the intensification rates of extreme humid-heat events, especially those resulting from the highly non-linear combination between T and RH as showcased by the HI index (Figures 3D–F; also Supplementary Figures S4A–C). Locally, an 1% decade^{-1} drying bias caused by the RH inhomogeneity leads to an underestimation of intensification rates (absolute trends normalized by local index climatology, for the purpose of objective comparison amongst indices) for HI extremes by around .19% decade^{-1}, equivalent to a bias around .07°C decade^{-1} there (Supplementary Figure S4).

For the domain-average series of frequency, with reference to the trend evaluated *via* homogenized data, all non-homogenized datasets discernably underestimate the increase, by the magnitudes ranging from .5 to 2 days decade^{-1}, basically proportional to the regional drying biases (both the *X*-axis and *Y*-axis represent the homogenized OBS-1 minus other datasets). The limited sample size (~9 datasets) prohibits us from further evaluating the significance of such relationship. Despite being widely used, the HadISD and ERA5 datasets are amongst the worst that considerably underestimate past increases in the frequency of humid-heat extremes (Figure 4). Their bad performance arises jointly from an overestimation of the RH drying rate and an underestimation of the warming trend (Supplementary Figure S5).

Notably, despite significant negative correlation between air temperature and relative humidity at the regional scale, we did not find the cancellation or say compensation effect between greater warming and stronger RH reduction biases in the same dataset (Supplementary Figure S5) as reported in historical simulations and future projections (Fischer and Knutti, 2013), except for NCEP2 which shows the strongest negative correlation between the two variables. Rather, slightly weaker warming trends and drying bias in RH trends in tandem contribute to an underestimation of regional increases in humid-heat extremes in frequency and intensity, with the "out-of-range" RH bias (outside the grey shadings in Supplementary Figure S5) dominating in most datasets. Even for NCEP2 seemingly most faithfully reproducing extremes' statistics, such better performance apparent arises from the wrong reason, and therefore should not be further leveraged as a reliable benchmark for model evaluation and impact quantification (Casanueva et al., 2019). Similar "right statistics for wrong reason" might exist at local scales where the T-RH anti-correlation is even stronger (e.g., <−.85).

When referring to extreme humid-heat conditions, the combination in a fashion of high temperature and high humidity comes to one's mind first and naturally. But as a matter of fact, extreme humid-heat events represent a typical case that not all of its components are necessarily

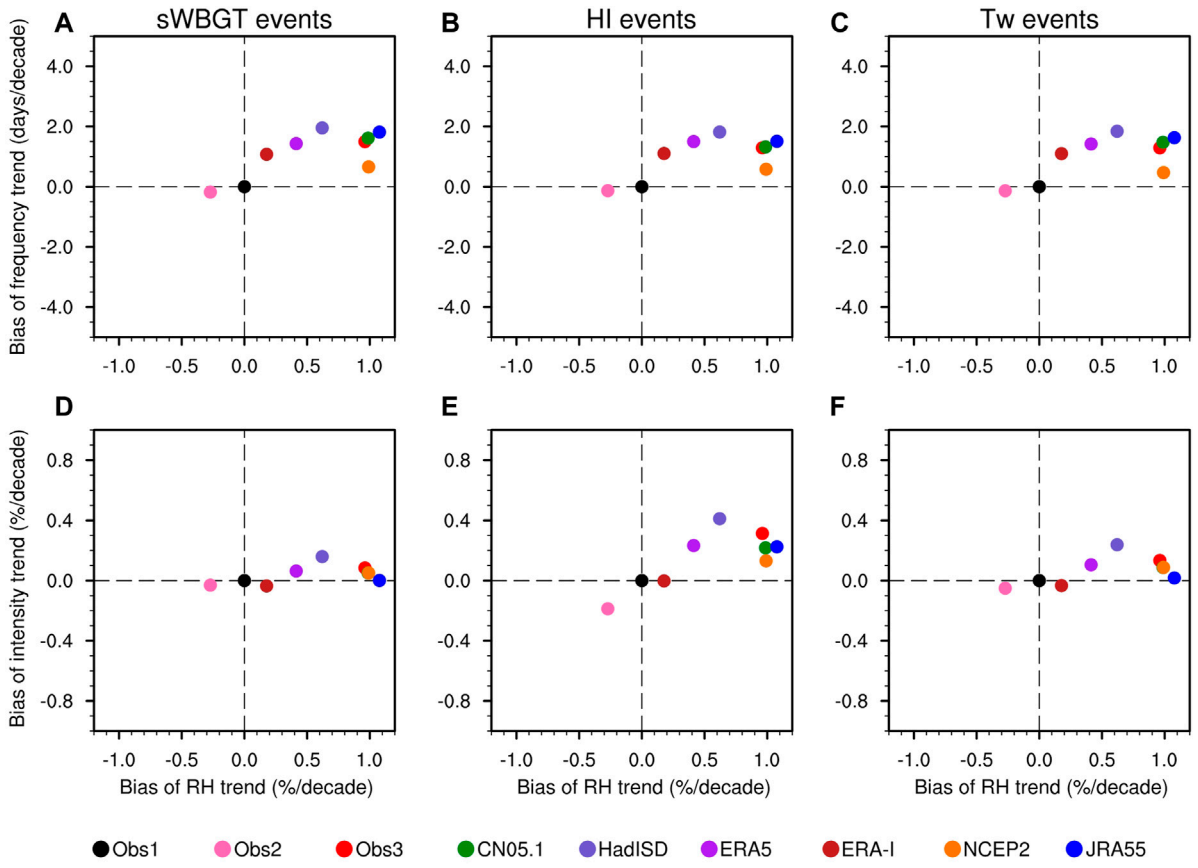

FIGURE 4
Scatter plot–between regional-mean (southeast China) RH trend bias and extreme events' frequency **(A–C)**/intensity **(D–F)** trend bias, amongst inhomogeneous datasets with reference to homogenized one (OBS-1, black dot in the center).

extreme, but their combination leads to an extreme impact (Zscheischler et al., 2018). Different forms of joint distributions of temperature and humidity during extreme humid-heat events are worth further sorting out, because they might cause distinct impacts on human health (Mora et al., 2017; Asseng et al., 2021).

Compared to humid-heat extremes previously identified by non-homogenized observations (OBS-3), counterparts from homogenized observations are similarly warm (mostly within the range of 25–33°C, Supplementary Figure S6) but not necessarily that moist, regardless of indicators selected (Figure 5). Quantitatively, we used to believe that the majority of extremes (around 60%–80% events across the region) occurred in the context of RH wetter than 70%; while subject to the homogenization correction, the understanding is revised into that the conventionally favorable thermodynamic environment host only half of extremes. Such a contrast in the RH constituent to extremes is also ubiquitous amongst other observation and reanalysis datasets (Supplementary Figure S7). In particular, though the bivariate distribution difference is largely determined by RH biases, the temperature difference also plays a non-trivial role in shaping the differential joint distribution structure in some datasets, e.g., ERA5 (Supplementary Figure S7E) and NCEP2 (Supplementary Figure S7G). In addition to the absolute magnitude for humid-heat extremes, the accurate mapping of typical bivariate configuration constituting the extremes, based on homogenized datasets, matters to identification of key thresholds for early warning against health-damaging events (Han et al., 2022; Vecellio et al., 2022). In light of the distinct bivariate distribution structures (Supplementary Figure S7) along with the harder-detectable inhomogeneity in the bivariate combined indices (e.g., Supplementary Figure S2, Tw), a component-wise bias correction technique might be superior to an "one-step" correction scheme with respect to the combined index, for both observations and simulations (Casanueva et al., 2019).

4 Discussion and conclusion

4.1 Discussion

We here addressed the issue of ubiquitous inhomogeneity of relative humidity in most observational and reanalysis datasets, with a specific focus on its influences on the estimate for changes in daily humid-heat extremes in China. We acknowledge that the intrinsic diurnal cycle of humid heat stress, resulting from quasi out-of-phase variations of air temperature and relative humidity (Fischer and Knutti, 2013), makes the daily-mean value conservative to represent daily maxima, the most concerning value to human health (Schär, 2016; Kang and Eltahir, 2018; Raymond et al., 2020). The current unavailability of homogenized hourly to sub-daily (e.g., 6-h) RH observations, however, prohibits us from moving forward in this regard (Wang and Sun, 2021), Our analysis clearly demonstrates

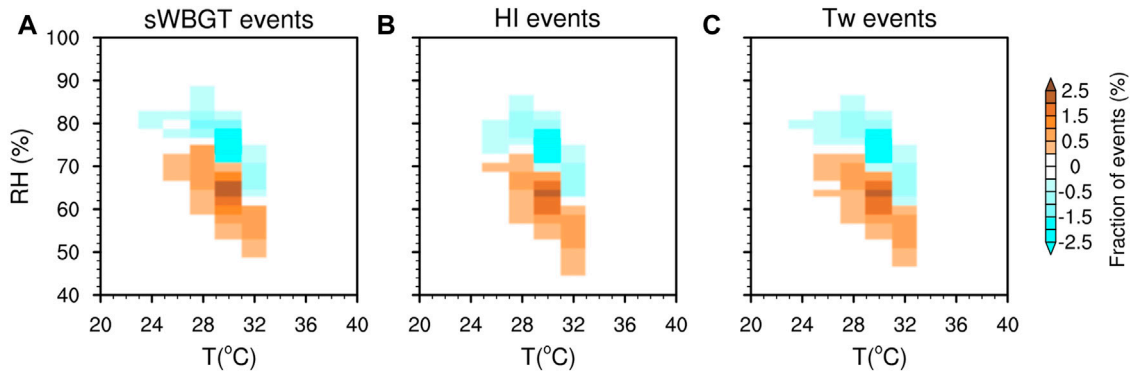

FIGURE 5
The difference (homogenized minus non-homogenized) in the bivariate joint distribution of T and RH which produce three type extreme events **(A-C)** of corresponding indicators. Temperature and humidity are firstly binned by 2°C and 2% intervals, and the fraction of extreme-producing (all cases during the study period across the domain) T-RH configurations that fall into corresponding bivariate bins are calculated and presented.

that using sub-daily records from ERA-5 or raw HadISD observations to achieve the goal is problematic. As a result, efforts are badly needed to collect, quality-control and homogenize hourly temperature and relative humidity, to revisit and better inform changing risks of impact-relevant heat stress in the populous region, as well as in other vulnerable regions around the world.

The data inhomogeneity-caused bias in the estimate for past changes in humid-heat extremes would propagate into their future projections, as all of model validation, bias correction (Casanueva et al., 2019), selection (Ridder et al., 2022) and weighting scheme (Ribes et al., 2021) as well as the design of emergent constraints (Freychet et al., 2021) are contingent on thorough comparisons of historical simulations to observations. By leveraging homogenized RH records as an observational constraint, follow-up efforts are therefore worth extending into projection analyses, in terms of both magnitudes and width of the uncertainty range for projected frequency and intensity of humid-heat extremes.

To the other end of spectrum of T-RH configuration, low relative humidity combined with high temperatures aggravates risks for wildfire occurrence and agricultural impacts (Chiodi et al., 2021; Balch et al., 2022). The unrealistically strong drying trend for RH is expected to result in an overestimation of increasing fire risks, which also remains under-appreciated in the region because of little attention paid to hot-dry-fire compound events there for now.

5 Conclusion

We present the most comprehensive comparison to date on long-term changes in relative humidity across China, based on ~10 widely-used observational and reanalysis datasets subject to different levels of homogenization. We report an artificially sharp decline in RH around 2000–2005 in most datasets due mainly to the massive transition from manual observation practices to automatic observations with observational instruments replaced at the time. The inhomogeneity issue stands out particularly stark in warm-moist southern China, leading to unrealistically strong and significant drying trends there.

The biased drying trends in these inhomogeneous datasets lead to underestimation of changes in humid-heat extremes, with a drying bias of 1% decade^{-1} attenuating the magnitude for increases in extremes' frequency (intensity) by more than 1.2 days decade^{-1} (.07% decade^{-1}) locally, regardless of metrics considered. For the region as a whole, these inhomogeneous records have underestimated domain-averaged frequency (intensity) of extremes by .47–1.95 days decade^{-1} (−.04%~.41% decade^{-1}). Humid-heat extremes identified by homogenized and non-homogenized datasets also differ in the T-RH joint anomalies, with most cases in the latter equivalently hot or slightly cooler yet discernably moister.

Our results call for emphasis on data quality of observed/reanalyzed relative humidity, not only in China but also in other parts of the world, and the need of re-evaluating past changes of humid-heat extremes to improve projections of deadly heat stress worldwide.

Data availability statement

The raw data supporting the conclusion of this article will be made available by the authors, without undue reservation.

Author contributions

YC designed the research; XL carried out most calculations and result interpretations, created all figures and wrote the original draft, further reviewed and edited by YC and YZ developed and provided the homogenized observation dataset, and took part in result discussion. NA and ZL participated in result discussion.

Funding

The research is financially supported by the National Key Research and Development Program of China (Grant No. 2018YFC1507700). The study is also supported by S&T Development Fund of CAMS (2021KJ014).

Acknowledgments

We thank the data developer, i.e., National Meteorological Information Center, for collecting, quality controlling, homogenizing and kindly providing the observational data.

Conflict of interest

The authors declare that the research was conducted in the absence of any commercial or financial relationships that could be construed as a potential conflict of interest.

Publisher's note

All claims expressed in this article are solely those of the authors and do not necessarily represent those of their affiliated organizations, or those of the publisher, the editors and the reviewers. Any product that may be evaluated in this article, or claim that may be made by its manufacturer, is not guaranteed or endorsed by the publisher.

Supplementary material

The Supplementary Material for this article can be found online at: https://www.frontiersin.org/articles/10.3389/fenvs.2022.1104039/full#supplementary-material

References

ACSM (1984). Prevention of thermal injuries during distance running. *Med. J. Aust.* 141 (12-13), 876–879.

Asseng, S., Spänkuch, D., Hernandez-Ochoa, I. M., and Laporta, J. (2021). The upper temperature thresholds of life. *Lancet Planet. Health* 5 (6), e378–e385. doi:10.1016/S2542-5196(21)00079-6

Balch, J. K., Abatzoglou, J. T., Joseph, M. B., Koontz, M. J., Mahood, A. L., McGlinchy, J., et al. (2022). Warming weakens the night-time barrier to global fire. *Nature* 602 (7897), 442–448. doi:10.1038/s41586-021-04325-1

Brouillet, A., and Joussaume, S. (2019). Investigating the role of the relative humidity in the Co-occurrence of temperature and heat stress extremes in CMIP5 projections. *Geophys. Res. Lett.* 46 (20), 11435–11443. doi:10.1029/2019GL084156

Buzan, J. R., and Huber, M. (2020). Moist heat stress on a hotter earth. *Annu. Rev. Earth Planet. Sci.* 48 (1), 623–655. doi:10.1146/annurev-earth-053018-060100

Byrne, M. P., and O'Gorman, P. A. (2018). Trends in continental temperature and humidity directly linked to ocean warming. *Proc. Natl. Acad. Sci.* 115 (19), 4863–4868. doi:10.1073/pnas.1722312115

Byrne, M. P., and O'Gorman, P. A. (2016). Understanding decreases in land relative humidity with global warming: Conceptual model and GCM simulations. *J. Clim.* 29 (24), 9045–9061. doi:10.1175/JCLI-D-16-0351.1

Casanueva, A., Kotlarski, S., Herrera, S., Fischer, A. M., Kjellstrom, T., and Schwierz, C. (2019). Climate projections of a multivariate heat stress index: The role of downscaling and bias correction. *Geosci. Model Dev.* 12 (8), 3419–3438. doi:10.5194/gmd-12-3419-2019

China Climate Bulletin (2014). *China climate Bulletin 2014*. Beijing: China Meteorological Administration.

Chiodi, A. M., Potter, B. E., and Larkin, N. K. (2021). Multi-decadal change in western US nighttime vapor pressure deficit. *Geophys. Res. Lett.* 48 (15), e2021GL092830. doi:10.1029/2021GL092830

Dee, D. P., Uppala, S. M., Simmons, A. J., Berrisford, P., Poli, P., Kobayashi, S., et al. (2011). The ERA-Interim reanalysis: Configuration and performance of the data assimilation system. *Q. J. R. Meteorological Soc.* 137 (656), 553–597. doi:10.1002/qj.828

Delworth, T. L., Mahlman, J. D., and Knutson, T. R. (1999). Changes in heat index associated with CO2-induced global warming. *Clim. Change* 43 (2), 369–386. doi:10.1023/A:1005463917086

Diffenbaugh, N. S., Pal, J. S., Giorgi, F., and Gao, X. (2007). Heat stress intensification in the Mediterranean climate change hotspot. *Geophys. Res. Lett.* 34 (11), L11706. doi:10.1029/2007GL030000

Douville, H., Decharme, B., Delire, C., Colin, J., Joetzjer, E., Roehrig, R., et al. (2020). Drivers of the enhanced decline of land near-surface relative humidity to abrupt 4xCO2 in CNRM-CM6-1. *Clim. Dyn.* 55 (5), 1613–1629. doi:10.1007/s00382-020-05351-x

Douville, H., and Plazzotta, M. (2017). Midlatitude summer drying: An underestimated threat in CMIP5 models? *Geophys. Res. Lett.* 44 (19), 9967–9975. doi:10.1002/2017GL075353

Dunn, R. J. H., Willett, K. M., Ciavarella, A., and Stott, P. A. (2017). Comparison of land surface humidity between observations and CMIP5 models. *Earth Syst. Dyn.* 8 (3), 719–747. doi:10.5194/esd-8-719-2017

Dunn, R. J. H., Willett, K. M., Morice, C. P., and Parker, D. E. (2014). Pairwise homogeneity assessment of HadISD. *Clim. Past* 10 (4), 1501–1522. doi:10.5194/cp-10-1501-2014

Dunn, R. J. H., Willett, K. M., Parker, D. E., and Mitchell, L. (2016). Expanding HadISD: Quality-controlled, sub-daily station data from 1931. *Geoscientific Instrum. Methods Data Syst.* 5 (2), 473–491. doi:10.5194/gi-5-473-2016

Dunne, J. P., Stouffer, R. J., and John, J. G. (2013). Reductions in labour capacity from heat stress under climate warming. *Nat. Clim. Change* 3 (6), 563–566. doi:10.1038/nclimate1827

Fischer, E. M., and Knutti, R. (2013). Robust projections of combined humidity and temperature extremes. *Nat. Clim. Change* 3 (2), 126–130. doi:10.1038/nclimate1682

Freychet, N., Hegerl, G., Mitchell, D., and Collins, M. (2021). Future changes in the frequency of temperature extremes may be underestimated in tropical and subtropical regions. *Commun. Earth Environ.* 2 (1), 28. doi:10.1038/s43247-021-00094-x

Freychet, N., Tett, S. F. B., Yan, Z., and Li, Z. (2020). Underestimated change of wet-bulb temperatures over east and South China. *Geophys. Res. Lett.* 47 (3), e2019GL086140. doi:10.1029/2019GL086140

Han, Q., Liu, Z., Jia, J., Anderson, B. T., Xu, W., and Shi, P. (2022). Web-based data to quantify meteorological and geographical effects on heat stroke: Case study in China. *GeoHealth* 6 (8), e2022GH000587. doi:10.1029/2022GH000587

Hersbach, H., de Rosnay, P., Bell, B., Schepers, D., Simmons, A., Soci, C., et al. (2018). *Operational global reanalysis: Progress, future directions and synergies with NWP*, 27. doi:10.21957/tkic6g3wm

Hoag, H. (2014). Russian summer tops 'universal' heatwave index. *Nature* 2014, 16250. doi:10.1038/nature.2014.16250

ISO (1989). *Hot Environments – estimation of the heat stress on working man, based on the WBGT-index (wet bulb globe temperature)*. Geneva: International Standards Organization. ISO 7243.

Kanamitsu, M., Ebisuzaki, W., Woollen, J., Yang, S.-K., Hnilo, J. J., Fiorino, M., et al. (2002). NCEP–DOE AMIP-II reanalysis (R-2). *Bull. Am. Meteorological Soc.* 83 (11), 1631–1644. doi:10.1175/BAMS-83-11-1631

Kang, S., and Eltahir, E. A. B. (2018). North China Plain threatened by deadly heatwaves due to climate change and irrigation. *Nat. Commun.* 9 (1), 2894. doi:10.1038/s41467-018-05252-y

Kobayashi, S., Ota, Y., Harada, Y., Ebita, A., Moriya, M., Onoda, H., et al. (2015). The JRA-55 reanalysis: General specifications and basic characteristics. *J. Meteorological Soc. Jpn. Ser II* 93 (1), 5–48. doi:10.2151/jmsj.2015-001

Kong, D., Gu, X., Li, J., Ren, G., and Liu, J. (2020). Contributions of global warming and urbanization to the intensification of human-perceived heatwaves over China. *J. Geophys. Res. Atmos.* 125 (18), e2019JD032175. doi:10.1029/2019JD032175

Li, C., Sun, Y., Zwiers, F., Wang, D., Zhang, X., Chen, G., et al. (2020a). Rapid warming in summer wet bulb globe temperature in China with human-induced climate change. *J. Clim.* 33 (13), 5697–5711. doi:10.1175/JCLI-D-19-0492.1

Li, D., Yuan, J., and Kopp, R. E. (2020b). Escalating global exposure to compound heat-humidity extremes with warming. *Environ. Res. Lett.* 15 (6), 064003. doi:10.1088/1748-9326/ab7d04

Li, Z., Yan, Z., Zhu, Y., Freychet, N., and Tett, S. (2020c). Homogenized daily relative humidity series in China during 1960–2017. *Adv. Atmos. Sci.* 37 (4), 318–327. doi:10.1007/s00376-020-9180-0

Liao, J., Wang, H., Zhou, Z., Liu, Z., Jiang, L., and Yuan, F. (2021). Integration, quality assurance, and usage of global aircraft observations in CRA. *J. Meteorological Res.* 35 (1), 1–16. doi:10.1007/s13351-021-0093-3

Luo, M., and Lau, N.-C. (2018). Increasing heat stress in urban areas of eastern China: Acceleration by urbanization. *Geophys. Res. Lett.* 45 (2313), 13060–13069. doi:10.1029/2018GL080306

IPCC (2021). "Chapter 3: Human influence on the climate system," in *Climate change 2021: The physical science basis, contribution of working group I to the sixth assessment report of the intergovernmental panel on climate change*. Editors V. Masson-Delmotte, P. Zhai, A. Pirani, S. L. Connors, C. Pean, S. Berger, et al. (Cambridge University Press), 3–31. –3-33 In press Available at: https://www.ipcc.ch/report/sixth-assessment-report-working-group-i/.

Mora, C., Dousset, B., Caldwell, I. R., Powell, F. E., Geronimo, R. C., Bielecki, C. R., et al. (2017). Global risk of deadly heat. *Nat. Clim. Change* 7 (7), 501–506. doi:10.1038/nclimate3322

Raymond, C., Matthews, T., and Horton, R. M. (2020). The emergence of heat and humidity too severe for human tolerance. *Sci. Adv.* 6 (19), eaaw1838. doi:10.1126/sciadv.aaw1838

Ribes, A., Qasmi, S., and Gillett, N. P. (2021). Making climate projections conditional on historical observations. *Sci. Adv.* 7 (4), eabc0671. doi:10.1126/sciadv.abc0671

Ridder, N. N., Ukkola, A. M., Pitman, A. J., and Perkins-Kirkpatrick, S. E. (2022). Increased occurrence of high impact compound events under climate change. *Npj Clim. Atmos. Sci.* 5 (1), 3. doi:10.1038/s41612-021-00224-4

Rogers, C. D. W., Ting, M., Li, C., Kornhuber, K., Coffel, E. D., Horton, R. M., et al. (2021). Recent increases in exposure to extreme humid-heat events disproportionately affect populated regions. *Geophys. Res. Lett.* 48 (19), e2021GL094183. doi:10.1029/2021GL094183

Rothfusz, L. (1990). *The heat index equation*. Camp Springs, Maryland, USA: National Weather Service Technical Attachment, 23–90.

Saeed, F., Schleussner, C.-F., and Ashfaq, M. (2021). Deadly heat stress to become commonplace across south asia already at 1.5°C of global warming. *Geophys. Res. Lett.* 48 (7), e2020GL091191. doi:10.1029/2020GL091191

Schär, C. (2016). The worst heat waves to come. *Nat. Clim. Change* 6 (2), 128–129. doi:10.1038/nclimate2864

Schröder, M., Lockhoff, M., Shi, L., August, T., Bennartz, R., Brogniez, H., et al. (2019). The GEWEX water vapor assessment: Overview and introduction to results and recommendations. *Remote Sens.* 11 (3), 251. Article 3. doi:10.3390/rs11030251

Sherwood, S. C. (2018). How important is humidity in heat stress? *J. Geophys. Res. Atmos.* 123 (2111), 11808–11810. doi:10.1029/2018JD028969

Sherwood, S. C., and Huber, M. (2010). An adaptability limit to climate change due to heat stress. *Proc. Natl. Acad. Sci.* 107 (21), 9552–9555. doi:10.1073/pnas.0913352107

Smith, A., Lott, N., and Vose, R. (2011)., 92. JSTOR, 704–708. doi:10.1175/2011bams3015.1The integrated surface database: Recent developments and partnerships*Bull. Am. Meteorological Soc.*6

Speizer, S., Raymond, C., Ivanovich, C., and Horton, R. M. (2022). Concentrated and intensifying humid heat extremes in the IPCC AR6 regions. *Geophys. Res. Lett.* 49 (5), e2021GL097261. doi:10.1029/2021GL097261

Stull, R. (2011). Wet-bulb temperature from relative humidity and air temperature. *J. Appl. Meteorology Climatol.* 50 (11), 2267–2269. doi:10.1175/JAMC-D-11-0143.1

Tuholske, C., Caylor, K., Funk, C., Verdin, A., Sweeney, S., Grace, K., et al. (2021). Global urban population exposure to extreme heat. *Proc. Natl. Acad. Sci.* 118 (41), e2024792118. doi:10.1073/pnas.2024792118

Vargas Zeppetello, L. R., Raftery, A. E., and Battisti, D. S. (2022). Probabilistic projections of increased heat stress driven by climate change. *Commun. Earth Environ.* 3 (1), 183. doi:10.1038/s43247-022-00524-4

Vecellio, D. J., Wolf, S. T., Cottle, R. M., and Kenney, W. L. (2022). Evaluating the 35°C wet-bulb temperature adaptability threshold for young, healthy subjects (PSU HEAT Project). *J. Appl. Physiology* 132 (2), 340–345. doi:10.1152/japplphysiol.00738.2021

Wang, D., and Sun, Y. (2021). Long-term changes in summer extreme wet bulb globe temperature over China. *J. Meteorological Res.* 35 (6), 975–986. doi:10.1007/s13351-021-1080-4

Wang, P., Leung, L. R., Lu, J., Song, F., and Tang, J. (2019). Extreme wet-bulb temperatures in China: The significant role of moisture. *J. Geophys. Res. Atmos.* 124 (22), 11944–11960. doi:10.1029/2019JD031477

Wang, S., and Zhu, J. (2020). Amplified or exaggerated changes in perceived temperature extremes under global warming. *Clim. Dyn.* 54 (1), 117–127. doi:10.1007/s00382-019-04994-9

Wang, X. L. (2008b). Accounting for autocorrelation in detecting mean shifts in climate data series using the penalized maximal t or F test. *J. Appl. Meteorology Climatol.* 47 (9), 2423–2444. doi:10.1175/2008JAMC1741.1

Wang, X. L. (2008a). Penalized maximal F test for detecting undocumented mean shift without trend change. *J. Atmos. Ocean. Technol.* 25 (3), 368–384. doi:10.1175/2007JTECHA982.1

Willett, K. M., Dunn, R. J. H., Thorne, P. W., Bell, S., de Podesta, M., Parker, D. E., et al. (2014). HadISDH land surface multi-variable humidity and temperature record for climate monitoring. *Clim. Past* 10 (6), 1983–2006. doi:10.5194/cp-10-1983-2014

Willett, K. M., and Sherwood, S. (2012). Exceedance of heat index thresholds for 15 regions under a warming climate using the wet-bulb globe temperature. *Int. J. Climatol.* 32 (2), 161–177. doi:10.1002/joc.2257

Wu, J., and Gao, X. J. (2013). A gridded daily observation dataset over China region and comparison with the other datasets. *Chin. J. Geophys.* 56 (4), 1102–1111. doi:10.6038/cjg20130406

Xu, F., Chan, T. O., and Luo, M. (2021). Different changes in dry and humid heat waves over China. *Int. J. Climatol.* 41 (2), 1369–1382. doi:10.1002/joc.6815

Xu, W., Li, Q., Wang, X. L., Yang, S., Cao, L., and Feng, Y. (2013). Homogenization of Chinese daily surface air temperatures and analysis of trends in the extreme temperature indices. *J. Geophys. Res. Atmos.* 118 (17), 9708–9720. doi:10.1002/jgrd.50791

Yaglou, C. P., and Minard, D. (1957). Control of heat casualties at military training centers. *Ama Arch. Ind. Health* 16 (4), 302–316.

Yu, J., and Mu, R. (2008). Research on the cause of difference between AWS-and MAN-relative humidity observations. *Met. EOROLOGICAL Mon.* 34 (12), 96–102. In Chinese. (with English abstract).

Zhang, J., Zhao, T., Li, Z., Li, C., Li, Z., Ying, K., et al. (2021). Evaluation of surface relative humidity in China from the CRA-40 and current reanalyses. *Adv. Atmos. Sci.* 38 (11), 1958–1976. doi:10.1007/s00376-021-0333-6

Zhu, Y. N., Cao, L., Tang, G., and Zhou, Z. (2015). Homogenization of surface relative humidity over China. *Clim. Change Res.* 11 (6), 379. In Chinese. (with English abstract).

Zscheischler, J., Westra, S., van den Hurk, B. J. J. M., Seneviratne, S. I., Ward, P. J., Pitman, A., et al. (2018). Future climate risk from compound events. *Nat. Clim. Change* 8 (6), 469–477. doi:10.1038/s41558-018-0156-3

frontiers | Frontiers in Environmental Science

TYPE Original Research
PUBLISHED 19 January 2023
DOI 10.3389/fenvs.2023.1117443

OPEN ACCESS

EDITED BY
Zhen Liu,
Institute for Basic Science, Republic of Korea

REVIEWED BY
Weilin Liao,
Sun Yat-sen University, China
Yong Xu,
Guangzhou University, China

*CORRESPONDENCE
Meiyu Guo,
meiyuguo@hkbu.edu.hk

SPECIALTY SECTION
This article was submitted to Interdisciplinary Climate Studies, a section of the journal Frontiers in Environmental Science

RECEIVED 06 December 2022
ACCEPTED 06 January 2023
PUBLISHED 19 January 2023

CITATION
Lin L and Guo M (2023), Effects of urbanization on multiple human perceived temperatures in South China.
Front. Environ. Sci. 11:1117443.
doi: 10.3389/fenvs.2023.1117443

Effects of urbanization on multiple human perceived temperatures in South China

Lijie Lin[1] and Meiyu Guo[2]*

[1]School of Management, Guangdong University of Technology, Guangzhou, China, [2]Department of Geography, Hong Kong Baptist University, Kowloon, Hong Kong SAR, China

Under the combined effects of global warming and local human activities such as urbanization, increasing populations are exposed to the threat of extreme heat events. While the effects of regional urbanization on the changes in air temperature and its extremes have been well studied, the effects on mean and extreme human perceived temperatures (HPT) are still to be explored. Based on a dynamic meteorological station classification approach, this study quantitatively assessed the impacts and relative contribution of urbanization on the mean and extreme human perceived temperatures in South China by analyzing ten different human perceived temperatures indicators and taking Guangdong Province as an example. It was found that for all human perceived temperatures indicators, the mean human perceived temperatures and the frequency of extreme human perceived temperatures events in South China notably increased from 1971 to 2020, especially in the regions with comparatively higher levels of local urbanization (*e.g.*, the Pearl River Delta). Urbanization contributed significantly to the long-term changes in both mean and extreme human perceived temperatures in Guangdong. On average, the relative contributions of urbanization to the total increases in mean human perceived temperatures and the frequency of extreme human perceived temperatures events were 15.5% and 15.1%, respectively. These contributions vary across different human perceived temperatures indicators, and the urbanization contributions to the human perceived temperatures indicators that consider the combined effects of wind speed were even higher than those merely related to near-surface air temperature and humidity. Among different seasons, the contributions of urbanization to mean and extreme human perceived temperatures in both fall and winter were greater than that in spring and summer. The findings reported here provide scientific advice for governments' policy-making and adaption for human-perceived thermal comfort in subtropical humid climate zones.

KEYWORDS

urbanization effects, extreme weather events, South China, compound heat-humidity extremes, human perceived temperature

1 Introduction

In the context of global climate change, air temperatures have been increasing and will continue to rise worldwide, with posing impacts on human society and the ecological environment (Sun et al., 2014; Mishra et al., 2015; Hua et al., 2021; IPCC, 2021; Tuholske et al., 2021; Wang and Yan, 2021). Accordingly, extreme heat events are becoming more frequent and intense and will exhibit a significant increase tendency in the near future (Liu et al., 2018; Perkins-Kirkpatrick and Lewis, 2020; Ning et al., 2022). With rapid economic growth and urbanization since the reform and opening up, China has become one of the most vulnerable and sensitive regions suffering from extreme heat (Lin et al., 2020; Wang et al., 2021a; Luo and

Lau, 2021; Tian et al., 2021). The increasing risk of high temperature has been a growing threat to China's social environment and ecosystem over the past half-century (Chen and Zhai, 2017; You et al., 2017).

Land use changes together with the anthropogenic release of greenhouse gases and heat during the process of urbanization have contributed to increasing the occurrence of extreme heat events in Guangdong, especially in the Pearl River Delta (PRD) (Hao et al., 2018; Lin et al., 2020). People living in urban areas are exposed to both global warming and urbanization effects, such as the Urban Heat Island (UHI), which intensifies the risk of urban residents to heat events (Oke, 1973; Oke, 1982; Kim, 1992; Li et al., 2019). Additionally, the low albedo of the urban subsurface leads to increased absorption of short-wave radiation, creating a heating effect on urban areas. Also, urban buildings increase surface roughness and frictional resistance, thus leading to lower surface wind speeds and inhibiting heat exchange at the air-land interface. The slowed wind speed hinders the exchange of

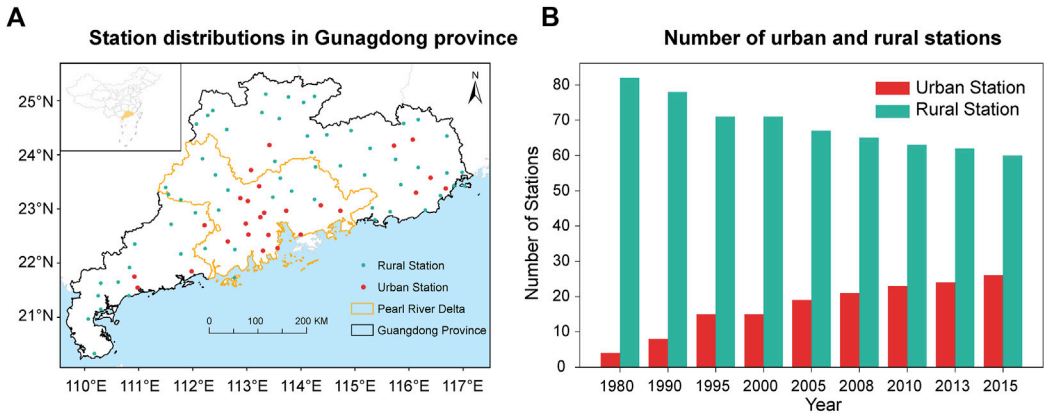

FIGURE 1
Spatial distribution and classification of urban and rural meteorological stations in Guangdong Province. **(A)** Spatial distribution of 86 meteorological stations in Guangdong Province, with red and cyan dots representing urban and rural stations in 2015, respectively; **(B)** Changes in urban and rural stations from 1980 to 2015, with red and cyan representing the number of urban and rural stations, respectively.

TABLE 1 Summary of multiple human perceived temperature (HPT) indicators in this study.

Indicators	Full name	Equation	Reference
AT_{in}	Apparent Temperature (indoors)	$AT_{in} = -1.3 + 0.92 \times T + 2.2 \times E_a$	Steadman (1979)
AT_{out}	Apparent Temperature (outdoors, in the shade)	$AT_{out} = -2.7 + 1.04 \times T + 2 \times E_a - 0.65 \times V$	
DI	Discomfort Index	$DI = 0.5 \times WBT + 0.5 \times T$	Epstein and Moran (2006)
ET	Effective Index	$ET = T - 0.4 \times (T - 10) \times (1 - 0.001 \times RH)$	Gagge et al. (1972)
HI	Heat Index	$HI = -8.784695 + 1.61139411 \times T - 2.338549 \times RH - 0.14611605 \times T \times RH - 1.2308094 \times 10^{-2} \times T^2$ $-1.6424828 \times 10^{-2} \times RH^2 + 2.211732 \times 10^{-3} \times T^2 \times RH + 7.2546 \times 10^{-4} \times T \times RH^2 + 3.582 \times 10^{-6} \times T^2 \times RH^2$	Rothfusz (1990)
HMI	Humidex	$HMI = T + 0.5555 \times (0.1 \times E_a - 10)$	Masterton et al. (1979)
MDI	Modified Discomfort Index	$MDI = 0.75 \times WBT + 0.38 \times T$	Moran et al. (1998)
sWBGT	Simplified Wet Bulb Temperature	$sWBGT = 0.567 \times T + 0.0393 \times E_a + 3.94$	Willett and Sherwood (2012)
NET	Net Effective Temperature	$NET = 37 - \frac{37-T}{0.68-0.0014 \times RH + \frac{1}{1.76+1.4 \times V^{0.75}}} - 0.29 \times T \times (1 - 0.01 \times RH)$	Houghton and Yaglou (1923)
WCT	Wind Chill Temperature	$WCT = 13.12 + 0.6215 \times T - 11.37 \times (V \times 3.6)^{0.16} + 0.3965 \times T \times (V \times 3.6)^{0.16}$	Osczevski and Bluestein (2005)

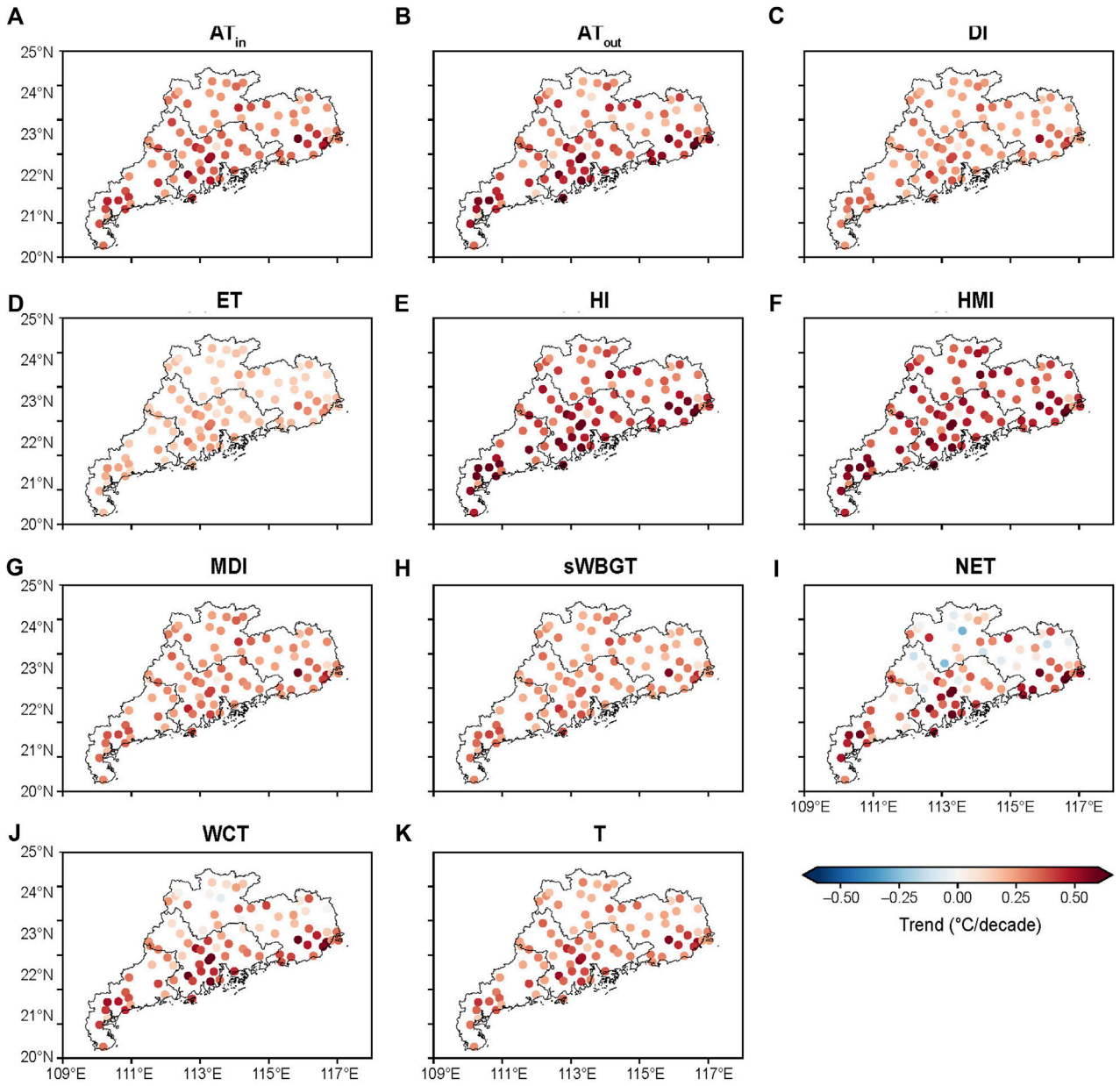

FIGURE 2
Spatial distribution of the long-term trends in annual mean HPT and actual air temperature (T) in Guangdong from 1971 to 2020: **(A)** AT_{in}, **(B)** AT_{out}, **(C)** DI, **(D)** ET, **(E)** HI, **(F)** HMI, **(G)** MDI, **(H)** sWBGT, **(I)** NET, **(J)** WCT, and **(K)** T.

heat and air emitted from the human surface, making the temperature felt by the human body higher (Wang et al., 2021b).

Compared with extensive studies on surface temperature or near-surface temperature warming, fewer studies have focused on the effects of rapid urbanization on the changes in human perceived temperature (HPT) (Liu et al., 2018; Wang et al., 2021b; Luo and Lau, 2021), which describes the joint influences of multiple surrounding atmospheric factors, including air temperature, relative humidity, and wind speed, *etc.* HPT is a bio-meteorological indicator that measures human comfort in different environments from a meteorological perspective based on the heat exchange between the human organism and the surrounding environment. It plays an important role in urban environmental meteorological services. However, there is still no universally accepted or unified indicator of HPT currently (Blazejczyk et al., 2012; Li et al., 2018; Zhang et al., 2022). On the one hand, previous studies on extreme high temperatures mainly focused on near-surface air temperature, such as daily maximum and minimum temperatures, yet few considered the combined effects of multiple environmental factors on HPT (Liu et al., 2018; Wang et al., 2021b). On the other hand, previous studies mostly focused on a single indicator of HPT, but there was a scarcity of cross-sectional comparisons of HPT defined by multiple methods.

With more and more people moving to urban areas, the world's urbanization level has climbed from 36.6% in 1970% to 56.6% in 2021. It is projected to reach 60.4% in 2030 (United Nations Department of Economic Social Affairs, 2018). As the largest provincial economy in China, Guangdong Province has a high urbanization level of 74.63%. The high level of industrialization and urbanization attracts a large

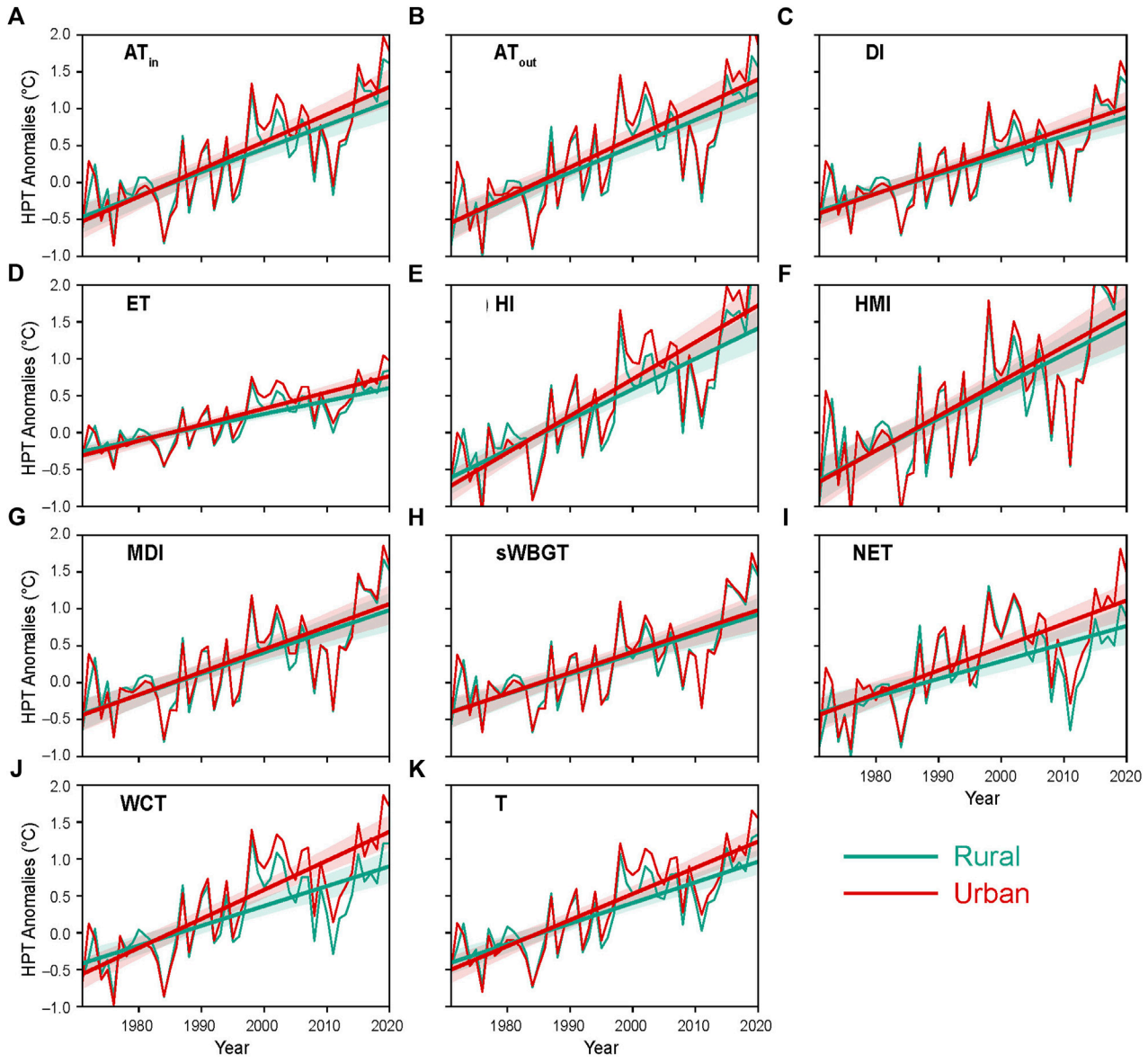

FIGURE 3
Temporal changes of the annual mean of HPT and T in the urban (red) and rural (cyan) areas of Guangdong from 1971 to 2020: **(A)** AT_{in}, **(B)** AT_{out}, **(C)** DI, **(D)** ET, **(E)** HI, **(F)** HMI, **(G)** MDI, **(H)** sWBGT, **(I)** NET, **(J)** WCT, and **(K)** T. The red and cyan straight lines indicate the linear trends of urban and rural mean series, respectively, with the shading denoting their corresponding 95% confidence intervals.

number of labor force extremely concentrated in Guangdong. However, it is still unclear whether and to what extent regional urbanization affects the long-term changes in HPT in Guangdong and its extremes as defined by multiple indicators. It is also unclear whether the distinctions exist in the effects of urbanization on various definitions of HPT under global warming. Therefore, it is of great significance to examine the changes in multiple HPT indicators and their extremes to understand regional climate change with urbanization effects comprehensively.

This study aims to examine the spatial and temporal changes in HPT based on multiple definitions and their extremes in South China from 1971 to 2020 by taking Guangdong Province as an example, and to quantitatively assess the effect of urbanization on the long-term changes of mean and extreme HPT. Exploring the risk of increasing HPT and its extremes under global warming and regional urbanization has great implications for governmental decision-makers and urban planners in mitigating extreme weather events and severe thermal conditions.

2 Data and methods

2.1 Study area

In southern China, Guangdong Province is characterized by a subtropical monsoon climate with long, hot, and humid summers and relatively short and cool winters. Although Guangdong accounts for only 1.87% of the country's land area, it holds the largest provincial economy in

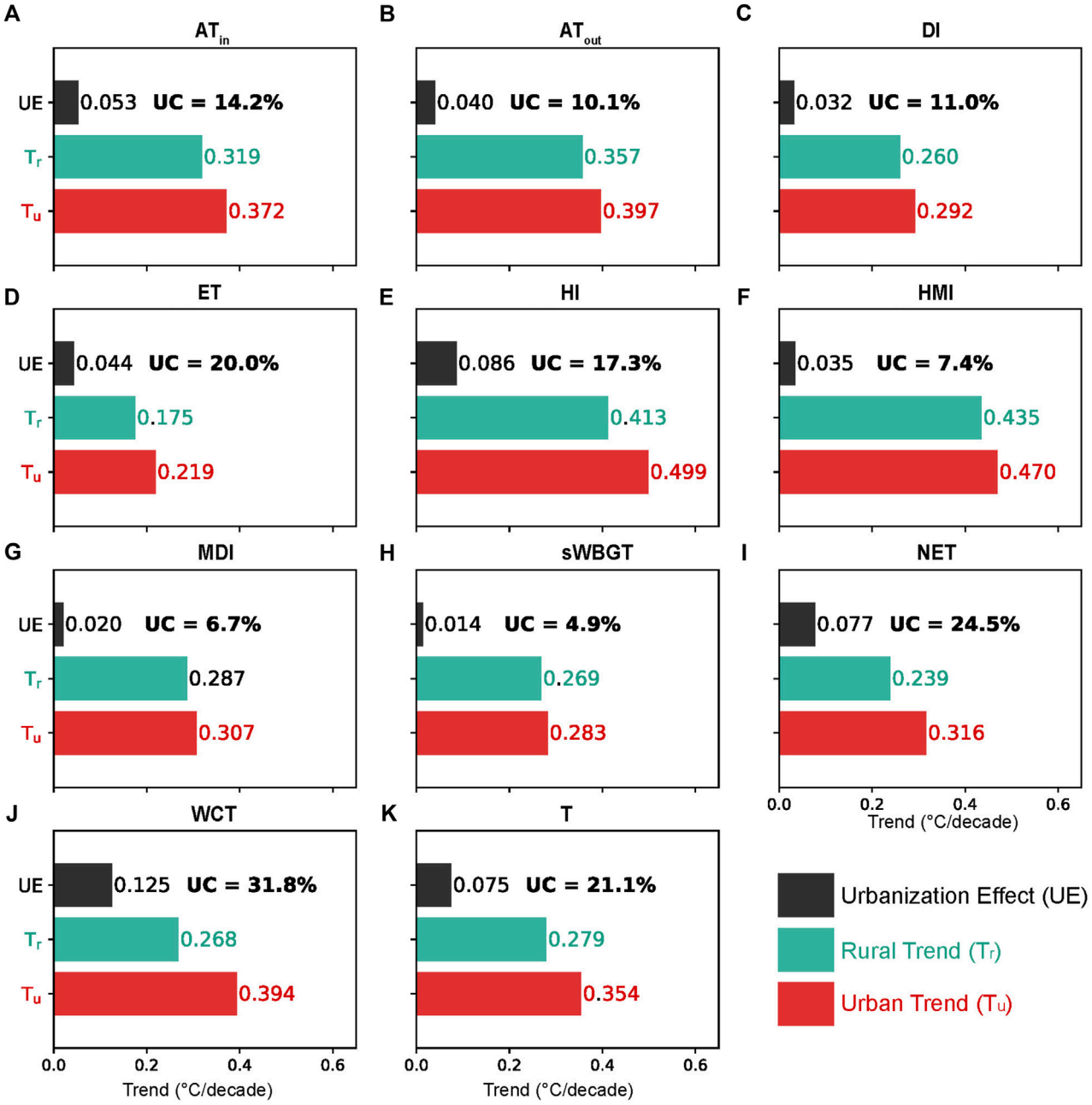

FIGURE 4
Long-term trends in urban (red) and rural (cyan) means of HPT and T in Guangdong from 1971 to 2020 and their urbanization effects (black): **(A)** AT_{in}, **(B)** AT_{out}, **(C)** DI, **(D)** ET, **(E)** HI, **(F)** HMI, **(G)** MDI, **(H)** sWBGT, **(I)** NET, **(J)** WCT, and **(K)** T. The percentage number in black color indicates the corresponding relative urbanization contribution (UC).

China, contributing 10.87% of its Gross Domestic Product (GDP). In 2021, the resident population in Guangdong reached 126.84 million, accounting for 8.23% of the country's total population. The urbanization level in Guangdong reached 74.6% in 2021, notably 87.5% in the PRD in central Guangdong. PRD gathers 53.35% of the total population of the whole province but with less than one-third of the provincial land area (National Bureau of Statistics of China, 2020; Statistics Bureau of Guangdong Province, 2020). As one of the most highly urbanized and populated provinces in China, Guangdong Province has been experiencing pronounced regional climate change extremes, resulting in severe impacts on the local human social and economic development (Luo and Lau, 2017; Lin et al., 2020).

2.2 Classification of urban and rural sites

In this study, meteorological observations were collected from the China Meteorological Data Service Center (http://data.cma.cn/). The data have been homogenized, homogeneity-checked, and widely used in climate change studies (Xu et al., 2013). To ensure time

TABLE 2 Long-term trends in seasonal mean HPT in Guangdong from 1971 to 2020 and their urbanization effects and contributions. It includes the average urban trend (T_u, °C/10a), average rural trend (T_r, °C/10a), urbanization effect (UE, °C/10a), and urbanization contribution (UC, %), and the HPT_{mean} column indicates the mean value by averaging all HPT indicators (by excluding T). All trends are significant at the 0.05 level, as evaluated by the modified non-parametric Mann-Kendall trend test.

Season		AT_{in}	AT_{out}	DI	ET	HI	HMI	MDI	sWBGT	NET	WCT	T	HPT_{mean}
Spring	T_u	0.3	0.33	0.23	0.18	0.39	0.37	0.24	0.22	0.27	0.3	0.33	0.28
	T_r	0.26	0.3	0.21	0.15	0.32	0.35	0.22	0.21	0.19	0.26	0.3	0.25
	UE	0.04	0.03	0.02	0.03	0.07	0.02	0.01	0.01	0.08	0.04	0.03	0.04
	UC	12.4	10.1	9	17.9	17.7	5.6	4.4	3.2	28.9	34.1	18.9	14.3
Summer	T_u	0.3	0.3	0.22	0.17	0.58	0.4	0.23	0.24	0.23	0.32	0.27	0.30
	T_r	0.26	0.28	0.19	0.13	0.49	0.38	0.21	0.24	0.19	0.23	0.2	0.26
	UE	0.05	0.02	0.03	0.04	0.09	0.02	0.01	0	0.04	0.09	0.07	0.04
	UC	15	8	12.4	24	16.2	5.1	6.4	1.8	17.2	28.6	25.8	13.5
Autumn	T_u	0.49	0.52	0.39	0.29	0.62	0.63	0.41	0.38	0.42	0.53	0.47	0.47
	T_r	0.41	0.46	0.34	0.23	0.5	0.57	0.38	0.35	0.33	0.38	0.36	0.4
	UE	0.08	0.06	0.05	0.06	0.13	0.06	0.04	0.03	0.09	0.15	0.11	0.08
	UC	16.1	11.6	12.9	21.8	20.6	9.4	8.7	7.1	21.1	28.6	22.9	15.8
Winter	T_u	0.43	0.47	0.36	0.26	0.44	0.54	0.39	0.32	0.39	0.44	0.42	0.4
	T_r	0.34	0.39	0.3	0.2	0.35	0.45	0.33	0.27	0.25	0.25	0.32	0.31
	UE	0.09	0.08	0.06	0.06	0.09	0.09	0.06	0.05	0.14	0.18	0.1	0.09
	UC	20	17.5	16.7	22.8	20.8	16.8	14.2	15.7	36.3	42	23.2	22.3

continuity and data completeness, a total of 86 meteorological observations in Guangdong from 1971 to 2020 were selected (Figure 1A).

To classify urban and rural stations and then further quantify the urbanization effects on HTP changes, land use change data were obtained from the Resources and Environmental Science Data Center, the Chinese Academy of Sciences (http://www.resdc.cn/). This dataset contains the land use information of China in nine individual years (i.e., 1980, 1990, 1995, 2000, 2005, 2008, 2010, 2013, and 2015) at a horizontal resolution of 30 m. As suggested by previous studies (Yang et al., 2017; Luo and Lau, 2019; Tong et al., 2022), a circular buffer zone with a radius of 7 km was first established at the center of each station, and then the built-up area fraction (BAF) within each buffer zone was calculated. A larger value of BAF indicates a higher level of urbanization around the station and *vice versa*. A station is considered as an urban type only if its BAF within the buffer zone of the site is greater than 20%, and *vice versa* for a rural station (Yang et al., 2017; Luo and Lau, 2019; Tong et al., 2022). Figure 1A maps the spatial distribution of urban and rural sites in Guangdong in 2015, showing that urban stations in Guangdong are mainly distributed within the PRD region and the Chaozhou-Shantou region, suggesting the high level of urbanization in these regions. Rural stations are mainly distributed in the mountainous areas of northern Guangdong. Figure 1B depicts the time-varying classification of urban sites and rural stations from 1980 to 2015, and shows that a large number of rural stations have been transformed into urban types during the process of urbanization since the 1970s.

2.3 Definition of HPT indicators

To ensure a comprehensive investigation, we compared the HPT changes based on ten different definitions in this study. As listed in Table 1, most of these HPT indicators are calculated from temperature (T, unit: °C) and relative humidity (RH, unit: %) or water vapor pressure (Ea), and outdoor apparent temperature (AT_{out}), net effective temperature (NET) and wind chill temperature (WCT) consider the additional effect of wind velocity (V, unit: m/s). In this study, we first calculated daily HPT values from daily T, RH, and V values, and then aggregated daily HPT to monthly means.

To exclude the possible influence of the absolute HPT magnitudes in different subregions of Guangdong, we examined the HPT anomalies in this study. The yearly and seasonal mean HPT anomalies were obtained by averaging the monthly anomalies, which were calculated by subtracting the multi-year climatological mean in the same calendar month of the reference period of 1971–2000 from the original monthly HPT value. For example, the HPT anomalies for January 1971 are equal to the HPT value in January 1971 minus the average of 30 HPT values in 30 Januaries of 1971–2000. In addition to the mean HPT, this paper also explored the long-term changes and effects of extremely high HPT events. An extremely high HPT day was defined as when daily HPT exceeds the 90^{th} quantile of HPT over a 15-day window centering the same calendar day of the reference period (Wang et al., 2019; Wang et al., 2021b).

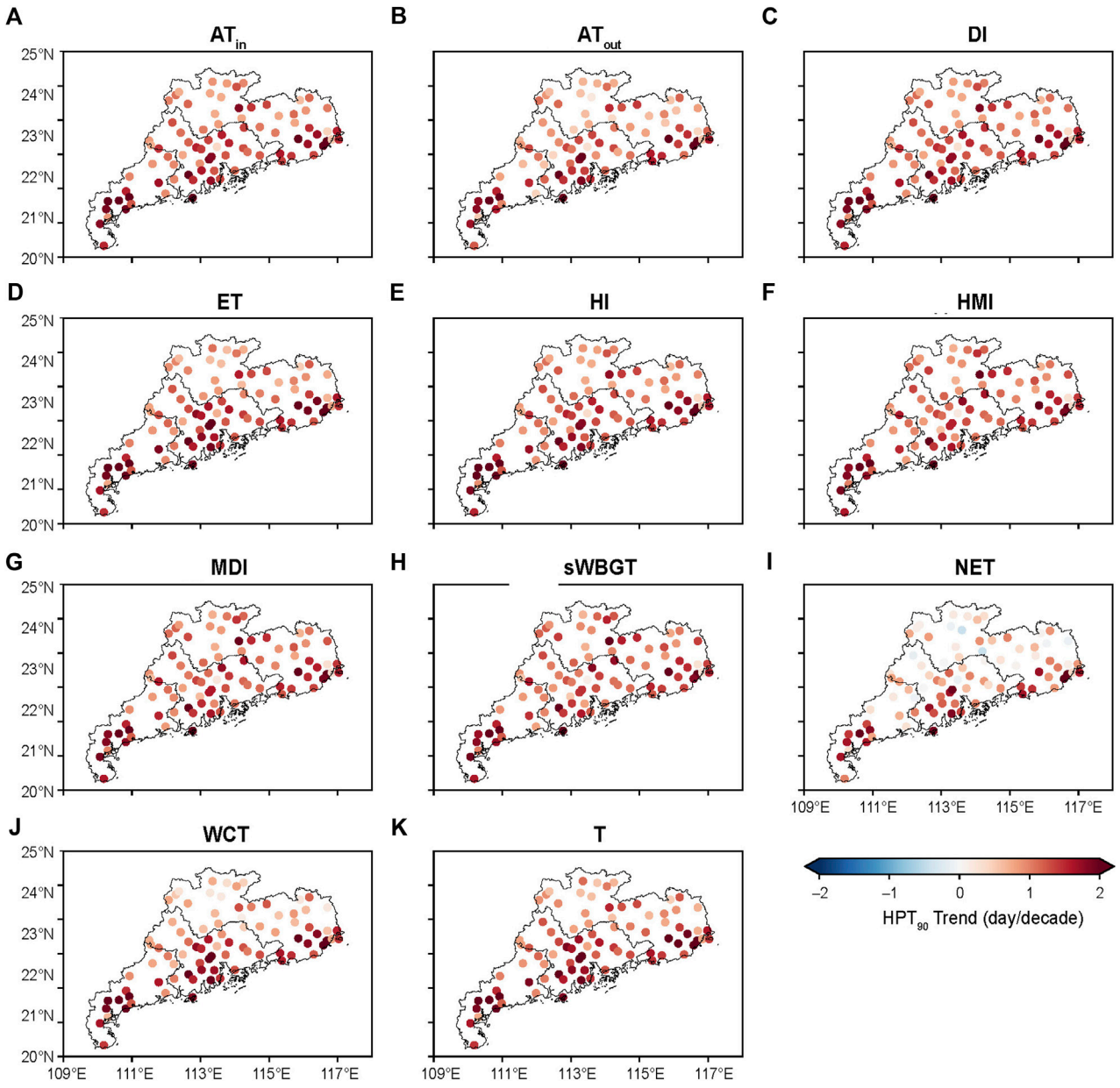

FIGURE 5
Spatial distribution of the long-term trends in annual frequencies of extremely hot HPT and T days in Guangdong from 1971 to 2020: **(A)** AT_{in}, **(B)** AT_{out}, **(C)** DI, **(D)** ET, **(E)** HI, **(F)** HMI, **(G)** MDI, **(H)** sWBGT, **(I)** NET, **(J)** WCT, and **(K)** T.

2.4 Evaluation of urbanization effects

In this study, the urbanization effect (UE) was quantified as the difference in the long-term trends between urban and rural time series of HPT (Ren and Zhou, 2014; Sun et al., 2016; Luo and Lau, 2018): $UE = T_u - T_r$, where T_u and T_r represent the HPT trends in urban and rural areas (by averaging the corresponding urban and rural stations), respectively, over the whole study period of 1971–2020. The relative urbanization contribution (UC) was calculated from *UE* and T_u: $UC = |(T_u - T_r)/T_u| \times 100\%$. Here, the long-term trends were estimated by simple linear regression, and their significance was assessed by a modified non-parametric Mann-Kendall trend test (Hamed and Rao, 1998).

3 Results

3.1 Long-term changes in mean HPT and urbanization effects

Figure 2 shows the spatial distribution of the long-term trend in annual mean HPT based on different definitions from 1971 to 2020. Figures 2A–J represent trends of different HPT indicators in Guangdong Province, and Figure 2K represents the actual air temperature (T) for comparison. As the figure shows, all T and HPT indicators exhibit increasing trends during 1971–2020, and the warming trends of mean HPT and T in the PRD and Chaozhou-Shantou regions are generally stronger than those in

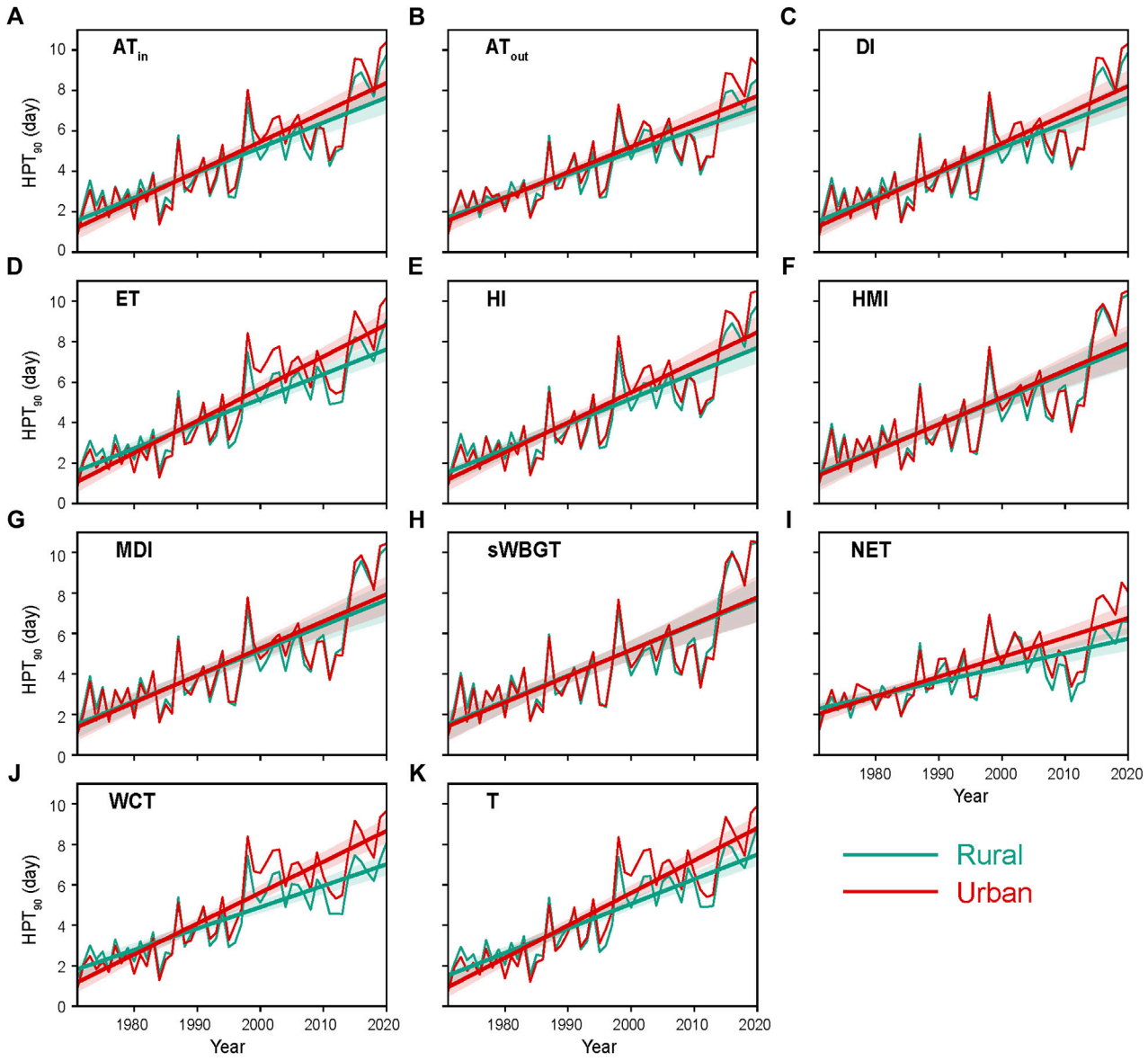

FIGURE 6
Temporal changes in urban (red) and rural (cyan) means frequencies of extremely hot HPT and T days in Guangdong from 1971 to 2020 and their urbanization effects (black): **(A)** AT_{in_90p}, **(B)** AT_{out_90p}, **(C)** DI_{90p}, **(D)** ET_{90p}, **(E)** HI_{90p}, **(F)** HMI_{90p}, **(G)** MDI_{90p}, **(H)** $sWBGT_{90p}$, **(I)** NET_{90p}, **(J)** WCT_{90p}, and **(K)** T_{90p}. The red and cyan straight lines indicate the linear trends of urban and rural mean series, respectively, with the shading denoting their corresponding 95% confidence intervals.

other regions. Among different HPT indicators, HI and HMI have stronger increasing tendencies, while ET and DI exhibit relatively smaller increases. Also, compared with other indicators, NET and WCT that consider the combined effect of wind speed warm even faster, especially in more urbanized areas such as the PRD region. Rural areas such as northern Guangdong experienced a relatively slower warming trend in all temperature indicators. These differences suggest that urbanization may have a greater effect on wind speed-related HPT, such as NET and WCT, than other HPT indicators.

Figure 3 shows the temporal changes of annual mean HPT and T in urban and rural areas of Guangdong. All temperature indicators in both rural and urban areas show significant increasing trends since the 1970s. Interestingly, the magnitudes of the increasing HPT trend in urban areas are stronger than those in rural areas, demonstrating a prominent urbanization effects on increasing temperature, either for actual air temperature or human perceived ones. Comparatively, the increasing tendencies and fluctuation of HI, HMI, and NET were much stronger than other temperature indicators, and that of ET and DI were much weaker. The differences between urban and rural series are also larger in HI, HMI, and NET.

The magnitudes of the long-term trend of annual mean of multiple HPTs and T from 1971 to 2020, as well as the effect and contribution of urbanization on these trends, are depicted in Figure 4. In urban areas, HI exhibits the largest increase of 0.499°C/10a, while ET receives the smallest increase of 0.219°C/10a. In rural areas, HMI has the largest increasing trend of 0.435°C/10a, and ET gets the smallest increase of 0.175°C/10a. Clearly, both urban and rural temperatures show

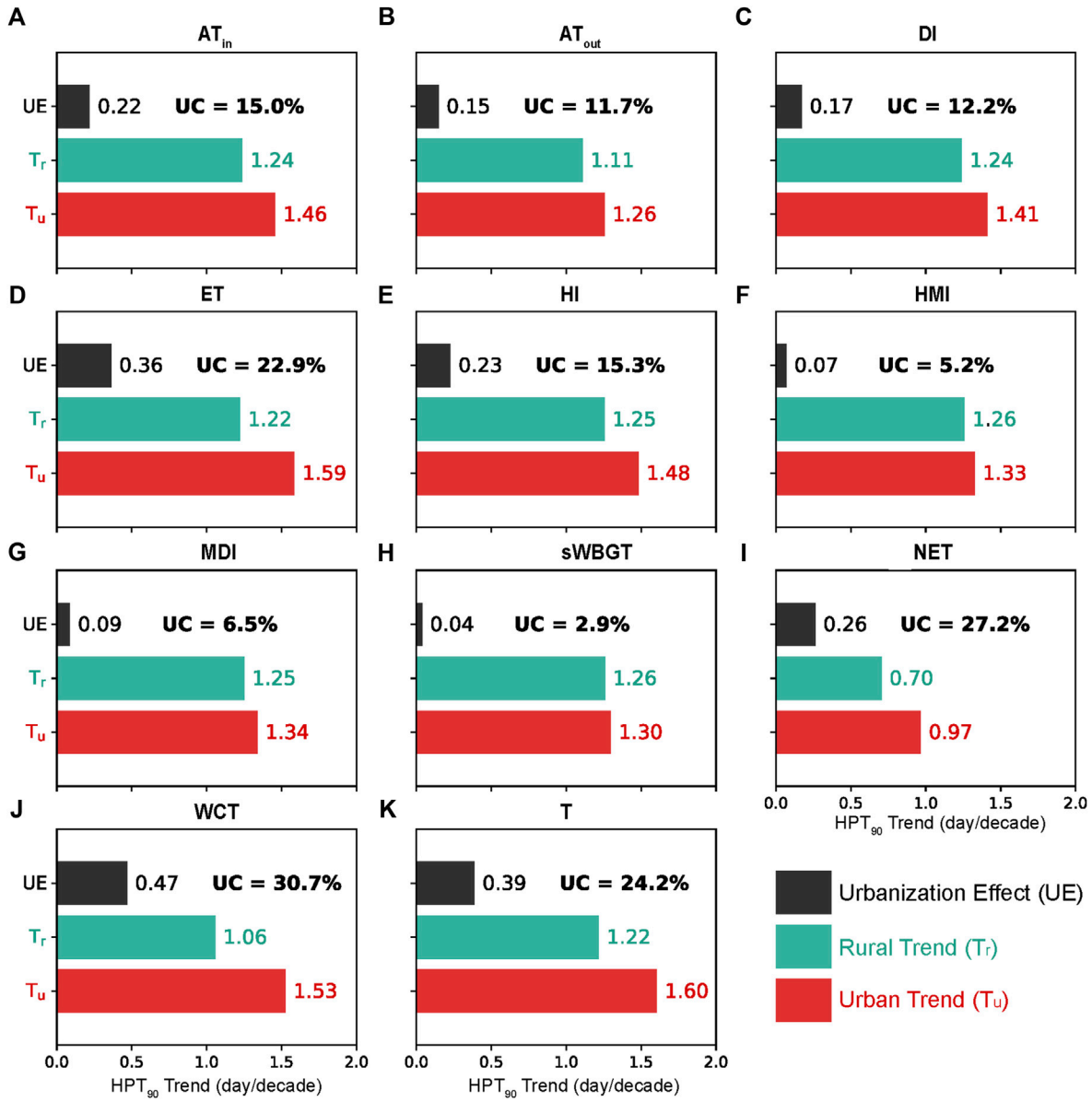

FIGURE 7
Long-term trends in urban (red) and rural (cyan) means of the annual frequency of extreme HPT and T days in Guangdong from 1971 to 2020 and their urbanization effects (black): **(A)** AT_{in_90p}, **(B)** AT_{out_90p}, **(C)** DI_{90p}, **(D)** ET_{90p}, **(E)** HI_{90p}, **(F)** HMI_{90p}, **(G)** MDI_{90p}, **(H)** $sWBGT_{90p}$, **(I)** NET_{90p}, **(J)** WCT_{90p}, and **(K)** T_{90p}. The percentage number in black color indicates the corresponding relative urbanization contribution (UC).

growing trends, and the growth is even higher in urban than rural areas. This difference characterizes the significant effects of local urbanization, which exists in all temperature indicators.

By averaging the relative urbanization contributions for all HPT indicates, it is estimated that regional urbanization contributed to 15.5% of the total increases in HPT since the 1970s. It is also noted that various HPT indicators receive different urbanization effects and relative contributions. For example, urbanization effects contributed to 31.8% of the total increase in WCT, while it contributed to only 4.9% of the rise in sWBGT. Also, urbanization induced a relatively larger contribution to the increases in NET by 24.5% (0.077°C/10a), which is higher than that to air temperature (0.075°C/10a, 21.1%). The larger contributions to WCT and NET are due to the fact that both indicators consider the combined effects of wind velocity, which is often slowed down by the increases in surface roughness caused by the presence of built-ups in urban areas. In particular, the higher roughness of the sub-bedding surface of the urban areas and the higher friction have a deceleration effect on wind speed; and the higher density of buildings in urban areas forms a natural baffle, which has a hindering and gridding effect on wind speed (Xu et al., 2017; Li et al., 2019; Moon et al., 2020). Note that wind speed can accelerate the airflow around the human body, speeding up the heat exchange between the human body surface and the air to play a cooling effect (Edwards et al., 2015; Roshan et al., 2020), so the wind speed in urban areas is reduced due to the impact of urbanization, which in turn leads to a higher local body temperature than the surrounding areas. The urbanization contribution to other HPT indicators without considering the effect of wind speed is generally smaller than that on air temperature, which may be related to the urban

TABLE 3 As Table 2 but for the frequencies of extreme HPT and T days. All trends are significant at the 0.05 level, as evaluated by the modified non-parametric Mann-Kendall trend test.

Season		AT_{in_90p}	AT_{out_90p}	DI_{90p}	ET_{90p}	HI_{90p}	HMI_{90p}	MDI_{90p}	$sWBGT_{90p}$	NET_{90p}	WCT_{90p}	T_{90p}	HTP_{mean_90p}
Spring	T_u	1	0.98	0.98	1.04	1.03	0.97	0.96	0.96	0.79	1.02	1.06	0.97
	T_r	0.9	0.9	0.91	0.86	0.88	0.94	0.95	0.95	0.59	0.76	0.85	0.86
	UE	0.11	0.08	0.07	0.18	0.15	0.02	0.01	0.01	0.21	0.26	0.2	0.11
	UC	12.4	10.1	9	17.9	17.7	5.6	4.4	3.2	28.9	34.1	18.9	14.3
Summer	T_u	2.11	1.68	2.11	2.16	2.02	1.98	2.03	1.96	1.42	2.18	2.14	1.97
	T_r	1.82	1.53	1.85	1.66	1.82	1.96	1.93	1.99	1.06	1.64	1.61	1.73
	UE	0.29	0.15	0.26	0.5	0.2	0.03	0.1	−0.04	0.36	0.55	0.52	0.24
	UC	13.9	9	12.1	23.1	10.1	1.3	5	−1.8	25.5	25	24.5	12.3
Autumn	T_u	1.74	1.44	1.64	2.03	1.84	1.48	1.51	1.43	1.04	1.98	2.1	1.61
	T_r	1.48	1.28	1.46	1.55	1.53	1.41	1.42	1.39	0.76	1.36	1.56	1.36
	UE	0.26	0.16	0.18	0.48	0.31	0.07	0.09	0.04	0.27	0.62	0.53	0.25
	UC	15	11.3	11	23.6	16.7	4.4	6.3	2.6	26.3	31.3	25.4	14.9
Winter	T_u	0.98	0.92	0.92	1.11	1.04	0.88	0.85	0.84	0.62	0.92	1.13	0.91
	T_r	0.77	0.73	0.73	0.82	0.79	0.72	0.71	0.71	0.41	0.48	0.84	0.69
	UE	0.22	0.19	0.19	0.29	0.25	0.16	0.14	0.14	0.21	0.45	0.29	0.22
	UC	22.1	21	20.2	26.1	23.9	18.3	16.8	16.3	33.8	48.5	25.9	24.7

dry island (UDI) effect due to urbanization, which may reduce the atmospheric humidity and thus offsetting the HPT increases to some extent (Hao et al., 2018; Luo and Lau, 2019; Huang et al., 2022; Wang et al., 2022).

Table 2 summarizes the mean urban trend (T^u), rural trend (T_r), urbanization effect (UE), and urbanization contribution (UC) of the HPT under different seasons by averaging all HPT indicators. In this study, spring refers to March, April, and May, summer includes June, July, and August, autumn comprises September, October, and November, and winter includes December, January, and February. The HPT trend in both urban and rural areas was significantly greater than zero in all four seasons, indicating a significant increasing trend in four seasons. In all four seasons, the increases in mean HPT in urban areas were again greater than in rural areas. Seasonally, the increases in mean HPT in both urban and rural areas in the fall and winter were greater than in the spring and summer. The largest gains in both urban (0.47°C/10a) and rural mean HPT (0.39°C/10a) were observed in autumn, and the smallest increases were observed in spring, i.e., 0.29°C/10a and 0.24°C/10a for urban and rural series, respectively. Among different HPT indicators, the fastest increases in mean HPT in both urban and rural were observed in HI and HMI in all seasons, i.e., 0.62°C/10a and 0.63°C/10a for HI and HMI, respectively.

Urbanization has a significant effect on mean HPT changes in all four seasons, with the magnitudes of 0.04°C/10a, 0.04°C/10a, 0.08°C/10a, and 0.09°C/10a and the corresponding relative contributions of 14.3%, 13.5%, 15.8%, and 22.3%, for spring, summer, autumn, and winter, respectively. It can be seen that the effects and contributions of urbanization on HPT in autumn and winter were greater than those in spring and summer. Among them, the impacts and contributions of urbanization on wind speed-related HPT indicators (i.e., NET and WCT) are higher in the spring and winter seasons than the air temperature T. The UE and UC values for WCT in all seasons are higher than in T. In spring, summer, and fall, sWBGT tends to receive the smallest relative contribution of urbanization (i.e., 3.2%, 1.8%, 7.1%, respectively), compared with other HPT indicators, whereas, in the winter season, MDI receives the smallest urbanization effect and contribution.

3.2 Long-term changes in extreme HPT and the effects of urbanization

Compared with mean HPT, extreme HPT poses even greater threats to the human body (Wang et al., 2019; Wang et al., 2021b). This subsection defines an extremely hot HPT day (HPT_{90p}) when the daily HPT value exceeds the 90% quantile of the reference period (recall Section 2). Figure 5 shows the spatial distribution of the long-term trend of the annual occurrence frequency of HPT_{90p} in Guangdong Province from 1971 to 2020. It is observed in Figure 5 that the annual frequency of extremely hot days in Guangdong Province exhibited an increasing trend over the past 5 decades, and such an increase appears in all temperature indicators (including both HPT and T). Spatially, the growing frequency of HPT_{90p} in the coastal areas (especially in densely populated and highly urbanized regions such as the Pearl River Delta and Chaozhou-Shantou) was higher than in the northern regions of mountainous Guangdong. This regional disparity indicates that urbanization may be one of the inducing factors for increasing the occurrence of HPT_{90p}. Figure 6 shows the long-term changes in the average annual frequencies of HPT_{90p} and T_{90p} in both urban and rural areas of Guangdong Province. Overall, the average annual HPT_{90p} and T_{90p} in both rural and urban areas showed a fluctuating but upward trend, and the increases in urban areas (including both HPT_{90p} and T_{90p}) were greater than those in rural areas, proving that the urbanization effect contributed to the occurrence of both HPT_{90p} and T_{90p}.

Figure 7 shows the quantitative trends of the average frequency of HPT_{90p} and T_{90} in urban and rural areas of Guangdong. The frequency trend of HPT_{90p} in urban and rural areas exceeded 1.0 days/10a for all HPT indicators except for NET. On average, the frequencies of HPT_{90p} were 1.37 days/10a in urban areas and 1.16 days/10a in rural areas. This difference measures an urbanization effect of 0.21 days/10a, and the relative contribution of urbanization was 15.1%. Among different indicators in urban areas, the largest increase is seen in extreme ET (1.59 days/10a), while the smallest increase is in extreme NET (0.97 days/10a). In rural areas, the largest increases are observed in extreme HMI and sWBGT (both at 1.26 days/10a), and the smallest increase is still in extreme NET (0.7 days/10a). The largest urbanization contribution to the change of HPT_{90p} was WCT (30.7%), while the smallest contribution was in sWBGT (2.9%). Notably, the relative contribution of urbanization to the HPT_{90p} changes in both NET and WCT is higher than the relative contribution made by the T_{90p} changes.

Table 3 summarizes the quantitative long-term trends of urbanization contribution to HPT_{90p} in Guangdong in different seasons. It is seen that the trends of the frequencies of HPT_{90p} in both urban and rural areas are greater than 0 in all four seasons, indicating increasing risks of HPT_{90p} throughout the calendar year. As expected, the increases in HPT_{90p} in urban areas are even stronger than those in rural areas in all four seasons, demonstrating the remarkable role of urbanization in intensifying HPT_{90p} risks. Seasonally, the increases in HPT_{90p} in urban and rural areas are greater in summer and autumn than in spring and winter. On average, the summer season experienced the largest increase of HPT_{90p} in urban (1.97 days/10a) and rural areas (1.73 days/10a), and winter witnessed the smallest increase, i.e., 0.91 days/10a and 0.69 days/10 for urban and rural areas, respectively. Urbanization had posed significant effects on increasing HPT_{90p} in all four seasons, with the exception of extreme sWBGT days in the summer season.

Regarding the relative contribution of urbanization, by averaging all HPT_{90p} indicators, the HPT_{90p} frequency in the winter (24.7%) and autumn (14.9%) and seasons receive a larger relative urbanization contribution than spring (14.3%) and summer (12.3%). Similarly, the contribution of urbanization to the frequency of extreme events based on wind speed-related HTP indicators (i.e., NET and WCT) is notably higher than that of other HPT indicators with the consideration of wind. Among all HPT indicators, the HPT_{90p} based on sWBGT receives the smallest contribution of urbanization in all four seasons.

4 Conclusion and discussion

Over the past half-century, China has experienced rapid urbanization, which has brought about significant changes in urban structure and land use (Fang, 2015). These changes have exerted profound effects on local a regional climate change in terms of increasing temperature and extreme heat events (Sun et al., 2014; Sun et al., 2016). However, fewer studies have fully delved into the extent to which urbanization affects human perceived temperature changes (HPT), especially the comparison of multiple HPT indicators is not yet clear. Hence, this study explored the long-term changes in mean and extreme HPT based on ten different HPT indicators in South China from 1971 to 2020 by taking Guangdong Province as an example, and further quantitatively assessed the impact of urbanization on long-term changes in mean HPT and extreme HPT on the basis of a dynamic classification of urban and rural weather stations.

The analysis results show that the mean HPT and extreme HPT (i.e., HPT_{90p}) in Guangdong have increased significantly, with higher increases in more urbanized and populated regions such as the Pearl River Delta and Chaozhou-Shantou region. The increasing trends in annual mean HPT based on HI and HMI are ~0.5°C/10a, which is much higher than the warming trend of air temperature (0.354°C/10a). Seasonally, the average increase in HPT was higher in autumn and winter than in spring and summer for both urban and rural areas. In contrast, the increasing trend of HPT_{90p} was greater in summer and autumn than in spring and winter. Urbanization contributed significantly to the long-term changes in both mean HPT and HPT_{90p}. On average, urbanization contributed to 15.5% of the increase in annual mean HPT and 15.1% of the rise in the HPT_{90p} frequency. In addition, the relative contributions of urbanization to both mean HPT and HPT_{90p} were larger in fall and winter than in spring and summer. Specifically, the urbanization contributions to HPT and HPT_{90p} exceeded 20% in winter.

We also noted that the contribution of urbanization to wind speed-related HPT indicators (for both mean HPT and HPT_{90p}), such as NET and WCT exceeds the contribution to air temperature. In contrast, the contribution to the other indicators is smaller than that to air temperature. The possible reasons are discussed as follows. Firstly, the UDI effect offsets the role of increasing air temperature in increasing HPT, thus leading to a lower contribution of urbanization to HPT than to air temperature. Secondly, the high wind resistance caused by the higher roughness of urban areas and the natural blocking effect of tall urban buildings lead to a significant decrease in wind speed in urban areas compared to the surrounding areas, which consequently leads to a rise in heat sensation in urban areas, thus leading to a stronger urbanization contribution to wind speed relative HPT indicators.

Our examinations of the spatio-temporal changes in multiple HPT indicators and their extremes, and the urbanization effects on these changes are based on the observations recorded at 86 weather stations across Guangdong. We also discussed possible reasons for these changes. It should be acknowledged that further investigations based on regional climate model simulations are also of interest and significance. Such examinations help reveal the underlying mechanism of urbanization effects on various meteorological parameters, and warrant further investigations in the future.

Data availability statement

The original contributions presented in the study are included in the article/Supplementary Material, further inquiries can be directed to the corresponding author.

Author contributions

LL and MG designed the research; LL carried out the analyses and wrote the first draft of the paper; all co-authors interpreted the results and edited the paper.

Funding

This research is supported by the Guangdong Basic and Applied Basic Research Foundation (2019A1515011025) and the National Natural Science Foundation of China (42001148).

Acknowledgments

The authors are thankful to Peng Wang for collecting and preparing the data used in this research. The authors are also thankful to two reviewers who provided helpful comments on an earlier version of the paper.

Conflict of interest

The authors declare that the research was conducted in the absence of any commercial or financial relationships that could be construed as a potential conflict of interest.

Publisher's note

All claims expressed in this article are solely those of the authors and do not necessarily represent those of their affiliated organizations, or those of the publisher, the editors and the reviewers. Any product that may be evaluated in this article, or claim that may be made by its manufacturer, is not guaranteed or endorsed by the publisher.

References

Blazejczyk, K., Epstein, Y., Jendritzky, G., Staiger, H., and Tinz, B. (2012). Comparison of UTCI to selected thermal indices. *Int. J. Biometeor.* 56, 515–535. doi:10.1007/s00484-011-0453-2

Chen, Y., and Zhai, P. (2017). Revisiting summertime hot extremes in China during 1961-2015: Overlooked compound extremes and significant changes. *Geophys. Res. Lett.* 44, 5096–5103. doi:10.1002/2016gl072281

Edwards, N. M., Myer, G. D., Kalkwarf, H. J., Woo, J. G., Khoury, P. R., Hewett, T. E., et al. (2015). Outdoor temperature, precipitation, and wind speed affect physical activity levels in children: A longitudinal cohort study. *J. Phys. Act. Health* 12, 1074–1081. doi:10.1123/jpah.2014-0125

Epstein, Y., and Moran, D. (2006). Thermal comfort and the heat stress indices. *Ind. Health* 44, 388–398. doi:10.2486/indhealth.44.388

Fang, C. (2015). Important progress and future direction of studies on China's urban agglomerations. *J. Geog. Sci.* 25, 1003–1024. doi:10.1007/s11442-015-1216-5

Gagge, A., Stolwijk, J., and Nishi, Y. (1972). An effective temperature scale based on a simple model of human physiological regulatiry response. *Memoirs Fac. Eng. Hokkaido Univ.* 13, 21–36.

Hamed, K. H., and Rao, A. R. (1998). A modified Mann-Kendall trend test for autocorrelated data. *J. Hydro.* 204, 182–196. doi:10.1016/s0022-1694(97)00125-x

Hao, L., Huang, X., Qin, M., Liu, Y., Li, W., and Sun, G. (2018). Ecohydrological processes explain urban dry island effects in a wet region, southern China. *Water Resour. Res.* 54, 6757–6771. doi:10.1029/2018wr023002

Houghton, F. C., and Yaglou, C. P. (1923). Determining equal comfort lines. *J. Am. Soc. Heat. Vent. Engl.* 29, 165–176.

Hua, J., Zhang, X., Ren, C., Shi, Y., and Lee, T.-C. (2021). Spatiotemporal assessment of extreme heat risk for high-density cities: A case study of Hong Kong from 2006 to 2016. *Sustain. Cities Soc.* 64 (2021), 102507. doi:10.1016/j.scs.2020.102507

Huang, X., Hao, L., Sun, G., Yang, Z., Li, W., and Chen, D. (2022). Urbanization aggravates effects of global warming on local atmospheric drying. *Geophys. Res. Lett.* 49 (2022), e2021GL095709. doi:10.1029/2021gl095709

IPCC (2021). *Climate change 2021: The physical science basis. Contribution of working group I to the sixth assessment report of the intergovernmental panel on climate change*. Editor V. P. Masson-Delmotte, A. Zhai, S. L. Pirani, C. Connors, S. Péan, N. Berger, et al. (Cambridge, United Kingdom and New York, NY: Cambridge University Press), *p.* 2391. doi:10.1017/9781009157896

Kim, H. H. (1992). Urban heat island. *Int. J. Remote Sens.* 13, 2319–2336. doi:10.1080/01431169208904271

Li, J., Chen, Y. D., Gan, T. Y., and Lau, N.-C. (2018). Elevated increases in human-perceived temperature under climate warming. *Nat. Clim. Change* 8, 43–47. doi:10.1038/s41558-017-0036-2

Li, D., Liao, W., Rigden, A. J., Liu, X., Wang, D., Malyshev, S., et al. (2019). Urban heat island: Aerodynamics or imperviousness? *Sci. Adv.* 5, eaau4299. doi:10.1126/sciadv.aau4299

Lin, L., Chan, T. O., Ge, E., Wang, X., Zhao, Y., Yang, Y., et al. (2020). Effects of urban land expansion on decreasing atmospheric moisture in Guangdong, South China. *Urban Clim.* 32, 100626. doi:10.1016/j.uclim.2020.100626

Liu, X., Tang, Q., Zhang, X., and Sun, S. (2018). Projected changes in extreme high temperature and heat stress in China. *J. Meteorological Res.* 32, 351–366. doi:10.1007/s13351-018-7120-z

Luo, M., and Lau, N.-C. (2017). Heat waves in southern China: Synoptic behavior, long-term change, and urbanization effects. *J. Clim.* 30, 703–720. doi:10.1175/jcli-d-16-0269.1

Luo, M., and Lau, N. C. (2018). Increasing heat stress in urban areas of eastern China: Acceleration by urbanization. *Geophys. Res. Lett.* 45, 13060–13069. doi:10.1029/2018gl080306

Luo, M., and Lau, N. C. (2019). Urban expansion and drying climate in an urban agglomeration of East China. *Geophys. Res. Lett.* 46, 6868–6877. doi:10.1029/2019gl082736

Luo, M., and Lau, N.-C. (2021). Increasing human-perceived heat stress risks exacerbated by urbanization in China: A comparative study based on multiple metrics. *Earth's Future* 9, e2020EF001848. doi:10.1029/2020ef001848

Masterton, J. M., Service, C. A. E., Richardson, F. A., and Canada, C. E. (1979). *Humidex: A method of quantifying human discomfort due to excessive heat and humidity*. Downsview, Ontario: Environment Canada, Atmospheric Environment.

Mishra, V., Ganguly, A. R., Nijssen, B., and Lettenmaier, D. P. (2015). Changes in observed climate extremes in global urban areas. *Environ. Res. Lett.* 10, 024005. doi:10.1088/1748-9326/10/2/024005

Moon, M., Li, D., Liao, W., Rigden, A. J., and Friedl, M. A. (2020). Modification of surface energy balance during springtime: The relative importance of biophysical and meteorological changes. *Agric. For. Meteorology* 284, 107905. doi:10.1016/j.agrformet.2020.107905

Moran, D., Shapiro, Y., Epstein, Y., Matthew, W., and Pandolf, K. (1998). *A modified discomfort index (MDI) as an alternative to the wet bulb globe temperature (WBGT)*. Editor J. A. Hodgdon, J. H. Heaney, and M. J. Buono. San Diego, CA: Environmental Ergonomics VIII, 77–80.

National Bureau of Statistics of China (2020). *China statistical yearbook 2020*. Beijing, China Statistics Press.

Ning, G., Luo, M., Zhang, W., Liu, Z., Wang, S., and Gao, T. (2022). Rising risks of compound extreme heat-precipitation events in China. *Int. J. Climatol.* 42, 5785–5795. doi:10.1002/joc.7561

Oke, T. R. (1973). City size and the urban heat island. *Atmos. Environ.* 7, 769–779. doi:10.1016/0004-6981(73)90140-6

Oke, T. R. (1982). The energetic basis of the urban heat island. *Q. J. R. Meteorological Soc.* 108, 1–24. doi:10.1002/qj.49710845502

Osczevski, R., and Bluestein, M. (2005). The new wind chill equivalent temperature chart. *Bull. Amer. Meteor. Soc.* 86, 1453–1458. doi:10.1175/bams-86-10-1453

Perkins-Kirkpatrick, S. E., and Lewis, S. C. (2020). Increasing trends in regional heatwaves. *Nat. Commun.* 11, 3357. doi:10.1038/s41467-020-16970-7

Ren, G., and Zhou, Y. (2014). Urbanization effect on trends of extreme temperature indices of national stations over mainland China, 1961–2008. *J. Clim.* 27, 2340–2360. doi:10.1175/jcli-d-13-00393.1

Roshan, G., Moghbel, M., and Attia, S. (2020). Evaluating the wind cooling potential on outdoor thermal comfort in selected Iranian climate types. *J. Therm. Biol.* 92, 102660. doi:10.1016/j.jtherbio.2020.102660

Rothfusz, L. P. (1990). *The heat index equation (or, more than you ever wanted to know about heat index)*. Fort Worth, TX: National Oceanic and Atmospheric Administration, National Weather Service, Office of Meteorology. SR 90-23.

Statistics Bureau of Guangdong Province (2020). *Guangdong statistical yearbook 2020*. Beijing, China: Statistics Press.

Steadman, R. G. (1979). The assessment of sultriness. Part I: A temperature-humidity index based on human physiology and clothing science. *J. Appl. Meteorology Climatol.* 18, 861–873. doi:10.1175/1520-0450(1979)018<0861:taospi>2.0.co;2

Sun, Y., Zhang, X., Zwiers, F. W., Song, L., Wan, H., Hu, T., et al. (2014). Rapid increase in the risk of extreme summer heat in Eastern China. *Nat. Clim. Change* 4, 1082–1085. doi:10.1038/nclimate2410

Sun, Y., Zhang, X., Ren, G., Zwiers, F. W., and Hu, T. (2016). Contribution of urbanization to warming in China. *Nat. Clim. Change* 6, 706–709. doi:10.1038/nclimate2956

Tian, H., Zhou, Y., Wang, Z., Huang, X., Ge, E., Wu, S., et al. (2021). Effects of high-frequency temperature variabilities on the morbidity of chronic obstructive pulmonary

disease: Evidence in 21 cities of Guangdong, South China. *Environ. Res.* 201, 111544. doi:10.1016/j.envres.2021.111544

Tong, X., Wang, P., Wu, S., and Luo, M. (2022). Urbanization effects on high-frequency temperature variability over South China. *Urban Clim.* 42 (2022), 101092. doi:10.1016/j.uclim.2022.101092

Tuholske, C., Caylor, K., Funk, C., Verdin, A., Sweeney, S., Grace, K., et al. (2021). Global urban population exposure to extreme heat. *Proc. Natl. Acad. Sci.* 118, e2024792118. doi:10.1073/pnas.2024792118

United Nations Department of Economic Social Affairs (2018). *World urbanization prospects. The 2018 revision, highlights.* New York, NY: United Nations Department of Economic Social Affairs.

Wang, J., and Yan, Z. W. (2021). Rapid rises in the magnitude and risk of extreme regional heat wave events in China. *Weather Clim. Extrem.* 34, 100379. doi:10.1016/j.wace.2021.100379

Wang, Y., Chen, L., Song, Z., Huang, Z., Ge, E., Lin, L., et al. (2019). Human-perceived temperature changes over South China: Long-term trends and urbanization effects. *Atmos. Res.* 215, 116–127. doi:10.1016/j.atmosres.2018.09.006

Wang, J., Chen, Y., Liao, W., He, G., Tett, S. F. B., Yan, Z., et al. (2021a). Anthropogenic emissions and urbanization increase risk of compound hot extremes in cities. *Nat. Clim. Change* 11, 1084–1089. doi:10.1038/s41558-021-01196-2

Wang, P., Luo, M., Liao, W., Xu, Y., Wu, S., Tong, X., et al. (2021b). Urbanization contribution to human perceived temperature changes in major urban agglomerations of China. *Urban Clim.* 38, 100910. doi:10.1016/j.uclim.2021.100910

Wang, P., Tong, X., Qiu, J., Chen, Y., Wu, S., Chan, T. O., et al. (2022). Amplification effect of urbanization on atmospheric aridity over China under past global warming. *Earth's Future* 10, e2021EF002335. doi:10.1029/2021ef002335

Willett, K. M., and Sherwood, S. (2012). Exceedance of heat index thresholds for 15 regions under a warming climate using the wet-bulb globe temperature. *Int. J. Climatol.* 32, 161–177. doi:10.1002/joc.2257

Xu, W., Li, Q., Wang, X. L., Yang, S., Cao, L., and Feng, Y. (2013). Homogenization of Chinese daily surface air temperatures and analysis of trends in the extreme temperature indices. *J. Geophys. Res. Amos.* 118, 9708–9720. doi:10.1002/jgrd.50791

Xu, Y., Ren, C., Ma, P., Ho, J., Wang, W., Lau, K. K. L., et al. (2017). Urban morphology detection and computation for urban climate research. *Landsc. Urb. Plan.* 167, 212–224. doi:10.1016/j.landurbplan.2017.06.018

Yang, X., Ruby Leung, L., Zhao, N., Zhao, C., Qian, Y., Hu, K., et al. (2017). Contribution of urbanization to the increase of extreme heat events in an urban agglomeration in east China. *Geophys. Res. Lett.* 44, 6940–6950. doi:10.1002/2017gl074084

You, Q., Jiang, Z., Kong, L., Wu, Z., Bao, Y., Kang, S., et al. (2017). A comparison of heat wave climatologies and trends in China based on multiple definitions. *Clim. Dyn.* 48, 3975–3989. doi:10.1007/s00382-016-3315-0

Zhang, H., Luo, M., Zhao, Y., Lin, L., Ge, E., Yang, Y., et al. (2022). HiTIC-monthly: A high spatial resolution (1 km×1 km) monthly human thermal index collection over China from 2003 to 2020. *Earth Syst. Sci. Data*. doi:10.5194/essd-2022-5257

frontiers | Frontiers in Environmental Science

TYPE Original Research
PUBLISHED 20 January 2023
DOI 10.3389/fenvs.2022.1054235

OPEN ACCESS

EDITED BY
Zengyun Hu,
Chinese Academy of Sciences (CAS), China

REVIEWED BY
Aihong Cui,
Hong Kong Baptist University, Hong Kong SAR, China
Yuanjian Yang,
Nanjing University of Information Science and Technology, China

*CORRESPONDENCE
Shuliang Zhang,
zhangshuliang@njnu.edu.cn

SPECIALTY SECTION
This article was submitted to Atmosphere and Climate, a section of the journal Frontiers in Environmental Science

RECEIVED 26 September 2022
ACCEPTED 28 November 2022
PUBLISHED 20 January 2023

CITATION
Zhu K, Yang Q, Zhang S, Jiang S, Wang T, Liu J and Ye Y (2023), Long lead-time radar rainfall nowcasting method incorporating atmospheric conditions using long short-term memory networks.
Front. Environ. Sci. 10:1054235.
doi: 10.3389/fenvs.2022.1054235

Long lead-time radar rainfall nowcasting method incorporating atmospheric conditions using long short-term memory networks

Kexin Zhu[1,2,3,4], Qiqi Yang[2,3,4], Shuliang Zhang[2,3,4]*, Shuai Jiang[1,2,3,4], Tianle Wang[2,3,4], Jinchen Liu[2,3,4] and Yuxuan Ye[2,3,4]

[1]Honors College, Nanjing Normal University, Nanjing, China, [2]Key Laboratory of VGE of Ministry of Education, Nanjing Normal University, Nanjing, China, [3]Jiangsu Center for Collaborative Innovation in Geographical Information Resource Development and Application, Nanjing, China, [4]School of Geography, Nanjing Normal University, Nanjing, China

High-resolution radar rainfall data have great potential for rainfall predictions up to 6 h ahead (nowcasting); however, conventional extrapolation approaches based on in-built physical assumptions yield poor performance at longer lead times (3–6 h), which limits their operational utility. Moreover, atmospheric factors in radar estimate errors are often ignored. This study proposed a radar rainfall nowcasting method that attempts to achieve accurate nowcasting of 6 h using long short-term memory (LSTM) networks. Atmospheric conditions were considered to reduce radar estimate errors. To build radar nowcasting models based on LSTM networks (LSTM-RN), approximately 11 years of radar, gauge rainfall, and atmospheric data from the UK were obtained. Compared with the models built on optical flow (OF-RN) and random forest (RF-RN), LSTM-RN had the lowest root-mean-square errors (RMSE), highest correlation coefficients (COR), and mean bias errors closest to 0. Furthermore, LSTM-RN showed a growing advantage at longer lead times, with the RMSE decreasing by 17.99% and 7.17% compared with that of OF-RN and RF-RN, respectively. The results also revealed a strong relationship between LSTM-RN performance and weather conditions. This study provides an effective solution for nowcasting radar rainfall at long lead times, which enhances the forecast value and supports practical utility.

KEYWORDS

nowcasting, radar, rainfall, atmospheric conditions, deep learning, long short-term memory

1 Introduction

Nowcasting is defined as local detailed forecasting at lead times of 1–6 h using any method, along with a full description of the current weather (Wang et al., 2017). It is a key instrument for predicting rapidly changing and severe weather (Sun et al., 2022), such as heavy rain and violent thunderstorms (Pulkkinen et al., 2019). It is also critical for small, mountainous, and urban watersheds, where stream flow responds rapidly to rainfall (Imhoff et al., 2020). Generally, nowcasting offers benefits to many sectors of the real world, such as emergency services, energy management, and flood early warning systems (Wilson et al., 2010).

Numerical weather prediction (NWP) and radar-based rainfall prediction (radar nowcasting) are the two main approaches to nowcasting with different application scales (Pulkkinen et al., 2019). By feeding current weather conditions into atmospheric models, NWP models try to simulate atmospheric behavior and provide rainfall predictions on a global and mesoscale (Cuo et al., 2011). However, the predictions offered by NWP systems for short lead times (0–2 h) are often unsatisfactory because of their coarse temporal resolution and low update frequency (Imhoff et al., 2020), along with the difficulties in model spin-up and data assimilation (Sun, 2005; Pierce et al., 2012; Sun et al., 2014; Buehner and Jacques, 2020). Consequently, alternative methods based on radar that provide more timely and accurate predictions have been widely used. With high spatial and temporal resolutions, typically 1 km and 5 min, respectively, radar rainfall products are regarded as having great potential for short-term rainfall forecasts (Ravuri et al., 2021). Radar nowcasting is the process of extrapolating rainfall based on apparent motion that has been analyzed using the most recent radar images (Wang al., 2017). Currently, radar extrapolation methods can be classified as object- or pixel-based (Zahraei et al., 2013). The object-based methods, as represented by Storm Cell Identification and Tracking (SCIT) and Thunderstorm Identification, Tracking, Analysis and Nowcasting (TITAN) proposed by the US, consider storm events as separate objects thus performing well in detecting and tracking specific thunderstorm cells (Dixon and Wiener, 1993; Vila et al., 2008). The pixel-based methods, on the contrary, outperform in forecasting convective storms and precipitation in stratocumulus clouds by using full motion fields (Grecu and Krajewski, 2000; Berenguer et al., 2011). One recent progress is the optical flow-based method. It introduces computer vision techniques to make extrapolation of radar maps, and displays high flexibility and accuracy (Bowler et al., 2004).

However, owing to the separated tracking and extrapolation steps, as well as the in-built non-linear physical assumptions, the conventional extrapolation approaches have limited success. They struggle to capture complex rainfalls, and show a decreasing skill at longer lead times (Golding, 1998; Liguori and Rico-Ramirez, 2013; Ravuri et al., 2021). In this context, machine learning methods, especially artificial neural networks (NNs), have been introduced in nowcasting. Based on self-adaptive principles that learn from samples and grasp functional relationships between data, NN has been widely used to predict, recognize, and classify a wide range of weather events, and is also one of the most appealing strategies for nowcasting (Valverde Ramírez et al., 2005; Hernández et al., 2016). Koizumi (Koizumi, 1999) found that models built on NN have higher skill scores than other nowcasting models, when using weather data of 1 year for training. Apart from the improved prediction accuracy, the NN trained by Foresti et al. (2019) using 10-year weather radar data in the Swiss Alps effectively learned and reproduced growth and decay patterns in the atmosphere, which is intrinsically challenging to predict. With the development of computer science, deep learning has risen drastically and expanded swiftly in many data-rich scientific disciplines, including nowcasting (Ayzel et al., 2020). Composed of multiple processing layers, the improved networks support the exploration of insight and complex structures of datasets. They overcome the drawbacks of traditional NNs, such as ineffective training practices and inability to manage extensive data, thus, becoming popular in handling complicated issues (Jia et al., 2017; Van et al., 2020). For example, Agrawal et al. (2019) presented a nowcasting model based on convolutional NN that, compared with other commonly used methods, performed favorably. For time-series problems, Chen et al. (2021) used long short-term memory (LSTM) networks to build a nowcasting model, and the results exhibited an evidently reduced prediction error. A wide variety of fantastic networks have been proposed and have made significant progress in nowcasting (Shi et al., 2015; Shi et al., 2017; Tian et al., 2019; Kumar et al., 2020; Luo et al., 2020), but a critical problem is that lead times in past studies have been relatively short (usually 0–2 h) (Schmidhuber, 2015; Kang et al., 2020). In fact, deep learning, particularly LSTM networks with fantastic memory ability (Gers et al., 2002), have great promise for achieving longer lead times in nowcasting.

In addition, previous research has focused on upgrading nowcasting algorithms while disregarding the many errors in radar rainfall estimates, which could result in numerous uncertainties. These uncertainties in radar data are carried over into radar nowcasting and grow with increasing rainfall rates (Ebert et al., 2004; Liguori et al., 2012). It is well known that the accuracy of radar rainfall estimates is affected by various factors, such as spurious echoes (e.g., from the ground, sea, and aero-planes), attenuation of the radar signal (Krämer et al., 2005; Villarini and Krajewski, 2009), and beam blockage (Joss and Lee, 1995). Actually, apart from the radar measurement instruments, weather conditions can also lead to radar estimation errors,

which have rarely been explored in previous studies (Seo et al., 1999; Song et al., 2017). Recently, researchers have begun to focus on this issue. Dai and Han (Dai and Han, 2014) were the first to incorporate the wind field into the construction of a radar rainfall uncertainty model, and the proposed model improved the correlation coefficients of most rainfall events by over 10%. Yang et al. (2020) considered multiple atmospheric fields to build a radar rainfall uncertainty adjustment model, and the results indicated a satisfactory performance of the model under high relative humidity and wind speed.

Therefore, this study incorporated atmospheric data into radar rainfall nowcasting with the aim of reducing radar estimate errors and improving prediction accuracy. A framework for nowcasting radar rainfall with long lead times of 1–6 h using LSTM networks was established. To investigate the performance of the proposed models at different altitudes and weather conditions, models were built using approximately 11 years of radar, gauge rainfall, and atmospheric data across the UK. Two other methods, optical flow (OF) and random forest (RF), were also built to further demonstrate the strengths of the proposed models.

2 Study area and data

The UK is located on Europe's western shore, between 49°N and 61°N. Influenced by the west wind and the Atlantic Ocean, the UK has a cloudy and rainy climate, with an average of 1,000 mm rainfall every year. Rainfall in the UK is affected by geographic location to some extent; generally, the further west and the higher the altitude, the greater the rainfall. Extreme rainfall events are predicted to become more common as global temperatures rise, and the increased intensity of rainfall affects the frequency and severity of surface water floods, particularly in urban areas.

The radar rainfall data used in this study, with a spatial resolution of 1 km and temporal resolution of 5 min, were downloaded from the website (https://catalogue.ceda.ac.uk/) supplied by the UK Met Office. Sufficient data were collected from 2007 to 2017. The data were subjected to extensive processing by the NIMROD system for corrections with regards to several sources of radar errors (Song et al., 2017). The NIMROD radar rainfall data are one of the best available sources of rainfall information (Zhu et al., 2014). The 5-min radar rainfall data were adjusted at a 1-h rate to make it compatible with the hourly gauge data. Then, the radar rainfall value of the corresponding gauge was extracted for modelling at each station.

Gauge rainfall data with resolutions of .2 mm and 1 h from 40 tilting bucket rain gauges between 2007 and 2017 (except for very few sites) were collected from the Met Office Integrated Data Archive System Land and Marine Surface Stations dataset. Atmospheric data, including air pressure, relative humidity, temperature, wind direction, and wind speed, were obtained from the same source (Met Office, 2019). The Met Office built the Meteorological Monitoring System at each station to collect data at a resolution of 1 min. The data were then aggregated into hourly data. The Met Office was responsible for ensuring the quality of the data (Met Office, 2012). Forty gauging stations were used for modeling, as shown in Figure 1 (the labeled stations KOI and EGDM were used as demonstration examples in Section 4.1). The lowest and highest altitudes of these stations were 4.27 m, and 246.21 m, respectively. These stations were separated into three classes depending on altitude for subsequent analysis (Sections 4.2–4.4).

3 Methodology

3.1 Radar rainfall nowcasting models based on LSTM networks (LSTM-RN)

The basic architecture of a NN includes the input, output, and hidden layers. Recurrent NNs (RNNs) are a variant of traditional NNs that introduce a cyclic structure. Owing to this structure, the outputs of a given input can be influenced not only by the current input but also by the residual state left over from prior calculations (Warner and Misra, 1996). RNNs are, thus, well-suited in simulating time series and other dynamical processes that are clearly reliant on history (Le et al., 2017). LSTM, an improved type of RNN, replaces the neurons in a regular RNN with an upgraded memory unit; each LSTM memory unit includes an input gate, output gate, a forget gate, and memory cells. Compared with RNN, LSTM can solve complicated, artificial long-time-lag challenges that earlier RNNs could not (Hochreiter and Schmidhuber, 1997).

The LSTM architecture used in this study consisted of three layers: an input layer (radar rainfall and atmospheric data at each time step), a hidden layer, and an output layer (gauge rainfall at a certain lead time). Figure 2 shows the LSTM architecture used for modeling at 1-h lead time. The models were constructed based on this architecture according to the following steps:

Step 1: Build the initial model (the selection of hyper-parameters can be found in Section 4.1).

Step 2: Normalize the data. Perform MinMaxScaler normalization on the datasets x (input) and h (output). The MinMaxScaler normalization formula is as follows:

$$X_{ijstd} = \frac{X_{ij} - X_{jmin}}{X_{jmax} - X_{jmin}} \tag{1}$$

$$X_{ijscaled} = X_{ijstd} \times (max - min) + min \tag{2}$$

Where $X_{ijscaled}$ and X_{ij} are the data before and after normalization, respectively, at time i and of variable j, X_{ijstd} is the temporary standardization result. X_{jmin} and X_{jmax} are the minimum and maximum values, respectively, of variable j; max and min are the maximum and minimum values of the interval to be mapped, which are typically 0 and 1, respectively.

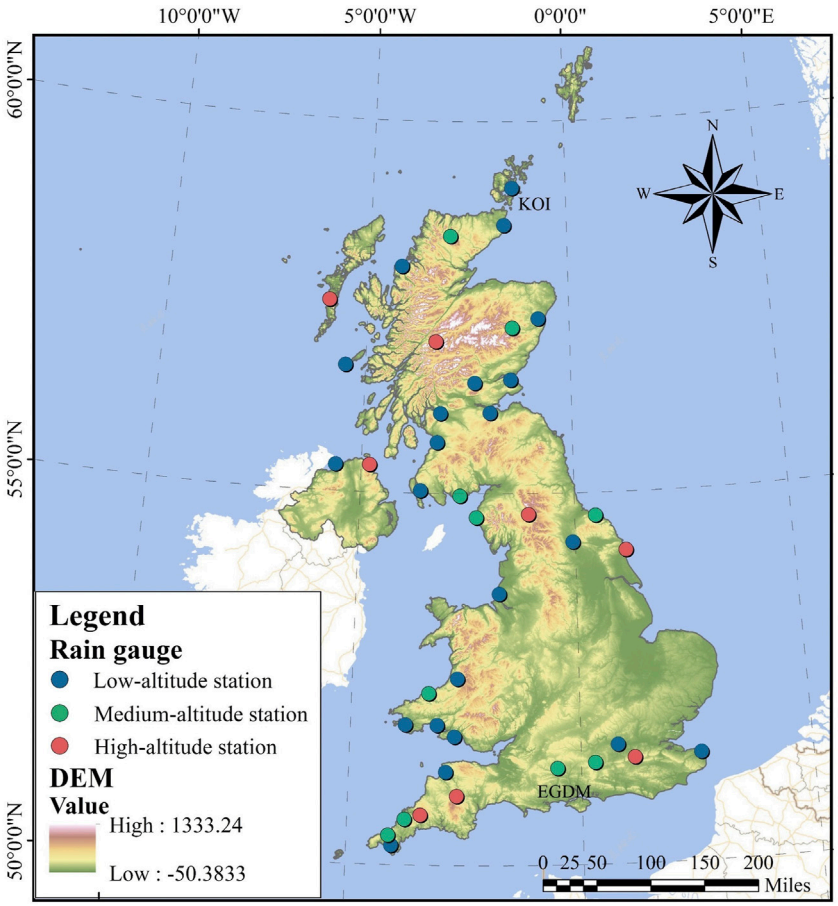

FIGURE 1
Locations of 40 stations in the UK study area with terrain elevation.

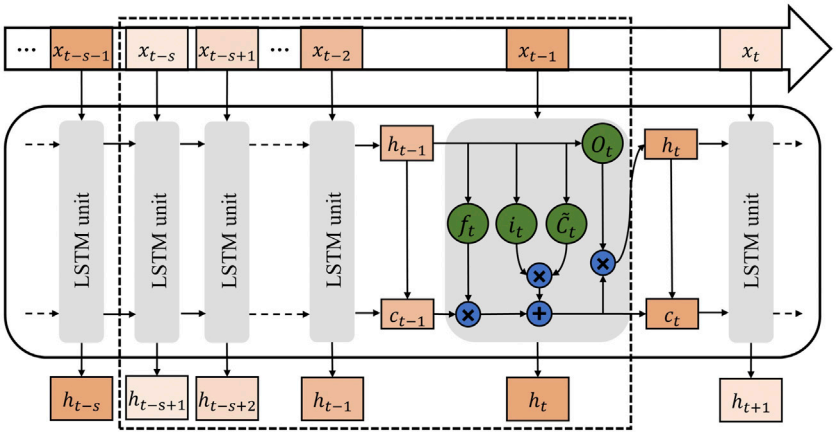

FIGURE 2
Architecture of the LSTM networks used in this study: x_t, h_t, and C_t are the input, output, and cell state at time step t, respectively; s is the length of input nodes at a time, while inputting the sequence x_{t-s} to x_{t-1}, the model outputs the predicted rainfall h_t (at 1 h lead time); f_t: forget gate; i_t: input gate; $\tilde{C}_t$: cell update; O_t: output gate.

Step 3: Divide the data. Take normalized datasets x and h before 2016 as training data and the rest as test data.

Step 4: Organize the data and train the model. The training data and test data were organized as the architecture illustrated in Figure 2. The radar rainfall series and corresponding atmospheric data were used as input nodes, with the gauge rainfall serving as the target variable. To improve the generalization ability of the model and avoid overfitting, the organized data were randomly shuffled. The rainfall predicted by this model was denormalized before it was used as the final result.

The LSTM-RN models of the 40 stations with 1-h lead time were generated using the prior process. Similar procedures were performed to build the LSTM-RN models with lead times of 2–6 h.

3.2 Radar rainfall nowcasting models based on RF (RF-RN)

Random forest (Breiman, 2001) is a conceptually simple machine-learning algorithm that combines the bagging ensemble learning theory with the random subspace method. It is made up of numerous decision tree classification modules and is highly efficient with large datasets. The tree-based machine learning method displayed high prediction accuracy (Speiser et al., 2019); therefore, it was adopted in this study to build comparative models.

The RF-RN models used in this study were constructed as follows:

Step 1: Randomly select N separate sample datasets from the training datasets as the training subset of each decision tree (the selection of N is discussed in Section 4.1).

Step 2: Establish a categorical regression tree for each sample dataset to generate N decision trees. For each node of the decision tree, the variable subset was randomly sampled from the original dataset, and the optimal variable was selected from the subset using the Gini index minimum criterion for node splitting and branching.

Step 3: Each categorical regression tree grew recursively from top to bottom, and stopped growing when the minimum size of the leaf nodes was reached. Subsequently, all the decision trees were combined into a random forest.

Step 4: The radar rainfall data and atmospheric data from the test sets were fed into the constructed model, and N decision trees were used to predict. The regression value was the average of the predicted outcomes of each decision tree.

3.3 Radar rainfall nowcasting models based on OF (OF-RN)

In the field of computer vision, OF is typically considered as a collection of techniques to infer velocity patterns or fields from a series of image frames (Liu et al., 2015; Woo and Wong, 2017). For rainfall prediction, Ayzel et al. (2019) developed a set of tracking models based on two OF formulations, Sparse (Lucas and Kanade, 1981) and Dense (Kroeger et al., 2016), as well as two extrapolation techniques. The OF models built were an open benchmark for radar nowcasting. In this study, we used the dense model, which utilized a dense inverse search (DIS) algorithm to construct a continuous displacement field from two consecutive radar images. The DIS, a global OF algorithm proposed by Kroeger et al. (2016), can explicitly estimate the velocity of each image pixel based on the analysis of two continuous radar images.

This study used the "rainymotion" codebase, provided by Ayzel et al., to build the second type of comparative models, which is available at the following link: https://github.com/hydrogo/rainymotion.

3.4 Experimental design and evaluation indicators

Figure 3 shows the experimental flowchart. The data division and model construction processes have been described above, and the following paragraphs describe the three analysis parts.

First, the accuracy of the LSTM-RN models at different lead times and altitudes was investigated to better understand the performance pattern and further explore the causes of the difference in accuracy. The lead times ranged from 1 h to 6 h, as described in Section 3.1. Owing to the large number of gauges, it was impossible to obtain the exact performance of each model; however, roughly averaging the error indicator results of all models would miss the underlying causes of the models' varied performance. Thus, we divided the stations into three classes based on their altitude (Figure 2) and compared the performance of the models at different altitude classes. Models with altitudes <75 m, >75 m and <150 m, and >150 m and <250 m were classified as low, medium, and high altitudes, respectively. Similar studies have also divided the gauge stations into three altitude classes (Milewski et al., 2015). The thresholds in this study were determined based on the characteristics of the data. With such thresholds, the number of data points in each class was approximately the same, and the differences between classes were enlarged as much as possible. The corresponding results are presented in Section 4.2.

Second, we constructed two types of comparative models, the RF-RN and OF-RN models, and ran identical rainfall nowcasting experiments. Four rainfall events were chosen to visually evaluate the prediction abilities of the models, and error indices were calculated to quantitatively assess the performance of the models from 1 to 6 h lead times. The corresponding results are presented in Section 4.3.

Finally, to investigate the relationship between the LSTM-RN model performance and diverse weather conditions, the test sets were divided into five classes depending on the rainfall rate (R) and relative humidity (H): classes A1–A5: R = (0, .2] (.2, .4] (.4,

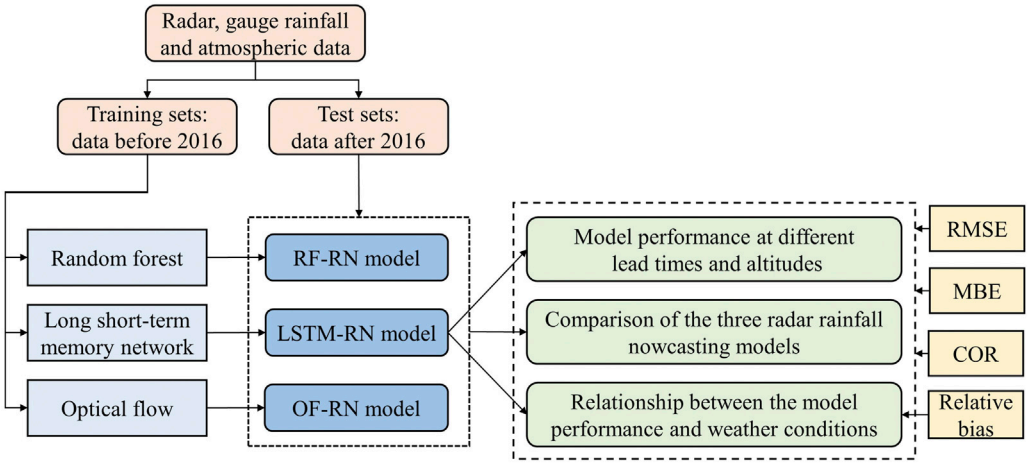

FIGURE 3
Schematic diagram of the experimental design.

TABLE 1 Hyper-parameters of the LSTM-RN models.

Hyper-parameter	Value
Training data division	80%/20%
Hidden nodes	9
Initial learning rate	0.01
Loss function	Mean square error
Batch size	256
Timesteps	7
Epochs	100–150

.8] (.8, 1.6], and R > 1.6 mm/h by rainfall rate; classes B1–B5: H = [0,80) [80,85) [85,90) [90,95), and H > 95% by relative humidity. The corresponding results are presented in Section 4.4.

Three error indices, namely, root-mean-square error (RMSE), mean bias error (MBE), and correlation coefficient (COR), were selected to evaluate the models. The RMSE, MBE, and COR were defined as follows:

$$\mathrm{RMSE} = \sqrt{\frac{\sum_{i=1}^{N}(y_i - x_i)^2}{N}} \tag{3}$$

$$\mathrm{MBE} = \frac{\sum_{i=1}^{N}(y_i - x_i)}{N} \tag{4}$$

$$\mathrm{COR} = \frac{\sum_{i=1}^{N}(x_i - \bar{x})(y_i - \bar{y})}{\sqrt{\sum_{i=1}^{N}(x_i - \bar{x})^2}\sqrt{\sum_{i=1}^{N}(y_i - \bar{y})^2}} \tag{5}$$

where y_i and x_i are the rainfall at time i predicted by the model and obtained from the rain gauge, respectively; $\bar{y}$ and $\bar{x}$ are the average rainfall of the series predicted by the model and obtained from the rain gauge, respectively; and N is the length of the rainfall series.

The RMSE is the square root of the average of squared errors and is often used to measure the differences between the predicted or simulated values and the true values. This metric was chosen to quantify the accuracy of the prediction results, and a lower RMSE suggested a better match to the true value. The MBE assesses the average overestimation or underestimation of accumulated rainfall, with a perfect score of 0. This index was selected to investigate the deviation direction and extent of the model's prediction, that is, the model's tendency to underestimate or overestimate rainfall. The COR provides correlation information between the predicted or simulated values and the true values, which can indicate the model's ability to capture the subsequent rain-fall trends in this study. COR ranges from −1 to 1, with a higher COR indicating better recognition.

Moreover, to eliminate the effect of magnitude, we used relative bias to explore the bias at different rainfall rates as follows:

$$\sigma_R = \sum_{i=1}^{N}\frac{(y_i - x_i)}{y_i} \tag{6}$$

where y_i and x_i are the rainfall at time i predicted by the model and obtained from the rain gauge, respectively; and N is the length of the rainfall series.

4 Results and discussion

4.1 Selection of hyper-parameters of the LSTM-RN and RF-RN models

The performance of the LSTM-RN models is significantly influenced by the hyper-parameters selection, such as data division, the number of hidden layer nodes, and epochs. We used identical hyperparameters (excluding epochs) for all 240 LSTM-

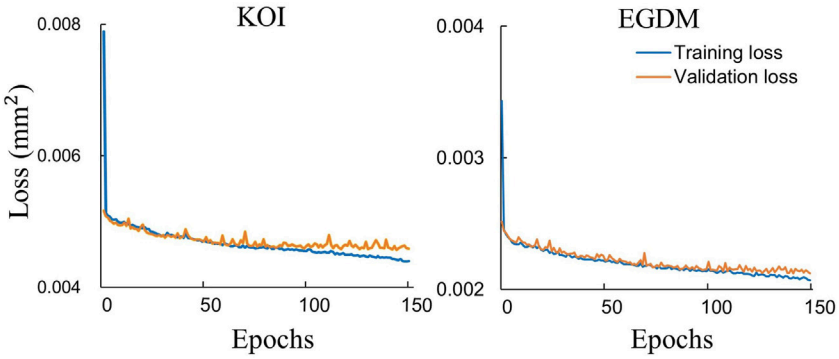

FIGURE 4
Training progress of the LSTM-RN models at stations KOI and EGDM.

RN models (40 stations with 6 different lead times) in this study, as listed in Table 1. After training, it was assumed that this setting was appropriate for almost all the models.

As described in Section 3.1, the data were divided into training and testing sets. Furthermore, a reasonable 20% of the training set was treated as a validation set, which was used to optimize the network parameters during the training process. The number of hidden layer nodes was a key hyperparameter; if it was small, the data characteristics could not be fully retrieved and if it was large, the network's complexity would increase and eventually overfit. Based on the empirical formula proposed by Xia et al. (2005), nine hidden layer nodes were determined; overfitting or underfitting phenomena were not apparent. The initial learning rate was set to .01, and it gradually decayed during the training process. The batch size determined the frequency with which the weights of the network were updated. It was set to 256 owing to the large amount of data used in this study.

The mean-square error (MSE) was used as the loss of the LSTM-RN models, which decreased with increasing epochs, and the epochs where both validation loss and training loss converged was used as the final epochs. Figure 4 shows the training progress of two randomly selected models, station KOI and EGDM. After training, all the LSTM-RN models in this study converged when the epochs were between 100 and 150. Timesteps was the lengths of the input nodes at a time (Figure 2). The RMSEs of the training sets of all the LSTM-RN models at different time steps were averaged, and the results are shown in Figure 5. In this study, the timesteps of all models were determined to be seven according to the results, while considering the correlation between rainfall periods.

Error backpropagation algorithms were used to update the parameters of the networks during training. These included stochastic gradient descent (Graves and Schmidhuber, 2005),

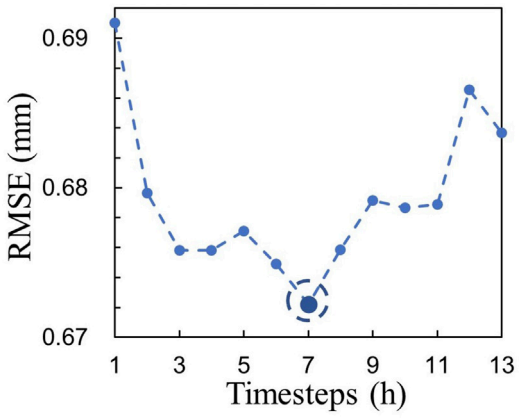

FIGURE 5
Average RMSE of the training sets of all LSTM-RN models at different timesteps.

adaptive gradient (AdaGrad), root mean square prop (RMSProp) (Duchi et al., 2011), and adaptive moment estimation (Adam). The Adam optimization algorithm is an effective gradient-based stochastic optimization method. It combines the advantages of the AdaGrad and RMSProp algorithms to calculate adaptive learning rates for different parameters while using less storage space. It outperformed other stochastic optimization methods in practical applications (Kingma and Ba, 2014); hence, it was used in this study.

For the RF-RN models, the critical parameters were Ntree and Mtry. Ntree represents the number of decision trees (N in Section 3.2). A larger number of decision trees will develop more accurate results, but require more memory. Mtry, the number of input features per leaf node, was usually set to 1/3 of the total number of variables. In our RF-RN models, Ntree was set to 400, according to the out-of-bag error (Figure 6), and Mtry was set to

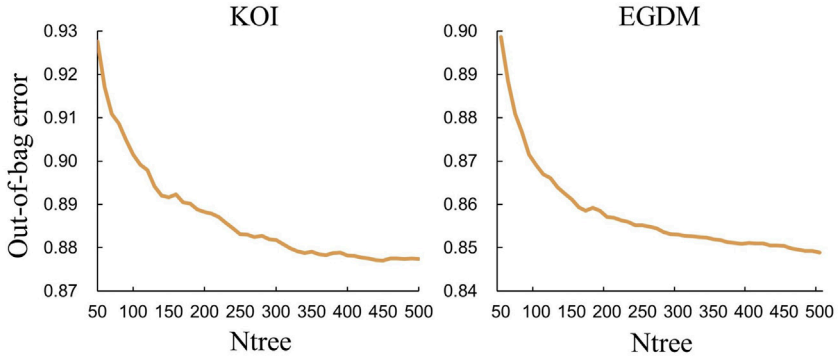

FIGURE 6
The out-of-bag error of the RF-RN models at stations KOI and EGDM.

TABLE 2 RMSE, MBE, and COR of the LSTM-RN models at different altitudes.

Classes	RMSE (mm)	MBE (mm)	COR
Low-altitude	0.66	0.02	0.47
Medium-altitude	0.78	0.00	0.48
High-altitude	0.79	-0.05	0.57

2. The out-of-bag error served as an indicator of the generalization error, and was used to determine the parameters of an RF model.

4.2 Model performance at different lead times and altitudes

As rain gauges vary in geographical location, the ability of the LSTM-RN models may be influenced by a variety of environmental conditions. As described in Section 3.4, the RMSE, MBE, and COR of LSTM-RN at different altitudes were calculated. In addition, because the LSTM-RN models have long memory ability and are suitable for multi-step-ahead prediction, three metrics of the models at lead times of 1–6 h were also calculated.

Table 2 shows the RMSE, MBE, and COR of the test sets of the models at different altitudes. It is evident that the RMSE of the low-altitude models was lower than that of the medium- and high-altitude models, possibly because rainfall in low-altitude areas is usually small, so even if the model fails to predict accurately, the results would not significantly deviate from the actual value. However, in medium- and high-altitude areas, where heavy rainfall occurs frequently, the predicted results could deviate more from the real values when the model fails to predict accurately, leading to a high RMSE.

The MBE of the models was positive at low altitude, zero at middle altitude, and negative at high altitude. It demonstrated that the models showed a tendency to overestimate rainfall at low altitude while underestimating it at high altitude, with the highest variation at high altitude.

The COR of the models between the predicted values and the true values was slightly smaller at low and medium altitudes compared with that at high altitude. The results indicated that the models could perform better when recognizing heavy rainfall trends.

The RMSE, MBE, and COR of the test sets of the LSTM-RN models at different lead times are listed in Table 4. The results revealed that the RMSE increased as the lead time extended, from .72 at 1-h lead time to .77 at 6-h lead time, an increase of 6.94%. The COR decayed with increasing lead time, from .68 at 1-h lead time to .36 at 6-h lead time, a decrease of 47.06%. In general, the performance of the designed models was satisfying, with a slight decay at long lead times.

4.3 Comparison of the three radar rainfall nowcasting models

To assess the performance of the LSTM-RN models, we constructed RF-RN and OF-RN models for comparison. The LSTM-RN and RF-RN models were constructed using radar, gauge rainfall, and atmospheric data, whereas the OF-RN models used only radar rainfall. Four rainfall events were selected from the test sets to visually present the predictive ability of the three types of models at 1-h lead time. To ensure the spatial diversity of the selected events, four randomly selected rainfall events at four stations with large altitude differences were included (see Table 3). The four events almost covered all seasons, with accumulated rainfall ranging from 22.4 mm to 60.4 mm.

Figure 7 depicts the gauge rainfall and the predicted results using the three types of models for the four rainfall events.

TABLE 3 Durations and accumulated rainfall of selected storm events.

Event ID	Station height (m)	Start time	End time	Duration (h)	Accumulated rainfall (mm)
1	11.04	2017-08-22 15:00:00	2017-08-23 07:00:00	16	60.4
2	64.67	2017-02-22 05:00:00	2017-02-23 03:00:00	22	31.0
3	120.72	2017-06-27 14:00:00	2017-06-28 14:00:00	24	22.4
4	133.09	2017-12-10 01:00:00	2017-12-10 17:00:00	16	31.6

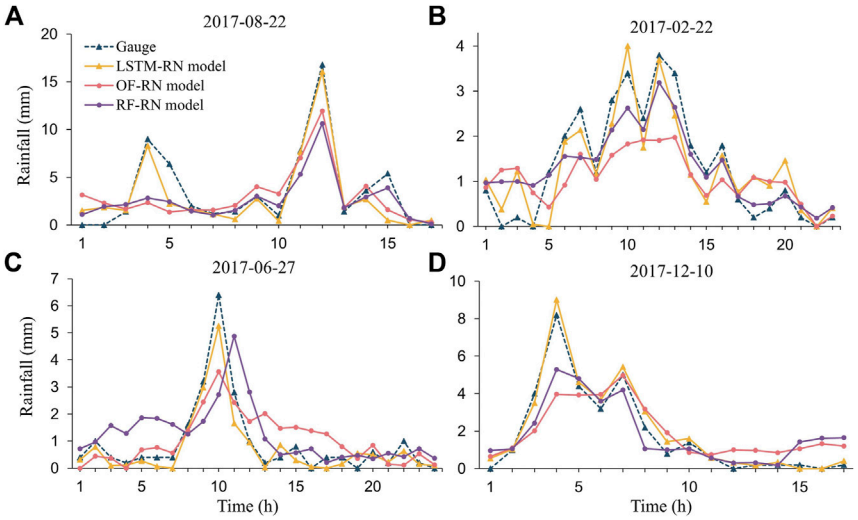

FIGURE 7
The gauge rainfall and the predicted results using three types of models of four rainfall events.

TABLE 4 RMSE, MBE, and COR of three types of models at different lead times.

Lead time (h)	RMSE (mm)			MBE (mm)			COR		
	OF-RN	RF-RN	LSTM-RN	OF-RN	RF-RN	LSTM-RN	OF-RN	RF-RN	LSTM-RN
1	0.84	0.77	0.72	0.10	0.10	−0.01	0.33	0.63	0.68
2	0.88	0.78	0.73	0.07	0.09	−0.02	0.37	0.58	0.59
3	0.90	0.80	0.75	0.07	0.09	0.00	0.36	0.51	0.52
4	0.91	0.81	0.76	0.06	0.11	−0.01	0.35	0.46	0.47
5	0.94	0.83	0.77	0.06	0.11	−0.03	0.34	0.39	0.40
6	0.96	0.84	0.77	0.06	0.12	0.01	0.32	0.34	0.36

Generally, the LSTM-RN models exhibited the best performance compared to the other two models. This was supported by the fact that the LSTM-RN models were able to predict rainfall more accurately at both high and low rainfall rates as well as precisely capture rainfall trends. The performance of the RF-RN model was the second best. They tended to underestimate rainfall at

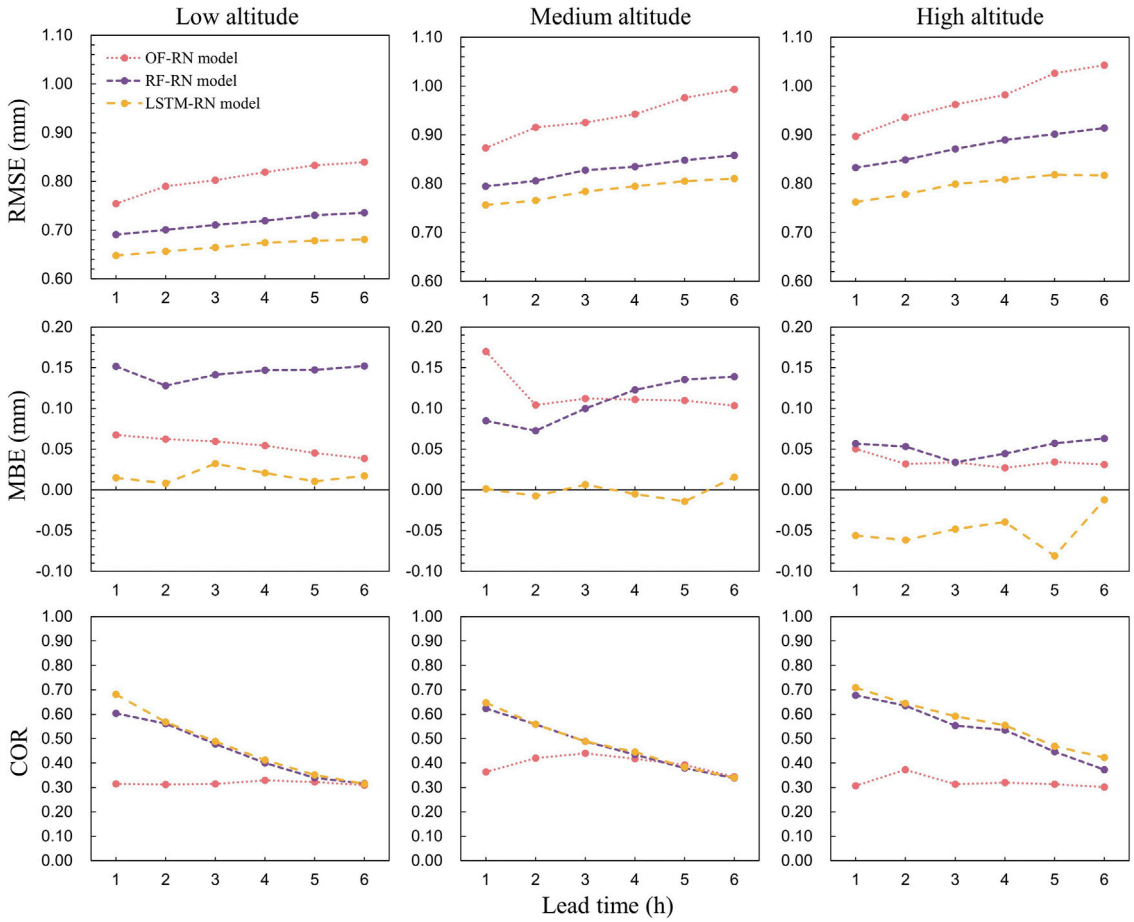

FIGURE 8
Comparison of RMSE, MBE, and COR of three types of models at different lead times and altitudes.

high rainfall rates and overestimate rainfall at low rainfall rates (Figure 7C). However, they could recognize the rainfall trends to some extent. The OF-RN models performed the worst, deviating severely from the gauge rainfall, and sometimes even failing to capture the rainfall trends (Figure 7B).

To quantitatively evaluate the prediction performance of the different models, the RMSE, MBE, and COR were calculated at different lead times for the three types of models. Models were categorized into three classes based on altitude, similar to the classification in Section 4.2. Thus, we can compare the performances of the three types of models more easily.

Figure 8 shows the RMSE, MBE, and COR of the three types of models at different lead times and altitudes. In terms of RMSE, it can be seen that the LSTM-RN models performed the best at any lead time and altitude, followed by the RF-RN and OF-RN. As the lead time increased, the RMSE of all models increased, among which the LSTM-RN grew the slowest, followed by RF-RN, while OF-RN grew rapidly. As the altitude increased, the RMSEs of all models also increased, but the LSTM-RN had the smallest gain, while the OF-RN had the largest gain. The results demonstrate that although the accuracy of the models decayed with increasing lead time and altitude, the LSTM-RN models consistently outperformed the others. This may be attributed to the strong memory and excellent learning abilities of LSTM networks, which allow the LSTM-RN to adapted better to changing conditions. The RF-RN models also performed well, with RF being a popular machine-learning method. The OF-RN models, however, showed large errors, especially at longer lead times, owing to a lack of learning ability and reliance solely on the correlation between adjacent frames in the image sequence.

In terms of MBE, it can be seen that LSTM-RN models generally fluctuated around 0 at low and medium altitudes and were <0 at high altitudes. For the other two models, the MBE values were >0 at all altitudes. In other words, the RF-RN and OF-RN models tended to overestimate rainfall compared to LSTM-RN. In general, the LSTM-RN with the minimum deviation performed the best, implying that it rarely

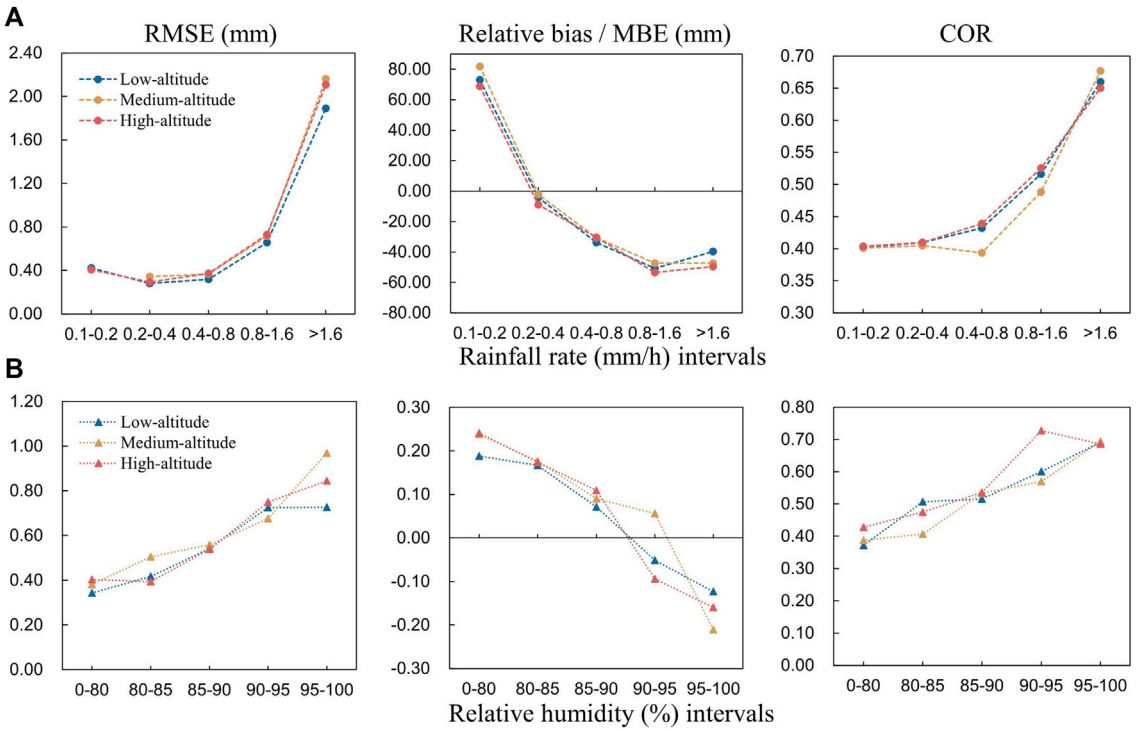

FIGURE 9
RMSE, relative bias (MBE), and COR of three classes of models at different rainfall rate and relative humidity, respectively.

TABLE 5 Comparison of RMSE, relative bias, and COR among the five rainfall rate classes (A1–A5).

Classes	RMSE (mm)	Relative bias	COR
A1	0.42	74.66	0.40
A2	0.31	−5.06	0.41
A3	0.35	−31.52	0.42
A4	0.70	−50.51	0.51
A5	2.05	−45.48	0.66

TABLE 6 Comparison of RMSE, MBE, and COR among the five relative humidity classes (B1–B5).

Classes	RMSE (mm)	MBE (mm)	COR
B1	0.38	0.22	0.40
B2	0.44	0.17	0.46
B3	0.55	0.09	0.53
B4	0.72	−0.03	0.63
B5	0.85	−0.16	0.69

overestimated or underestimated rainfall, or the accumulated overestimation and underestimation were virtually equal.

The CORs of the OF-RN were maintained at a low level between .31 and .33, while those of the LSTM-RN and RF-RN decayed with increasing lead time, from ~.70 to .30. There was no significant difference between the LSTM-RN and RF-RN, except at the 1-h lead time, where the LSTM-RN performed slightly better. In general, both the RF-RN and LSTM-RN performed well at short lead times (1–2 h) with CORs ranging from ~.50 to .70, and at long lead times (3–6 h) with CORs between ~.30 and .50. OF-RN was underperforming, with consistently low CORs.

To further compare the performances of the three types of models, we averaged the three metrics for all stations. The RMSE, MBE, and COR of the three types of models at different lead times are listed in Table 4. In terms of RMSE, compared with the OF-RN, the LSTM-RN decreased by 14.15%, 16.72%, 16.45%, 16.98%, 18.80%, and 19.73% at lead times of 1 h–6 h, respectively. Generally, the LSTM-RN decreased by 15.43% at short lead times (1–2 h) and by 17.99% at long lead times (3–6 h). Similarly, compared with that of RF-RN, the RMSE of LSTM-RN decreased by 6.52%, 6.60%, 6.73%, 6.80%, 7.22%, and 7.96% at lead times of 1–6 h, respectively. The RMSE of the LSTM-RN decreased by 6.56% at short lead times (1–2 h) and by 7.17% at long lead times (3–6 h). In other words, although the prediction accuracy of the three types of models decreased as lead time increased, the LSTM-RN with

strong learning and memory ability performed best, with the lowest RMSEs at any given lead time, and a growing advantage at longer lead times.

In terms of COR, compared with the OF-RN, the LSTM-RN increased by 106.99%, 60.41%, 47.21%, 32.62%, 17.15%, and 12.72% at lead times of 1 h–6 h, respectively, with an average of 46.18%. Similarly, compared with the RF-RN, the LSTM-RN increased by 7.04%, .98%, 3.20%, 3.06%, 3.48%, and 4.80% at lead times of 1 h–6 h, respectively, with an average of 3.76%. In general, the OF-RN did not perform satisfactorily in capturing the rainfall trends, and both the RF-RN and LSTM-RN performed well, with the LSTM-RN showing a slight advantage.

4.4 Relationship between the model performance and weather conditions

In Section 4.2, the performance of the LSTM-RN model at different lead times and altitudes was discussed, and it was apparent that model performance displayed regular patterns at different altitudes. Since altitude is highly relevant to weather conditions, this study investigated the relationship between LSTM-RN models and weather conditions. Through pre-experiments, we discovered that the model performance was related to rainfall rates and relative humidity; therefore, we focused on these two factors to further evaluate the model performance under various weather conditions.

As described in Section 3.4, the test sets were divided into five classes based on rainfall rate, and three metrics (RMSE, relative bias, and COR) were calculated. Similar to the division in Section 4.2, the models were divided into three classes based on altitude, and the metrics were averaged for each class of models.

Figure 9A shows the RMSE, relative bias, and COR of the three classes of models at different rainfall rates. The blue, yellow, and orange lines represent the low-altitude, medium-altitude, and the high-altitude models, respectively. It can be clearly observed that the curves are highly similar in terms of altitude. The RMSE generally increased as the rainfall rate increased, from ~.40 to 2.00. We noted that the smallest rainfall rate (A1) did not correspond to the lowest RMSE, that is, light rain was more difficult to predict accurately than moderate rain (A2–A3). Furthermore, the relative bias of light rain (A1) was more pronounced than that of heavy rain (A5–A6). In addition, COR increased as the rainfall rate increased, which is consistent with the explanation in Section 4.2.

As the atmospheric factors are complicated, this study selected temperature, relative humidity, and wind speed for pre-experiments and discovered that relative humidity showed an obvious correlation with the model performance. Figure 9B shows the RMSE, MBE, and COR of the three classes of models at different relative humidities. As relative humidity increased, the RMSE increased from ~.40 to .80, the MBE decreased from ~.20 to –.20, and the COR increased from ~.40 to .70. The results demonstrated that the models showed low RMSEs at low relative humidity, low bias at medium relative humidity, and high CORs at high relative humidity.

As the results show a similar tendency in terms of altitude (Figure 9), error metrics were averaged at different rainfall rate and relative humidity classes, excluding the altitude (Tables 5, 6). The results revealed that the RMSE improved by 388.10% from A1 to A5 and by 123.68% from B1 to B5. COR improved by 65% from A1 to A5 and by 72.50% from B1 to B5. In general, the models showed a higher accuracy under light rain and low relative humidity, lower uncertainty under moderate rain and medium relative humidity, and better recognition of rainfall trends under heavy rain and high relative humidity.

Although the proposed LSTM-RN models achieved reasonable performance, the prediction at stations still has limitations. In future work, meteorological forecast fields, such as the European Centre for Medium-Range Weather Forecasts (ECMWF), the global forecast system from China T639, and the National Centers for Environmental Prediction (NCEP) Global Forecast System (GFS), will be employed to investigate regional predictions (Li et al., 2021). Using these data for radar nowcasting could produce more accurate and practical results over precipitation areas.

5 Conclusion

In this study, we constructed radar rainfall nowcasting models using LSTM networks, with radar rainfall data as input and rain gauge data as ground references. To correct radar estimate errors and improve the nowcasting ability under various weather conditions, atmospheric data were also used as input. The 40 scattered stations used for modeling roughly represented the various environments of the study area. Approximately 11 years of data from the stations were employed as training and test sets to confirm its adequacy. After adjusting the hyperparameters, we determined the optimal settings for all stations. The performance of the LSTM-RN was evaluated at various lead times and altitudes and was compared with that of the OF-RN and RF-RN. We also investigated the relationship between the performance of the LSTM-RN and weather conditions. The results are summarized as follows:

(1) The performance of LSTM-RN displayed regular patterns at different altitudes. The RMSEs of the models at high altitudes were generally higher than those at low altitudes; however, the CORs were also generally higher at high altitudes. Moreover, models at high altitudes tended to underestimate rainfall, while models at low altitudes tended to overestimate rainfall, with the highest variation at high altitudes.
(2) Compared with OF-RN and RF-RN, LSTM-RN demonstrated the highest accuracy in nowcasting, with the lowest RMSEs and MBEs closest to 0 at any lead time. Furthermore, the LSTM-RN had a growing advantage in longer lead times, with the RMSE decreasing by 15.43% and

6.56% at short lead times (1–2 h) and by 17.99% and 7.17% at long lead times (3–6 h). In addition, the LSTM-RN significantly outperformed the others in recognizing rainfall trends, with the highest CORs at any given lead time. On average, the COR of the LSTM-RN increased by 46.18% and 3.76%, compared with that of the OF-RN and RF-RN, respectively.

(3) A strong relationship between the performance of the LSTM-RN and weather conditions was observed. The models showed a higher accuracy under light rain and low relative humidity, lower uncertainty under moderate rain and medium relative humidity, and better recognition of rainfall trends under heavy rain and high relative humidity.

This study proposes a reliable and effective solution to nowcast radar rainfall at long lead times using an advanced deep learning technique, as well as considering the atmospheric impact on radar data. The results demonstrate that the designed models outperform traditional methods in prediction ability and are valuable for long lead-time nowcasting. However, owing to data limitations and the computational expenses for model training, this study can only realize nowcasting on stations. In future work, we intend to collect gauge data from more stations to achieve regional nowcasting.

Data availability statement

The original contributions presented in the study are included in the article/supplementary material, further inquiries can be directed to the corresponding author.

Author contributions

Conceptualization, KZ and QY; Methodology, KZ, QY, SZ, and YY; Validation, SJ, TW, and JL; Formal analysis, KZ and SJ; Investigation, KZ, TW, and JL; Data cura-tion, SJ; Writing—original draft preparation, KZ; Writing—review and editing, KZ and QY; Visualization, KZ; Supervision, SZ. All authors have read and agreed to the published version of the manuscript.

Funding

This study was supported by the National Natural Science Foundation of China (Nos. 42271483, 42101416, and 42071364).

Conflict of interest

The authors declare that the research was conducted in the absence of any commercial or financial relationships that could be construed as a potential conflict of interest.

Publisher's note

All claims expressed in this article are solely those of the authors and do not necessarily represent those of their affiliated organizations, or those of the publisher, the editors and the reviewers. Any product that may be evaluated in this article, or claim that may be made by its manufacturer, is not guaranteed or endorsed by the publisher.

References

Agrawal, S., Barrington, L., Bromberg, C., Burge, J., Gazen, C., and Hickey, J. (2019). Machine learning for precipitation nowcasting from radar images. arXiv e-prints, arXiv:1912.12132.

Ayzel, G., Heistermann, M., and Winterrath, T. (2019). Optical flow models as an open benchmark for radar-based precipitation nowcasting (rainymotion v0.1). *Geosci. Model Dev.* 12 (4), 1387–1402. doi:10.5194/gmd-12-1387-2019

Ayzel, G., Scheffer, T., and Heistermann, M. (2020). RainNet v1.0: A convolutional neural network for radar-based precipitation nowcasting. *Geosci. Model Dev.* 13 (6), 2631–2644. doi:10.5194/gmd-13-2631-2020

Berenguer, M., Sempere-Torres, D., and Pegram, G. G. S. (2011). SBMcast – an ensemble nowcasting technique to assess the uncertainty in rainfall forecasts by Lagrangian extrapolation. *J. Hydrology* 404 (3-4), 226–240. doi:10.1016/j.jhydrol.2011.04.033

Bowler, N. E. H., Pierce, C. E., and Seed, A. (2004). Development of a precipitation nowcasting algorithm based upon optical flow techniques. *J. Hydrology* 288 (1-2), 74–91. doi:10.1016/j.jhydrol.2003.11.011

Breiman, L. (2001). Random forests. *Mach. Learn.* 45 (1), 5–32. doi:10.1023/A:1010933404324

Buehner, M., and Jacques, D. (2020). Non-Gaussian deterministic assimilation of radar-derived precipitation accumulations. *Mon. Weather Rev.* 148 (2), 783–808. doi:10.1175/MWR-D-19-0199.1

Chen, S., Adjei, C. O., Tian, W., Onzo, B.-M., Kedjanyi, E. A. G., and Darteh, O. F. (2021). Rainfall forecasting in sub-sahara africa-Ghana using LSTM deep learning approach. *Int. J. Eng. Res. Technol.* 10 (3), 464–470. doi:10.17577/IJERTV10IS030244

Cuo, L., Pagano, T. C., and Wang, Q. J. (2011). A review of quantitative precipitation forecasts and their use in short- to medium-range streamflow forecasting. *J. Hydrometeorol.* 12 (5), 713–728. doi:10.1175/2011JHM1347.1

Dai, Q., and Han, D. (2014). Exploration of discrepancy between radar and gauge rainfall estimates driven by wind fields. *Water Resour. Res.* 50 (11), 8571–8588. doi:10.1002/2014wr015794

Dixon, M., and Wiener, G. (1993). Titan: Thunderstorm identification, tracking, analysis, and nowcasting—a radar-based methodology. *J. Atmos. Ocean. Technol.* 10 (6), 785–797. doi:10.1175/1520-0426(1993)010<0785:ttitaa>2.0.co;2

Duchi, J., Hazan, E., and Singer, Y. (2011). Adaptive subgradient methods for online learning and stochastic optimization. *J. Mach. Learn. Res.* 12 (7), 2121–2159.

Ebert, E. E., Wilson, L. J., Brown, B. G., Nurmi, P., Brooks, H. E., Bally, J., et al. (2004). Verification of nowcasts from the WWRP sydney 2000 forecast demonstration project. *Weather Forecast.* 19 (1), 73–96. doi:10.1175/1520-0434(2004)019<0073:vonftw>2.0.co;2

Foresti, L., Sideris, I. V., Nerini, D., Beusch, L., and Germann, U. (2019). Using a 10-year radar archive for nowcasting precipitation growth and decay: A probabilistic machine learning approach. *Weather Forecast.* 34 (5), 1547–1569. doi:10.1175/WAF-D-18-0206.1

Gers, F. A., Schraudolph, N. N., and Schmidhuber, J. (2002). Learning precise timing with LSTM recurrent networks. *J. Mach. Learn. Res.* 3, 115–143. doi:10.1162/153244303768966139

Golding, B. W. (1998). Nimrod: A system for generating automated very short range forecasts. *Meteorol. App.* 5 (1), S1350482798000577. doi:10.1017/S1350482798000577

Graves, A., and Schmidhuber, J. (2005). Framewise phoneme classification with bidirectional LSTM and other neural network architectures. *Neural Netw.* 18 (5-6), 602–610. doi:10.1016/j.neunet.2005.06.042

Grecu, M., and Krajewski, W. F. (2000). A large-sample investigation of statistical procedures for radar-based short-term quantitative precipitation forecasting. *J. Hydrology* 239 (1), 69–84. doi:10.1016/S0022-1694(00)00360-7

Hernández, E., Sanchez-Anguix, V., Julian, V., Palanca, J., and Duque, N. (2016). "Rainfall prediction: A deep learning approach," in *Hybrid artificial intelligent systems*. Editors F. Martínez-Álvarez, A. Troncoso, H. Quintián, and E. Corchado (New York: Springer International Publishing), 151–162.)

Hochreiter, S., and Schmidhuber, J. (1997). Long short-term memory. *Neural Comput.* 9 (8), 1735–1780. doi:10.1162/neco.1997.9.8.1735

Imhoff, R. O., Brauer, C. C., Overeem, A., Weerts, A. H., and Uijlenhoet, R. (2020). Spatial and temporal evaluation of radar rainfall nowcasting techniques on 1, 533 events. *Water Resour. Res.* 56 (8). doi:10.1029/2019wr026723

Jia, Y., Wu, J., and Xu, M. (2017). Traffic flow prediction with rainfall impact using a deep learning method. *J. Adv. Transp.* 2017, 1–10. doi:10.1155/2017/6575947

Joss, J., and Lee, R. (1995). The application of radar–gauge comparisons to operational precipitation profile corrections. *J. Appl. Meteor.* 34 (12), 2612–2630. doi:10.1175/1520-0450(1995)034<2612:taorct>2.0.co;2

Kang, J., Wang, H., Yuan, F., Wang, Z., Huang, J., and Qiu, T. (2020). Prediction of precipitation based on recurrent neural networks in jingdezhen, jiangxi province, China. *Atmosphere* 11 (3), 246. doi:10.3390/atmos11030246

Kingma, D. P., and Ba, J. (2014). Adam: A method for stochastic optimization. arXiv e-prints, arXiv:1412.6980.

Koizumi, K. (1999). An objective method to modify numerical model forecasts with newly given weather data using an artificial neural network. *Weather Forecast.* 14 (1), 109–118. doi:10.1175/1520-0434(1999)014<0109:aomtmn>2.0.co;2

Krämer, S., Verworn, H. R., and Redder, A. (2005). Improvement of X-band radar rainfall estimates using a microwave link. *Atmos. Res.* 77 (1-4), 278–299. doi:10.1016/j.atmosres.2004.10.028

Kroeger, T., Timofte, R., Dai, D., and Van Gool, L. (2016). "Fast optical flow using dense inverse search," in *Computer vision – eccv 2016*. Editors B. Leibe, J. Matas, N. Sebe, and M. Welling (New York: Springer International Publishing), 471–488.

Kumar, A., Islam, T., Sekimoto, Y., Mattmann, C., and Wilson, B. (2020). Convcast: An embedded convolutional LSTM based architecture for precipitation nowcasting using satellite data. *Plos one* 15 (3), e0230114. doi:10.1371/journal.pone.0230114

Le, J. A., El-Askary, H. M., Allali, M., and Struppa, D. C. (2017). Application of recurrent neural networks for drought projections in California. *Atmos. Res.* 188, 100–106. doi:10.1016/j.atmosres.2017.01.002

Li, X., Yang, Y., Mi, J., Bi, X., Zhao, Y., Huang, Z., et al. (2021). Leveraging machine learning for quantitative precipitation estimation from Fengyun-4 geostationary observations and ground meteorological measurements. *Atmos. Meas. Tech.* 14 (11), 7007–7023. doi:10.5194/amt-14-7007-2021

Liguori, S., and Rico-Ramirez, M. A. (2013). A review of current approaches to radar-based quantitative precipitation forecasts. *Int. J. River Basin Manag.* 12 (4), 391–402. doi:10.1080/15715124.2013.848872

Liguori, S., Rico-Ramirez, M. A., Schellart, A. N. A., and Saul, A. J. (2012). Using probabilistic radar rainfall nowcasts and NWP forecasts for flow prediction in urban catchments. *Atmos. Res.* 103, 80–95. doi:10.1016/j.atmosres.2011.05.004

Liu, Y., Xi, D.-G., Li, Z.-L., and Hong, Y. (2015). A new methodology for pixel-quantitative precipitation nowcasting using a pyramid Lucas Kanade optical flow approach. *J. Hydrology* 529, 354–364. doi:10.1016/j.jhydrol.2015.07.042

Lucas, B. D., and Kanade, T. (1981). "An iterative image registration technique with an application to stereo vision," in Proceedings of the 7th international joint conference on Artificial intelligence - Volume 2, Vancouver, BC, Canada, August 24 - 28, 1981 (Morgan Kaufmann Publishers Inc.).

Luo, C., Li, X., and Ye, Y. (2020). PFST-LSTM: A spatiotemporal LSTM model with pseudoflow prediction for precipitation nowcasting. *IEEE J. Sel. Top. Appl. Earth Obs. Remote Sens.* 14, 843–857. doi:10.1109/jstars.2020.3040648

Milewski, A., Elkadiri, R., and Durham, M. (2015). Assessment and comparison of TMPA satellite precipitation products in varying climatic and topographic regimes in Morocco. *Remote Sens.* 7 (5), 5697–5717. doi:10.3390/rs70505697

Met Office (2019). MIDAS Open: UK hourly weather observation data, v201901. Centre for Environmental Data Analysis. March, 01, 2019. doi:10.5285/c58c1af69b9745fda4cdf487a9547185

Pierce, C., Seed, A., Ballard, S., Simonin, D., and Li, Z. (2012). *Doppler radar observations: Weather radar, wind profiler, ionospheric radar, and other advanced applications*. London: IntechOpen, 97–142.

Pulkkinen, S., Nerini, D., Pérez Hortal, A. A., Velasco-Forero, C., Seed, A., Germann, U., et al. (2019). Pysteps: An open-source Python library for probabilistic precipitation nowcasting (v1.0). *Geosci. Model Dev.* 12 (10), 4185–4219. doi:10.5194/gmd-12-4185-2019

Ravuri, S., Lenc, K., Willson, M., Kangin, D., Lam, R., Mirowski, P., et al. (2021). Skilful precipitation nowcasting using deep generative models of radar. *Nature* 597 (7878), 672–677. doi:10.1038/s41586-021-03854-z

Schmidhuber, J. (2015). Deep learning in neural networks: An overview. *Neural Netw.* 61, 85–117. doi:10.1016/j.neunet.2014.09.003

Seo, D. J., Breidenbach, J. P., and Johnson, E. R. (1999). Real-time estimation of mean field bias in radar rainfall data. *J. Hydrology* 223 (3), 131–147. doi:10.1016/S0022-1694(99)00106-7

Shi, X., Chen, Z., Wang, H., Yeung, D.-Y., Wong, W.-K., and Woo, W.-c. (2015). "Convolutional LSTM network: A machine learning approach for precipitation nowcasting," in Advances in neural information processing systems, Montreal Canada, December 7 - 12, 2015.28

Shi, X., Gao, Z., Lausen, L., Wang, H., Yeung, D.-Y., Wong, W.-k., et al. (2017). "Deep learning for precipitation nowcasting: A benchmark and a new model," in Advances in neural information processing systems, Long Beach California USA, December 4 - 9, 2017.30

Song, Y., Han, D., and Zhang, J. (2017). Radar and rain gauge rainfall discrepancies driven by changes in atmospheric conditions. *Geophys. Res. Lett.* 44 (14), 7303–7309. doi:10.1002/2017gl074493

Speiser, J. L., Miller, M. E., Tooze, J., and Ip, E. (2019). A comparison of random forest variable selection methods for classification prediction modeling. *Expert Syst. Appl.* 134, 93–101. doi:10.1016/j.eswa.2019.05.028

Sun, J. (2005). Convective-scale assimilation of radar data: Progress and challenges. *Q. J. R. Meteorol. Soc.* 131 (613), 3439–3463. doi:10.1256/qj.05.149

Sun, J., Xue, M., Wilson, J. W., Zawadzki, I., Ballard, S. P., Onvlee-Hooimeyer, J., et al. (2014). Use of NWP for nowcasting convective precipitation: Recent progress and challenges. *Bull. Am. Meteorol. Soc.* 95 (3), 409–426. doi:10.1175/bams-d-11-00263.1

Sun, P., Ma, Z., Zhang, Q., Singh, V. P., and Xu, C.-Y. (2022). Modified drought severity index: Model improvement and its application in drought monitoring in China. *J. Hydrol.* 612, 128097.

Tian, L., Li, X., Ye, Y., Xie, P., and Li, Y. (2019). A generative adversarial gated recurrent unit model for precipitation nowcasting. *IEEE Geosci. Remote Sens. Lett.* 17 (4), 601–605. doi:10.1109/lgrs.2019.2926776

Valverde Ramírez, M. C., de Campos Velho, H. F., and Ferreira, N. J. (2005). Artificial neural network technique for rainfall forecasting applied to the São Paulo region. *J. Hydrology* 301 (1), 146–162. doi:10.1016/j.jhydrol.2004.06.028

Van, S. P., Le, H. M., Thanh, D. V., Dang, T. D., Loc, H. H., and Anh, D. T. (2020). Deep learning convolutional neural network in rainfall–runoff modelling. *J. Hydroinformatics* 22 (3), 541–561. doi:10.2166/hydro.2020.095

Vila, D. A., Machado, L. A. T., Laurent, H., and Velasco, I. (2008). Forecast and tracking the evolution of cloud clusters (ForTraCC) using satellite infrared imagery: Methodology and validation. *Weather Forecast.* 23 (2), 233–245. doi:10.1175/2007waf2006121.1

Villarini, G., and Krajewski, W. F. (2009). Review of the different sources of uncertainty in single polarization radar-based estimates of rainfall. *Surv. Geophys.* 31 (1), 107–129. doi:10.1007/s10712-009-9079-x

Warner, B., and Misra, M. (1996). Understanding neural networks as statistical tools. *Am. Statistician* 50 (4), 284–293. doi:10.1080/00031305.1996.10473554

Wilson, J. W., Feng, Y., Chen, M., and Roberts, R. D. (2010). Nowcasting challenges during the beijing olympics: Successes, failures, and implications for future nowcasting systems. *Weather Forecast.* 25 (6), 1691–1714. doi:10.1175/2010waf2222417.1

Woo, W.-c., and Wong, W.-k. (2017). Operational application of optical flow techniques to radar-based rainfall nowcasting. *Atmosphere* 8 (12), 48. doi:10.3390/atmos8030048

Wang, Y., Coning, E. D., Harou, A., Jacobs, W., Joe, P., Nikitina, L., et al. (2017). Guidelines for nowcasting techniques. Available at: public.wmo.int/en/resources/bulletin/nowcasting-guidelines-%E2%80%93-summary (Accessed December 3, 2022).

Xia, K.-W., Li, C.-B., and Shen, J.-Y. (2005). An optimization algorithm on the number of hidden layer nodes in feed-forward neural network. *Comput. Sci.* 32 (10), 143–145.

Yang, Q., Dai, Q., Han, D., Zhu, Z., and Zhang, S. (2020). Uncertainty analysis of radar rainfall estimates induced by atmospheric conditions using long short-term memory networks. *J. Hydrology* 590, 125482. doi:10.1016/j.jhydrol.2020.125482

Zahraei, A., Hsu, K.-l., Sorooshian, S., Gourley, J. J., Hong, Y., and Behrangi, A. (2013). Short-term quantitative precipitation forecasting using an object-based approach. *J. Hydrology* 483, 1–15. doi:10.1016/j.jhydrol.2012.09.052

Zhu, D., Xuan, Y., and Cluckie, I. (2014). Hydrological appraisal of operational weather radar rainfall estimates in the context of different modelling structures. *Hydrol. Earth Syst. Sci.* 18 (1), 257–272. doi:10.5194/hess-18-257-2014

frontiers | Frontiers in Environmental Science

TYPE Methods
PUBLISHED 11 April 2023
DOI 10.3389/fenvs.2023.1137372

OPEN ACCESS

EDITED BY
Shao Sun,
Chinese Academy of Meteorological Sciences, China

REVIEWED BY
Qinmei Han,
National Climate Center, China
Lu Gao,
Fujian Normal University, China

*CORRESPONDENCE
Haiyan Guo,
ghy-824@163.com

SPECIALTY SECTION
This article was submitted to Atmosphere and Climate, a section of the journal Frontiers in Environmental Science

RECEIVED 04 January 2023
ACCEPTED 17 March 2023
PUBLISHED 11 April 2023

CITATION
Xu Y, Guo H, Liu J, Sun R and Li X (2023), Wildfire risks under a changing climate: Synthesized assessments of wildfire risks over southwestern China.
Front. Environ. Sci. 11:1137372.
doi: 10.3389/fenvs.2023.1137372

Wildfire risks under a changing climate: Synthesized assessments of wildfire risks over southwestern China

Yuanxin Xu[1,2], Haiyan Guo[1,2]*, Jia Liu[1,2,3], Rui Sun[1,2] and Xiaolan Li[1,2]

[1]Sichuan Climate Center, Laboratory of Climate Resources Application, Sichuan Meteorological Administration, Chengdu, Sichuan, China, [2]Heavy Rain and Drought-Flood Disasters in Plateau and Basin Key Laboratory of Sichuan Province, Chengdu, Sichuan, China, [3]Research Center of Mountain Development, Institute of Mountain Hazards and Environment, Chinese Academy of Science, Chengdu, Sichuan, China

Wildfire events in southwestern China resulted in catastrophic loss of property and human life, and the localized wildfire risks show differentiated trends under global warming scenarios. In the case of quantitating climate impacts and localizing wildfire risks, synthesized assessments of wildfire risks of high-incident areas in southwestern China are established and mapped in this article, constituted by three essential elements: hazard, vulnerability, and disaster prevention/mitigation capacity. The hazard group includes vegetation ignitability and fire spreading related to climate and topography factors. Public and economic characteristic elements belong to the vulnerability and disaster prevention/mitigation capacity group based on their functions and influences on wildfire events. Each aspect and group are rated by the historical wildfire site records and weighted by the entropy weight method and analytic hierarchy process. Assessments indicate that most very high wildfire risk girds are distributed in the west of 103°E and the north of 28°N, covering an area of over 26,500 km^2, mainly in low-altitude suburban regions in basins and valleys with high climate hazards. The highly localized wildfire risk maps specified both stresses of fire prevention/mitigation in each grid cell and general spatial patterns of wildfire risks, thereby enhancing the understanding of both current and future patterns of wildfire risks and thus helping improve suppression and prevention policies.

KEYWORDS

wildfire, climate change, hazard, vulnerability, risk mapping, Southwest China

1 Introduction

Under the background of global warming, exposure to wildfire is a growing public health concern worldwide (Flannigan and Harrington, 1988; Flannigan et al., 2000; Ozturk et al., 2010; Diffenbaugh et al., 2017; Hallema et al., 2018; AghaKouchak et al., 2020). In southwestern China, frequency, severity, and extent of wildfire events have increased with the warming and drying trends over this region (Sun et al., 2014). The population growth and expansion of inhabited areas also amplify the risks and vulnerabilities to wildfires (Jolly et al., 2015; Gong et al., 2019a; Artés et al., 2019; Gong et al., 2019b). During 2004–2020, the total burnt areas in the high-wildfire frequency region of southwestern China increased at a rate of nearly 2 km^2 per year

(Wang et al., 2018), while the annual period of wildfire, referred to as "fire weather season," extends, with an earlier beginning date and a delayed ending date of wildfire events. Growing risks and vulnerabilities to wildfire result in unprecedented damage and public health problems in both the southwestern region and the whole of China.

Recent evidence suggests that the critical inducing factors of wildfires in southwestern China aim to increase disaster risks under a changing climate (IPCC, 2012; Ma, 2020; Zhao et al., 2021). As the most variable and most prominent drivers of regional wildfires, warmer and dryer weather conditions have led to more severe fires in recent years (Petoukhov et al., 2018; Ball et al., 2021). Since the 1970s, the temperature in southwestern China has been rising at the rate of 0.1°C–0.3°C per decade, and high-latitude areas have become warmer. Precipitation reduces at the rate of 9.4 mm per decade, with an increase in maximum continuous rain-free days, and related humidity decreases at the rate of 0.4% per decade, especially after 2010 (Ma, 2020; Zhao et al., 2021; Zhao et al., 2022). The increase in the number of climate extremes, like heat waves and aridity, also affect wildfire frequency and severity (Gao et al., 2017; Taufik et al., 2017; Wu et al., 2017).

Risk mappings are effective ways to manage natural disaster risks (Jaiswal et al., 2002; Pan et al., 2016; Pickell et al., 2017; Shi and Touge, 2022). Extensive research has shown that wildfire risk mappings can point out locations where a fire is likely to start and locations which enable easy fire spreading, thereby providing precise assessments of wildfire disasters and decisions on solution methods (Goetz et al., 2006; McKenney et al., 2008; Hijmans et al., 2010). Previous research on wildfire risk mapping mainly focuses on topography and vegetation factors (Bessie and Johnson, 1995; Jaiswal et al., 2002; Gralewicz et al., 2012; Collins et al., 2013; Salaheddine et al., 2017) but does not consider climate factors, especially spatial patterns of climate indices, in much detail.

The specific objective of this study is to provide a comprehensive and strict wildfire risk mapping in the areas with exceptionally high wildfire rates in southwestern China. The basic theoretical framework of risk assessment applied in this manuscript follows the natural disaster risk-based zonation method. The analysis of wildfire hazard refers to the probability distribution assessment of natural characteristics of the wildfire-formative environment and inducing factors, and vulnerability refers to the likelihood and severity of wildfire damage (Flannigan et al., 2000). Prevention/mitigation capacities represent the ability to avoid and mitigate possible wildfire damage. The risk of wildfire is the synthesis of hazard, vulnerability, and prevention/mitigation capacities, representing the levels of wildfire damage probability of specific space units. The multi-factor complete analysis method includes the assessments and interactions of climate and environmental inducing factors, vulnerabilities, and disaster prevention/mitigation capacities in this area. The paper is organized as follows: Section 2 provides method description. Section 3 deals with the factors responsible for wildfire risks, vulnerability, and disaster prevention. Section 4 describes each factor group's weighting processing and mapping results. Section 5 deals with relevant discussion and conclusion.

2 Data and methods

2.1 Study area

The study area is the wildfire high-incident areas in southwestern China, at 25.3°N~29°N, 99°E~104°E, covering an area of 120,440 km^2, neighboring the Tibet Plateau. Topographic features vary from the western mountain plateau to the eastern valley plain, which stretches over 39 county-level administrative units. Altitudes decline from west to east, and the highest point is located in the northeastern part of the study area with an altitude of 5,958 m (Figure 1). Climate data from 36 gauges are applied in this study, which are evenly distributed in the study area. According to the climatic regionalization of China, the four dominant climatic regions over the study area are the southern subtropical sub-humid zone, the northern and central subtropical humid zones, and the highland temperate humid-sub-humid zone. Most of the study area falls in the middle of the Jinsha River valley, featuring four obscure seasons and clear rainy and dry seasons, abundant sunshine, and intense evaporation; the annual evaporation in this region reaches three times the annual precipitation; 92% of the precipitation in this region falls from June to October, namely, the rainy season. March–May is the driest period in the year, with an average relative humidity of less than 40%.

The study area belongs to the southwestern forest zone. The vegetation in the sunny slope regions is mainly *Pinus densata* and Chinese pine (*Pinus tabuliformis*) while in the shady slope and gorge regions is theropencedrymions constituted by hemlocks (*Tsuga chinensis*), *Acer* spp., and *Betula* spp. Subalpine coniferous forests are also distributed in the high-latitude area.

2.2 Data sources

All the climate models are resolved using a 90 m*90 m digital elevation model of the study area, which is constructed using the 2000 global version 4 SRTM 90 m digital elevation data downloaded from the National Tibetan Plateau Data Center.

The observation datasets of daily temperature, precipitation, wind speed, and relative humidity for the period 1981–2021 are provided by the Sichuan Climate Center and Yunnan Climate Center, referring to 36 meteorological stations.

The land cover dataset is obtained from FROM-GLC (Finer Resolution Observation and Monitoring of Global Land Cover) which produces the first 30 m resolution global land cover maps using Landsat Thematic Mapper (TM) and Enhanced Thematic Mapper Plus (ETM+) data (http://data.ess.tsinghua.edu.cn/). The data sets of population density, settlements and road networks are provided by the Geographic Data Sharing Infrastructure of Peking University (http://geodata.pku.edu.cn).

2.3 Interpolation

Partial thin plate splines implemented in ANUSPLIN are applied for smoothing in this study (Hutchinson, 1991; Hutchinson, 1993; Hutchinson, 1995; Hutchinson, 2004). ANUSPLIN is a suite of programs that employs a multi-dimensional Laplacian partial thin

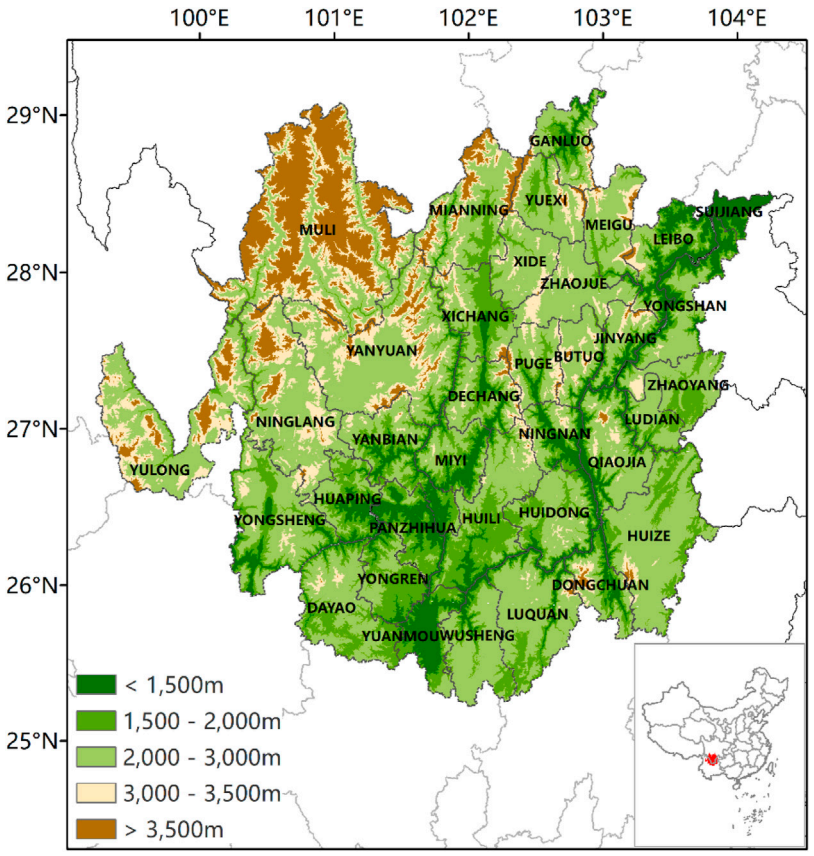

FIGURE 1
Topography and location of the study area.

TABLE 1 Weights assigned to factors and groups for wildfire risk modeling.

Element	Group	Factor
Hazards (weighting coefficient = 0.725)	Climate (weighting coefficient = 0.4601)	Ensemble mean of average daily temperature (weighting coefficient = 0.1327)
		Annual maximum of daily temperature maximum (weighting coefficient = 0.1549)
		Annual minimum of daily temperature minimum (weighting coefficient = 0.1517)
		Wind speed (weighting coefficient = 0.1691)
		Relative humidity (weighting coefficient = 0.1598)
		Annual consecutive precipitation-free days maximum (weighting coefficient = 0.2319)
	Topography (weighting coefficient = 0.2649)	Altitude (weighting coefficient = 0.6964)
		Slope (weighting coefficient = 0.215)
		Aspect (weighting coefficient = 0.0886)
Vulnerability (weighting coefficient = 0.1684)		Vegetation type (weighting coefficient = 0.4228)
		Vegetation coverage (weighting coefficient = 0.3383)
		Population density (weighting coefficient = 0.0648)
		Distance from habitats and settlements (weighting coefficient = 0.1742)
Prevention/mitigation capacity (weighting coefficient = 0.1066)		Distance from roads (weighting coefficient = 0.3889)
		Distance from waterbodies (weighting coefficient = 0.6111)

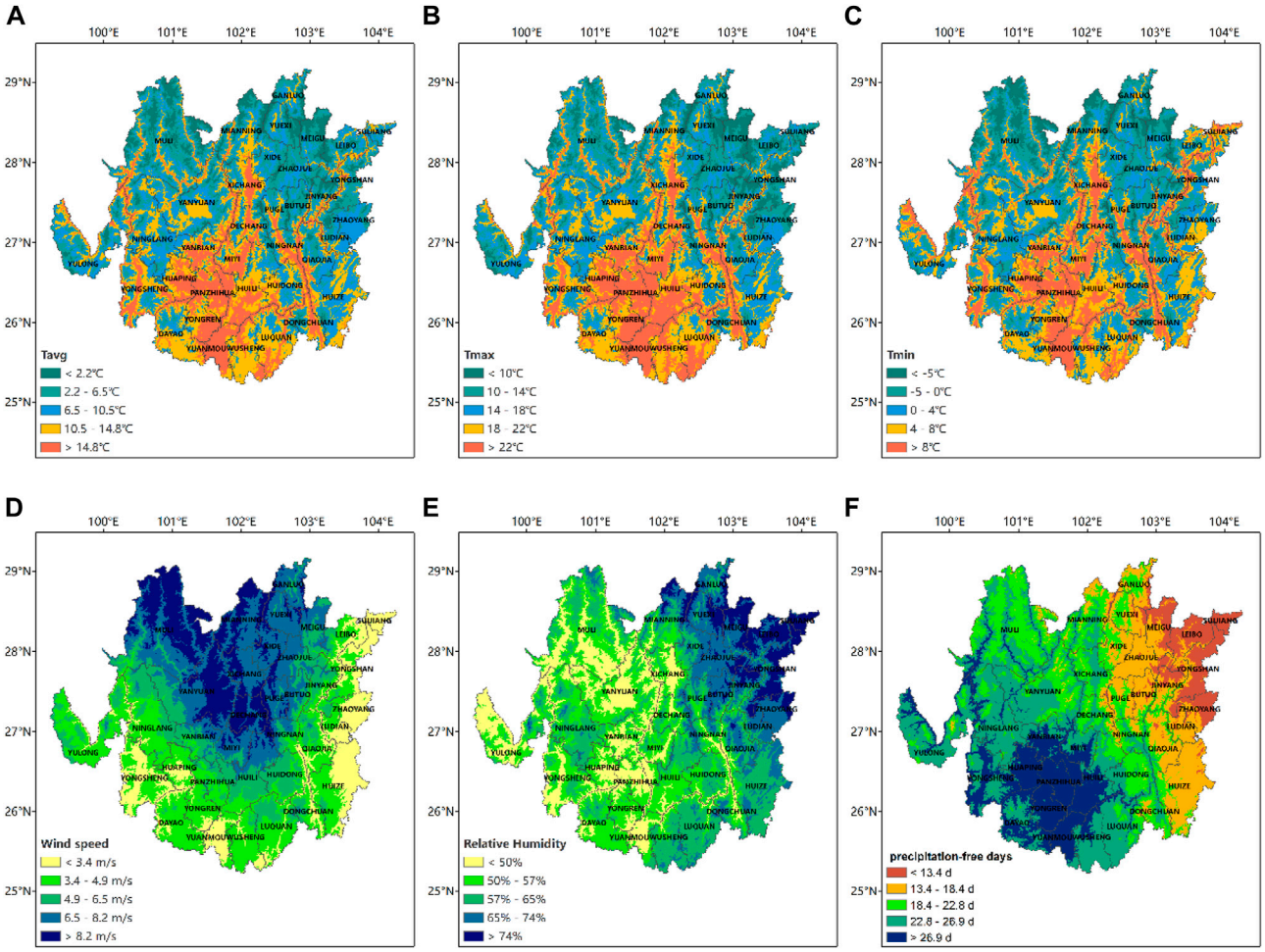

FIGURE 2
Spatial pattern of climate hazard factors in historical baseline (1981–2020) over high wildfire incident area of southwestern China. **(A)** Ensemble means of daily temperature average. **(B)** Annual maximum of daily temperature maximum. **(C)** Annual minimum of daily humidity. **(D)** Wind speed. **(E)** Relative humidity. **(F)** Annual consecutive precipitation-free days maximum.

plate smoothing spline method. The equation of the theoretical statistic model is listed as follows:

$$\boldsymbol{Z_i} = \boldsymbol{f}(\boldsymbol{x_i}) + \boldsymbol{b}^T \boldsymbol{y_i} + \boldsymbol{e_i} \quad (\boldsymbol{i} = \boldsymbol{1}, \cdots, \boldsymbol{N}), \tag{1}$$

where $\boldsymbol{Z_i}$ is the dependent variable at i point of the specified space, $\boldsymbol{f}(\boldsymbol{x_i})$ is the unascertained smooth function of $\boldsymbol{x_i}$, $\boldsymbol{x_i}$ is the independent variable, $\boldsymbol{y_i}$ is the p-dimensional independent concomitant variable, $\boldsymbol{b}$ is the p-dimensional coefficient of $\boldsymbol{y_i}$, and $\boldsymbol{e_i}$ is the random error.

In Eq. 1, the function of $\boldsymbol{f}(\boldsymbol{x_i})$ and coefficient b are estimated by the least square method:

$$\sum_{i=1}^{N} \left[\frac{z_i - \boldsymbol{f}(\boldsymbol{x_i}) - \boldsymbol{b}^T \boldsymbol{y_i}}{\boldsymbol{w_i}} \right]^2 + \rho \boldsymbol{J_m}(\boldsymbol{f}), \tag{2}$$

where $\boldsymbol{J_m}(\boldsymbol{f})$ is the roughness measure function of $\boldsymbol{f}(\boldsymbol{x_i})$, defined as the $\boldsymbol{m}$-order partial derivative of function $\boldsymbol{f}$, namely, the order of spline (roughness) function. $\boldsymbol{\rho}$ is the positive smoothing parameter.

2.4 Weighting functions

The entropy weight method estimates the weighting coefficient based on the variability of indices. For a specified index, the less the information entropy ($\boldsymbol{E_j}$) it holds, the higher the variability, the information it carries, its significance in synthesized evaluation, and *vice versa*. The entropy weight method is applied in the following manner:

If there are $\boldsymbol{n}$ factors and $\boldsymbol{m}$ indices, the orthogonal matrix is

$$\boldsymbol{X} = \begin{Bmatrix} \boldsymbol{x_{11}}, \boldsymbol{x_{12}}, \cdots, \boldsymbol{x_{1m}} \\ \boldsymbol{x_{21}}, \boldsymbol{x_{22}}, \cdots, \boldsymbol{x_{2m}} \\ \vdots \quad \vdots \quad \ddots \quad \vdots \\ \boldsymbol{x_{n1}}, \boldsymbol{x_{n2}}, \cdots, \boldsymbol{x_{nm}} \end{Bmatrix}. \tag{3}$$

If $\boldsymbol{Z}$ is the standardized matrix (3), then

$$\boldsymbol{Z_{ij}} = \frac{\boldsymbol{x_{ij}}}{\sqrt{\sum_{i=1}^{n} \boldsymbol{x_{ij}^2}}}. \tag{4}$$

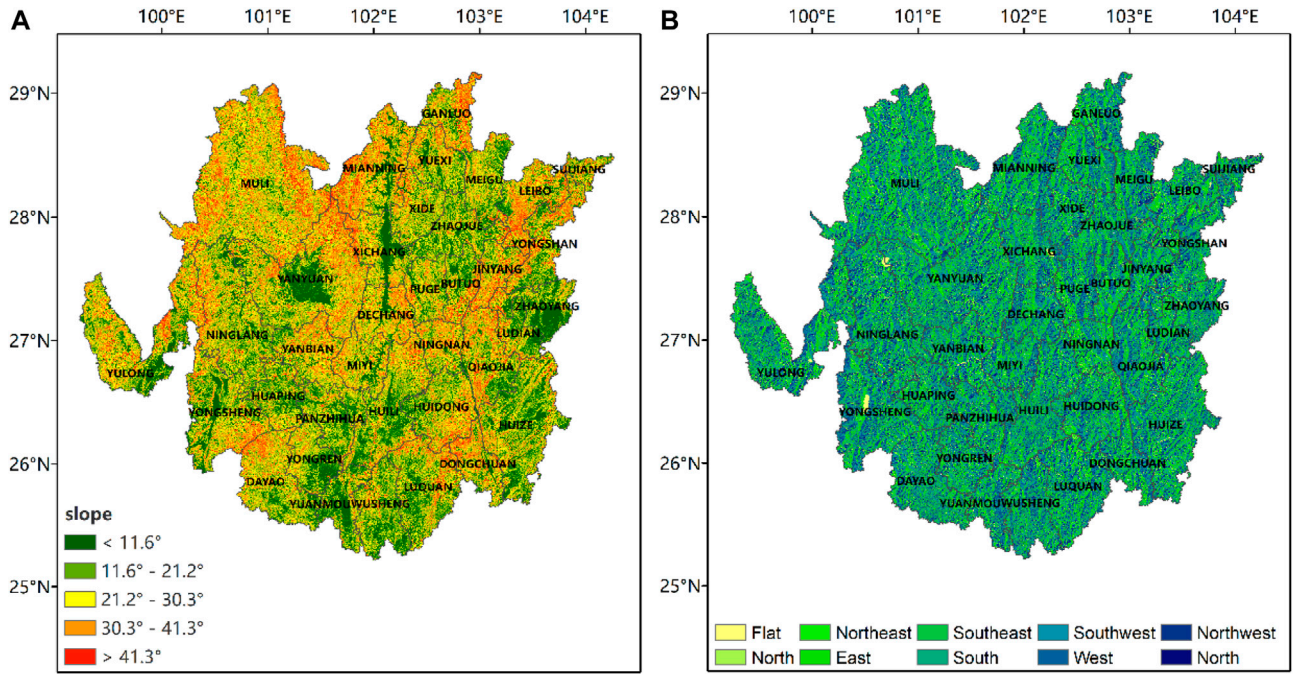

FIGURE 3
Spatial pattern of topography hazard factors over the high-wildfire incident area in southwestern China. **(A)** Slope. **(B)** Aspect.

TABLE 2 Classifications of altitudes.

Altitude/m	Frequency of fire site records	Proportion of fire site records/%	Risk level
956–1,356	63	29.03	4
1,356–1,776	66	30.41	5
1,776–2,196	39	17.97	3
2,196–2,576	31	14.29	2
2,576–3,048	18	8.3	1

If $\boldsymbol{P}$ is the probability matrix, then

$$\boldsymbol{P}_{ij} = \frac{\widetilde{\boldsymbol{Z}_{ij}}}{\sum_{i=1}^{n} \widetilde{\boldsymbol{Z}_{ij}}}. \tag{5}$$

The information entropy of index $\boldsymbol{j}$ is

$$\boldsymbol{e}_j = -\frac{1}{\ln \boldsymbol{n}} \sum_{i=1}^{n} \boldsymbol{p}_{ij} \ln\left(\boldsymbol{p}_{ij}\right) \left(\boldsymbol{j} = 1, 2, \cdots, \boldsymbol{m}\right). \tag{6}$$

$\boldsymbol{d}_j$ is defined as the information utility and given as

$$\boldsymbol{d}_j = 1 - \boldsymbol{e}_j \tag{7a}$$

Then, the entropy weight $\boldsymbol{W}_j$of index $\boldsymbol{j}$ is

$$\boldsymbol{W}_j = \frac{\boldsymbol{d}_j}{\sum_{j=1}^{m} \boldsymbol{d}_j}. \tag{7b}$$

2.5 Weighting coefficients

The synthesized wildfire risk mapping over the study area integrates weighted elements of hazard, vulnerability, and prevention/mitigation capacity. Each aspect is sub-superposed by weighted factors. The entropy weight method is applied when there is a linear correlation between a factor and the related risk element. Otherwise, an analytic hierarchy process is employed. Once the weighting results pass the consistency check, all the factors are rated on a scale of 1–5 except the factor of vegetation type (rated on a scale of 1–4). The weighting coefficients of chosen factors and risk mapping elements are listed in Table 1.

The weighting result indicates that the dominant factors are altitude and annual consecutive precipitation-free days maximum, followed by relative humidity, wind speed, and vegetation coverage. The factor rating of altitude reflects both human activities and

TABLE 3 Classifications of slopes.

Slope/°	Frequency	Proportion of fire site records/%	Risk level
0–11	59	27.19	4
11–22	65	29.95	5
22–33	53	24.42	3
33–44	32	14.75	2
44–54	8	3.69	1

TABLE 4 Classifications of aspects.

Aspect	Frequency of fire site records	Proportion of fire site records/%	Risk level
Flat	0	0	1
North	11	5.07	2
Northeast	19	8.76	3
East	17	7.83	3
Southeast	15	6.91	2
South	41	18.89	5
Southwest	40	18.43	5
West	43	19.82	5
Northwest	31	14.29	4

vegetation inflammability. Factors that point to vegetation desiccation and wildfire spreading also play essential roles in risk mapping. Prevention/mitigation capacity holds the lowest weight due to its uncertainty and high dependency on public infrastructures in actual situations.

2.6 Synthesized risk assessment model

According to the forming and spreading conditions of wildfire and hazard criticality assessment methodology, the synthesized assessment model is comprised of three main modules representing the core of the wildfire risk assessment: the hazard (comprising the climate group and topology group), vulnerability, and prevention modules. The modules and each element inside are composed based on the integrated weight linear method. The synthesized wildfire risk assessment model of southwestern China is listed as follows (all of the elements are normalized):

Hazard module: H = 0.4601*(0.1327* ensemble mean of daily temperature average + 0.1549* annual maximum of daily temperature maximum + 0.1517* annual minimum of daily temperature minimum + 0.1691* wind speed − 0.1598* relative humidity + 0.2319* annual consecutive precipitation-free days maximum) + 0.2649*(0.6964* altitude + 0.215* slope + 0.0886* aspect).

Vulnerability module: V = 0.4228* vegetation type + 0.3383* vegetation coverage + 0.0648* population density.

Prevention/mitigation capacity module: p = 0.1742* distance from habitats and settlements + 0.3889* distance from roads + 0.6111* distance from waterbodies.

The synthesized risk assessment model: Risk = 0.725*H + 0.1684*V − 0.1066*P.

3 Factors applied in the risk assessment

3.1 Wildfire hazard criticalities

3.1.1 Climate

The literature on wildfires has highlighted several climate-inducing factors: temperature, wind speed, relative humidity, and precipitation (Sun et al., 2014; Jolly et al., 2015; Pan et al., 2016; Pickell et al., 2017). All of these factors act on vegetation water content and ignition points. Wildfires are easy to start and spread in a high-temperature dry environment and *vice versa*. This study divides temperature factors into an ensemble mean of the daily average, annual maximum, and annual minimum. A significant advantage of this division is ensuring complete consideration of the effects of extreme temperature spatial patterns of wildfires. With the rapid increase in extreme precipitation events in this area, annual consecutive precipitation-free days maximum

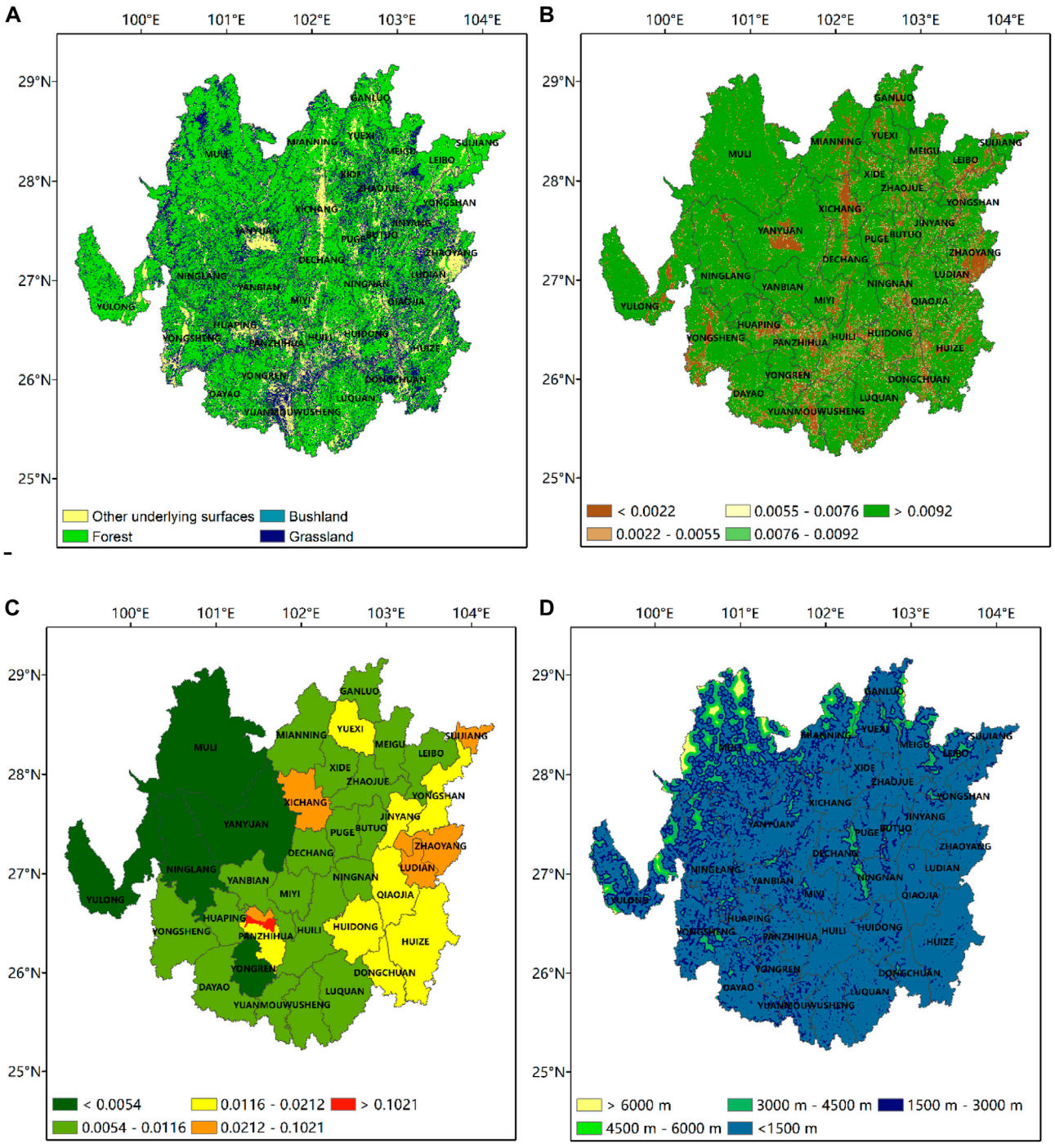

FIGURE 4
Spatial pattern of vulnerability factors over the high-wildfire incident area in southwestern China. **(A)** Vegetation type. **(B)** Vegetation coverage. **(C)** Population density. **(D)** Distance from habitats and settlements.

characterize the status of vegetation moisture content better than a single index of precipitation amount. The wind speed affects both combustible contents and wildfire spread by expediting evaporation and airflow. The aforementioned three factors are positive indices. Wildfire risks increase with an increase in the three factors. The relative humidity factor is an exception. With the increase in relative humidity, the moisture of vegetation increases, and ignitability declines after that.

All the aforementioned climate factors in a historical baseline of 1981–2020 are interpolated to the study area at a resolution of

TABLE 5 Classifications of distance from habitats and settlements.

Distance from habitats and settlements (m)	Proportion of fire site records (%)	Vulnerability level
<1,500	45.35	4
1,500–3,000	47.21	5
3,000–4,500	6.28	3
4,500–6,000	0.93	2
>6,000	0.23	1

TABLE 6 Classifications of distance from roads.

Distance from roads (m)	Prevention/mitigation capacity level
<500	5
500–1,000	4
1,000–1,500	3
1,500–2,000	2
>2,000	1

100 m*100 m using partial thin plate smoothing splines, as implemented in ANUSPLIN (Hutchinson, 1991; Hutchinson, 2004). These temperature maps show that the southern part of the study area experiences the highest ensemble mean of annual average temperature, especially in the belting river valley area. By comparison, the low-temperature area is mainly distributed in high-altitude localities. It is worth noting that in the northeastern part of the study area, the variations arising between the ensemble means of annual minimum and maximum are relatively less than those arising in the other factors (Figures 2A–C).

Annual consecutive precipitation-free day maximum of rain gauge records in the study area ranges from 7.8 to 37.6 d/a, with the highest exceeding 26.9 d/a in the southwestern part and west valley of the study area. Meanwhile, the lowest annual consecutive precipitation-free day maximum, i.e., less than 13.4 d/a, is recorded in the northeastern and eastern mountain areas (Figure 2D).

The ensemble mean of average daily wind speed records ranges from 1.0 to 9.1 m/s. Wind speed greater than 8.2 m/s is reported in the northern and central parts of the study area, which decreases toward the periphery. The lowest wind speed, i.e., less than 3.4 m/s, mainly occurs in the outer ring of the study area. The spatial pattern of wind speed is distinctly different from other climate factors (Figure 2E).

According to previous research, a wildfire is likely to occur when the relative humidity is below 65% (Pan et al., 2016). Relative humidity below 65% occurs in over 69.4% of the study area. Unlike the spatial patterns of temperature, the relative humidity of the study area decreases from west to east in general. Particularly, in the southwestern part, the low relative humidity occurs in low-altitude areas with intensive drainage networks abnormally (Figure 2F).

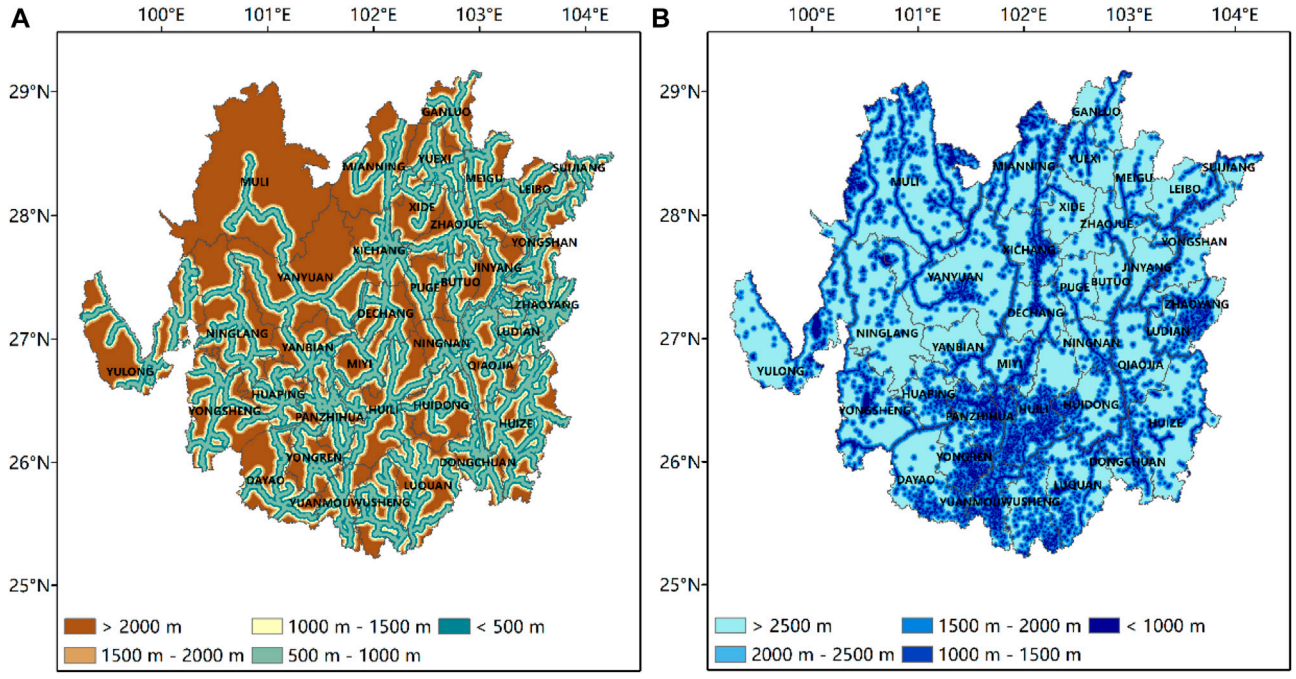

FIGURE 5
Spatial pattern of wildfire prevention/mitigation capacity factors over the high-wildfire incident area in southwestern China. **(A)** Distance from roads. **(B)** Distance from waterbodies.

TABLE 7 Classifications of distance from waterbodies.

Distance from waterbodies (m)	Prevention/mitigation capacity level
<500	5
500–1,000	5
1,000–1,500	4
1,500–2,000	3
2,000–2,500	2
2,500–3,000	1
>3,000	1

3.1.2 Topography

Since the relationship between topographical factors and wildfire risks is non-linear, in this study, the wildfire risk levels of altitude, slope degrees, and aspects are grouped based on the study area's 2017–2021 historical wildfire records, the spatial patterns of topographical factors can be seen in Figure 3. Detailed classifications of altitude, slope degrees, and aspects are listed in Tables 2–4.

3.2 Vulnerability

3.2.1 Vegetation types

According to the inflammability of different vegetation types (Dimitrakopoulos and Papaioannou, 2001; Hall et al., 2010; Corona et al., 2014), the study area is divided into grasslands, bushlands, forests, and other underlying surfaces, and the vulnerabilities of each type decrease in turn. Forests stretch over 57.54% of the study area and account for the most significant proportion. Grasslands hold the highest vulnerability level, accounting for 25.63% of the study area (Figure 4A).

3.2.2 Vegetation coverage

The vegetation proportion raster dataset is constituted by the vegetation coverage of each 100 m*100 m grid (Figure 4B). The vegetation coverage in the northeastern part is relatively higher than that in other parts. The distribution illustrates the urbanization rate of the study area as well. The details with low vegetation coverage often refer to urbanized regions.

3.2.3 Population exposure

With the densification of the population, the vulnerability to wildfires increases. The distribution of population density is in accordance with urbanization rates. The lowest population density

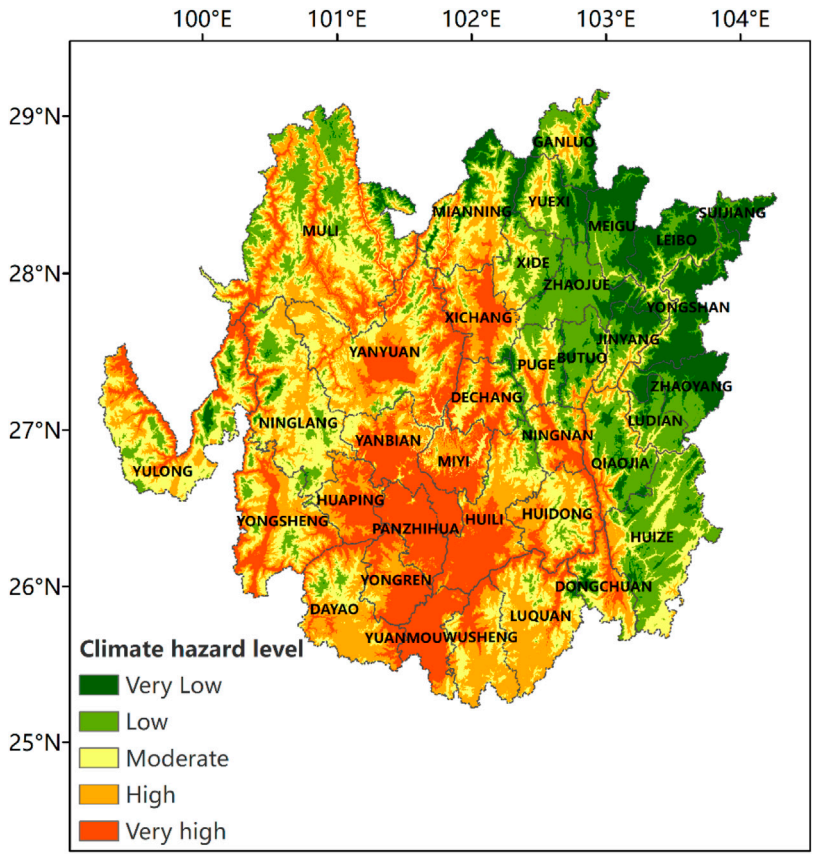

FIGURE 6
Spatial pattern of climate hazards.

occurs in the northeastern part of the study area, with a population density of less than 54 people/km^2. By comparison, the economic center located in the southern study area has a population density of over 1,000 people/km^2 (Figure 4C).

3.2.4 Distance from habitats and settlements

Human activities of habitation and culture can lead to accidental wildfires (Moreira et al., 2012). Meanwhile, the losses of wildfire disasters tend to increase with the distances from habitats and settlements. Wildfires rarely break out or spread very close (e.g., within a distance of 500 m) to habitats and colonies because of the cautious fire use and the rapid putting out. Hence, the correlation between vulnerability and distances from habitats and settlements is non-linear. Based on previous research, wildfire disasters most frequently occur between 1,500 and 3,000 m, followed by a space of less than 1,500 m. No wildfire records are found beyond 9,000 m from habitats and settlements (Figure 4D). The vulnerability levels of distances from habitats and settlements are listed in Table 5.

3.3 Wildfire prevention/mitigation capacity

3.3.1 Distance from roads

Distance from roads is the index that refers to both wildfire proneness and mitigation capacities. On the one hand, frequent human activities near roads induce accidental fire opportunities. On the other hand, emergency departments can monitor wildfires near roads at the preliminary stage, and fire engines and other fire control equipment can rapidly respond to fire alarms. As a factor of wildfire prevention/mitigation capacities, the effect of distances of 2 km from roads could be neglected. In this study, the county-level road networks and distances from roads are considered the practical parts of wildfire prevention/mitigation capacity due to the applicabilities of firefighting infrastructures. The prevention/mitigation capacity levels of distances from roads are listed in Table 6, and the spatial patterns are shown in Figure 5A.

3.3.2 Distance from waterbodies

As the source of the fire water system, the location and availability of natural waterbodies are important elements of wildfire prevention/mitigation capacity. The availability of a natural waterbody declines as the distance between fire points and the waterbody increases. The prevention/mitigation capacity levels of distance from waterbodies are listed in Table 7, and the spatial patterns are shown in Figure 5B.

4 Results

4.1 Hazard criticalities

The element of hazard manifests both ignition possibility and wildfire spreading. High and very high climate hazard areas are mainly located west of 103°E, with belts distributed along valleys and

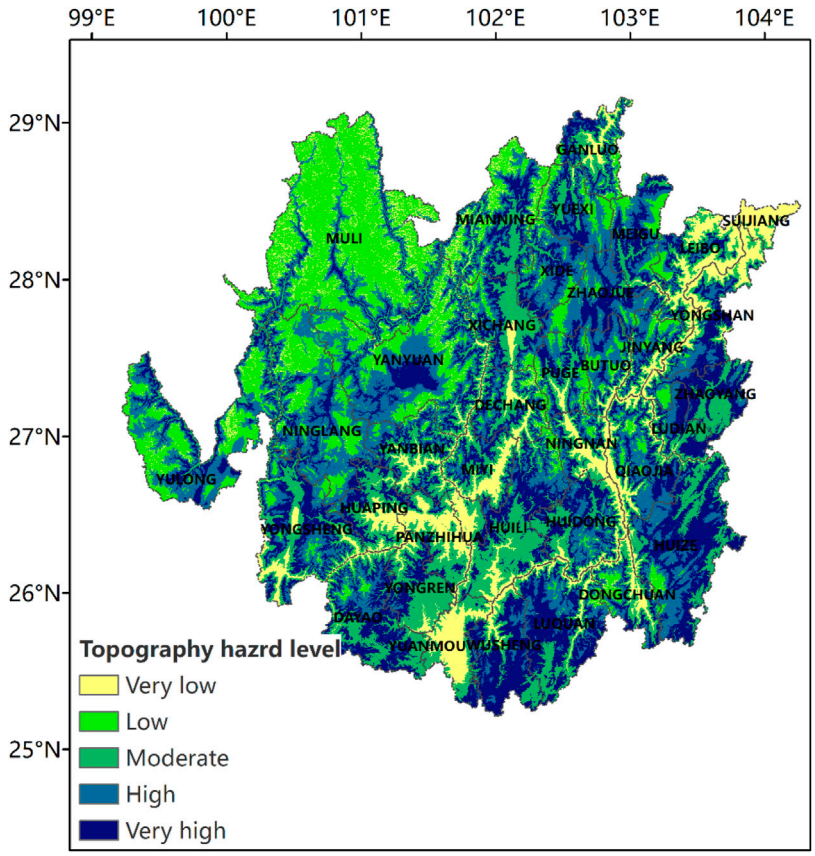

FIGURE 7
Spatial pattern of topography hazards.

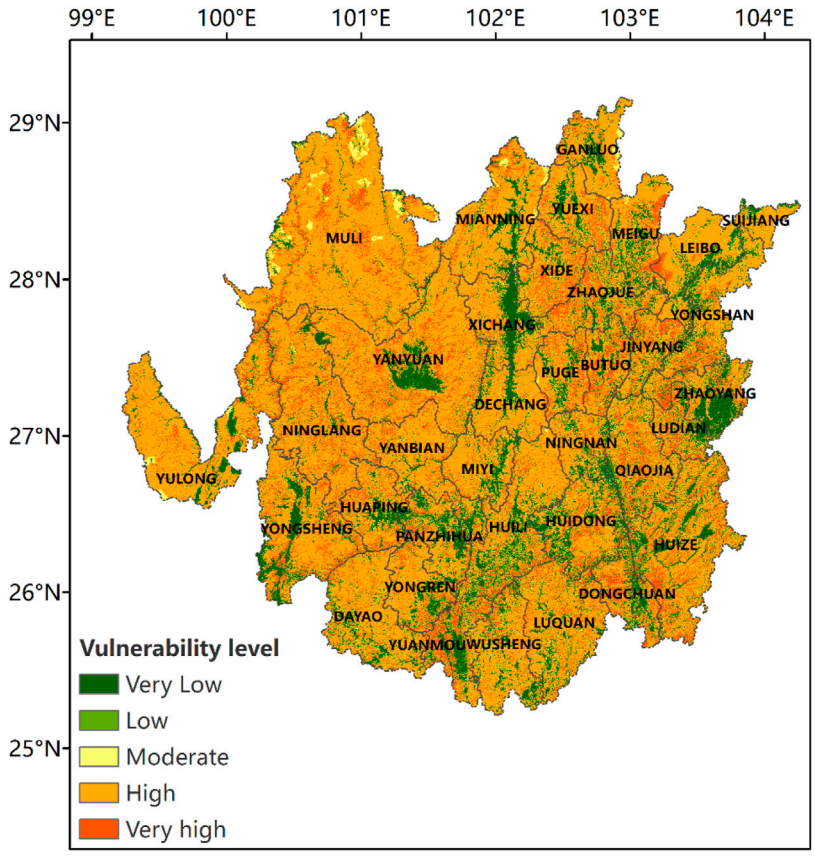

FIGURE 8
Spatial pattern of vulnerability.

basins, accounting for 45.81% of the study area. Universal features of high and very high climate hazard areas are relatively high temperatures, low relative humidity, and long consecutive precipitation-free days. Very low and low climate hazard areas fall in the northeastern study area, east of 103°E, between 27 and 29°N, accounting for 30.44% of the study area. These areas have relatively high relative humidity, low wind speed, and short consecutive precipitation-free days. Moderate climate hazard areas mainly fall in suburban areas and regions with a relatively low level of development, relatively high temperatures, long consecutive precipitation-free days but low wind speed, and high relative humidity (Figure 6).

Distributions of topography hazards are relatively scattered. Areas with above-moderate-level topography hazards mainly occur in canyons and cliffy mountain regions. Altitudes and slope degrees of these areas are easy for ignition and wildfire spreading, accounting for 47.93% of the study area. Very low topography hazard areas, with belts distributed mainly in valleys with gentle slopes and relatively low altitudes, account for 12.01% of the study area. The exception is the northwestern end of the study area. Although the terrain of this area is eminently steep, the altitude here is overly high for wildfires, making low topography hazards dominant here. Significantly, most very low topography hazard areas have coincided with very high-climate hazard areas except the northeastern corner of the study area (Figure 7).

4.2 Vulnerability

Grids with high vulnerability levels dominate the entire classified vulnerability distribution, accounting for 57.64% of the study area due to the high vegetation coverage. Divided by the line of 102°E, very high-vulnerability areas in the eastern part are vast stretches, while in the western region, they are more scattered since the habitats and settlements are more concentrated, and the vegetation type of grasslands (with the highest vulnerability level) hold a significant proportion in these regions. Low- and very low-vulnerability areas mainly occur in urban areas and waterbodies, with scarce vegetation coverage and the most inferior vulnerability level surfaces, accounting for 19.86% of the study area. Areas with the moderate vulnerability level account for only 5.48% of the study area, formed in different ways: divided by the lines of 102°E and 27°N, moderate vulnerability areas in the eastern and southern parts are formed by relatively low vegetation coverage and vegetation ignitability, under the background of dense population and habitats/settlements, while in the western and northern parts, vegetation coverage and ignitability are relatively high, but population and habitat/settlement density are relatively low (Figure 8).

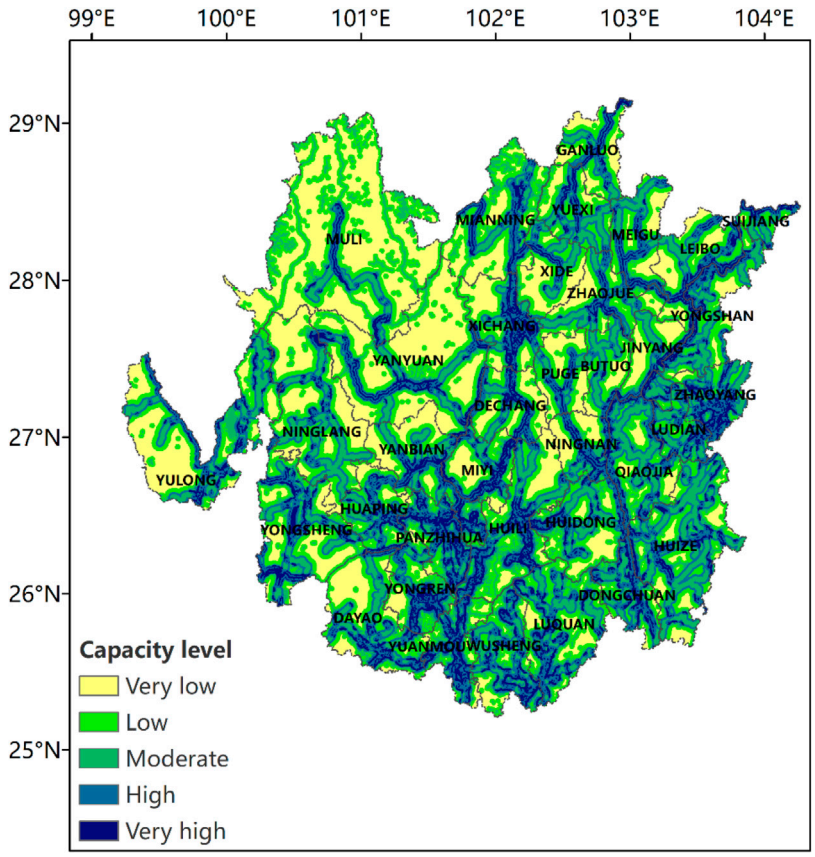

FIGURE 9
Spatial pattern of wildfire prevention/mitigation capacity.

4.3 Wildfire prevention/mitigation capacity

Prevention/mitigation capacity is a negative factor in wildfire risk mapping. With the increasing prevention/mitigation capacity, wildfire risks decline. Grids with very high prevention/mitigation levels mainly occur at the intersection of road networks and waterbody surroundings, accounting for 11.53% of the study area. High and moderate prevention/mitigation capacity grids, accounting for 21.57% and 18.09% of the study area, respectively, are areas alongside roads but far away from waterbodies. The most significant proportion held by low prevention/mitigation capacity grids is 25.16%, which mainly occurs in areas with inaccessible waterbody surroundings. Very low prevention/mitigation capacity grids occur in deep forests and upper mountain areas far away from fire water systems. Once these regions get ignited, it is hard to rescue. In general, the prevention/mitigation capacity of the study area is higher in the east of 102°E and the south of 27°N. These two lines can be regarded as the demarcations of wildfire risk mapping over the study area (Figure 9).

4.4 Synthesized risk mapping

Synthesized risk mapping in this study (Figure 10) reflects the probability of ignition, spreading, and rescue of wildfire: the climate hazard and topography hazard factors influence the inflammability of vegetation and spreading possibility. Vulnerability factors that describe the case of wildfire-inducing damage, combined with the ability of wildfire rescue, constitute the synthesized wildfire risk mapping over the high-incidence area of southwestern China. Most very high wildfire risk girds are distributed in the west of 103°E and the north of 28°N and intensively distributed in 101°E~102.5°E, 28°N~26°N. Broad similarities of very high-risk grids are urban area surroundings with relatively frequent human activities and high climate hazard levels, basins and valleys with altitudes between 1,500 and 3,000 m, high vegetation coverage, and areas away from waterbodies and road networks. Very high-risk grids account for 22.05% of the study area, covering over 26,500 km^2. There are 14 county-level regions with a very high wildfire risk area proportion of over 50% inside their administrative boundaries. High- and moderate-risk grids dominate the study area, accounting for 28.56% and 26.83%, respectively, covering a total area of over 66,600 km^2. Broad similarities between high- and moderate-risk grids are high–very high climate hazards and under-moderate topography hazards, whereas the difference is high and moderate grids at the west of 102.5°E under the background of above-moderate vulnerabilities and under-moderate prevention/mitigation capacities.

Nonetheless, in the eastern part, the reverse applies. Low- and very low-risk grids are mainly concentrated in the east part of 102°E, with minorities located in a small area between 100°E~100.5°E and 27°N~28°N, mainly for high mountain regions and waterbodies. The sum of low- and very low-risk grids accounts for 22.57% of the study

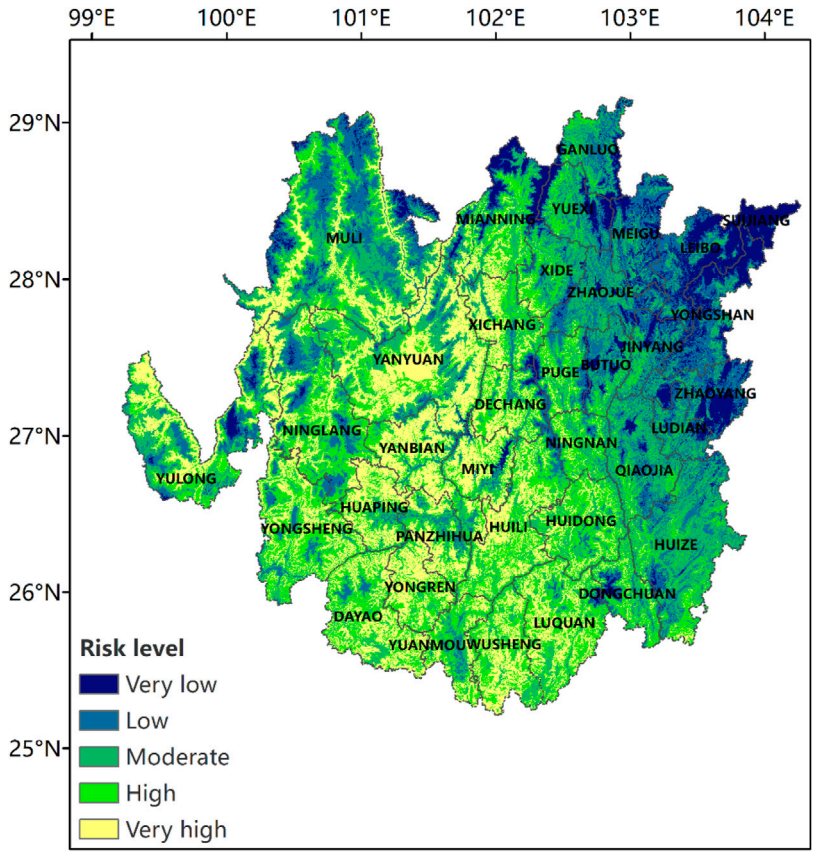

FIGURE 10
Spatial pattern of synthesized risk assessment.

area, covering an area of 27,000 km^2. Low- and very low-risk areas mainly occur in urban areas with low vegetation and dense public fire prevention infrastructures or humid regions in the northeastern study area. The risk mapping results are in general accordance with the climate regionalization. Areas with wildfire risks above moderate are mainly distributed in the southern subtropical sub-humid zone, while regions with risks below moderate occur in the northern and central subtropical humid zones. The northwestern end of the study area is located at the junction of the highland temperate humid zone and the highland temperate sub-humid zone. The contradictory vulnerability factors, namely, a large number of high ignitability grassland stretches and tiny population exposure, make this region unique over the study area.

5 Discussion and conclusion

Most previous studies of wildfire risk mapping emphasize topography factors, and climate factors are ignored or applied in low-resolution ways, thereby failing to notice some important details of wildfire risks. One instance is, in previous studies, the northwestern end of the study area (ranging from 28°N to 29°N and 100.5°E to 101.5°E) is classified as a low-fire risk area due to its low temperature. When the elevation model-related climate factors are applied, high- and very high-risk regions distributed in the belting ravines are revealed, which coincides with the actual wildfire records. Another fact is that with climate change and increasing precipitation extremes, the ensemble mean of annual precipitation accumulation, which is applied in most previous studies, is insufficient to characterize the humidity of vegetation solitarily. Our study suggests that the annual precipitation accumulation and annual consecutive precipitation-free day maximum are increasing, with a trend of expanded wildfire scales over the study area in recent years. The relationship between precipitation factors and wildfire needs advanced research.

The potential changes in climate hazards are the most critical and predictable factor among all the risk factors. The analysis of climate factors indicates that wind speed and relative humidity decline due to the changes in underlying surfaces under the background of large-scale urbanization. Meanwhile, the synchronous increase in precipitation accumulation and consecutive precipitation-free days points to more intense precipitations and longer dry seasons. Increasing human activities, combined with warming and drying climate conditions, uplift the frequency of wildfires. Nonetheless, wind speed declines limit wildfire spreading, explaining the synchronous increments in occurrences and reductions in scales of wildfire events in actual records.

The wildfire mapping result suggests that the hotspots of wildfire are mainly distributed in the area ranging 101°E~102.5°E and 26°N~28.5°N and stretch over 14 county-level administration units. The highly localized wildfire risk maps specified fire prevention/mitigation stresses in each grid cell and general spatial patterns of

wildfire risks. With the skyrocketing expansion of population and urbanization in southwestern China, policymakers should take changing climate hazards, localized vulnerabilities, and socio-economic characteristics into full consideration to manage wildfire risks and make tendentious construction policies of transportation systems and fire water systems toward existing and potential wildfire hotspots under the background of global warming.

Data availability statement

The original contributions presented in the study are included in the article/Supplementary Material; further inquiries can be directed to the corresponding author.

Author contributions

YX, JL, and HG contributed to the conception and design of the study. YX and RS collected and organized the original data. YX, JL, and XL performed the statistical analysis. YX wrote the first draft of the manuscript. All authors contributed to manuscript revision, read, and approved the submitted version.

Funding

This research was supported by the Innovation and Development Special Project of the China Meteorological Administration (CXFZ 2021J058) and the Development Project of Plateau Atmosphere and Environment Key Laboratory of Sichuan Province (PAEKL-2022-K07).

Conflict of interest

The authors declare that the research was conducted in the absence of any commercial or financial relationships that could be construed as a potential conflict of interest.

Publisher's note

All claims expressed in this article are solely those of the authors and do not necessarily represent those of their affiliated organizations, or those of the publisher, the editors, and the reviewers. Any product that may be evaluated in this article, or claim that may be made by its manufacturer, is not guaranteed or endorsed by the publisher.

References

AghaKouchak, A., Chiang, F., Huning, L. S., Love, C. A., Mallakpour, I., Mazdiyasni, O., et al. (2020). Climate extremes and compound hazards in a warming world. *Annu. Rev. Earth Planet. Sci.* 48, 519–548. doi:10.1146/annurev-earth-071719-055228

Artés, T., Oom, D., de Rigo, D., Durrant, T. H., Maianti, P., Libertà, G., et al. (2019). A global wildfire dataset for the analysis of fire regimes and fire behaviour. *Sci. Data* 6 (1), 296. doi:10.1038/s41597-019-0312-2

Ball, G., Regier, P., González-Pinzón, R., Reale, J., and Van Horn, D. (2021). Wildfires increasingly impact Western US fluvial networks. *Nat. Commun.* 12, 2484. doi:10.1038/s41467-021-22747-3

Bessie, W. C., and Johnson, E. A. (1995). The relative importance of fuels and weather on fire behavior in subalpine forests. *Ecology* 76 (3), 747–762. doi:10.2307/1939341

Collins, R. D., Neufville, R. D., Claro, J., Oiveira, T., and Pacheco, A. P. (2013). Forest fire management to avoid unintended consequences: A case study of Portugal using system dynamics. *J. Environ. Manag.* 130 (1), 1–9. doi:10.1016/j.jenvman.2013.08.033

Corona, P., Ferrari, B., Cartisano, R., and Barbati, A. (2014). Calibration assessment of forest flammability potential in Italy. *For. - Biogeosciences For.* 7 (5), 300–305. doi:10.3832/ifor1123-007

Flannigan, M. D., Stocks, B. J., and Wotton, B. M. (2000). Climate change and forest fires. *Sci. Total Environ.* 262 (3), 221–229.doi:10.1016/S0048-9697(00)00524-6

Diffenbaugh, N. S., Singh, D., Mankin, J. S., Horton, D. E., Swain, D. L., Touma, D., et al. (2017). Quantifying the influence of global warming on unprecedented extreme climate events. *Proc. Natl. Acad. Sci.* 114 (19), 4881–4886. doi:10.1073/pnas.1618082114

Dimitrakopoulos, A. P., and Papaioannou, K. K. (2001). Flammability assessment of Mediterranean forest fuels. *Fire Technol.* 37 (2), 143–152. doi:10.1023/A:1011641601076

Flannigan, Md, and Harrington, Jb (1988). A study of the relation of meteorological variables to monthly provincial area burned by wildfire in Canada (1953-80). *J. Appl. Meteorol.* 27, 441–452. doi:10.1175/1520-0450(1988)027<0441:asotro>2.0.co;2

Flannigan, M. D., Stocks, B. J., and Wotton, B. M. (2000). Climate change and forest fires. *Sci. Total Environ.* 262, 221–229. doi:10.1016/s0048-9697(00)00524-6

Gao, T., Wang, H. J., and Zhou, T. (2017). Changes of extreme precipitation and nonlinear influence of climate variables over monsoon region in China. *Atmospheric Research* 197 379–389. doi:10.1016/j.atmosres.2017.07.017

Geographic Data Sharing Infrastructure (2023). *Geographic data sharing infrastructure, college of urban and environmental science*. Peking University.

Goetz, S. J., Fiske, G. J., and Bunn, A. G. (2006). Using satellite time-series data sets to analyze fire disturbance and forest recovery across Canada. *Rem. Sens. Environ.* 101, 352–365. doi:10.1016/j.rse.2006.01.011

Gong, P., Li, X. C., and Zhang, W. (2019a). 40-Year(1978-2017) human settlement changes in China reflected by impervious surfaces from satellite remote sensing. *Sci. Bull.* 64, 756–763. doi:10.1016/j.scib.2019.04.024

Gong, P., Chen, B., Li, X., Liu, H., Wang, J., Bai, Y., et al. (2019b). Mapping essential urban land use categoriesin China (EULUC-China): Preliminary results for 2018. *Sci. Bull.* 65, 182–187. doi:10.1016/j.scib.2019.12.007

Gralewicz, N. J., Nelson, T. A., and Wulder, M. A. (2012). Factors influencing national scale wildfire susceptibility in Canada, *For. Ecol. Environ.*, 265, 20–29. doi:10.1016/j.foreco.2011.10.031

Hall, S. J., and Marchand, P. J. (2010). Effects of stand density on ecosystem properties of subalpine forests in the southern Rocky Mountains. *USA* 67 (1), 102. doi:10.1051/forest/2009083

Hallema, D. W., Sun, G., Caldwell, P. V., Norman, S. P., Cohen, E. C., Liu, Y., et al. (2018). Burned forests impact water supplies. *Nat. Commun.* 9, 1307. doi:10.1038/s41467-018-03735-6

Hijmans, R. J., Cameron, S. E., Parra, J. L., Jones, P. G., and Jarvis, A. (2010). Very high-resolution interpolated climate surfaces for global land areas. *Int. J. Climatol.* 25 (15), 1965–1978. doi:10.1002/joc.1276

Hutchinson, M. F. (2004). *ANUSPLIN version 4.3*. Canberra Australia: Centre for Resource and Environmental Studies, Australian National University.

Hutchinson, M. F. (1995). Interpolating mean rainfall using thin plate smoothing splines. *Int. J. GIS* 9, 385–403. doi:10.1080/02693799508902045

Hutchinson, M. F. (1993). "On thin-plate splines and kriging," in *In: Computing and science in statistics*. Editors M. E. Tarter and M. D. Lock (Berkeley: Interface Foundation of North America, University of California), 25, 55–62.

Hutchinson, M. F. (1991). "The application of thin plate smoothing splines to continent-wide data assimilation," in *BMRC research report No. 27, data assimilation systems*. Editor J. D. Jasper (Melbourne: Bureau of Meteorology), 104–113.

IPCC (2012). *Managing the risks of extreme events and disasters to advance climate change adaptation: Special report of the intergovernmental panel on climate change*. Cambridge, UK, New York, NY: Cambridge University Press.

Jaiswal, R. K., Mukherjee, S., Raju, K. D., and Saxena, R. (2002). Forest fire risk zone mapping from satellite imagery and GIS. *Int. J. Appl. Earth Observation Geoinformation* 4 (1), 1–10. doi:10.1016/s0303-2434(02)00006-5

Jolly, W. M., Cochrane, M. A., Freeborn, P. H., Holden, Z. A., Brown, T. J., Williamson, G. J., et al. (2015). Climate-induced variations in global wildfire danger from 1979 to 2013. *Nat. Commun.* 6, 7537. doi:10.1038/ncomms8537

Ma, Z. (2020). *Assessment report of climate changing in southwestern China(in Chinese)*.

McKenney., D. W., Sophie, P., Poissant., Y., Morris., R., Hutchinson., M., Papadopol., P., et al. (2008). Spatial insolation models for photovoltaic energy in Canada. *Sol. Energy* 82 (11), 1049–1061. doi:10.1016/j.solener.2008.04.008

Moreira, F., Arianoutsou, M., Corona, P., and De las Heras, J. (2012). Managing forest ecosystems] post-fire management and restoration of southern European forests volume. *Fire Hazard Flammabl. Eur. For. Types* 24. doi:10.1007/978-94-007-2208-8_4

Ozturk, M., Gucel, S., Kucuk, M., and Sakcali, S. (2010). Forest diversity, climate change and forest fires in the Mediterranean region of Turkey. *J. Environ. Biol.* 31 (1-2), 1–9.

Pan, J., Wang, W., and Li, J. (2016). Building probabilistic models of fire occurrence and fire risk zoning using logistic regression in Shanxi Province, China. *Nat. Hazards* 81 (3), 1879–1899. doi:10.1007/s11069-016-2160-0

Petoukhov, V., Petri, S., Kornhuber, K., Thonicke, K., Coumou, D., and Schellnhuber, H. J. (2018). Alberta wildfire 2016: Apt contribution from anomalous planetary wave dynamics. *Sci. Rep.* 8 (1), 12375. doi:10.1038/s41598-018-30812-z

Pickell, P. D., Coops, N. C., Ferster, C. J., Bater, C. W., Blouin, K. D., Flannigan, M. D., et al. (2017). An early warning system to forecast the close of the spring burning window from satellite-observed greenness. *Sci. Rep.* 7 (1), 14190. doi:10.1038/s41598-017-14730-0

Salaheddine, E., M'Hamed, H., Mohammed, Y., Mohammed, D., and Fahed, E. A. (2017). Assessment of flammability of Moroccan forest fuels: New approach to estimate the flammability index. *Forests* 8 (11), 443. doi:10.3390/f8110443

Shi, K., and Touge, Y. (2022). Characterization of global wildfire burned area spatiotemporal patterns and underlying climatic causes. *Sci. Rep.* 12, 644. doi:10.1038/s41598-021-04726-2

Sun, L., Wang, Q., Wei, S., Hu, H., Guan, D., and Chen, X. (2014). Response characteristics and prospect of forest fire disasters in the context of climate change in China. *J. catastrophology* 29, 12–17.

Taufik, M., Torfs, P. J. J. F., Uijlenhoet, R., Jones, P. D., Murdiyarso, D., Van Lanen, H. J. A., et al. (2017). Amplification of wildfire area burnt by hydrological drought in the humid tropics. *Nat. Clim. Change* 7, 428–431. doi:10.1038/nclimate3280

Wang, Y., Zhang, J., Zhang, H., et al. (2018). Application of MODIS AOD Products to Monitoring Forest Fire in Forest Area of Southwestern China. *Journal of Arid Meteorology* 36 (5), 820–827. doi:10.11755/j.issn.1006-7639(2018)-05-0820

Wu, J., Gao, X., Giorgi, F., and Chen, D. (2017). Changes of effective temperature and cold/hot days in late decades over China based on a high-resolution gridded observation dataset. *Int. J. Climatol.* 37 (1), 788–800. doi:10.1002/joc.5038

Zhao, P., Xiao, H., Liu, C., and Zhou, Y. (2021). Dependence of warm season cloud-to-ground lightning polarity on environmental conditions over sichuan, southwest China. *Adv. Meteorology* 2021, 1–12. doi:10.1155/2021/1500470

Zhao, P., Xiao, H., Liu, J., and Zhou, Y. (2022). Precipitation efficiency of cloud and its influencing factors over the Tibetan plateau. *Int. J. Climatol.* 42 (1), 416–434. doi:10.1002/joc.7251

frontiers | Frontiers in Environmental Science

TYPE Original Research
PUBLISHED 09 May 2023
DOI 10.3389/fenvs.2023.1127265

OPEN ACCESS

EDITED BY
Shuliang Zhang,
Nanjing Normal University, China

REVIEWED BY
Chi Yang,
Distinguished Professor of Nanjing University of Information Science and Technology, China
Albert Ossó,
University of Graz, Austria

*CORRESPONDENCE
Fasil M. Rettie,
fasil.mequanint@uni-hohenheim.de

SPECIALTY SECTION
This article was submitted to Atmosphere and Climate, a section of the journal Frontiers in Environmental Science

RECEIVED 19 December 2022
ACCEPTED 28 March 2023
PUBLISHED 09 May 2023

CITATION
Rettie FM, Gayler S, Weber TKD, Tesfaye K and Streck T (2023), Comprehensive assessment of climate extremes in high-resolution CMIP6 projections for Ethiopia.
Front. Environ. Sci. 11:1127265.
doi: 10.3389/fenvs.2023.1127265

Comprehensive assessment of climate extremes in high-resolution CMIP6 projections for Ethiopia

Fasil M. Rettie[1,2]*, Sebastian Gayler[1], Tobias K. D. Weber[1,3], Kindie Tesfaye[4] and Thilo Streck[1]

[1]Institute of Soil Science and Land Evaluation, Biogeophysics, University of Hohenheim, Stuttgart, Germany, [2]Ethiopian Institute of Agricultural Research (EIAR), Melkasa, Ethiopia, [3]Soil Science Section, Faculty of Organic Agricultural Sciences, University of Kassel, Witzenhausen, Germany, [4]International Maize and Wheat Improvement Center (CIMMYT), Addis Ababa, Ethiopia

Climate extremes have more far-reaching and devastating effects than the mean climate shift, particularly on the most vulnerable societies. Ethiopia, with its low economic adaptive capacity, has been experiencing recurrent climate extremes for an extended period, leading to devastating impacts and acute food shortages affecting millions of people. In face of ongoing climate change, the frequency and intensity of climate extreme events are expected to increase further in the foreseeable future. This study provides an overview of projected changes in climate extremes indices based on downscaled high-resolution (i.e., 10 × 10 km^2) daily climate data derived from global climate models (GCMs). The magnitude and spatial patterns of trends in the projected climate extreme indices were explored under a range of emission scenarios called Shared Socioeconomic Pathways (SSPs). The performance of the GCMs to reproduce the observed climate extreme trends in the base period (1983–2012) was evaluated, the changes in the climate projections (2020–2100) were assessed and the associated uncertainties were quantified. Overall, results show largely significant and spatially consistent trends in the projected temperature-derived extreme indices with acceptable model performance in the base period. The projected changes are dominated by the uncertainties in the GCMs at the beginning of the projection period while by the end of the century proportional uncertainties arise both from the GCMs and SSPs. The results for precipitation-related extreme indices are heterogeneous in terms of spatial distribution, magnitude, and statistical significance coverage. Unlike the temperature-related indices, the uncertainty from internal climate variability constitutes a considerable proportion of the total uncertainty in the projected trends. Our work provides a comprehensive insight into the projected changes in climate extremes at relatively high spatial resolution and the related sources of projection uncertainties.

KEYWORDS

climate extremes, CMIP 6, Ethiopa, precipiation, SSPS, temeprature, uncertainty, trend

1 Introduction

There is unequivocal and overwhelming evidence for the ongoing climate change. The projected 1.5°C increase in global average temperature by 2050s poses risks to humans and ecosystems (IPCC, 2022). The changing climate has manifested itself in higher climate extremes events (Myhre et al., 2019; Madakumbura et al., 2021). Climate extremes usually have more devastating effects than the mean shift in the climate. Expected increases in flash flood events following more frequent and extreme precipitation events, or droughts as a result of prolonged periods of extremely low precipitation are situations that may cost countries a huge price (IPCC, 2022). Extreme heat or cold waves have far-reaching socioeconomic and mental effects on the most vulnerable societies (IPCC, 2022). Since 2005, the world has witnessed 9 warmest years, and 2019 has been recorded as one of the three warmest years since the records have begun. This global phenomenon has significant implications, particularly for the most vulnerable part of the world's economy. Kemp et al. (2022) suspect that, together with other global threats, the changing climate may become catastrophic even at modest levels of warming.

Ethiopia's economy depends largely on agriculture and it is considered to be among the countries that are most vulnerable to climate extremes. The agricultural sector second contributes ~ 38% to the GDP (Gross Domestic Product) of the country but employs 67% of the population and contributes about 86% of export earnings (Eshetu and Mehare, 2020; World Bank, 2022b; World Bank, 2022c). Moreover, the largely subsistence agriculture relies on seasonal rains. The proportion of irrigated land was only 2.1% in 2018 (World Bank, 2022a) and agricultural mechanization was below 1% (Berhane et al., 2017). Ethiopia has faced recurrent climate extreme effects for a long period usually resulting in a devastating impact and leaving millions in acute food shortage (Kiros, 1991; Mohammed et al., 2018). The 2022 drought was one of the worst in 50 years, leaving 2.2 million livestock dead (FEWS NET, 2022). Considering the projected population of > 200 million by 2050 (World Bank, 2022d), the challenge of comparable drought periods for the already vulnerable economy would be enormous. Against this background, detailed quantification of climate extremes is particularly relevant for Ethiopia.

For the past climate, studies have documented consistent increasing temperature trends both in mean and extremes in East Africa in general (Gebrechorkos et al., 2019b; Muthoni et al., 2019; Afuecheta and Omar, 2021) and Ethiopia in particular (Gummadi et al., 2018; Gebrechorkos et al., 2019b; 2019a). However, precipitation has been reported as inconsistent across the region (Viste et al., 2013; Tierney et al., 2015; Cattani et al., 2018; Gummadi et al., 2018). For instance, Tierney et al. (2015) documented unusual drying of March-May rainfall in East Africa during the past century. Meanwhile, their assessment based on 23 CMIP5 models by the end of the 21st century show largely increasing seasonal as well as annual precipitation totals under high emission (RCP 8.5) scenario (Tierney et al., 2015). Drying spring and summer seasons have also been reported for southern Ethiopia. The drying springs have affected most parts of the country (Viste et al., 2013). However, local scale studies identified higher spatial variability both in the observed and projected climate trends, particularly for precipitation (Brown et al., 2017; Muthoni et al., 2019; Alaminie et al., 2021; Bayable et al., 2021). High spatial variability was also visible in past climate extremes (Cattani et al., 2018; Esayas et al., 2018; Ademe et al., 2020; Gemeda et al., 2021; Ali Mohammed et al., 2022; Birhan et al., 2022; Dendir and Birhanu, 2022). Understanding the time evolution of extreme climate events is of large interest for designing potential adaptation options and informed decision-making (Kemp et al., 2022). Ethiopia is characterized by diverse climate regimes modulated by its complex topography exerting strong elevation gradients (Diro et al., 2011; Van den Hende et al., 2021), which require finer spatial resolution to produce relevant results (El Kenawy et al., 2016).

The basic sources of projected climate data are the Global Climate Models (GCMs) running on coarse spatial resolution at > 70 × 70 km^2. The projected data are highly uncertain, mainly due to the structural and parametrization differences among the models (Murphy et al., 2004; Her et al., 2019; Lee et al., 2021). Therefore, adaptation to climate extremes should be based on multi-model-based simulation at high spatial resolution taking into account several emission scenarios (Fatichi et al., 2016). For Ethiopia, these GCM projections were recently downscaled to 10 × 10 km^2 spatial resolution for temperature and precipitation (Rettie et al., 2023). The data were derived from the most current GCMs in the Coupled Model Intercomparison Project Phase 6 (CMIP6) under three Shared Socioeconomic Pathways (SSPs) by employing a statistical downscaling technique (Hamlet et al., 2010; Maurer et al., 2010).

The present study provides an overview of observed and projected changes in climate extremes indices derived from the downscaled high-resolution daily climate data by Rettie et al. (2023). For this, we compared the historical simulation of the CMIP6 models and analyzed the temporal and spatial distributions of projected changes. The skill of the individual models in reproducing the observed trends of climate extremes in the base period (i.e., 1983–2012) was evaluated, and the uncertainties associated with the projected (i.e., 2020–2100) trends were quantified.

2 Materials and methods

2.1 Climate data

The climate hazards group database provides free daily climate data with a 5 × 5 km^2 spatial resolution with quasi-global coverage (50°S–50°N, ftp://ftp.chg.ucsb.edu/pub/org/chg/products/). Daily climate data is available for the study area (Figure 1A) from CHIRPS (Climate Hazards Group InfraRed Precipitation with Stations) for precipitation (Funk et al., 2015) and from CHIRTS (Climate Hazards Group InfraRed Temperature with Stations) for temperature (Verdin et al., 2020) (Figures 1B–D). The data were generated in several stages by blending satellite records and *in situ* station data and are available since 1981 for precipitation and from

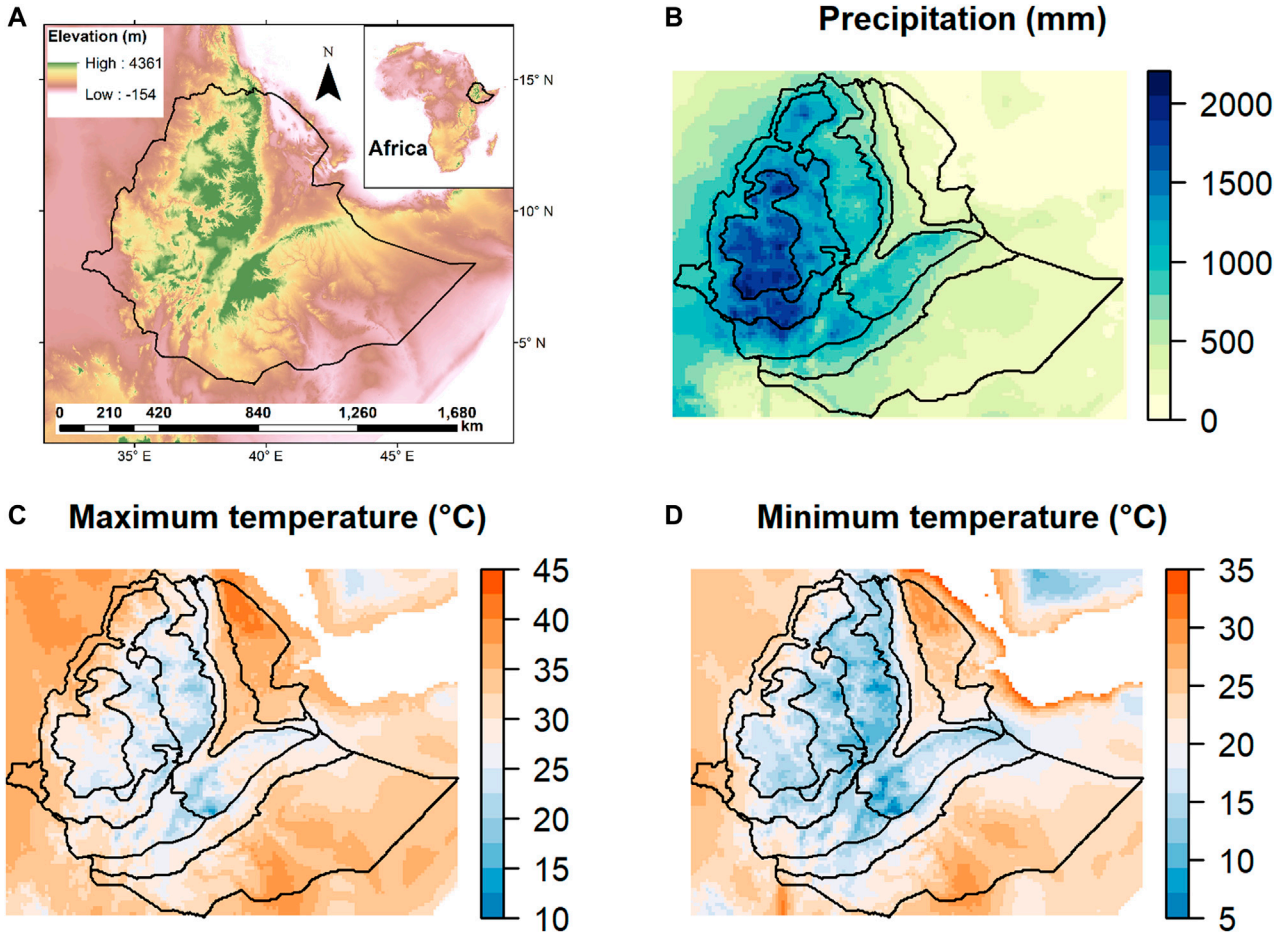

FIGURE 1
Maps of Ethiopia showing elevation **(A)**, annual total precipitation in mm **(B)**, and annual maximum **(C)** and minimum **(D)** temperatures based on observation data (1982–2012).

1983 to 2016 for temperature. The data has been evaluated for its ability to reliably reproduce the climatology and major meteorological systems of Ethiopia (Dinku et al., 2018; Belete et al., 2020; Taye et al., 2020; Kabite Wedajo et al., 2021; Malede et al., 2022) and other regions (Zambrano-Bigiarini et al., 2017; Saeidizand et al., 2018; Muthoni et al., 2019; Muthoni, 2020).

This work was conducted based on previously downscaled climate projections covering the period of 2020–2100 from a list of CMIP6 GCMs under three emission scenarios known as shared socioeconomic pathways (SSPs) (Rettie et al., 2023). The data was produced by applying a geospatial statistical downscaling technique to downscale the original coarse spatial resolution (i.e., > 70 × 70 km^2) GCM outputs to 10 × 10 km^2 spatial resolution covering entire Ethiopia (3°N—15°N and 32°E—48°E). The data includes projections of temperature and precipitation from 13 to 9 CMIP6 GCMs, respectively (Table 1). For a detailed description of the downscaling procedure and evaluation see there. In this study, we considered the downscaled climate projections datasets under three SSPs. The selected SSPs are SSP2-4.5, SSP3-7.0, and SSP5-8.5, which represent medium, medium-high, and high-forcing scenarios based on middle-of-the-road, regional rivalry, and fossil-fueled socioeconomic development scenarios, respectively (O'Neill et al., 2017; Meinshausen et al., 2020). The emission scenarios span a broad range of CO^2 concentration, with radiative forcing level of 4.5 Wm^{-2} and 8.5 Wm^{-2} by 2100 for SSP2-4.5 and SSP5-8.5, respectively (IPCC, 2021).

2.2 Climate extreme indices

Table 2 lists the 23 climate extreme indices investigated in this study. The indices were among the 27 climate change indicators which were developed by the Expert Team on Climate Change Detection, Monitoring Indices (ETCCDMI) and have been recommended by the World Meteorological Organization (WMO) (Zhang et al., 2011). The R package *climdex.pcic* (Pacific Climate Impacts Consortium (2020), http://cran.r-project.org/web/packages/climdex.pcic/index.html) was used to derive the climate indices at 10 × 10 km^2 grid

TABLE 1 List of GCMs and availability of data with respect to maximum (Tmax) and minimum (Tmin) temperatures and precipitation (Pr).

Model name	Institution name	Tmax	Tmin	Pr	Resolution (lon. by lat.)
ACCESS-CM2	Commonwealth Scientific and Industrial Research Organization (CSIRO) and Bureau of Meteorology (BOM), Australia	✓	✓	✓	1.9° × 1.3 °
ACCESS-ESM1-5	Commonwealth Scientific and Industrial Research Organization (CSIRO) and Bureau of Meteorology (BOM), Australia	✓	✓	✓	1.9° × 1.2°
AWI-CM-1-1-MR	Alfred Wegener Institute, Helmholtz Centre for Polar and Marine Research, Am Handelshafen 12, 27570 Bremerhaven, Germany	✓	✓	*o*	1.1° × 1.1 °
EC-Earth3-Veg	EC-Earth-Consortium	✓	✓	*o*	0.7° × 0.7 °
EC-Earth3	EC-Earth-Consortium	✓	✓	*o*	0.7 ° × 0.7 °
GFDL-ESM4	NOAA Geophysical Fluid Dynamics Laboratory	✓	✓	✓	1.3° × 1.0 °
INM-CM4-8	Institute for Numerical Mathematics	✓	✓	✓	2.0° × 1.5 °
INM-CM5-0	Institute for Numerical Mathematics	✓	✓	✓	2.0° × 1.5 °
IPSL-CM6A-LR	Institut Pierre Simon Laplace, Paris 75252, France	✓	✓	*o*	2.5° × 1.3 °
MIROC6	Japan Agency for Marine-Earth Science and Technology, Kanagawa 236–0001, Japan	✓	✓	✓	1.4° × 1.4 °
MPI-ESM1-2-HR	Max Planck Institute for Meteorology, Hamburg 20146, Germany	✓	✓	✓	0.9° × 0.9 °
MPI-ESM1-2-LR	Max Planck Institute for Meteorology, Hamburg 20146, Germany	✓	✓	✓	1.9° × 1.9 °
MRI-ESM2-0	Meteorological Research Institute	✓	✓	✓	1.1° × 1.1 °

resolution covering entire Ethiopia (i.e., 3°N - 15°N and 32°E - 48°E). To assess the skill of the GCMs in reproducing the observed climate extremes, the indices were calculated for a common 30-year period for which CHIRPS and CHIRTS data were both available. Hence, for each grid cell, the 23 climate extreme indices (Table 2) were calculated for the observed climate data (i.e., for the CHIRPS and CHIRTS data) and the historic GCMs climate outputs for the common 30-year period (i.e., 1983–2012). Similarly, the same climate extreme indices were calculated for the projected climate period (i.e., 2020–2100) for each GCM under each SSP. The indices were computed on High-Performance Cluster bwUniCluster 2.0.

2.3 Evaluation of models' skill

The performance of the GCMs in reproducing the observed climate extremes was evaluated based on the Taylor diagram (Taylor, 2001). Taylor diagram is a widely used tool to evaluate how well a model matches observed climate states (Guo et al., 2018; Rao et al., 2019; Li et al., 2021; Yang et al., 2021; Liu et al., 2022). A Taylor diagram simultaneously visualizes three summary statistics: the *standard deviation (σ)* of simulated (Y) data normalized to that of the observed (X) data, the *correlation coefficient (r)* between simulated and observed data, and the *centered root mean squared error (RMSE c)* between simulated and observed data (Table 3). For the Taylor diagrams, we computed the model skills of climate extreme indices over the area-averaged data across the entire grid cells for 30 years (i.e., 1983–2012).

2.4 Trend estimation and test

We used the Mann-Kendall (MK) method (Mann, 1945; Kendall, 1962; Pohlert, 2020) to test the trends in the respective climate extreme indices for both the baseline climate and future projections. The MK is a non-parametric test (i.e., the data does not have to meet the normality assumption) and widely used method because of its simplicity (Cattani et al., 2018; Esayas et al., 2018; Afuecheta and Omar, 2021; Li et al., 2021; Simanjuntak et al., 2022). The MK test determines the presence of monotonic (i.e., consistent) increasing or decreasing tendency of data in a given time. The magnitude of the trend is determined by using Sen's slope estimator (Sen, 1968) which is a non-parametric approach to estimate the overall slope in a data series (Beyene et al., 2022; Malaekeh et al., 2022; Pervin and Khan, 2022). All the MK tests and slope estimates were computed using the *"trend"* R software package (Pohlert, 2020).

2.5 Partitioning sources of uncertainty in the projected climate extremes

Climate change projections usually involve three main sources of uncertainty, namely: uncertainty due to GCMs (M^t), SSPs (S^t), and internal climate variability (V). Using the method proposed by Hawkins and Sutton (2009); Hawkins and Sutton (2011), we evaluated the projected climate extreme indices from the GCMs (Table 1) under the three emission scenarios (SSPs) for the period from 2020 to 2100. For the temperature-related indices, this gives a total of 39 projections from the 13 GCMs (N_m = 13) and 3 SSPs

TABLE 2 List of ETCCDMI-defined precipitation and temperature extreme indices computed and evaluated in this study.

Label	Index name	Index definition	Units
TN10p	Cold nights	Percentage of days when TN < 10 *th* percentile: Let TN *ij* be the daily minimum temperature on day *i* in period *j* and let TN *in* 10 be the calendar day 10 *th* percentile centred on a 5-day window for the period. The percentage of time the period is determined where: TN *ij* < TN *in* 10	%
TX10p	Cold days	Percentage of days when TX < 10 *th* percentile: Let TX *ij* be the daily maximum temperature on day *i* in period *j* and let TX *in* 10 be the calendar day 10 *th* percentile centred on a 5-day window for the period. The percentage of time the period is determined where: TX *ij* < TX *in* 10	%
TN90p	Warm nights	Percentage of days when TN > 90 *th* percentile: Let TN *ij* be the daily minimum temperature on day *i* in period *j* and let TN *in* 90 be the calendar day 90 *th* percentile centred on a 5-day window for the period. The percentage of time the period is determined where: TN *ij* > TN *in* 90	%
TX90p	Warm days	Percentage of days when TX > 90 *th* percentile: Let TX *ij* be the daily maximum temperature on day *i* in period *j* and let TX *in* 90 be the calendar day 90 *th* percentile centred on a 5-day window for the period. The percentage of time the period is determined where: TX *ij* > TX *in* 90	%
WSDI	Warm spell duration	Warm spell duration index: Annual count of days with at least 6 consecutive days when TX > 90 *th* percentile: Let TX *ij* be the daily maximum temperature on day *i* in period *j* and let TX *in* 90 be the calendar day 90 *th* percentile centred on a 5-day window for the period. Then the number of days per period is summed where, in intervals of at least 6 consecutive days: TX *ij* > TX *in* 90	days
CSDI	Cold spell duration	Cold spell duration index: Annual count of days with at least 6 consecutive days when TN < 10 *th* percentile: Let TN *ij* be the daily maximum temperature on day *i* in period *j* and let TN *in* 10 be the calendar day 10 *th* percentile centred on a 5-day window for the period. Then the number of days per period is summed where, in intervals of at least 6 consecutive days: TN *ij* < TN *in* 10	days
TXx	Max TX	Monthly maximum value of daily maximum temperature: Let TXx be the daily maximum temperatures in month *k*, period *j*. The maximum daily maximum temperature each month is then: TX x_{kj} = max(TX x_{kj})	°C
TXn	Min TX	Monthly minimum value of daily maximum temperature: Let TXn be the daily maximum temperatures in month *k*, period *j*. The minimum daily maximum temperature each month is then: TX n_{kj} = min(TX n_{kj})	°C
TNx	Max TN	Monthly maximum value of daily minimum temperature: Let TNx be the daily minimum temperatures in month *k*, period *j*. The maximum daily minimum temperature each month is then: TN x_{kj} = max(TN x_{kj})	°C
TNn	Min TN	Monthly minimum value of daily minimum temperature: Let TNn be the daily minimum temperatures in month *k*, period *j*. The minimum daily minimum temperature each month is then: TN n_{kj} = min(TN n_{kj})	°C
SU	Summer days	Number of summer days: Annual count of days when TX (daily maximum temperature) > 25°C. Let TX *ij* be daily maximum temperature on day *i* in year *j*. Count the number of days where: TX *ij* > 25°C.	days
TR	Tropical nights	Number of tropical nights: Annual count of days when TN (daily minimum temperature) > 20°C. Let TN *ij* be daily minimum temperature on day *i* in year *j*. Count the number of days where: TN *ij* > 20°C.	days
Rx1day	Max 1-day precipitation	Monthly maximum 1-day precipitation: Let RR *ij* be the daily precipitation amount on day i in period *j*. The maximum 1-day value for period *j* are: Rx1day *j* = max (RR *ij*)	mm
Rx5day	Max 5-day precipitation	Monthly maximum consecutive 5-day precipitation: Let RR *kj* be the precipitation amount for the 5-day interval ending *k*, period *j*. Then maximum 5-day values for period *j* are: Rx5day *j* = max (RR *kj*)	mm
SDII	Simple daily intensity	Simple precipitation intensity index: Let RR *wj* be the daily precipitation amount on wet days, w (RR = 1 mm) in period *j*. If W represents number of wet days in *j*, then: SDII $j = \frac{\sum_{w=1}^{W} RR_{wj}}{W}$	mm
R1mm	Number of wet days	Annual count of days when PRCP = nn mm, nn is a user defined threshold: Let RR *ij* be the daily precipitation amount on day *i* in period *j*. Count the number of days where: RR *ij* = nnmm	days
R10 mm	Heavy precipitation days	Annual count of days when PRCP = 10 mm: Let RR *ij* be the daily precipitation amount on day *i* in period *j*. Count the number of days where: RR *ij* = 10 mm	days
R20 mm	Very heavy precipitation days	Annual count of days when PRCP = 20 mm: Let RR *ij* be the daily precipitation amount on day *i* in period *j*. Count the number of days where: RR *ij* = 20 mm	days
CDD	Consecutive dry days	Maximum length of dry spell, maximum number of consecutive days with RR < 1 mm: Let RR *ij* be the daily precipitation amount on day *i* in period *j*. Count the largest number of consecutive days where: RR *ij* < 1 mm	days
CWD	Consecutive wet days	Maximum length of wet spell, maximum number of consecutive days with RR = 1 mm: Let RR *ij* be the daily precipitation amount on day *i* in period *j*. Count the largest number of consecutive days where: RR *ij* = 1 mm	days
R95p	Very wet days total precipitation	Annual total PRCP when RR > 95p. Let RR *wj* be the daily precipitation amount on a wet day w (RR = 1.0 mm) in period *i* and let RR *wn*95 be the 95 *th* percentile of precipitation on wet days in the reference period. If W represents the number of wet days in the period, then: R95p $j = \sum_{w=1}^{W} RR_{wj}$ where $RR_{wj} > RR_{wn}95$	mm

(Continued on following page)

TABLE 2 (*Continued*) List of ETCCDMI-defined precipitation and temperature extreme indices computed and evaluated in this study.

Label	Index name	Index definition	Units
R99p	Extremely wet days total precipitation	Annual total PRCP when RR > 99p: Let RR wj be the daily precipitation amount on a wet day w (RR = 1.0 mm) in period i and let RR $wn99$ be the 99 th percentile of precipitation on wet days in the reference period. If W represents the number of wet days in the period, then: R99p $j = \sum_{w=1}^{W} RR_{wj}$ where $RR_{wj} > RR_{wn}99$	mm
PRCPTOT	Total wet-day precipitation	Annual total precipitation in wet days: Let RR ij be the daily precipitation amount on day i in period j. If I represents the number of days in j, then PRCPTOT $j = \sum_{i=1}^{I} RR_{ij}$	mm

TABLE 3 Performance statistics on which the Taylor diagrams are based.

Symbol	Description	Notation
X, Y	Observed and simulated climate extreme indices	
σ_x, σ_y	Standard deviations of observed and simulated climate extreme indices	$\sigma_x = \sqrt{\frac{\sum_{n=1}^{N}(X_n-\bar{X})}{N}}$, $\sigma_y = \sqrt{\frac{\sum_{n=1}^{N}(Y_n-\bar{Y})}{N}}$
r	Correlation coefficient between observed and simulated climate extreme indices	$r = \frac{1}{N}\frac{\sum_{n=1}^{N}(X_n-\bar{X})(Y_n-\bar{Y})}{\sigma_x\sigma_y}$
RMSE c	Centered root mean squared error between observed and simulated climate extreme indices	$RMSE_c = \sqrt{\frac{1}{N}\sum_{n=1}^{N}[(X_n-\bar{X})-(Y_n-\bar{Y})]^2}$

($N_s = 3$). For the precipitation-related indices, the total was 27 with $N_m = 9$ and $N_s = 3$, because three GCMs simulations did not include precipitation.

The decomposition of the uncertainty was computed on the changes (denoted as $Y^{s,m,t}$) of climate extreme indices between a future and a baseline climate period for each grid cell following the studies of Hawkins and Sutton. (2011); Zhang and Chen (2021). Here, the period 1983–2012 was considered as a baseline period to calculate the changes ($Y^{s,m,t}$) due to climate change. The changes in temperature derived indices are expressed in terms of absolute changes as follows:

$$Y^{s,m,t} = p^{s,m,t} - \frac{1}{30} \times \sum_{t=1983}^{2012} p^{s,m,t} \tag{1}$$

and the changes in precipitation-related extreme indices are defined as percentage ratio:

$$Y^{s,m,t} = 100 \times \left(\frac{p^{s,m,t}}{\frac{1}{30} \times \sum_{t=1983}^{2012} p^{s,m,t}} - 1 \right)\% \tag{2}$$

where s = 1, . . . , N_s, m = 1, . . . , N_m, and t = 1, . . . , N_t refer to the number of SSPs, GCMs, and years, respectively, and $p^{s,m,t}$ refer to the projected extreme indices for the s^{th} SSPs, m^{th} GCM, and t^{th} year.

Subsequently, the resulting changes ($Y^{s,m,t}$) were then smoothed into rolling decadal (i.e., 10 years) means and subjected to uncertainty decomposition. The uncertainty decomposition procedures are summarized as follows. To quantify and decompose the uncertainty, the smoothed mean change ($Y^{s,m,t}$) for all GCMs and SSPs was partitioned into a climate change signal (the smooth fit, $i^{s,m,t}$) and a residual ($\varepsilon^{s,m,t}$) by fitting fourth-order and second-order polynomial models to precipitation and temperature indices, respectively (Hawkins and Sutton, 2011; Zhang and Chen, 2021).

$$Y^{s,m,t} = i^{s,m,t} + \varepsilon^{s,m,t} \tag{3}$$

The respective means of $i^{s,m,t}$ and $\varepsilon^{s,m,t}$ were calculated as follows (Eqs. 4–6); (Eq. 7):

$$\bar{i}_{s,t}^{M} = \frac{1}{N_m} \sum_{m=1}^{N_m} i^{s,m,t} \tag{4}$$

$$\bar{i}_{S}^{m,t} = \frac{1}{N_s} \sum_{s=1}^{N_s} i^{s,m,t} \tag{5}$$

$$\vec{i}_{S,M}^{t} = \frac{1}{N_m \times N_s} \sum_{s=1}^{N_s} \sum_{m=1}^{N_m} i^{s,m,t} \tag{6}$$

$$\bar{\varepsilon} = \frac{1}{N_m \times N_s \times N_t} \sum_{s=1}^{N_s} \sum_{m=1}^{N_m} \sum_{t=1}^{Nt} \varepsilon^{s,m,t} \tag{7}$$

The component of the uncertainty due to the GCMs was then estimated as the variance of the multi-scenario averages:

$$M^t = \frac{1}{N_m} \sum_{m=1}^{N_m} \left(\bar{i}_{S}^{m,t} - \vec{i}_{S,M}^{t} \right)^2 \tag{8}$$

Likewise, the component of the uncertainty due to the SSPs was then estimated as the variance of the multi-model averages:

$$S^t = \frac{1}{N_s} \sum_{s=1}^{N_s} \left(\bar{i}_{M}^{s,t} - \vec{i}_{S,M}^{t} \right)^2 \tag{9}$$

On the other hand, the uncertainty due to the internal climate variability corresponds to the variance of the residuals from the fits over all GCMs, SSPs, and projection period (i.e., 2020–2095, $N_t = 75$).

$$V = \frac{1}{N_m \times N_s \times N_t} \sum_{s=1}^{N_s} \sum_{m=1}^{N_m} \sum_{t=1}^{N_t} \left(\bar{\varepsilon} - \varepsilon^{s,m,t} \right)^2 \tag{10}$$

In our present study, we assumed no interaction effects between GCMs and SSPs, and equal weights were given for all GCMs despite the different performances (Zhang and Chen, 2021). The total uncertainty (T^t) is, therefore, the sum of the uncertainty due to GCMs, SSPs, and internal climate variability.

$$T^t = S^t + M^t + V \tag{11}$$

The signal-to-noise (S/N) ratio was calculated to understand the influence of uncertainties on projected climate extreme indices over time (Hawkins and Sutton, 2009).

$$(S/N)^t = \frac{\vec{i}^t}{1.65 \times \sqrt{T^t}} \quad (12)$$

A larger S/N ratio implies that the projected uncertainties are smaller relative to the average climate change signal (Hawkins and Sutton, 2011; Zhang et al., 2011). The uncertainty of projected climate extreme indices was analyzed for the nine sub-regions (denoted as R1-R9) of Ethiopia that were identified based on homogeneous rainfall zones by Rettie et al. (2023).

3 Results and discussion

3.1 Temperature indices

Measuring the performance of the climate models in capturing the observed climate extreme indices is an important part of climate studies. Figure 2 shows the Taylor diagrams comparing the performance of the GCMs and their ensemble average in reproducing the different temperature extreme indices in the observation data (i.e., CHIRPS and CHIRTS) during 1983–2012. For most of the temperature-related extreme indices, the correlation coefficients range from 0.2 to 0.60. A larger range of correlation coefficients is found for extremes such as TN10p, TX90p, TN10p, TN90p, SU, and TR (refer Table 2). For absolute temperature indices like TNn, TXn, WSDI, and CSDI, the correlation coefficients (r) are very low. However, the interannual variation expressed by the standard deviations (SD) of the observation was well reproduced by most of the GCMs. Most of the indices simulated were well below 1.5 SD relative to the SD of the observations. For TX10p, WSDI and CSDI indices, many of the GCMs produced lower variability compared to the observations. The diagrams also show that the *centered RMSE* is well below 1.5 units relative to the SD of observations. The smallest error was found for TX90p and TX10p. The *centered RMSE* quantified the differences in two fields, in our case the indices in the observation data and the indices simulated by the GCMs. The diagram further shows that the GCMs ensemble average reduced both the errors (*centered RMSE*) and the interannual variability (SD) while the correlation coefficients (r) were increased for majority of the temperature-related indices indicating that the GCMs ensemble average performance was better than individual GCMs. The individual model as well as their ensemble average performance also varied at the regional level (Supplementary Figures S1, S2). In their multi-model study in China, Wei et al. (2022) also reported that GCMs ensemble averages of climate extreme outperform those by individual models. The models' skill was much better for the drier and hotter sub-regions (i.e., R1, R2, and R4) compared to the cooler highland regions. More importantly, the improvement from the GCMs ensemble average was more pronounced at the regional scale (Supplementary Figure S2).

Figures 3–5 show the spatial distribution of annual trends in temperature-related extreme indices in the projected climate (2020–2100) under the three SSPs in comparison to the corresponding trends in the observed climate (1982–2012). The figures clearly show significant trends in both observations and projections for all indices except for projected cold spell duration indices (CSDI). Looking at the percentile indices, higher warm extreme indices (TX90p and TN90p) are expected in future climate ranging from 4% (SSP2-4.5) to 10% (SSP5-8.5) per decade compared to approximately 3% per decade increase in the observation period. Based on the CHIRPS data (i.e., the same observed data as in our study), Gebrechorkos et al. (2019b) reported similar patterns of extreme temperature trends for the pasty climate (1979–2010). Changes of higher magnitude of temperature extremes were reported at local level studies (Birhan et al., 2022). The increasing trend in warm extreme indices is confirmed by increasing trends in other warming indicators such as summary days (SU), tropical nights (TR), and warm spell duration (WSDI). The number of summer days (SU) and tropical nights (TR) are expected to increase by up to 35 days and 50 days, respectively, particularly in the highland regions under the SSP5-8.5 scenario. Similar increasing trends are expected for the warm spell duration index (WSDI), which could increase by up to 45 days per decade under the SSP5-8.5 scenario. The results also indicate that the magnitude the warm percentile indices expected to increase would be higher than the magnitude the cold percentile indices are expected to decrease. The relatively stronger downward trend of cold extreme indices (i.e., TX10p and TN10p) over the observation period (~4% per decade) is expected to decrease in future climate by ~1% per decade under the SSP5-8.5 scenario. On the other hand, the absolute extreme maximum and minimum temperature indices (TXx, TXn, TNn, and TNx) show spatially heterogeneous patterns, not solely, but particularly in the observations. However, largely significant increasing trends of the absolute extreme maximum and minimum temperature indices are expected in the future climate, especially under the higher emission scenarios (SSP3-7.0 and SSP5-8.5). For instance, under the SSP5-8.5 emission scenario, the predicted absolute maximum of maximum temperature (TXx) and minimum of minimum temperature (TNn) trends could reach up to 6° C (8° C) per decade in the warmest (northeastern) region of the country (see Figure1). This is a very relevant finding since a few incidences of such magnitude of extreme temperatures have harmful effects on crop growth (He and Chen, 2022) and would have a devastating impact on crop yields (Vogel et al., 2019). As to be expected, the projected trends consistently increase from lower (SSP2-4.5) to higher (SSP5-8.5) emission scenarios.

3.2 Precipitation indices

The Taylor diagrams in Figure 6 indicate the performance of the individual GCMs with respect to the precipitation-related extreme indices in the observation data (i.e., CHIRPS) during 1983–2012. The GCMs had difficulties reproducing the observed data even at the sub-regional level (Supplementary Figures S3, S4). The correlation coefficients (r) of most precipitation-related extreme indices were below 0.4. The simulated variability in precipitation was considerably higher than the observed one

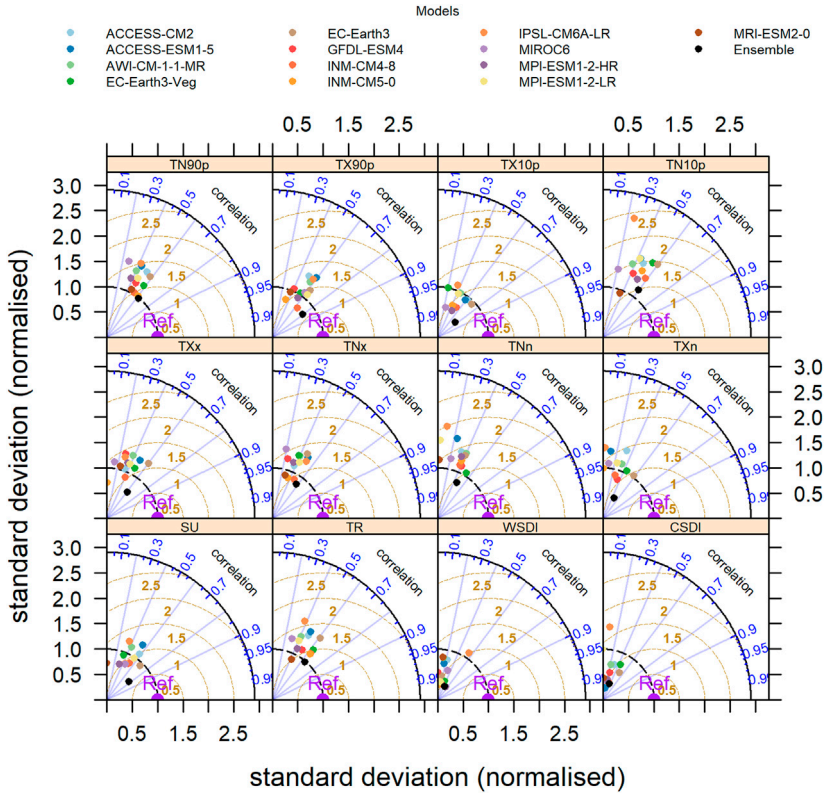

FIGURE 2
Taylor diagrams comparing the skill of the Global Climate Models (GCMs) in reproducing the observed (1983–2012) temperature related indices. The azimuthal axis shows the correlation coefficients. The radial distance from the origin represents the variability (SD), while the distance from the "Ref" point is the centered RMSE (brown dashed lines) difference between the GCMs and observed temperature related indices.

where the standard deviations normalized to the observations are mostly around 2, with R20mm, R95pTOT, and R99pTOT showing values up to 3. The errors between the GCMs and the observation (*centered RMSE*) were within 2 units. The diagrams reveal that the GCMs ensemble average reduced both the error (*centered RMSE*) and the interannual variability (SD). However, for the majority of the indices, the correlation coefficients did not improve. Overall, regarding the precipitation-related indices, the GCMs performed much less well than for the temperature-related indices. The spatial distribution of the trend in precipitation-related extreme indices in the observed climate (1982–2012) and the projected climate (2020–2100) under the three SPSs are presented in Figures 7–9. The spatial patterns show that the observed trends were largely statistically significant (i.e., shown as areas with patches) across most of the indices except for R1mm, R10mm, R20mm, and Rx5day for some pocket areas in the western and southeastern parts of the country. The southeastern part of the country which belongs to the driest regions of the country [see Figure 1A; also refer to Rettie et al. (2023)] exhibited a significant increase in maximum 5-day precipitation (Rx5day), which is equivalent to an increase of 10 days per decade. Beyene et al. (2022) also found a significantly increasing trend in Rx5day the southern region, mainly Omo-Gibe and Rift Valley lake basins. Whereas the western part bordering Sudan showed a significantly increasing number of wet days (R1mm) by roughly 5 days per decade. The trends in number of wet days were however not significant in all scenarios. Largely increasing trends were also reported in Beyene et al. (2022) for R10 mm indices for Ethiopia of which 20% of the grids were statistically significant. Cattani et al. (2018) analyzed seasonal rainfall variability and trends over East Africa for 1983–2015. They found that R1mm and R20 mm show decreasing trend during October-December and an increasing trend during March-May seasons for the larger part of East Africa. On the other hand, as in the observed climate, significantly increasing trends are projected for maximum 5-day precipitation (Rx5day) where the trends were significant across the large parts of the country. Likewise, generally increasing trends were projected for number of days with more than 10 mm (R10 mm) and 20 mm (R20 mm) indices. They were significant across large parts of the country. Regarding the precipitation totals and wet days, exceptionally higher increases were projected under SSP3-7.0 in a small pocket region in the northwestern part of the country, which was statistically significant as well (Figure 9). The projected change for the indicated pocket region was more than 25 days per year increase both for very wet (R95pTOT) and extremely very wet (R99pTOT) days. Our results are in line with Gebrechorkos et al.

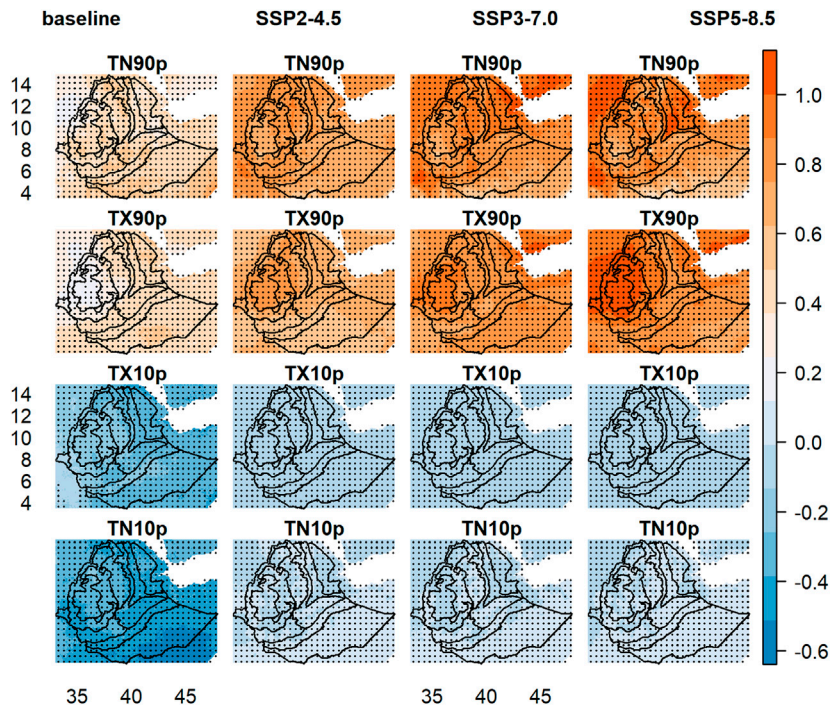

FIGURE 3
Spatial distribution of annual historical (1983–2012) and projected (2020–2100) trends (Sen's slope) in multi-GCMs averaged temperature indices (TN90p, TX90p, TX10p, and TN10p in % units) under the three SSPs. The areas under patches (depicted as signs) show significant ($p < 0.05$, MK test) trends.

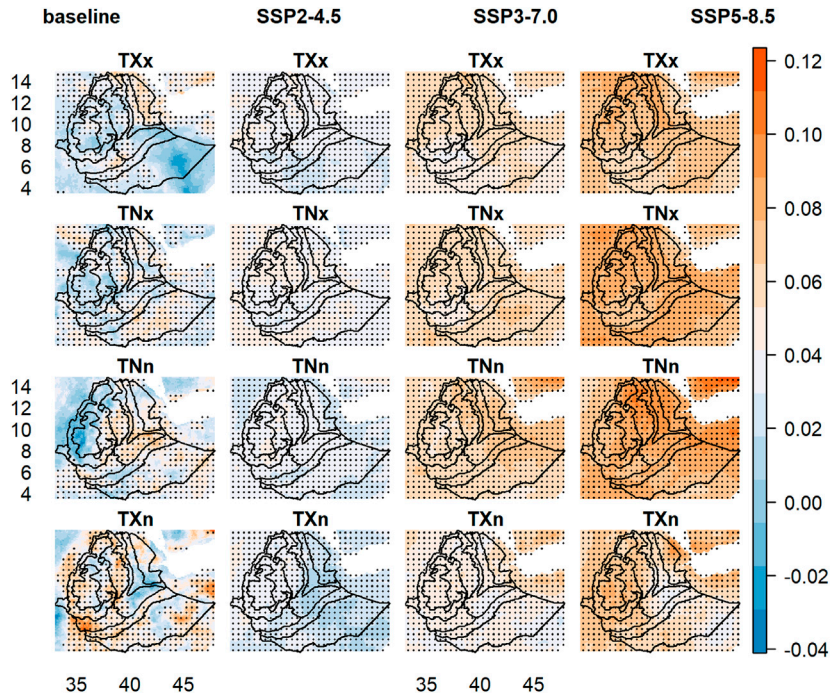

FIGURE 4
Same as Figure 3 but for indices: TXx, TNx, TNn and TXn in °C.

(2019a), who found a significantly increased trend in R99pTOT and R99pTOT in southern Ethiopia for the period of 1981–2010. Unlike the temperature indices, the trends in precipitation are generally heterogeneous in terms of spatial distribution, magnitude, and statistical significance as well as across the different emission scenarios (SSPs). Despite the large spatial

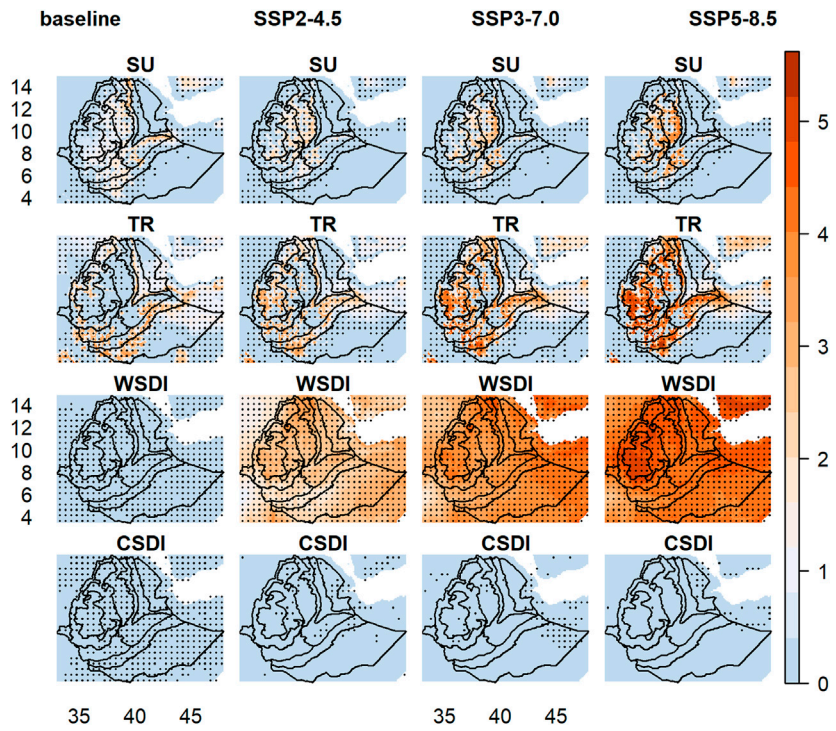

FIGURE 5
Same as Figure 3 but for indices: SU, TR, WSDI and CSDI in days.

inconsistency, the overall results suggested that there are indications for an increase in the frequency of the most intense precipitation events.

3.3 Projection uncertainty

We assessed the three components of climate change uncertainty (i.e., model (GCM), scenario (SSP), and internal climate variability) for all climate extreme indices for the 9 sub-regions defined by Rettie et al. (2023); Figures 10–13 present the evolution of the three components over time for the temperature-related indices (Figure 10; Figure 11) and precipitation-related indices (Figure 12; Figure 13). The figures show that, for temperature-related indices, a general decreasing contribution of uncertainties from the GCMs and internal variability to the total uncertainty while the reverse was true for the uncertainty from SSPs. These findings were largely consistent across the different regions of the country. Accordingly, the uncertainty from the GCMs accounts for about 64%–88% of the total uncertainty at the beginning of the projection period (i.e., 2020). This proportion decreased to about 45%–67% by the end of the projection period (i.e., 2100). Meanwhile, the contribution from the internal variability decreased from about 11%–32% at the beginning of the projected climate to less than 15% by the end of the century. Summer days (SU) are an exception here, with a slight projected increase. On the other hand, the fraction of uncertainty from the SSPs increased from less than 1% in 2020 to 18%–54% by the end of the century. Our results are consistent with previous studies that in the beginning projections are usually dominated by uncertainties from GCMs and internal variability (Zhang and Chen, 2021). The results were consistent across the temperature indices except for the cold spell duration index (CSDI) where the SSPs' contribution to the total uncertainty remained negligible.

In contrast to the temperature indices, the total projection uncertainty of precipitation-related indices was dominated by the contribution from the GCMs and the internal climate variability, with marginal contribution from the SSPs. However, the fractional contribution from the GCMs and internal variability varies among the different indices. For CDD, CWD, R1mm, and Rx1day, a large proportion (~57–87%) of the total uncertainty was due to the internal climate variability whereas, for the rest of the precipitation indices, the contribution from the GCMs is considerable. Mendoza Paz and Willems. (2022) also found that the larger proportions of the uncertainty in the projected precipitation extremes were related to the GCMs. In addition, the contribution of model uncertainty increases with a lead time for most of the precipitation indices except for CDD, CWD, R1mm, and Rx1day. Results were consistent across the different sub-regions. Compared to the temperature indices, internal climate variability was an important source of uncertainty for precipitation-related indices. Previous studies also showed the relative importance of the uncertainty from

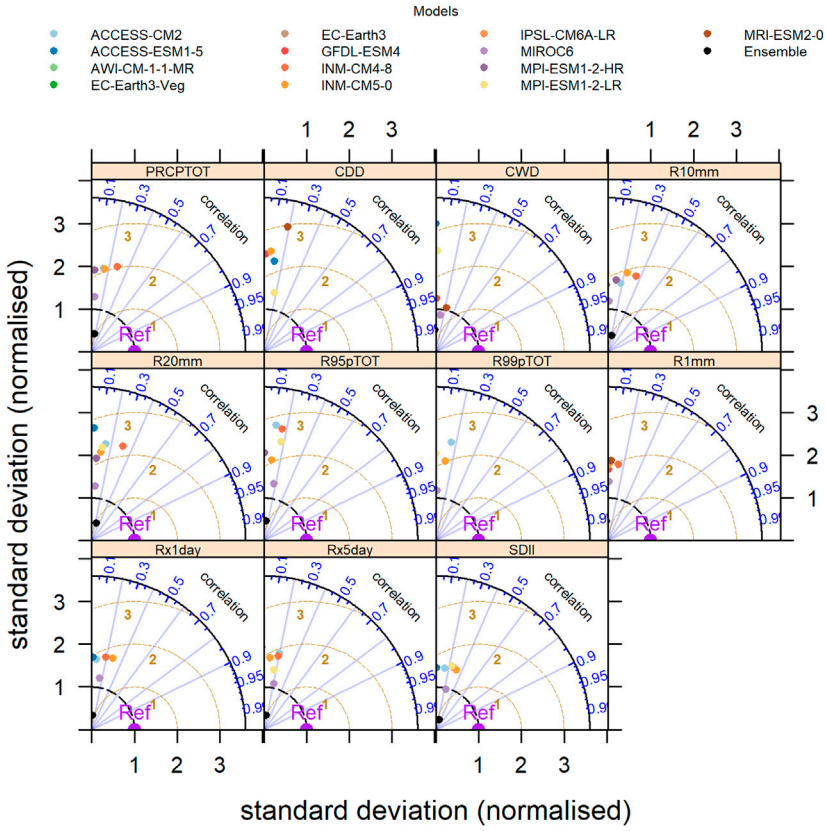

FIGURE 6
Taylor diagrams comparing the skill of the Global Climate Models (GCMs) in reproducing the observed (1983–2012) precipitation related indices. The azimuthal axis shows the correlation coefficients. The radial distance from the origin represents the variability (SD), while the distance from the "Ref" point is the centered RMSE (brown dashed lines) difference between the GCMs and observed precipitation related indices.

the internal climate variability for precipitation-related indices (e.g., Hawkins and Sutton, 2011; Fatichi et al., 2016; Gu et al., 2018).

To reduce the high uncertainty associated with the precipitation indices, we suggest further investigation based on multiple reference data sets (Grusson and Barron, 2021; Madakumbura et al., 2021) and as far as possible, station-based observation data (Cattani et al., 2018; Kim et al., 2019). Fatichi et al. (2016) claimed that the rigorous assessment of historic climate variability may give sufficient information about future changes in precipitation extremes. In addition, seasonal level analysis (Cattani et al., 2018; Ademe et al., 2020; Gemeda et al., 2021; Ali Mohammed et al., 2022; Beyene et al., 2022; Teshome et al., 2022) could also help to reduce the uncertainty compared to annual level analysis (this study) given the high spatial variability in the country.

3.4 Robustness of the projections

Finally, we quantified the signal-to-noise ratio (S/N) to demonstrate the influence of uncertainties on projected climate extreme indices over time (Hawkins and Sutton, 2009) and hence to evaluate the robustness of the projected changes in climate extremes (Hawkins and Sutton, 2009; 2011; Zhang et al., 2011). Figure 14 and Figure 15 present the S/N ratio for the temperature and precipitation-related indices, respectively, for the different sub-regions.

Largely consistent across the temperature-related indices, the signal-to-noise values increased in general with time, but with considerable regional variation (Figure 14). This implies that the magnitude of projected changes was greater than the magnitude of the associated uncertainty and hence the projected changes are reliable. However, the S/N ratio reaches peak values by the mid of the century (i.e., between 2050–2060) for temperature intensity indices (TXx, TXn, TNx, and TNn) with slightly decreasing values with projection time. The peaks around the mid of the century could be related to the shift in the contribution of uncertainties from the different sources (i.e., GCMs, SSPs, and internal climate variability). Zhang et al. (2011) reported a similar period where the shift in the contribution of uncertainty among the various sources occur. Regional comparisons show that sub-region R8 (which is the wettest region in the country, cf. Rettie et al. (2023)) shows a higher S/N ratio for most of the temperature-related indices while sub-region R1 (which belongs to the driest regions in the country) shows relatively lower S/N, particularly for coldness indices (i.e., CSDI, and TX10p).

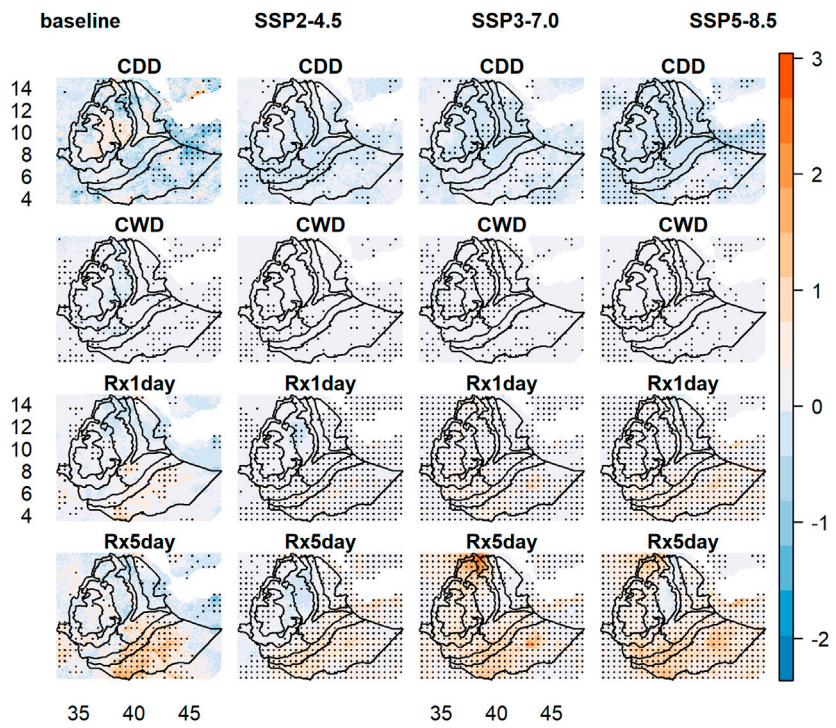

FIGURE 7
Spatial distribution of observation (1983–2012) and projected (2020–2100) trends (Sen's slope) in multi-GCMs averaged precipitation indices (CDD and CWD in days, and Rx1day and Rx5day in mm) under the three SSPs. The patches show significant ($p < 0.05$, MK test) trends.

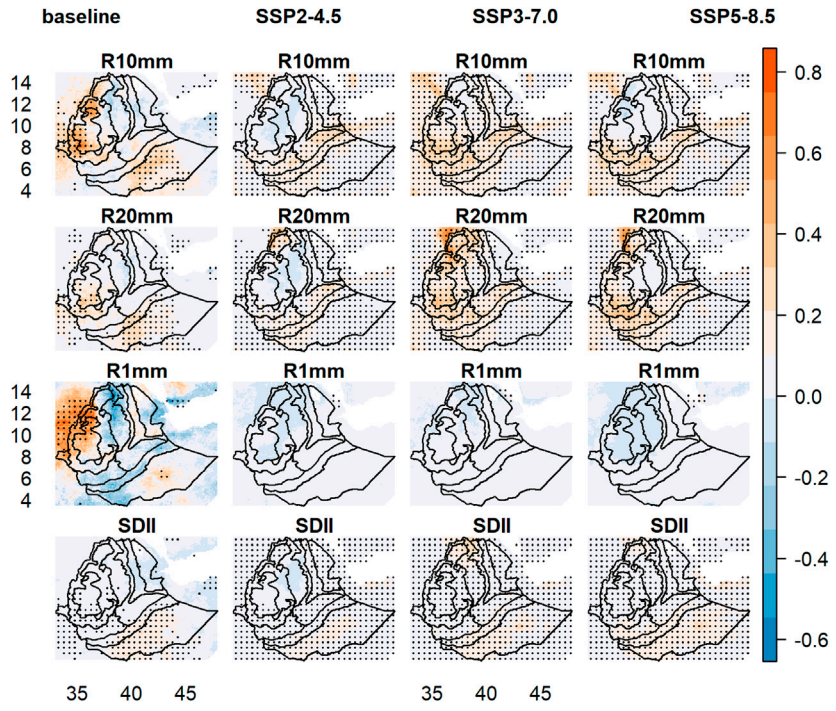

FIGURE 8
Same as Figure 7 but for indices: Number of heavy precipitation days with at least 10 mm (R10 mm) and 20 mm (R20 mm), number of wet days (R1mm), and simple daily intensity (SDII, mm).

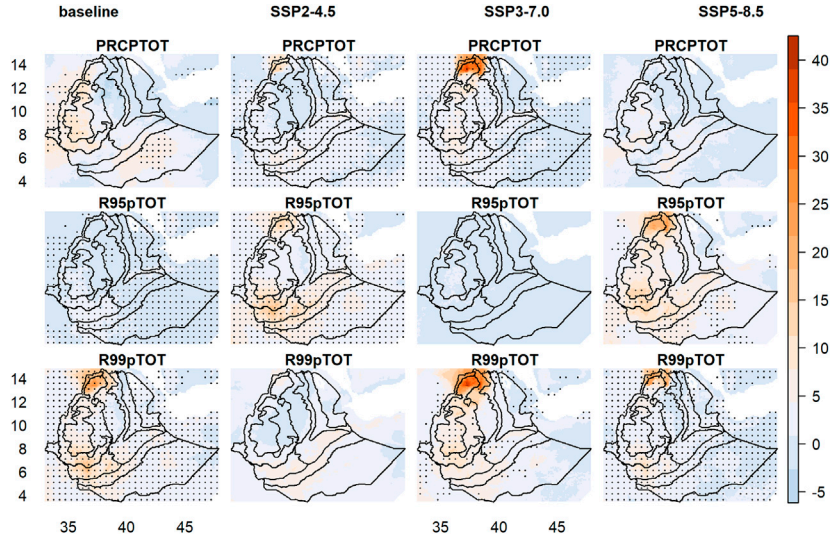

FIGURE 9
Same as Figure 7 but for indices: Total wet-day precipitation (PRCPTOT), very wet days total (R95pTOT), and extremely wet days total (R99pTOT) all in mm.

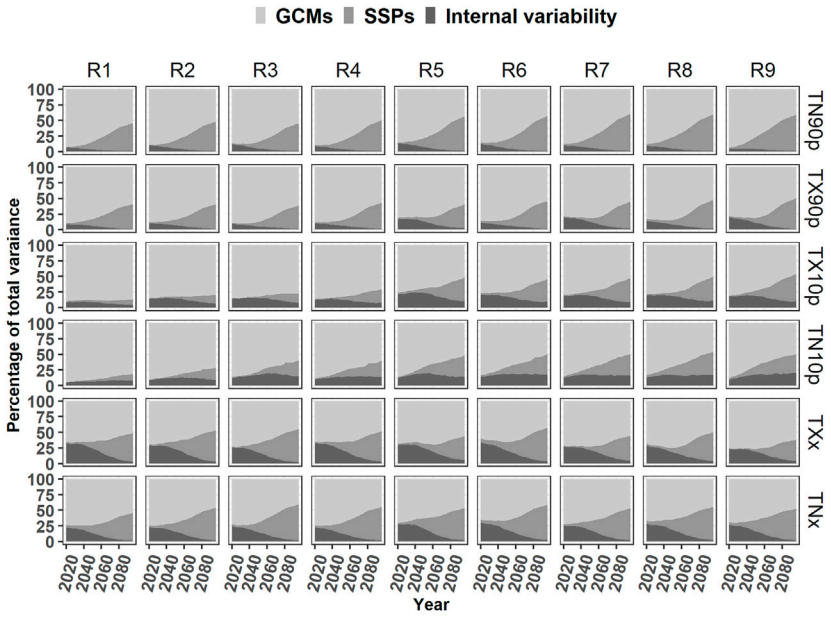

FIGURE 10
Percentage share of uncertainty for temperature indices depicted by sub-regions over 2020–2100.

Precipitation-related extremes are key for climate change adaptation as the country's economy is heavily dependent on rainfed agriculture. The S/N ratio was below unity despite a slight increment with projection time (Figure 15) for most of the precipitation indices indicating that the magnitude of projected changes was smaller than the associated uncertainty. This implies that the projected changes are associated with high uncertainty and make the projection less reliable and not well-suited as a basis for decision-making. Achieving reliable projections for precipitation has been a challenge due to its associated higher uncertainties compared to temperature (Madakumbura et al., 2021; Zhang and Chen, 2021; Birhan et al., 2022). On the other hand, located near the

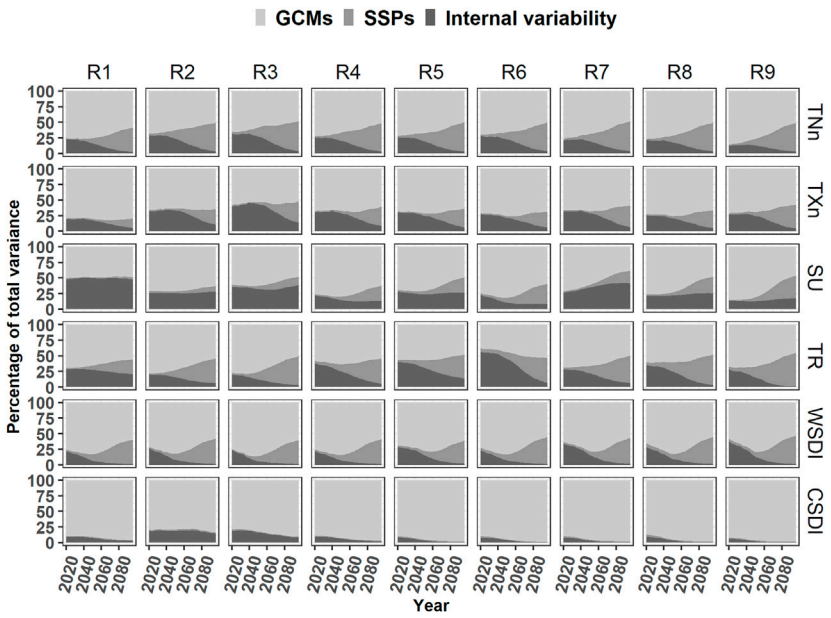

FIGURE 11
Same as Figure 10 but for indices: TNn, TXn, WSDI, CSDI, SU, and TR.

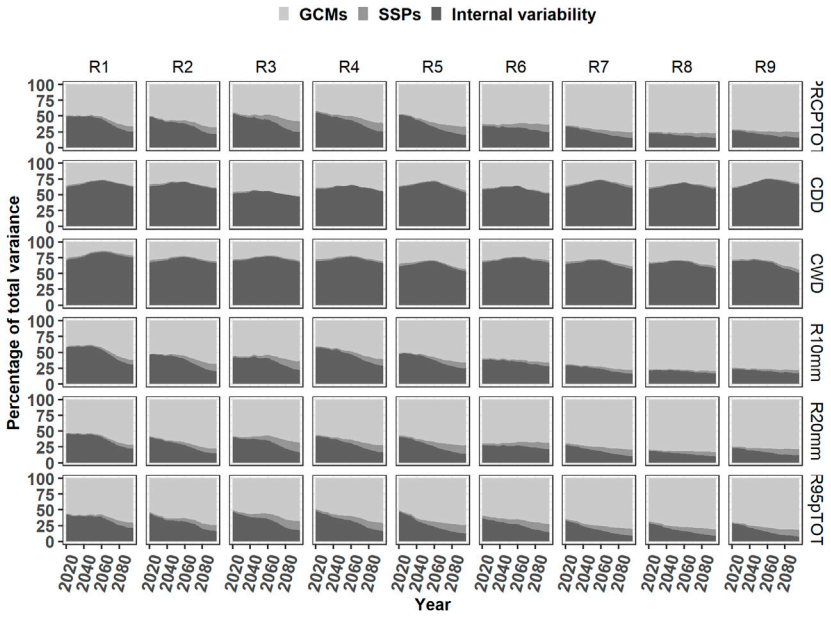

FIGURE 12
Percentage share of uncertainty for precipitation indices depicted by sub-regions over 2020–2100.

equator and the Indian Ocean, the effects of the bi-annual migration of the Inter-Tropical Convergence Zone (ITCZ) and the El Niño–Southern Oscillation (ENSO) are the most important climate systems governing precipitation across Ethiopia (Korecha and Barnston, 2007). In this regard, one of the limitations of the current study is attributed to the structural deficiency of the climate models used in the study in reasonably simulating these major climate systems. The majority of state-of-the-art GCMs fail to simulate realistic ENSO characteristics (Beobide–Arsuaga et al., 2021) and the double- ITCZ bias remains one of the most

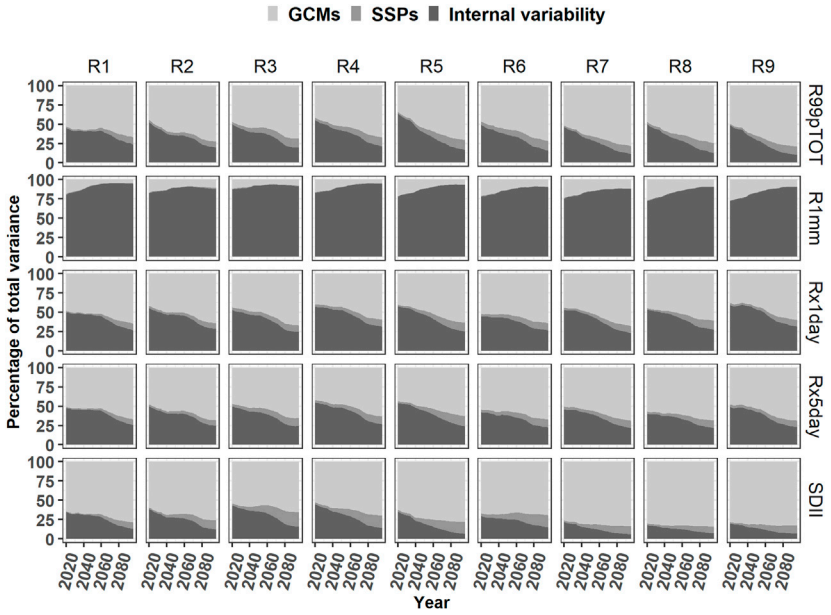

FIGURE 13
Same as Figure 12 but for indices: SDII, Rx1day, Rx5day, CDD, and CWD.

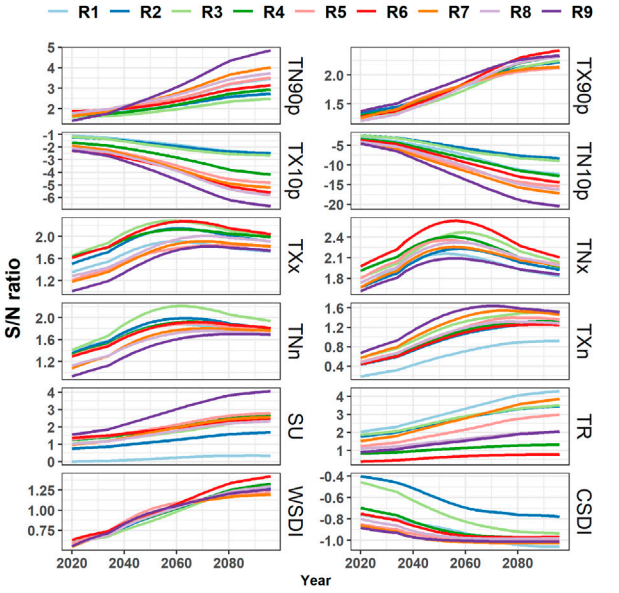

FIGURE 14
Signal-to-noise ratios for temperature indices depicted by sub-regions over 2020–2100.

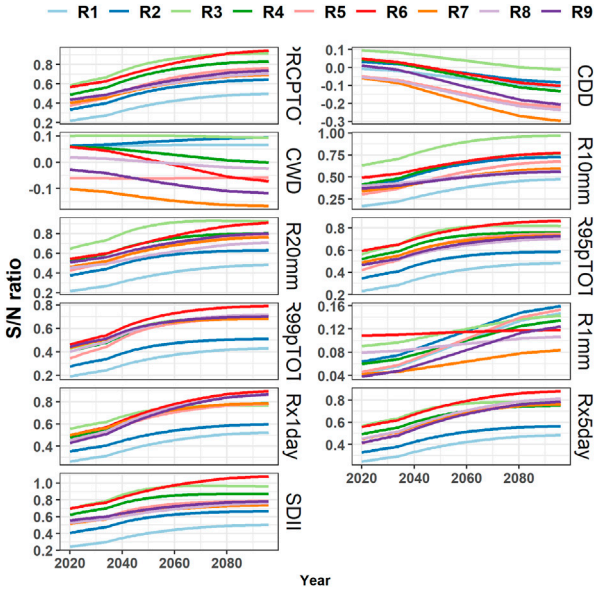

FIGURE 15
Signal-to-noise ratios for precipitation indices depicted by sub-regions over 2020–2100.

outstanding errors in the models (Tian and Dong, 2020). Given these model deficiencies, their long-term prediction of climate extremes might be affected as well. Therefore, the results of our study particularly those of precipitation-derived extreme indices should be taken with caution. Despite these limitations, the regional comparisons suggest that fewer homogeneous clusters could be sufficient for the kind of studies treated in this paper (Ware et al., 2022).

4 Conclusion

Climate extremes in Ethiopia were comprehensively assessed until the end of the 21st century by producing and evaluating a large set of extreme climate indicator indices. The study constitutes a large number of state-of-the-art CMIP6 models covering a spectrum of emission scenarios at high spatial resolution. By evaluating the

individual model performance during the base period, we estimated the possible change in the trends of projected climate extremes. The results were supplemented by a rigorous assessment of the uncertainties associated with the projected extremes. The projected trends for temperature-related indices are largely statistically significant and spatially consistent and much more reliable than the precipitation-related indices. Our study on projected changes in climate extremes at the national level was produced to serve as a baseline for future national or regional level analysis. In this context, we recommend further assessments to evaluate the effects of projected climate extremes on crop model and/or hydrological model outputs.

Data availability statement

Publicly available datasets were analyzed in this study. This data can be found here: figshare.com.

Author contributions

Conceptualization: FR, SG, and TS; methodology, formal analysis, visualization, software and validation and writing—original draft preparation: FR; supervision, investigation and resources: SG, TW, and TS; writing–review and editing: FR, SG, TW, KT, and TS; project administration and funding acquisition: SG and TS; All authors have read and agreed to the published version of the manuscript.

Funding

This publication is an output of a PhD scholarship at the University of Hohenheim in the framework of the project "German-Ethiopian SDG Graduate School: Climate Change Effects on Food Security (CLIFOOD)" between the University of Hohenheim (Germany) and the Hawassa University (Ethiopia), supported by the DAAD with funds from the Federal Ministry for Economic Cooperation and Development (BMZ), funding code 57316245. Additionally, this work was supported by the Collaborative Research Center 1253 CAMPOS (Project 7: Stochastic Modelling Framework), funded by the German Research Foundation (DFG, Grant Agreement SFB 1253/1 2017). The funders had no role in study design, data collection and analysis, decision to publish, or preparation of the manuscript.

Acknowledgments

The authors acknowledge the support by the state of Baden-Württemberg through bwHPC.

Conflict of interest

The authors declare that the research was conducted in the absence of any commercial or financial relationships that could be construed as a potential conflict of interest.

Publisher's note

All claims expressed in this article are solely those of the authors and do not necessarily represent those of their affiliated organizations, or those of the publisher, the editors and the reviewers. Any product that may be evaluated in this article, or claim that may be made by its manufacturer, is not guaranteed or endorsed by the publisher.

Supplementary material

The Supplementary Material for this article can be found online at: https://www.frontiersin.org/articles/10.3389/fenvs.2023.1127265/full#supplementary-material

References

Ademe, D., Ziatchik, B. F., Tesfaye, K., Simane, B., Alemayehu, G., and Adgo, E. (2020). Climate trends and variability at adaptation scale: Patterns and perceptions in an agricultural region of the Ethiopian Highlands. *Weather Clim. Extrem.* 29, 100263. doi:10.1016/j.wace.2020.100263

Afuecheta, E., and Omar, M. H. (2021). Characterization of variability and trends in daily precipitation and temperature extremes in the Horn of Africa. *Clim. Risk Manag.* 32, 100295. doi:10.1016/j.crm.2021.100295

Alaminie, A. A., Tilahun, S. A., Legesse, S. A., Zimale, F. A., Tarkegn, G. B., and Jury, M. R. (2021). Evaluation of past and future climate trends under CMIP6 scenarios for the UBNB (Abay), Ethiopia. *WaterSwitzerl.* 13, 2110. doi:10.3390/w13152110

Ali Mohammed, J., Gashaw, T., Worku Tefera, G., Dile, Y. T., Worqlul, A. W., and Addisu, S. (2022). Changes in observed rainfall and temperature extremes in the upper blue nile basin of Ethiopia. *Weather Clim. Extrem.* 37, 100468. doi:10.1016/j.wace.2022.100468

Bayable, G., Amare, G., Alemu, G., and Gashaw, T. (2021). Spatiotemporal variability and trends of rainfall and its association with pacific ocean sea surface temperature in west harerge zone, eastern Ethiopia. *Environ. Syst. Res.* 10, 7. doi:10.1186/s40068-020-00216-y

Belete, M., Deng, J., Wang, K., Zhou, M., Zhu, E., Shifaw, E., et al. (2020). Evaluation of satellite rainfall products for modeling water yield over the source region of Blue Nile Basin. *Sci. Total Environ.* 708, 134834. doi:10.1016/j.scitotenv.2019.134834

Beobide-Arsuaga, G., Bayr, T., Reintges, A., and Latif, M. (2021). Uncertainty of ENSO-amplitude projections in CMIP5 and CMIP6 models. *Clim. Dyn.* 56, 3875–3888. doi:10.1007/s00382-021-05673-4

Berhane, G., Dereje, M., Minten, B., and Tamru, S. (2017). *The rapid–but from a low base–uptake of agricultural mechanization in Ethiopia: Patterns, implications and challenges*. Washington, D.C.; Addis Ababa, Ethiopia: International Food Policy Research Institute. Available at: http://ebrary.ifpri.org/cdm/ref/collection/p15738coll2/id/131146.

Beyene, T. K., Jain, M. K., Yadav, B. K., and Agarwal, A. (2022). Multiscale investigation of precipitation extremes over Ethiopia and teleconnections to large-scale climate anomalies. *Stoch. Environ. Res. Risk Assess.* 36, 1503–1519. doi:10.1007/s00477-021-02120-y

Birhan, D. A., Zaitchik, B. F., Fantaye, K. T., Birhanu, B. S., Damot, G. A., and Tsegaye, E. A. (2022). Observed and projected trends in climate extremes in a tropical highland region: An agroecosystem perspective. *Agroecosystem perspective* 42, 2493–2513. doi:10.1002/joc.7378

Brown, M. E., Funk, C., Pedreros, D., Korecha, D., Lemma, M., Rowland, J., et al. (2017). A climate trend analysis of Ethiopia: Examining subseasonal climate impacts on crops and pasture conditions. *Clim. Change* 142, 169–182. doi:10.1007/s10584-017-1948-6

Cattani, E., Merino, A., Guijarro, J. A., and Levizzani, V. (2018). East Africa Rainfall trends and variability 1983-2015 using three long-term satellite products. *Remote Sens.* 10, 931–1026. doi:10.3390/rs10060931

IPCC (2022). "Climate change 2022: Impacts, adaptation and vulnerability," in *Contribution of working group II to the sixth assessment report of the intergovernmental panel on climate change* Editors, D. C. Roberts, M. Tignor,

E. S. Poloczanska, K. Mintenbeck, A. Alegría, M. Craig, et al. (Cambridge, UK; New York, NY, USA: Cambridge University Press). doi:10.1017/9781009325844

Dendir, Z., and Birhanu, B. S. (2022). Analysis of observed trends in daily temperature and precipitation extremes in different agroecologies of gurage zone, southern Ethiopia. *Adv. Meteorology* 2022, 1–13. doi:10.1155/2022/4745123

Dinku, T., Funk, C., Peterson, P., Maidment, R., Tadesse, T., Gadain, H., et al. (2018). Validation of the CHIRPS satellite rainfall estimates over eastern Africa. *Q. J. R. Meteorological Soc.* 144, 292–312. doi:10.1002/qj.3244

Diro, G. T., Grimes, D. I. F., and Black, E. (2011). Large scale features affecting ethiopian rainfall. *Adv. Glob. change Res.* 43, 1–50. doi:10.1007/978-90-481-3842-5_2

El Kenawy, A. M., McCabe, M. F., Vicente-Serrano, S. M., López-Moreno, J. I., and Robaa, S. M. (2016). Changes in the frequency and severity of hydrological droughts over Ethiopia from 1960 to 2013. *Cuad. Investig. Geogr.* 42, 145–166. doi:10.18172/cig.2931

Esayas, B., Simane, B., Teferi, E., Ongoma, V., and Tefera, N. (2018). Trends in extreme climate events over three agroecological zones of southern Ethiopia. *Adv. Meteorology* 2018, 1–17. doi:10.1155/2018/7354157

Eshetu, F., and Mehare, A. (2020). Determinants of ethiopian agricultural exports: A dynamic panel data analysis. *Rev. Mark. Integration* 12, 70–94. doi:10.1177/0974929220969272

Fatichi, S., Ivanov, V. Y., Paschalis, A., Peleg, N., Molnar, P., Rimkus, S., et al. (2016). Uncertainty partition challenges the predictability of vital details of climate change. *Earth's Future* 4, 240–251. doi:10.1002/2015EF000336

FEWS NET (2022). Extreme food insecurity persists in the north while outcomes deteriorate in the south amid historic drought. Available at: https://reliefweb.int/report/ethiopia/ethiopia-food-security-outlook-june-2021-january-2022.

Funk, C., Peterson, P., Landsfeld, M., Pedreros, D., Verdin, J., Shukla, S., et al. (2015). The climate hazards infrared precipitation with stations - a new environmental record for monitoring extremes. *Sci. Data* 2, 150066–150121. doi:10.1038/sdata.2015.66

Gebrechorkos, S. H., Hülsmann, S., and Bernhofer, C. (2019a). Changes in temperature and precipitation extremes in Ethiopia, Kenya, and Tanzania. *Int. J. Climatol.* 39, 18–30. doi:10.1002/joc.5777

Gebrechorkos, S. H., Hülsmann, S., and Bernhofer, C. (2019b). Long-term trends in rainfall and temperature using high-resolution climate datasets in East Africa. *Sci. Rep.* 9, 11376–11379. doi:10.1038/s41598-019-47933-8

Gemeda, D. O., Korecha, D., and Garedew, W. (2021). Evidences of climate change presences in the wettest parts of southwest Ethiopia. *Heliyon* 7, e08009. doi:10.1016/j.heliyon.2021.e08009

Grusson, Y., and Barron, J. (2021). Challenges in reanalysis products to assess extreme weather impacts on yield underestimate drought. *Plos Clim.* 2021, 1–11. doi:10.21203/rs.3.rs-908090/v1

Gu, H., Yu, Z., Yang, C., Ju, Q., Yang, T., and Zhang, D. (2018). High-resolution ensemble projections and uncertainty assessment of regional climate change over China in CORDEX East Asia. *Hydrology Earth Syst. Sci.* 22, 3087–3103. doi:10.5194/hess-22-3087-2018

Gummadi, S., Rao, K. P. C., Seid, J., Legesse, G., Kadiyala, M. D. M., Takele, R., et al. (2018). Spatio-temporal variability and trends of precipitation and extreme rainfall events in Ethiopia in 1980–2010. *Theor. Appl. Climatol.* 134, 1315–1328. doi:10.1007/s00704-017-2340-1

Guo, L. Y., Gao, Q., Jiang, Z. H., and Li, L. (2018). Bias correction and projection of surface air temperature in LMDZ multiple simulation over central and eastern China. *Adv. Clim. Change Res.* 9, 81–92. doi:10.1016/j.accre.2018.02.003

Hamlet, A. F., Salathé, E. P., and Carrasco, P. (2010). *Statistical downscaling techniques for global climate model simulations of temperature and precipitation with application to water resources planning studies*. University of Washington, Seattle: Center for Science in the Earth System.

Hawkins, E., and Sutton, R. (2011). The potential to narrow uncertainty in projections of regional precipitation change. *Clim. Dyn.* 37, 407–418. doi:10.1007/s00382-010-0810-6

Hawkins, E., and Sutton, R. (2009). The potential to narrow uncertainty in regional climate predictions. *Bull. Am. Meteorological Soc.* 90, 1095–1108. doi:10.1175/2009BAMS2607.1

He, X., and Chen, Z. (2022). Weather, cropland expansion, and deforestation in Ethiopia. *J. Environ. Econ. Manag.* 111, 102586. doi:10.1016/j.jeem.2021.102586

Her, Y., Yoo, S. H., Cho, J., Hwang, S., Jeong, J., and Seong, C. (2019). Uncertainty in hydrological analysis of climate change: Multi-parameter vs. multi-GCM ensemble predictions. *Sci. Rep.* 9, 4974–5022. doi:10.1038/s41598-019-41334-7

IPCC (2021). *Climate change 2021: The physical science basis. Contribution of working group i to the sixth assessment report of the intergovernmental panel on climate change*. Cambridge, UK; New York, NY, USA: Cambridge University Press. doi:10.1017/9781009157896

Kabite Wedajo, G., Kebede Muleta, M., and Gessesse Awoke, B. (2021). Performance evaluation of multiple satellite rainfall products for Dhidhessa River Basin (DRB), Ethiopia. *Atmos. Meas. Tech.* 14, 2299–2316. doi:10.5194/amt-14-2299-2021

Kemp, L., Xu, C., Depledge, J., Ebi, K. L., Gibbins, G., and Kohler, T. A. (2022). Climate Endgame: Exploring catastrophic climate change scenarios. *EARTH, Atmos. Planet. Sci.* 119, 1–9. doi:10.1073/pnas.2108146119/-/DCSupplemental

Kendall, M. G. (1962). *Rank correlation methods*. Oxford, England: Griffin.

Kim, I. W., Oh, J., Woo, S., and Kripalani, R. H. (2019). Evaluation of precipitation extremes over the asian domain: Observation and modelling studies. *Clim. Dyn.* 52, 1317–1342. doi:10.1007/s00382-018-4193-4

Kiros, F. G. (1991). Economic consequences of drought, crop failure and famine in Ethiopia, 1973-1986. *Ambio* 20, 183–185.

Korecha, D., and Barnston, A. G. (2007). Predictability of june-september rainfall in Ethiopia. *Mon. Weather Rev.* 135, 628–650. doi:10.1175/MWR3304.1

Lee, S., Qi, J., McCarty, G. W., Yeo, I. Y., Zhang, X., Moglen, G. E., et al. (2021). Uncertainty assessment of multi-parameter, multi-GCM, and multi-RCP simulations for streamflow and non-floodplain wetland (NFW) water storage. *J. Hydrology* 600, 126564. doi:10.1016/j.jhydrol.2021.126564

Li, J., Miao, C., Wei, W., Zhang, G., Hua, L., Chen, Y., et al. (2021). Evaluation of CMIP6 global climate models for simulating land surface energy and water fluxes during 1979–2014. *J. Adv. Model. Earth Syst.* 13, 1–32. doi:10.1029/2021MS002515

Liu, L. Y., Wang, X. J., Gou, X. H., Yang, M. X., and Zhang, Z. H. (2022). Projections of surface air temperature and precipitation in the 21st century in the Qilian Mountains, Northwest China, using REMO in the CORDEX. *Adv. Clim. Change Res.* 13, 344–358. doi:10.1016/j.accre.2022.03.003

Madakumbura, G. D., Thackeray, C. W., Norris, J., Goldenson, N., and Hall, A. (2021). Anthropogenic influence on extreme precipitation over global land areas seen in multiple observational datasets. *Nat. Commun.* 12, 3944. doi:10.1038/s41467-021-24262-x

Malaekeh, S. M., Safaie, A., Shiva, L., and Tabari, H. (2022). Spatio-temporal variation of hydro-climatic variables and extreme indices over Iran based on reanalysis data. *Stoch. Environ. Res. Risk Assess.* 36, 3725–3752. doi:10.1007/s00477-022-02223-0

Malede, D. A., Agumassie, T. A., Kosgei, J. R., Pham, Q. B., and Andualem, T. G. (2022). Evaluation of satellite rainfall estimates in a rugged topographical basin over south gojjam basin, Ethiopia. *J. Indian Soc. Remote Sens.* 50, 1333–1346. doi:10.1007/s12524-022-01530-x

Mann, H. B. (1945). Nonparametric tests against trend. *Econ. J. Econ. Soc.* 13, 245–259. doi:10.2307/1907187

Maurer, E. P., Hidalgo, H. G., Das, T., Dettinger, M. D., and Cayan, D. R. (2010). The utility of daily large-scale climate data in the assessment of climate change impacts on daily streamflow in California. *Hydrology Earth Syst. Sci.* 14, 1125–1138. doi:10.5194/hess-14-1125-2010

Meinshausen, M., Nicholls, Z. R. J., Lewis, J., Gidden, M. J., Vogel, E., Freund, M., et al. (2020). The shared socio-economic pathway (SSP) greenhouse gas concentrations and their extensions to 2500. *Geosci. Model. Dev.* 13, 3571–3605. doi:10.5194/gmd-13-3571-2020

Mendoza Paz, S., and Willems, P. (2022). Uncovering the strengths and weaknesses of an ensemble of quantile mapping methods for downscaling precipitation change in Southern Africa. *J. Hydrology Regional Stud.* 41, 101104. doi:10.1016/j.ejrh.2022.101104

Mohammed, Y., Yimer, F., Tadesse, M., and Tesfaye, K. (2018). Meteorological drought assessment in north east highlands of Ethiopia. *Int. J. Clim. Change Strategies Manag.* 10, 142–160. doi:10.1108/IJCCSM-12-2016-0179

Murphy, J. M., Sexton, D. M. H., Barnett, D. H., Jones, G. S., Webb, M. J., Collins, M., et al. (2004). Quantification of modelling uncertainties in a large ensemble of climate change simulations. *Nature* 430, 768–772. doi:10.1038/nature02771

Muthoni, F. K., Odongo, V. O., Ochieng, J., Mugalavai, E. M., Mourice, S. K., Hoesche-Zeledon, I., et al. (2019). Long-term spatial-temporal trends and variability of rainfall over Eastern and Southern Africa. *Theor. Appl. Climatol.* 137, 1869–1882. doi:10.1007/s00704-018-2712-1

Muthoni, F. (2020). Spatial-temporal trends of rainfall, maximum and minimum temperatures over West Africa. *IEEE J. Sel. Top. Appl. Earth Observations Remote Sens.* 13, 2960–2973. doi:10.1109/JSTARS.2020.2997075

Myhre, G., Alterskjær, K., Stjern, C. W., HodnebrogMarelle, L., Samset, B. H., Sillmann, J., et al. (2019). Frequency of extreme precipitation increases extensively with event rareness under global warming. *Sci. Rep.* 9, 16063. doi:10.1038/s41598-019-52277-4

O'Neill, B. C., Kriegler, E., Ebi, K. L., Kemp-Benedict, E., Riahi, K., Rothman, D. S., et al. (2017). The roads ahead: Narratives for shared socioeconomic pathways describing world futures in the 21st century. *Glob. Environ. Change* 42, 169–180. doi:10.1016/j.gloenvcha.2015.01.004

Pacific Climate Impacts Consortium (2020). Climdex.pcic: PCIC implementation of climdex routines. Available at: https://CRAN.R-project.org/package=climdex.pcic.

Pervin, L., and Khan, M. S. M. (2022). Variability and trends of climate extremes indices from the observed and downscaled GCMs data over 1950–2020 period in Chattogram City, Bangladesh. *J. Water Clim. Change* 13, 975–998. doi:10.2166/wcc.2021.331

Pohlert, T. (2020). Trend: Non-parametric trend tests and change-point detection. Available at: https://CRAN.R-project.org/package=trend.

Rao, X., Lu, X., and Dong, W. (2019). Evaluation and projection of extreme precipitation over Northern China in CMIP5 models. *Atmosphere* 10, 691. doi:10.3390/atmos10110691

Rettie, F. M., Gayler, S., Weber, T. K. D. D., Tesfaye, K., and Streck, T. (2023). *High-resolution CMIP6 climate projections for Ethiopia using the gridded statistical downscaling method*. Scientific Data.

Saeidizand, R., Sabetghadam, S., Tarnavsky, E., and Pierleoni, A. (2018). Evaluation of CHIRPS rainfall estimates over Iran. *Q. J. R. Meteorological Soc.* 144, 282–291. doi:10.1002/qj.3342

Sen, P. K. (1968). Estimates of the regression coefficient based on kendall's tau. *J. Am. Stat. Assoc.* 63, 1379–1389. doi:10.1080/01621459.1968.10480934

Simanjuntak, C., Gaiser, T., Ahrends, H. E., and Srivastava, A. K. (2022). Spatial and temporal patterns of agrometeorological indicators in maize producing provinces of South Africa. *Sci. Rep.* 12, 12072–12118. doi:10.1038/s41598-022-15847-7

Taye, M., Sahlu, D., Zaitchik, B. F., and Neka, M. (2020). Evaluation of satellite rainfall estimates for meteorological drought analysis over the upper blue nile basin, Ethiopia. *Geosci. Switz.* 10, 352–422. doi:10.3390/geosciences10090352

Taylor, K. E. (2001). Summarizing multiple aspects of model performance in a single diagram. *J. Geophys. Res. Atmos.* 106, 7183–7192. doi:10.1029/2000JD900719

Teshome, H., Tesfaye, K., Dechassa, N., Tana, T., and Huber, M. (2022). Analysis of past and projected trends of rainfall and temperature parameters in eastern and western hararghe zones, Ethiopia. *Atmosphere* 13, 67. doi:10.3390/atmos13010067

Tian, B., and Dong, X. (2020). The double-ITCZ bias in CMIP3, CMIP5, and CMIP6 models based on annual mean precipitation. *Geophys. Res. Lett.* 47, 1–11. doi:10.1029/2020GL087232

Tierney, J. E., Ummenhofer, C. C., and DeMenocal, P. B. (2015). Past and future rainfall in the horn of africa. *Sci. Adv.* 1, e1500682–e1500689. doi:10.1126/sciadv.1500682

Van den Hende, C., Van Schaeybroeck, B., Nyssen, J., Van Vooren, S., Van Ginderachter, M., and Termonia, P. (2021). Analysis of rain-shadows in the Ethiopian Mountains using climatological model data. *Clim. Dyn.* 56, 1663–1679. doi:10.1007/s00382-020-05554-2

Verdin, A., Funk, C., Peterson, P., Landsfeld, M., Tuholske, C., and Grace, K. (2020). Development and validation of the CHIRTS-daily quasi-global high-resolution daily temperature data set. *Sci. Data* 7, 303–314. doi:10.1038/s41597-020-00643-7

Viste, E., Korecha, D., and Sorteberg, A. (2013). Recent drought and precipitation tendencies in Ethiopia. *Theor. Appl. Climatol.* 112, 535–551. doi:10.1007/s00704-012-0746-3

Vogel, E., Donat, M. G., Alexander, L. V., Meinshausen, M., Ray, D. K., Karoly, D., et al. (2019). The effects of climate extremes on global agricultural yields. *Environ. Res. Lett.* 14, 054010. doi:10.1088/1748-9326/ab154b

Ware, M. B., Mori, P., Warrach-Sagi, K., Jury, M., Schwitalla, T., Beyene, K. H., et al. (2022). Climate regionalization using objective multivariate clustering methods and characterization of climatic regions in Ethiopia. *Meteorol. Z.* 31, 431–453. doi:10.1127/metz/2022/1093

Wei, L., Xin, X., Li, Q., Wu, Y., Tang, H., Li, Y., et al. (2022). Simulation and projection of climate extremes in China by multiple coupled model Intercomparison project Phase 6 models. *Int. J. Climatol.* 43, 219–239. doi:10.1002/joc.7751

World Bank (2022a). Agricultural irrigated land (% of total agricultural land) - Ethiopia. Available at: https://data.worldbank.org/indicator/AG.LND.IRIG.AG.ZS?view=chart&locations=ET.

World Bank (2022b). Agriculture, forestry, and fishing, value added (% of GDP) - Ethiopia. Available at: https://data.worldbank.org/indicator/NV.AGR.TOTL.ZS?locations=ET.

World Bank (2022c). Employment in agriculture (% of total employment) (modeled ILO estimate) - Ethiopia. Available at: https://data.worldbank.org/indicator/SL.AGR.EMPL.ZS?locations=ET.

World Bank (2022d). Health nutrition and population statistics: Population estimates and projections – Ethiopia. Available at: https://databank.worldbank.org/source/population-estimates-and-projections.

Yang, X., Yong, B., Yu, Z., and Zhang, Y. (2021). An evaluation of CMIP5 precipitation simulations using ground observations over ten river basins in China. *Hydrology Res.* 52, 676–698. doi:10.2166/nh.2021.151

Zambrano-Bigiarini, M., Nauditt, A., Birkel, C., Verbist, K., and Ribbe, L. (2017). Temporal and spatial evaluation of satellite-based rainfall estimates across the complex topographical and climatic gradients of Chile. *Hydrology Earth Syst. Sci.* 21, 1295–1320. doi:10.5194/hess-21-1295-2017

Zhang, S., and Chen, J. (2021). Uncertainty in projection of climate extremes: A comparison of CMIP5 and CMIP6. *J. Meteorological Res.* 35, 646–662. doi:10.1007/s13351-021-1012-3

Zhang, X., Alexander, L., Hegerl, G. C., Jones, P., Tank, A. K., Peterson, T. C., et al. (2011). Indices for monitoring changes in extremes based on daily temperature and precipitation data. *Wiley Interdiscip. Rev. Clim. Change* 2, 851–870. doi:10.1002/wcc.147

frontiers | Frontiers in Ecology and Evolution

TYPE Original Research
PUBLISHED 16 June 2023
DOI 10.3389/fevo.2023.1127875

OPEN ACCESS

EDITED BY
Edward A. Byers,
International Institute for Applied Systems Analysis (IIASA), Austria

REVIEWED BY
Mohammed Magdy Hamed,
Arab Academy for Science, Technology and Maritime Transport (AASTMT), Egypt
Shuang Yu,
Lawrence Livermore National Laboratory (DOE), United States

*CORRESPONDENCE
Yanxia Zhao
✉ zhaoyanxia@cma.gov.cn

RECEIVED 20 December 2022
ACCEPTED 15 May 2023
PUBLISHED 16 June 2023

CITATION
Sun S, Zhao Y, He Y, Xia Z, Chen S, Zhang Y and Sun Q (2023) Exacerbated climate risks induced by precipitation extremes in the Yangtze River basin under warming scenarios.
Front. Ecol. Evol. 11:1127875.
doi: 10.3389/fevo.2023.1127875

Exacerbated climate risks induced by precipitation extremes in the Yangtze River basin under warming scenarios

Shao Sun[1], Yanxia Zhao[1]*, Yan He[1], Zhihong Xia[2,3], Sining Chen[1,4], Yi Zhang[1] and Qing Sun[1]

[1]State Key Laboratory of Severe Weather, Chinese Academy of Meteorological Sciences, Beijing, China, [2]Wuhan Regional Climate Centre, Wuhan, China, [3]Three Gorges National Climatological Observatory, Yichang, China, [4]Tianjin Climate Centre, Tianjin, China

The Yangtze River basin is a typical region of the world that has a well-developed economy but is also greatly affected by multiple climate extremes. An improved understanding of future climate trends and associated exposures in this region is urgent needed to address socioeconomic risks. This research aims to quantify historical and future projected population exposure to precipitation extremes in the Yangtze basin using meteorological records and downscaled climate models. The study found that the hazard zone for precipitation extremes during baseline period was primarily located in the mid-lower Yangtze basin, particularly around the Poyang Lake watershed. Climate projections for 2050 indicate a further increase in the occurrence of precipitation extremes in this hazard zone, while a decrease in extreme events is detectable in the upper Yangtze basin under higher radiative forcing. Future socioeconomic scenarios suggest a tendency for population growth and migration towards the lower Yangtze basin, resulting in aggravated climate risks in megacities. Multi-model simulations indicate that population exposure to precipitation extremes in the lower Yangtze basin will increase by 9–22% around 2050, with both climate and population factors contributing positively. Shanghai, Changsha, Hangzhou, Ganzhou, and Huanggang are identified as hotspot cities facing the highest foreseeable risks of precipitation extremes in the Yangtze basin.

KEYWORDS

climate projection, precipitation extremes, population exposure, future scenarios, attribution analysis, Yangtze River basin

Highlights

- Climate warming leads to intensified precipitation extremes in the Yangtze basin.
- City clusters in the mid-lower Yangtze basin face elevated population exposure.
- A low-carbon pathway could substantially mitigate socioeconomic risks.

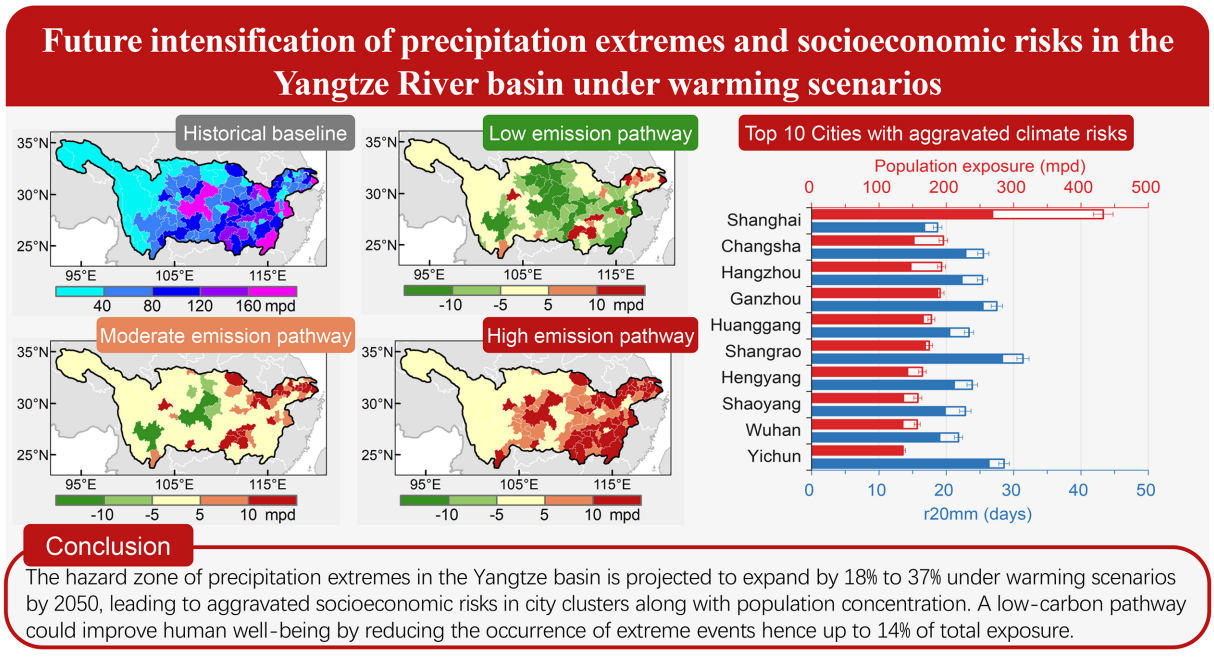

GRAPHICAL ABSTRACT

1. Introduction

The widespread emergence of precipitation extremes triggers off acute stresses on natural and human systems, and has caused extensive losses of human life, property, and infrastructures (Coumou and Rahmstorf, 2012; James et al., 2014). A warmer climate is believed to accelerate water cycle and alter precipitation patterns, leading to more extreme events in the coming future (Scoccimarro et al., 2013; Toreti et al., 2013). Recent decades, trends in the frequency, intensity, and duration of precipitation extremes have already been detected (Allan and Soden, 2008; Donat et al., 2013; Diffenbaugh et al., 2017), along with the amplified hazards and liability of climate related risks (Carleton and Hsiang, 2016). Clarification of regional complexities of extreme events has become an explicit motivation for decision makers and the public, which proves the urgency and necessity of localized climate projections.

The research into precipitation extremes has progressed enormously, partly due to the increasing number of unprecedent extreme events (Westra et al., 2014; Prein et al., 2016). Previous studies suggest that inland floods derived by precipitation extremes are likely to ascend in both frequency and magnitude as global warming (Arnell and Gosling, 2016; Wobus et al., 2017; Tellman et al., 2021). In the past half century, a rising trend of both average and extreme precipitation in China has been detected, especially in the Yangtze River basin (Guan et al., 2016; Zhou et al., 2016). Future simulations suggest that the frequency and intensity of precipitation extremes over the Yangtze basin will continue to enhance under radiative forcing (Pan et al., 2016; Li et al., 2021).

Precipitation extremes and associated secondary hazards (e.g., flash floods, landslides) are among the most destructive hazards in China. Intensified precipitation demonstrates the importance of risk projection, and population exposure is a widely used indicator to quantify potential socioeconomic risks (Jones et al., 2015). Under moderate-emission scenario, population exposure to precipitation extremes in China is expected to increase by nearly 22% by the end of 21st century (Chen and Sun, 2020), and the Yangtze Basin is identified as a global hotspot region threatened by precipitation extremes (Li et al., 2018; Sun et al., 2021). In the foreseeable future, urban land expansion and population aggregation will lead to elevated exposure to climate extremes in metropolitan regions (AghaKouchak et al., 2020). Hence, a city-level assessment of climate risks is critical for the formulation of land-use planning and urban adaptation measures.

Given that previous studies on climate risk projections are primarily conducted at global or national scales, here we take Yangtze basin, the largest river basin in China, as study region, to investigate whether there will be a significant trend in climate risks under future scenarios. We use historical observations, multi-model simulations, and socioeconomic pathways to identify (a) changes in the spatial pattern of precipitation extremes, (b) hotspot cities confronting higher socioeconomic risks, and (c) sources causing the changes in population exposure. According to hydrological and geographical differentiations, the Yangtze basin is divided into 3 sub-basins (i.e., upper, middle, and lower Yangtze basin) and 11 watersheds, as shown in Figure 1.

2. Materials and methods

2.1. Data sources

The observation dataset of gridded daily precipitation over 1981–2010 is provided by National Meteorological Information Center, China Meteorological Administration, with a spatial resolution of $0.25° \times 0.25°$. The dataset is constructed by anomaly approach method based on 2,472 meteorological stations in China, which has been widely applied as a reference to evaluate and calibrate model

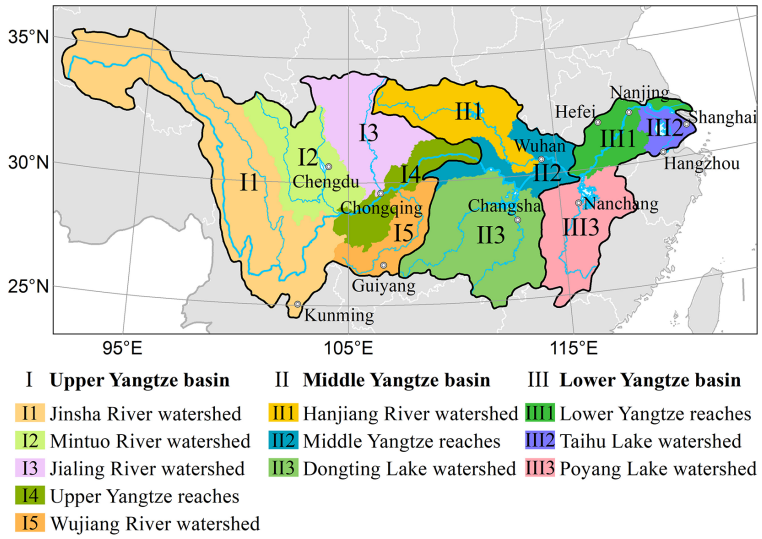

FIGURE 1
The watershed divisions and capital cities in the (I) upper, (II) middle, and (III) lower Yangtze River basin.

simulations over China (Chen et al., 2014; Wu et al., 2017). Here, we define 1981–2010 as baseline period, in consistent with the historical simulations of climate models.

The simulations from 10 climate models in the CMIP6 project (Supplementary Table S1) are selected through the availability of daily precipitation for historical run and future scenario runs (i.e., SSP1-2.6, SSP2-4.5, and SSP3-7.0; Taylor et al., 2012). The multimodel ensemble (MME) method can effectively reduce the uncertainty of the simulations, and well presents the observed patterns of daily precipitation extremes, which has been verified in numerous researches (Kharin et al., 2013; Scoccimarro et al., 2013; Sillmann et al., 2013). Only the first ensemble member ("r1i1p1f1") of each model simulation is adopted. To facilitate the intercomparison of different models, we reformat all outputs to a common $0.25° \times 0.25°$ resolution by bi-linearly interpolation, and only the values over the Yangtze basin are involved.

Shared Socioeconomic Pathways (SSPs) are coupled with representative concentration pathways (RCPs), and are often applied to project future scenarios of socioeconomic development (O'Neill et al., 2017). The projected population dataset is available at Socioeconomic Data and Applications Center (SEDAC), with 10-year intervals for 2010–2100 and a resolution of 1 km × 1 km on global land. SSP1, SSP2 and SSP3 scenarios in Shared.

Socioeconomic Pathways are selected to present population changes, which are corresponding to low-, moderate-, and high-emission scenarios (i.e., RCP2.6, RCP4.5, and RCP7.0), respectively.

2.2. Downscaling method

The Delta method is applied to calibrate and downscale the outputs of global climate models, in order to enhance resolution and reduce uncertainty of simulations at regional scales (Ramirez-Villegas and Jarvis, 2010). It is assumed the deviation between scenario and historical simulations is more reliable than both of them, and the observational datasets present local climate characteristics better than model simulations. For each output of climate models, the downscaling process consists of the following steps: (1) calculating the average of climate extremes in observational datasets of historical baseline period; (2) calculating the average of climate extremes in historical simulations of baseline period; (3) calculating the annual anomalies as absolute difference between scenario values and baseline values of model simulations; (4) interpolating annual anomalies into a higher-resolution grids in consistent with observation dataset by bi-linearly method; (5) appending the interpolated anomalies to observation baseline; (6) repeating the above steps for other model outputs; and (7) creating ensemble datasets of climate extremes under future scenarios by multi-model ensemble mean (MME) method.

2.3. Calculation of population exposure

The Expert Team on Climate Change Detection and Indices (ETCCDI) has defined a set of indices to facilitate analysis of the characteristics and evolution of climate extremes. Considering the warning criterion for meteorological hazards in the Yangtze basin, we adopt r20mm (count of days with daily precipitation amount ≥ 20 mm, also refer to as heavy precipitation days), r20mmtot (total precipitation within r20mm days), cr20mmd (maximum length of consecutive r20mm days), and rx5day (maximum 5-day precipitation) as extreme indices to reveal the changes in precipitation extremes over the Yangtze River basin. The historical baseline period is defined as 1981–2010, and the projected period is set as 2036–2065 to present climate state around 2050, driven by different future scenarios.

The population exposure is defined as the count of extreme events multiplied by the total population in each region (Jones et al., 2015). Gridded population datasets for 2000 and 2050 are used to represent population in baseline and future period, respectively. In order to avoid new errors in upscaling of gridded population, we resample all the extreme indices onto the same grid networks consistent with

population data, then all the spatial calculations and mappings are conducted on 1 km × 1 km grid cells.

Changes in population exposure to climate extremes are linked to climate change, population growth, and their interaction effects. By factorization formula (Equations 1), the contribution of climate factor, population factor, and interaction factor can be separated and quantitatively estimated. Specifically, climate factor is represented as baseline population multiplied by extreme events anomaly, population factor is represented as baseline extreme events multiplied by population growth, and interaction factor is represented as extreme events anomaly multiplied by population growth.

$$\Delta E_P = P_b \times \Delta C + C_b \times \Delta P + \Delta C \times \Delta P \quad (1)$$

where ΔE_P presents the change in population exposure between baseline period and projected period, P_b presents baseline population, ΔC presents extreme events anomaly, C_b presents baseline extreme events, and ΔP presents population growth.

3. Results

3.1. Precipitation extremes in historical observation

The spatial average of r20mm in baseline period is 13.4 days/year in the Yangtze basin, while the spatial pattern shows significant regionality between sub-basins (Figure 2A). For the lower basin, the average of r20mm reaches 22.8 days/year, with 40% grids above 25 days, chiefly located in Poyang Lake watershed. The middle basin has an annual r20mm of 17.7 days in baseline period, in which the Dongting Lake watershed exceeds 20 days and Hanjiang River watershed holds less than 15 days. The frequency of heavy precipitation is comparatively lower in the upper basin, with an average of 8.5 days/year in baseline, among which the northern parts of Jinsha River and Mintuo River watershed occur less than 5 days/year.

The spatial pattern of r20mmtot is highly consistent with that of r20mm, and their correlation coefficient reaches 0.98 (Figure 2B). The averages of r20mmtot in the upper, middle, and lower basin are 314.7, 692.2, and 912.6 mm/year, respectively. Most of the Poyang Lake watershed has an annual r20mmtot of more than 1,000 mm in baseline. A range from 600 to 1,000 mm takes place in the mid-lower Yangtze basin, as well as Taihu and Dongting Lake watersheds. The rest of Yangtze basin broadly receives a r20mmtot below 600 mm/year, in which the northern part of Jinsha watershed less than 100 mm/year.

From the perspective of the maximum length of consecutive r20mm days, the lower Yangtze basin is still detected as the hazard zone in historical period, and the correlation coefficient is 0.83 between the spatial pattern of r20mm and cr20mmd (Figure 2C). The spatial averages of cr20mmd in the upper, middle, and lower basin are 3.0, 4.5, and 5.6 days/year, respectively. Broadly, the mid-lower basin has recorded a r20mm of more than 3 days/year in baseline period, among which the central and northern parts of Poyang Lake watershed exceed 5 days/year.

Rx5day reveals the peak intensity of heavy rainfall and is widely adopted in water-related hazard assessment. The spatial pattern of rx5day in the Yangtze basin is similar to that of r20mm, with a correlation coefficient of 0.87 (Figure 2D). The spatial averages of rx5day in the upper, middle, and lower basin are 138.9, 235.8, and 321.9 mm/year, respectively. About 80% grid cells in the lower basin have recorded a rx5day of more than 250 mm/year, and the most of Dongting Lake and Jialing River watersheds has also exceeded 200 mm/year in historical observation.

3.2. Future projection of precipitation extremes

Multi-model ensemble reveals the spatial pattern of precipitation extremes around 2050 under different emission scenarios. Given the highly correlation between extreme indices, we adopt r20mm as dominant indicator to investigate the changes in precipitation extremes across the Yangtze basin. Along the low-emission pathway, r20mm will reach 14.8 (±0.3) days in the Yangtze basin around 2050, among which the grids with r20mm > 25 days and > 30 days accounts for 11.2% and 2.3%, respectively, principally distributed in the Poyang Lake watershed (Figure 3A). Under moderate-emission scenario, the Yangtze basin will experience an additional increase of r20mm to 15.4 (±0.5) days around 2050, and the proportion of grids with r20mm >25 days and > 30 days will rise to 13.7% and 3.0%, respectively (Figure 3B). As for high-emission scenario, the proportion of grids with r20mm > 30 days will further expand to 23.7% in the lower Yangtze basin, or 3.9% in the whole basin (Figure 3C).

While the hazard zone expands in the mid-lower basin, it is notable that the pattern of upper basin remains basically stable, with only a very slight increase under the highest emission scenario. It indicates that the response of precipitation extremes to climate warming in the Yangtze basin is regionally varying. By comparing the spatial differences between SSP3-7.0 and SSP1-2.6 scenarios, about one-third of grids in the upper basin show a decrease in r20mm, whereas almost all the grids in the mid-lower basin show varying degrees of increment (Figure 3D). In summarize, precipitation extremes in the Yangtze basin are projected to show a Matthew effect in radiative forcing, that is, the high-intensity zone (i.e., the mid-lower basin) will continue to expand, whereas the low-intensity zone (i.e., the upper basin) will remain stable or even gradually weaken in a warmer world.

3.3. Changes in population exposure

Population exposure to climate extremes delineates potential socioeconomic risks in the future. The combinations of socioeconomic pathways and emission pathways (e.g., SSP1-2.6) are adopted to estimate the future changes in population exposure. The SSPs are reference pathways that describe plausible alternative trends in socioeconomic evolution independently with climate change, of which SSP1, SSP2, and SSP3 denote low, intermediate, and high challenges for mitigation and adaptation, respectively (O'Neill et al., 2017). Given the limitations of visual identification caused by discontinuous population distribution in the Yangtze basin, the mappings are carried out on prefecture-level cities by spatial summation, while all the calculations are based on the population grids with a precision of 1 km × 1 km.

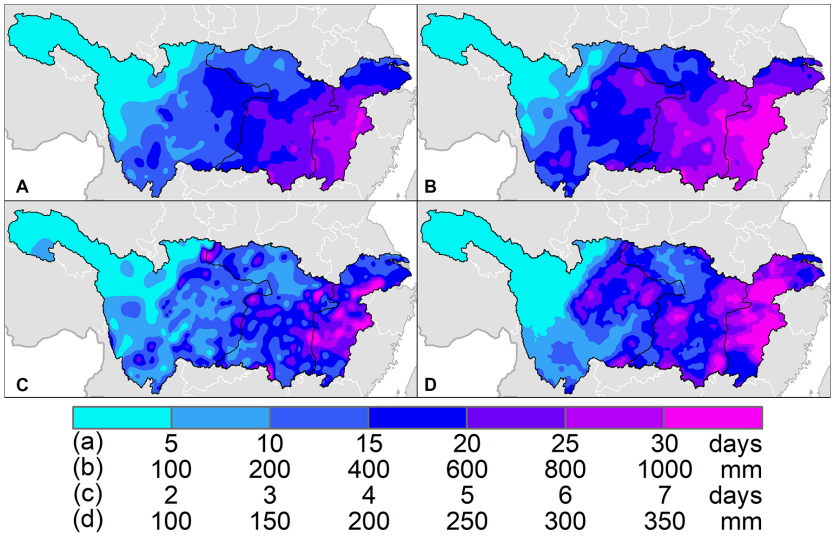

FIGURE 2
Spatial pattern of observed precipitation extremes in historical baseline. **(A)** Annual r20mm, **(B)** annual r20mmtot, **(C)** cr20mmd, and **(D)** rx5day.

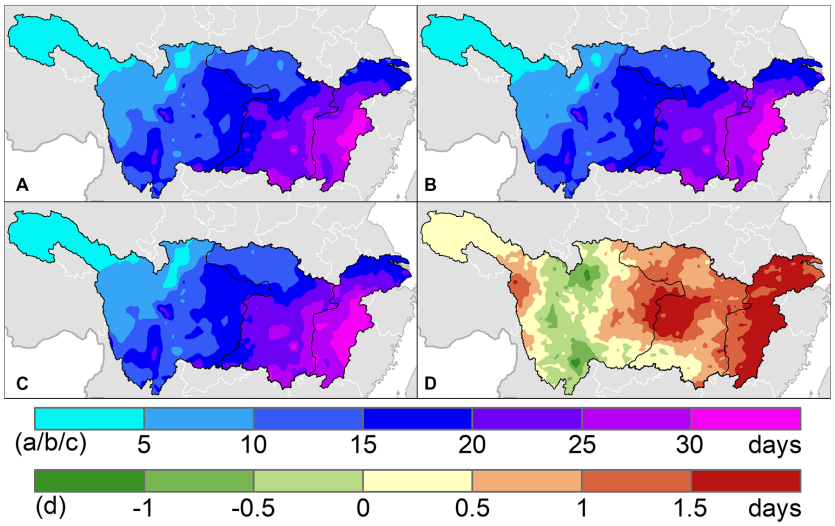

FIGURE 3
Spatial pattern of projected precipitation extremes around 2050 under **(A)** SSP1-2.6, **(B)** SSP2-4.5, and **(C)** SSP3-7.0 future scenarios over the Yangtze River basin. **(D)** The spatial difference between SSP3-7.0 and SSP1-2.6 scenarios.

Under future scenarios, the evolution of population distribution in the Yangtze basin also shows a Matthew effect, that is, the population move toward coastal megacities and provincial capitals, while the population among small-medium cities outflows gradually, particularly in the upper and middle basin. The prefectural average of population exposure to precipitation extremes is 68.7 million person-days (hereafter mpd) in baseline. High-exposure cities are principally scattered among Poyang and Dongting Lake watersheds, as well as the two megacities of Shanghai and Chongqing (Figure 4A). Along the low-emission pathway, about two-thirds of cities show a decrease in population exposure by 2050, among which the cities of Chongqing, Enshi, Liangshan, and Dazhou in the upper basin drop by more than 15 mpd (Figure 4B). The cities with increased exposure are broadly located in the lower basin and Taihu Lake watershed, among which the big cities such as Shanghai, Changsha, Hangzhou, and Nanjing experience an increase of more than 30 mpd in population exposure.

Along the moderate pathway, an increased exposure to precipitation extremes is detected in about two-thirds of cities around 2050 that mainly concentrated in the mid-lower Yangtze basin (Figure 4C). The prefectural average of population exposure raises to 74.3 (±2.8) mpd, and large coastal cities and provincial capitals remain

the most exposed areas. Under the influence of population loss, some large cities in the upper basin, such as Chongqing and Liangshan, are expected to experience a decrease in total exposure.

As for high-emission scenario (i.e., SSP3-7.0), which assumes a continuous increase in greenhouse gases and a maintenance of high fertility in the future, it seems unlikely to happen from current situation. However, revealing the potential changes under SSP3-7.0 scenario has important implications for understanding the worst situation. In this scenario, the exposure is projected to reach 78.3 (±2.9) mpd at prefectural average, with more than 90% cities experiencing increased exposure to precipitation extremes, and the increment of some majority cities in the lower basin exceeds 10 mpd (Figure 4D).

3.4. Regional evolution and contributing factors

The changes in total population exposure can be decomposed into climate contribution, population contribution and their interaction. There are large differences between future scenarios regarding exposure changes in the Yangtze basin. Along the low-emission pathway, the total exposure in whole basin will remain unchanged around 2050 due to counteraction between intensified extremes and reduced population (Figure 5A). Under moderate-emission scenario, the exposure will increase by 600 (±201) mpd on baseline, of which climate change brings a positive contribution of 888 (±210) mpd, whereas population growth brings a negative contribution of 255 mpd. As for high-emission scenario, the total exposure is projected to increase by 1,032 (±202) mpd on baseline, of which climate factor holds major contribution at 91%, while population factor only accounts for less than 8% of positive contribution.

By comparing the exposure changes from three sub-basins, it can be seen that their climate contribution rates are relatively close under multiple scenarios, while the population contributions are quite different or even opposite. The upper basin is projected to face the greatest population decline by 2050, followed by the middle basin, whereas the lower basin shows an overall increase in population simulations. In the upper basin, the climate contribution is around 200–280 mpd, while the total exposure varies with population contributions ranging from −188 (±39) mpd under low-emission scenario, to 20 (±66) mpd under moderate-emission scenario, and then to 162 (±70) mpd under high-emission scenario (Figure 5B). In the middle basin, the total exposure increment is generally higher than that of the upper basin, despite the negative contribution of population growth (Figure 5C). To be specific, the positive contribution of intensified climate is not enough to offset population decline under low-emission scenario; under moderate-emission scenario, climate contribution greatly exceeds population effect; under high-emission scenario, exposure increment is almost entirely contributed by climate change. In the lower basin, both climate factor and population factor contribute positively to the elevated exposure, which is projected to increase by 200–517 mpd under multiple scenarios around 2050 (Figure 5D). From low to high emission forcing, the absolute contribution of climate factor increases step-wisely in the range of 150–337 mpd, and the population contribution also shows a positive response.

3.5. Hot spots in the future

Hot spots refer to areas that response dramatically to climate change and confront great risk of extreme events in the coming future (Piontek et al., 2014; Turco et al., 2015; Diffenbaugh et al., 2017; Xu et al., 2019). Here, we take totally 113 prefecture-level cities in the Yangtze basin as basic units to analyze the baseline state of population exposure to precipitation extremes, and further project its changes by 2050 under moderate-emission scenario (Supplementary Table S2). In terms of precipitation extremes, Chongqing is a big city in Southwest China with the highest population exposure in both historical baseline and future scenarios, but its absolute amount is projected to decrease from 457 to 440.4 (±20.9) mpd due to population decline (Figure 6). Shanghai, the most developed city on China's east coast, has about half of Chongqing's population but only a tenth of its total area. The

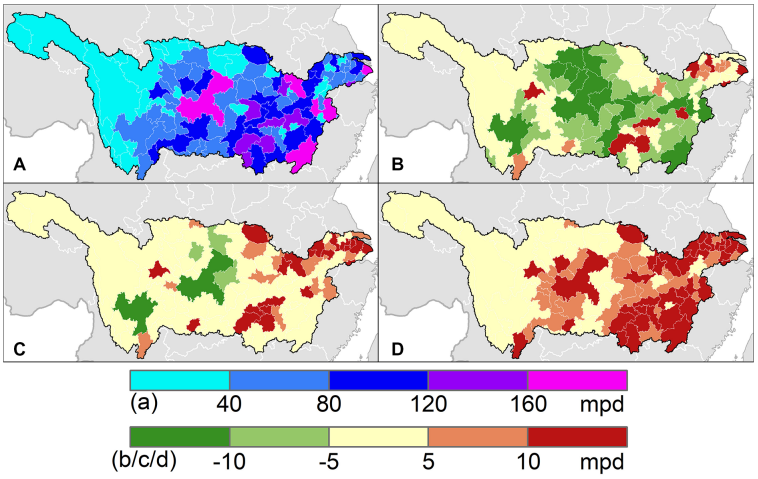

FIGURE 4
Spatial pattern of population exposure to precipitation extremes in **(A)** historical baseline, and differences from historical baseline under **(B)** SSP1-2.6 scenario, **(C)** SSP2-4.5 scenario, and **(D)** SSP3-7.0 scenario at prefecture level in the Yangtze River basin around 2050.

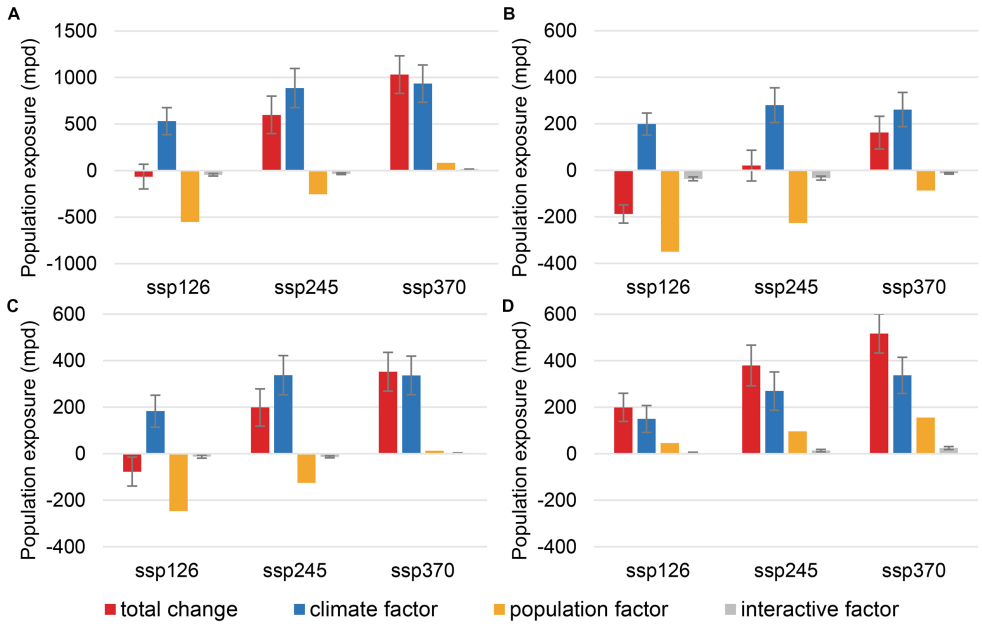

FIGURE 5
The changes in total population exposure to precipitation extremes around 2050 and its components under moderate-emission scenarios in **(A)** the whole Yangtze basin, **(B)** upper Yangtze basin, **(C)** middle Yangtze basin, and **(D)** lower Yangtze basin. The deviation range shows multi-model uncertainty.

population of Shanghai is growing rapidly which is expected to reach 22.2 million by 2050. As a result, the exposure to precipitation extremes nearly doubled from 268.6 to 433.1 (±14.5) mpd, ranking it top on the city list for intensified socioeconomic risks. The following hotspot cities are Changsha, Hangzhou, Ganzhou, Huanggang, Shangrao, Hengyang, Shaoyang, Wuhan, and Yichun. Most of these hotspots are provincial capitals and mid-sized cities with a population between 6 and 8 million, which are projected to confront a higher hazard intensity in the future, with more than 20 days of heavy precipitation per year, resulting in significantly higher population exposure than other cities in the Yangtze basin.

4. Conclusion

The incremental public understanding of explicit climate extremes assessments generates the urgency of calibrated and downscaled climate simulations. In this article, the Yangtze basin is taken as the study area, and the changes in precipitation extremes are analyzed on the basis of historical precipitation observations and the ensemble of multi-models. A series of assessments are established through quantitative models to reveal the evolution trends of precipitation extremes and population exposure in the Yangtze basin, laying a foundation for hotspot identification.

Historical observations indicate the hazard zone of precipitation extremes in the Yangtze basin are mainly located in the mid-lower basin and Dongting Lake watershed, where the indices of heavy precipitation, peak intensity, and maximum duration are ahead of the rest parts. Extreme precipitation events in the Yangtze basin are also observed with a broadly increasing trend in the past decades, among which the Poyang Lake watershed has seen the most significant changes. Future projections suggest a consistent intensification of precipitation extremes in the mid-lower basin as radiative forcing increases, while a stable or even slightly weakened trend has been detected in the upper Yangtze basin.

Population exposure to precipitation extremes represents potential socioeconomic risks under a combination of population growth pathways and carbon emission scenarios. The simulation shows that the future population distribution is expected to gather toward large cities in the lower Yangtze basin, while small and medium-sized cities in the middle and upper basins will face long-term population loss. As a result, although the total population exposure is expected to increase compared to baseline period, there are significant differences among the three sub-basins. To be specific, the population exposure in the upper Yangtze basin declines under low-emission scenario, remains unchanged under moderate-emission scenario, and goes up under high-emission scenario; the population exposure in the middle Yangtze basin shows a slight decrease along low-emission scenario, but increases significantly under both moderate- and high-emission scenarios; the population exposure in the lower Yangtze basin increases in all scenarios with both population and climate factors contribute positively.

From the perspective of socioeconomic risks, the top three hotspot cities are Shanghai, Changsha and Hangzhou, where the risk management of floods, waterlogs, and water-related compound hazards should be listed as priority issues. Other hotspot cities with higher hazard intensity (e.g., Ganzhou, Huanggang, Shangrao, Hengyang, Shaoyang, Wuhan) should also update their prevention standards in line with accelerated climate warming, while improving early-warning capabilities and developing emergency protocols to mitigate the risk of water-related disasters.

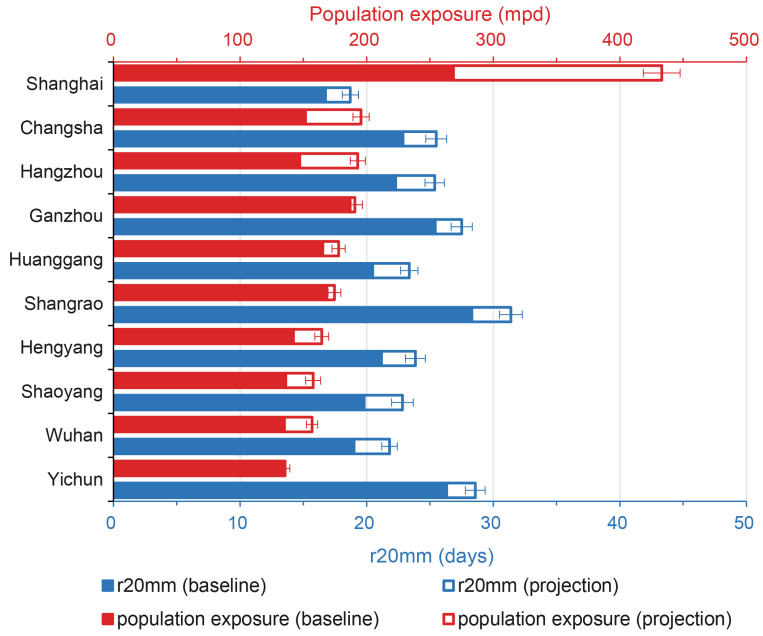

FIGURE 6
Top 10 cities with increased population exposure to precipitation extremes around 2050 in the Yangtze basin under moderate-emission scenario. The deviation range shows multimodel uncertainty.

Data availability statement

The original contributions presented in the study are included in the article/Supplementary material, further inquiries can be directed to the corresponding author.

Author contributions

YaZ: conceptualization, resources, and supervision. SS: data curation, writing—original draft preparation, and visualization. SS and YaZ: methodology. SS, YH, and SC: formal analysis. YaZ and ZX: investigation. YiZ and QS: validation. YH and SC: writing—review and editing. All authors contributed to the article and approved the submitted version.

Funding

This research was supported by the National Key Research and Development Program of China (grant no. 2022YFD2300200), the National Natural Science Foundation of China (grant no. 41701103), the Basic Research Fund of Chinese Academy of Meteorological Sciences (grant no. 2021Z010), and Hubei low-carbon pioneer project "Action plan for climate change adaptation in Hubei Province" and "Climate change facts and impact analysis in Hubei Province."

Acknowledgments

The authors would like to thank World Climate Research Programme for providing multimodel simulations based on representative concentration pathways (https://esgfnode.llnl.gov/), and the NASA Socioeconomic Data and Applications Center (SEDAC) for providing the population projections based on the Shared Socioeconomic Pathways (https://sedac.ciesin.columbia.edu/data/set/popdynamics-1-km-downscaled-pop-base-yearprojection-ssp-2000-2100-rev01).

Conflict of interest

The authors declare that the research was conducted in the absence of any commercial or financial relationships that could be construed as a potential conflict of interest.

Publisher's note

Supplementary material

The Supplementary material for this article can be found online at: https://www.frontiersin.org/articles/10.3389/fevo.2023.1127875/full#supplementary-material

References

AghaKouchak, A., Chiang, F., Huning, L. S., Love, C. A., Mallakpour, I., Mazdiyasni, O., et al. (2020). Climate extremes and compound hazards in a warming world. *Annu. Rev. Earth Planet. Sci.* 48, 519–548. doi: 10.1146/annurev-earth-071719055228

Allan, R. P., and Soden, B. J. (2008). Atmospheric warming and the amplification of precipitation extremes. *Science* 321, 1481–1484. doi: 10.1126/science.1160787

Arnell, N., and Gosling, S. (2016). The impacts of climate change on river flood risk at the global scale. *Clim. Change* 134, 387–401. doi: 10.1007/s10584-014-1084-5

Carleton, T. A., and Hsiang, S. M. (2016). Social and economic impacts of climate. *Science* 353:aad9837. doi: 10.1126/science.aad9837

Chen, H., and Sun, J. (2020). Increased population exposure to precipitation extremes in China under global warming scenarios. *Atmospher Ocean Sci Lett* 13, 63–70. doi: 10.1080/16742834.2020.1697168

Chen, X. C., Xu, Y., Xu, C. H., and Yao, Y. (2014). Assessment of precipitation simulations in China by cmip5 multi-models. *Adv. Clim. Chang. Res.* 10:217. doi: 10.3969/j.issn.1673-1719.2014.03.011

Coumou, D., and Rahmstorf, S. (2012). A decade of weather extremes. *Nat. Clim. Chang.* 2, 491–496. doi: 10.1038/nclimate1452

Diffenbaugh, N. S., Singh, D., Mankin, J. S., Horton, D. E., Swain, D. L., Touma, D., et al. (2017). Quantifying the influence of global warming on unprecedented extreme climate events. *Proc. Natl. Acad. Sci.* 114, 4881–4886. doi: 10.1073/pnas.1618082114

Donat, M. G., Alexander, L. V., Yang, H., Durre, I., Vose, R., Dunn, R. J. H., et al. (2013). Updated analyses of temperature and precipitation extreme indices since the beginning of the twentieth century: the HadEX2 dataset. *J. Geophys. Res. Atmos.* 118, 2098–2118. doi: 10.1002/jgrd.50150

Guan, Y., Zheng, F., Zhang, X., and Wang, B. (2016). Trends and variability of daily precipitation and extremes during 1960-2012 in the Yangtze River basin, China. *Int. J. Climatol.* 37, 1282–1298. doi: 10.1002/joc.4776

James, R., Otto, F., Parker, H., Boyd, E., Cornforth, R., Mitchell, D., et al. (2014). Characterizing loss and damage from climate change. *Nat. Clim. Chang.* 4:938939, 938–939. doi: 10.1038/nclimate2411

Jones, B., O'Neill, B. C., Mcdaniel, L., Mcginnis, S., Mearns, L. O., and Tebaldi, C. (2015). Future population exposure to US heat extremes. *Nat. Clim. Chang.* 5, 652–655. doi: 10.1038/nclimate2631

Kharin, V. V., Zwiers, F. W., Zhang, X., and Wehner, M. (2013). Changes in temperature and precipitation extremes in the cmip5 ensemble. *Clim. Change* 119, 345–357. doi: 10.1007/s10584-013-0705-8

Li, H., Chen, H., Wang, H., and Yu, E. (2018). Future precipitation changes over China under 1.5°C and 2.0°C global warming targets by using cordex regional climate models. *Sci. Total Environ.* 640-641, 543–554. doi: 10.1016/j.scitotenv.2018.05.324

Li, X., Zhang, K., Gu, P., Feng, H., Yin, Y., Chen, W., et al. (2021). Changes in precipitation extremes in the Yangtze River basin during 1960–2019 and the association with global warming, ENSO, and local effects. *Sci. Total Environ.* 760:144244. doi: 10.1016/j.scitotenv.2020.144244

O'Neill, B. C., Kriegler, E., Ebi, K. L., Kemp-Benedict, E., Riahi, K., Rothman, D. S., et al. (2017). The roads ahead: narratives for shared socioeconomic pathways describing world futures in the 21st century. *Glob. Environ. Chang.* 42, 169–180. doi: 10.1016/j.gloenvcha.2015.01.004

Pan, Z., Zhang, Y., Liu, X., and Gao, Z. (2016). Current and future precipitation extremes over Mississippi and Yangtze River basins as simulated in CMIP5 models. *J. Earth Sci.* 27, 22–36. doi: 10.1007/s12583-016-0627-2

Piontek, F., Müller, C., Pugh, T. A. M., Clark, D. B., Deryng, D., Elliott, J., et al. (2014). Multisectoral climate impact hotspots in a warming world. *Proc. Natl. Acad. Sci.* 111, 3233–3238. doi: 10.1073/pnas.1222471110

Prein, A., Rasmussen, R., Ikeda, K., Liu, C., Clark, M., and Holland, G. (2016). The future intensification of hourly precipitation extremes. *Nat. Clim. Chang.* 7, 48–52. doi: 10.1038/nclimate3168

Ramirez-Villegas, J., and Jarvis, A. (2010). Downscaling global circulation model outputs: the Delta method decision and policy analysis. Working paper no. 1. *Policy Anal.* 1, 1–18.

Scoccimarro, E., Gualdi, S., Bellucci, A., Zampieri, M., and Navarra, A. (2013). Heavy precipitation events in a warmer climate: results from cmip5 models. *J. Climate* 26, 7902–7911. doi: 10.1175/JCLI-D-12-00850.1

Sillmann, J., Kharin, V. V., Zhang, X., Zwiers, F. W., and Bronaugh, D. (2013). Climate extremes indices in the CMIP5 multimodel ensemble: part 1. Model evaluation in the present climate. *J. Geophys. Res. Atmos.* 118, 1716–1733. doi: 10.1002/jgrd.50203

Sun, S., Shi, P., Zhang, Q., Wang, J., Wu, J., and Chen, D. (2021). Evolution of future precipitation extremes: viewpoint of climate change classification. *Int. J. Climatol.* 42, 1220–1230. doi: 10.1002/joc.7298

Taylor, K. E., Stouffer, R. J., and Meehl, G. A. (2012). An overview of CMIP5 and the experiment design. *Bull. Am. Meteorol. Soc.* 93, 485–498. doi: 10.1175/BAMS-D-11-00094.1

Tellman, B., Sullivan, J. A., Kuhn, C., Kettner, A. J., Doyle, C. S., Brakenridge, G. R., et al. (2021). Satellite imaging reveals increased proportion of population exposed to floods. *Nature* 596, 80–86. doi: 10.1038/s41586-021-03695-w

Toreti, A., Naveau, P., Zampieri, M., Schindler, A., Scoccimarro, E., Xoplaki, E., et al. (2013). Projections of global changes in precipitation extremes from coupled model intercomparison project phase 5 models. *Geophys. Res. Lett.* 40, 4887–4892. doi: 10.1002/grl.50940

Turco, M., Palazzi, E., Hardenberg, J., and Provenzale, A. (2015). Observed climate change hotspots. *Geophys. Res. Lett.* 42, 3521–3528. doi: 10.1002/2015GL063891

Westra, S., Fowler, H., Evans, J., Alexander, L., Berg, P., Johnson, F., et al. (2014). Future changes to the intensity and frequency of short duration extreme rainfall. *Rev. Geophys.* 52, 522–555. doi: 10.1002/2014RG000464

Wobus, C., Gutmann, E., Jones, R., Rissing, M., and Martinich, J. (2017). Climate change impacts on flood risk and asset damages within mapped 100-year floodplains of the contiguous United States. *Nat. Hazards Earth Syst. Sci.* 17, 2199–2211. doi: 10.5194/nhess-2017-152

Wu, J., Gao, X., Giorgi, F., and Chen, D. (2017). Changes of effective temperature and cold/hot days in late decades over China based on a high resolution gridded observation dataset. *Int. J. Climatol.* 37, 788–800. doi: 10.1002/joc.5038

Xu, L., Wang, A., Wang, D., and Wang, H. (2019). Hot spots of climate extremes in the future. *J. Geophys. Res. Atmos.* 124, 3035–3049. doi: 10.1029/2018JD029980

Zhou, B., Xu, Y., Wu, J., Dong, S., and Shi, Y. (2016). Changes in temperature and precipitation extreme indices over China: analysis of a high-resolution grid dataset. *Int. J. Climatol.* 36, 1051–1066. doi: 10.1002/joc.4400

Frontiers in
Environmental Science

Explores the anthropogenic impact on our natural world

An innovative journal that advances knowledge of the natural world and its intersections with human society. It supports the formulation of policies that lead to a more inhabitable and sustainable world.

Discover the latest Research Topics

See more →

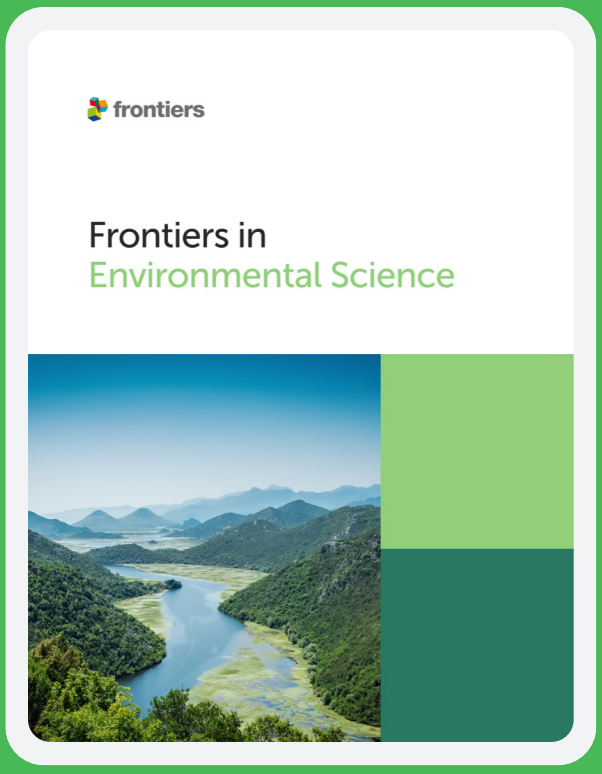

Frontiers

Avenue du Tribunal-Fédéral 34
1005 Lausanne, Switzerland
frontiersin.org

Contact us

+41 (0)21 510 17 00
frontiersin.org/about/contact